Searches for Point-like Sources of Astrophysical Neutrinos with the IceCube Neutrino Observatory

By
Jacob Feintzeig

A dissertation submitted in partial fulfillment of
the requirements for the degree of

Doctor of Philosophy
(Physics)

at the
UNIVERSITY OF WISCONSIN–MADISON
2014

Date of final oral examination: August 22, 2014

The dissertation is approved by the following members of the Final Oral Committee:

Amy Connolly, Assistant Professor, Physics
John S Gallagher, Professor, Astronomy
Francis Halzen, Professor, Physics
Albrecht Karle, Professor, Physics
Dan McCammon, Professor, Physics

ACKNOWLEDGMENTS

I am incredibly fortunate to have many supportive mentors and peers who made this work possible. I'd like to first thank my advisor Albrecht for giving me the opportunity to work on IceCube, for providing valuable guidance and advice throughout this project, and for giving me the independence to pursue ideas I found interesting.

I'd like to thank Naoko for helping me troubleshoot analysis problems and brainstorm ideas when I was stuck, and providing advice from all issues large to small. Thanks to Chad for encouraging me to think in new ways and approach problems from different angles. I'd like to express my appreciation for Chris Wendt and Gary Hill for teaching me how to do statistics, dig into the details of the data, and complete a rigorous analysis. Thanks to John Kelley for helping me get to Pole and for teaching me how to do everything once we were there. Thanks to Dima and Juan Carlos for explaining the technical details of reconstruction and simulation in many times of need. Many thanks to Markus for our many valuable physics discussions.

I owe a debt of gratitude to the large number of students and postdocs who helped me debug my code, brainstorm ideas, develop analyses, and offered their support in a myriad of small, invisible ways (not to mention provided entertaining office banter). Thanks Mike, Nathan, Claudio, Marcos, Jakob, Chris, Laura, Ben, Kyle, Moriah, Melanie, Greg, Rameez, Juanan, Kai, Rob, Mike, Leif, Ian, Frank, Zig, Dan, and undoubtedly many others.

I'd like to thank my parents, Elise and Irwin, and my siblings, Ben and Rachel, for fostering my interest in science, encouraging me to pursue grad school, and supporting me along the way. Finally, I'd like to thank Deirdre for moving to Madison, offering so much support and encouragement at every step, and now leading the way for the next adventure.

DISCARD THIS PAGE

TABLE OF CONTENTS

Page

DISCARD THIS PAGE

LIST OF TABLES

DISCARD THIS PAGE

LIST OF FIGURES

Figure Page

Figure Page

Figure Page

Chapter 1

Neutrino Astronomy

Although neutrinos are produced ubiquitously in the cosmos, the catalog of confirmed astrophysical neutrinos sources consists of only Supernova 1987A and the Sun. This leaves much uncharted territory.

The unique properties of the neutrino make them suitable as an astrophysical messenger. Interacting only via the weak force, their low cross-section allows them to travel astronomical distances without experiencing significant absorption. Neutral in charge, neutrinos follow straight paths through space even in the presence of magnetic fields. If astrophysical neutrinos are observed, they are guaranteed to point back to their location of origin.

Neutrinos are produced in hadronic interactions. Their existence was first hypothesized in 1930 by Wolfgang Pauli to solve the outstanding problem of conservation of momentum and energy in beta decay [1]. It wasn't until 26 years later that the first neutrinos were actually detected by the Cowan-Reines nuclear reactor experiment [2]. Common processes that produce neutrinos include beta decay, nuclear fission and fusion, and proton-proton (pp) collisions. On Earth, neutrinos are produced in nuclear reactors, particle accelerators, radioactive decays in the Earth's crust, and in collisions of cosmic rays with the Earth's atmosphere. Figure 1.1 shows the flux of expected neutrinos over 25 orders of magnitude in energy.

In astrophysical environments, neutrinos probe different phenomena from those normally observed in electromagnetic radiation. Nuclear fusion in the Sun produces neutrinos that

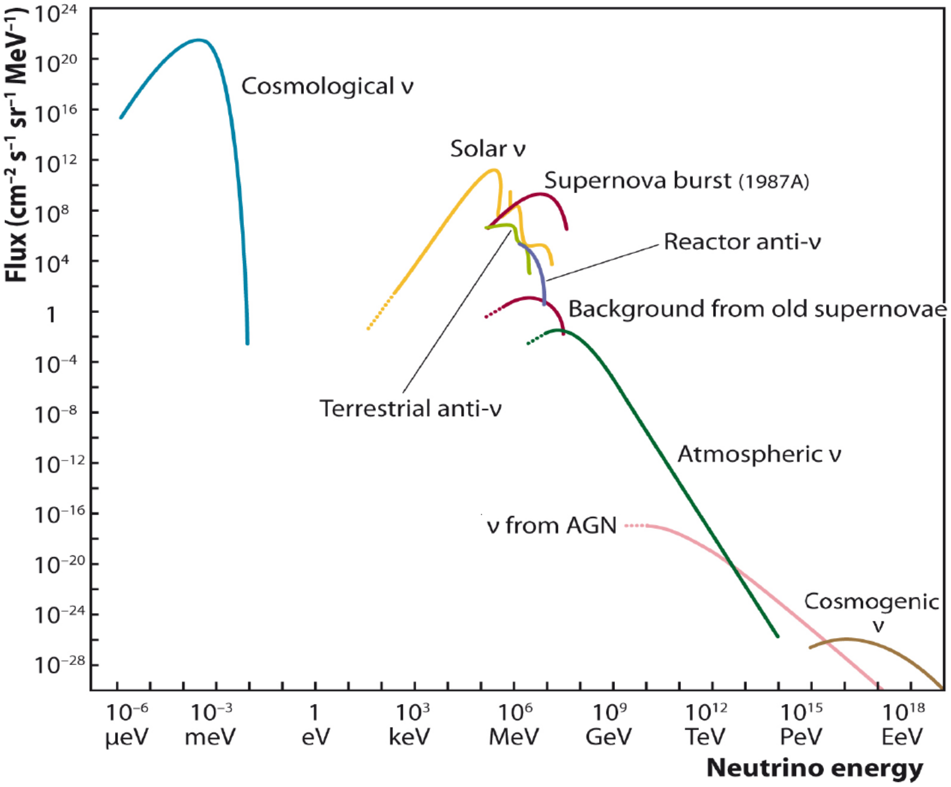

Figure 1.1: Expected and measured fluxes of neutrinos. Solar and supernova neutrinos peak in the MeV range, while neutrinos produced by cosmic ray interactions in the Earth's atmosphere dominate at GeV – TeV energies. This thesis is mainly concerned with neutrinos at TeV energies and above, where contributions from astrophysical sources such as supernova remnants and active galactic nuclei are hypothesized. Plot taken from [3].

carry information about the temperature and composition of the core. Solar neutrinos were first observed in the 1960s by the Homestake experiment [4], which found a deficit of neutrinos with respect to the expectations from the Standard Solar Model. Known as the solar neutrino problem, this anomaly was not resolved until the discovery of neutrino oscillations by the Super-Kamiokande experiment [5] and the Sudbury Neutrino Observatory [6]. An image of the neutrino emission from the Sun is shown in Figure 1.2.

The collapse of a massive star and resulting supernova explosion produces a burst of neutrinos [7]. The only supernova neutrino burst yet observed was Supernova 1987A, formed by the death of a blue supergiant star in the Large Magellanic Cloud. Three neutrino detectors - Kamiokande II, IMB, and Baksan - observed significantly elevated neutrino rates over a 13 second interval, approximately 2 hours before light from the explosion reached Earth. This not only confirmed the general mechanism of stellar collapse, but also provided robust limits on the neutrino mass, charge, and velocity [7].

This thesis is mainly concerned with astrophysical neutrinos at TeV energies and above [3, 8–11]. Until quite recently, such neutrinos had never been observed. However, IceCube has observed an excess of high-energy events that is inconsistent with the backgrounds but consistent with a diffuse flux of high-energy astrophysical neutrinos [12, 13]. The observed flux follows an energy spectrum of $E^2\phi(E) = 1.5 \times 10^{-8}(E/100\mathrm{TeV})^{-0.3}$ $\mathrm{GeVcm^{-2}s^{-1}sr^{-1}}$, is consistent with isotropic expectations, and appears to follow a $1:1:1$ neutrino flavor ratio. While this marks the beginning of high-energy neutrino astronomy, the sources of this flux remain unknown.

Neutrinos, being electrically neutral, cannot themselves be accelerated to high-energies. High-energy neutrinos must therefore be produced in the interactions of high-energy hadrons or the decay of very massive particles. Cosmic rays therefore provide a natural production mechanism for high-energy astrophysical neutrinos. Here we provide a survey of the properties of cosmic rays, cosmic-ray-induced neutrino production mechanisms, and potential sources of Galactic and extragalactic high-energy neutrinos.

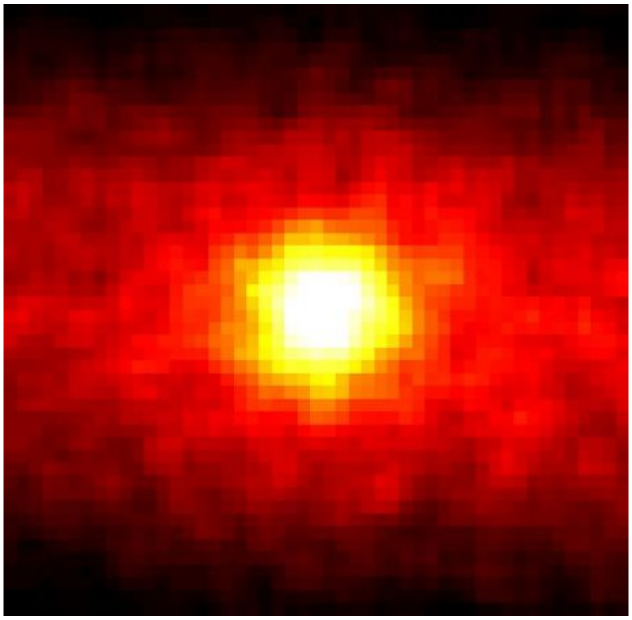

Figure 1.2: Image of neutrino emission from the Sun in data from the Super-Kamiokande experiment [5]. Brighter colors represent higher fluxes, and the image shows 90° × 90° region of sky around the sun. Image credit: R. Svoboda and K. Gordan.

1.1 The Origin of the Cosmic Rays

Cosmic rays are protons and nuclei originating from beyond the Earth, and they were first discovered by Victor Hess via a series of balloon experiments in 1911. These measurements found the rate of ionizing radiation increased at higher altitudes, signifying the origin of the radiation must be beyond the Earth [14].

Since their discovery over 100 years ago, much has been learned about the energy, composition, and angular distribution of cosmic rays. Their observed energy spectrum (Figure 1.3) extends from $\sim$ GeV to $\sim 10^{11}$ GeV. The highest energy single particles ever observed are cosmic rays. The spectrum nearly follows a single $E^{-2.7}$ power law over these 11 orders of magnitude, suggesting a common acceleration mechanism for the entire population.

The spectrum does, however, have a number of features. A break around 3×10^6 GeV is referred to as the "knee", and a spectral hardening at $\sim 10^9$ GeV is referred to as the "ankle". Cosmic rays below the knee are primarily protons, while heavier elements may dominate at higher energies [15, 16].

The spectral features likely signify the transition from a population of Galactic cosmic rays to extragalactic cosmic rays [10, 17]. At energies above the knee the gyroradius of the proton becomes larger than the size of the Galaxy, creating a softer spectrum because higher energy particles are more likely to escape. The shape of the knee is likely caused by a change in composition towards heavier nuclei, since higher-charge particles require higher energies to escape. At energies above the ankle, Galactic source classes are not believed to have the required magnetic field strength and size to accelerate particles [18]. Additionally, the observed angular distribution of the highest energy cosmic rays shows no significant correlation with the galaxy, suggesting an extragalactic origin [19, 20]. If the particles were created locally, the deflections from Galactic magnetic fields would not be large enough to explain the data.

A spectral cutoff in the cosmic-ray spectrum is observed at 4×10^{19} eV [21]. This is believed to evidence of the Greisen-Zatsepin-Kuzmin (GZK) mechanism, in which cosmic

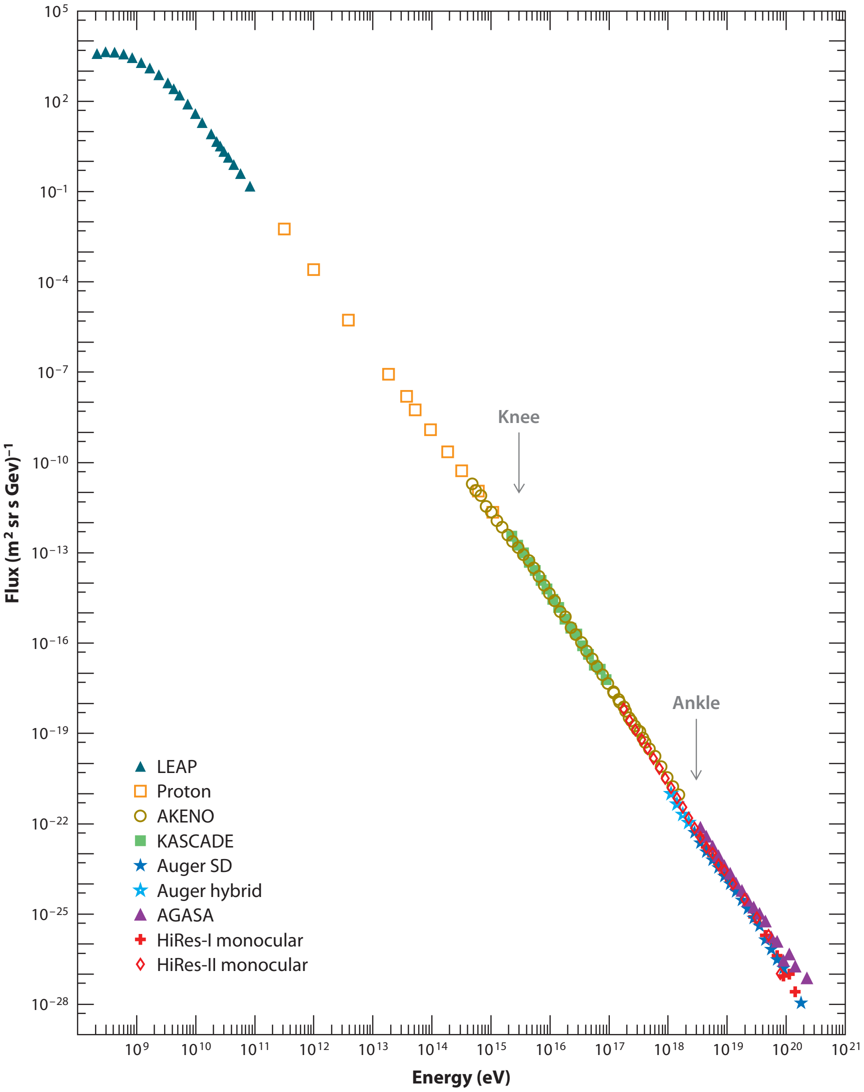

Figure 1.3: The cosmic ray energy spectrum nearly follows a single $E^{-2.7}$ power law over 11 orders of magnitude in energy. A spectral softening around 3 PeV is referred to as the knee and the spectral hardening around 4 EeV is known as the ankle. The figure shows data from air shower experiments, and is taken from [16].

rays are absorbed on cosmic microwave background (CMB) photons via the Δ^+ resonance (see Section 1.2.1) [22, 23]. This energy loss process limits the propagation of high-energy protons to ~50 Mpc (the GZK Horizon).

The mechanism by which cosmic rays acquire such extreme energies is still an active area of research. The baseline model for most scenarios is called the first-order Fermi process [24, 25]. In this process, charged particles are magnetically contained near an astrophysical shock front. A shock front is characterized by an abrupt change in density and pressure and is formed when the speed of material exceeds the speed of sound in the medium. Particles bounce back and forth across the shock front as it expands, gaining energy with each crossing [26]. This process is dominated by magnetic interactions - particles are reflected across the shock not due to collisions with other particles but due to scattering off inhomogeneities in the magnetic field on either side of the shock. Assuming particles gain a fractional amount of energy with each crossing and escape from the shock probabilistically, this resulting particle energies naturally form a power-law spectrum [26]. In strong shocks, where the shock speed is much faster than the speed of sound, an E^{-2} energy spectrum is predicted by this mechanism. Recent work in simulating the microphysics of these processes suggest deviations from straight power law spectra are also possible [27].

The Fermi mechanism requires that particles are magnetically confined in the source region for sufficient time to reach the required energies. A source of size R and magnetic field strength B can accelerate particles with charge Z to an energy $E_{\max}$ [10]:

$$E_{\max} \sim 10^{18}\mathrm{eV}\ \beta_s\ Z \left(\frac{B}{\mu\mathrm{G}}\right)\left(\frac{R}{\mathrm{kpc}}\right) \quad . \tag{1.1}$$

β_s is the relative velocity of the shock wave. This is visualized in the so-called Hillas diagram, an example of which is shown in Figure 1.4.

1.2 High-energy Astrophysical Messengers

To observe sources of high-energy cosmic rays, an observer can use the arrival directions of the cosmic rays themselves. However, since cosmic rays are charged their velocities will

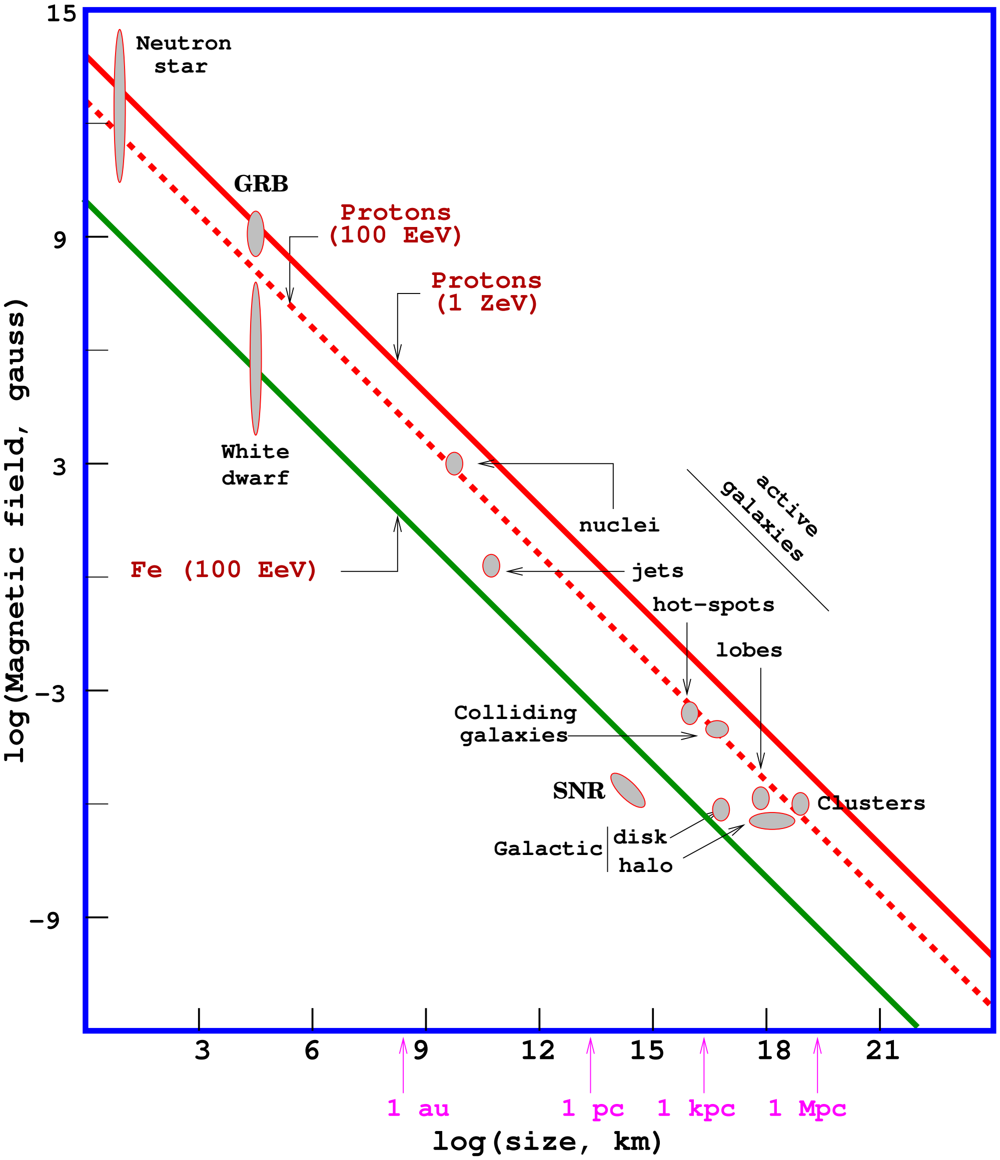

Figure 1.4: Hillas diagram [18] illustrating magnetic field strength and size of astrophysical object required to contain cosmic rays of a certain energy. Parameters of potential cosmic-ray sources are also shown, including gamma-ray bursts (GRBs), galaxy clusters, and supernova remnants (SNRs). Plot taken from [28].

change as they pass through magnetic fields. At most energies, cosmic-ray arrival directions are expected to be completely randomized upon reaching Earth due to Galactic magnetic fields. This is true to first order, although anisotropies of one part in 10^4 have been observed [29, 30]. At EeV energies, the total deflection after traveling from the source to Earth may be only a few degrees, although the exact amount depends not only on the charge and energy of the particle but also on the exact configuration of the magnetic field [9, 31].

Searching for indirect evidence of cosmic-ray acceleration using secondaries produced in cosmic-ray interactions may provide more robust evidence for a source (Figure 1.5). When high-energy hadrons interact with matter or photons near the source, charged and neutral pions are produced. These pions generally decay before interacting, producing gamma rays in the case of neutral pions and neutrinos in the case of charged pions. These gamma rays are observed by space-based and ground-based telescopes. However, multiple astrophysical processes create high-energy gamma rays. Electrons can also be accelerated via Fermi acceleration, resulting in synchrotron emission in Radio wavelengths and inverse-Compton emission at MeV – TeV energies [26]. While this emission follows a unique energy spectrum with parameters that can be constrained with lower-energy observations, attempts to disambiguate hadronic emission from leptonic emission is often difficult. Recently, the Fermi satellite has found compelling evidence for hadronic interactions using 100-MeV gamma rays from two supernova remnants interacting with molecular clouds [32]. However, attempts to fit gamma-ray emission at higher energies requires many model assumptions [26,33–35]. This method has not yet unambiguously discovered a high-energy cosmic-ray source. Additionally, gamma-rays can be absorbed by interstellar dust and intergalactic radiation fields [36], greatly suppressing the flux of TeV – PeV gamma rays available to observe.

An observation of TeV-EeV neutrino emission from a source would, however, provide unambiguous evidence for cosmic-ray interactions. The following section reviews neutrino production mechanisms.

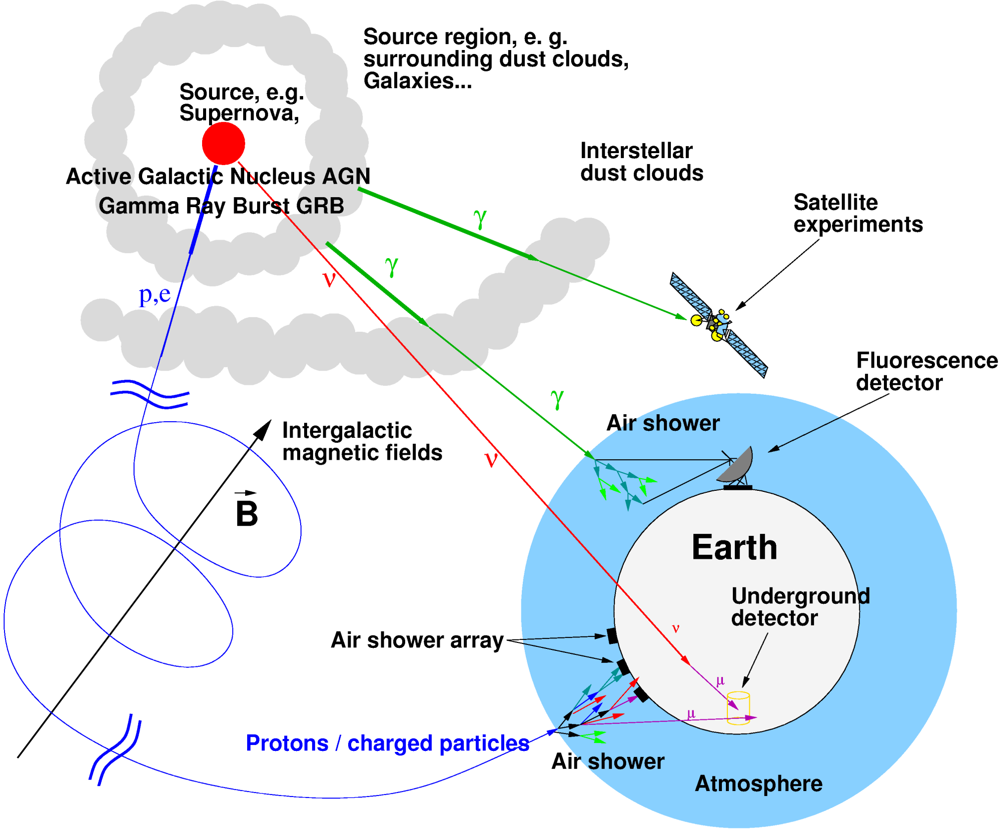

Figure 1.5: Diagram of multi-messenger astronomy. Sources can emit cosmic rays, photons, and neutrinos. Cosmic rays are deflected by magnetic fields before being observed by air shower arrays. High-energy photons are detected by space-based and ground-based telescopes, but can be absorbed by dust or low-energy background photons. Neutrinos travel straight from the source to Earth without absorption. Image credit: Wolfgang Rhode.

1.2.1 Neutrino production

After being accelerated in astrophysical sources, cosmic rays can produce neutrinos by colliding with surrounding matter or photons. The dominant interactions are [10]:

$$p\gamma\,(\rightarrow \Delta^+) \rightarrow \begin{cases} p + \pi^0 \\ n + \pi^+ \end{cases}$$

$$pp \rightarrow \begin{cases} p + p + \pi^0 \\ p + n + \pi^+ \end{cases}$$

For $n\gamma$ or pn interactions, π^- particles are created instead of π^+.

Charged pions have a mean lifetime of 10^{-8} seconds, decaying via the weak interaction to a muon and a muon neutrino. The muon will then also decay, producing additional neutrinos. Neutral pions decay electromagnetically to two gamma rays [10]:

$$\begin{aligned} \pi^+ \rightarrow & \mu^+ + \nu_\mu \\ & \quad \mu^+ \rightarrow e^+ + \nu_e + \bar{\nu}_\mu \\ \pi^- \rightarrow & \mu^- + \bar{\nu}_\mu \\ & \quad \mu^- \rightarrow e^- + \bar{\nu}_e + \nu_\mu \\ \pi^0 \rightarrow & \gamma\gamma \end{aligned}$$

This process produces neutrinos with the flavor ratio of $\nu_e : \nu_\mu : \nu_\tau = 1 : 2 : 0$ at the source. However, neutrinos oscillate as they propagate through space. For distances much larger than the oscillation length, oscillation probabilities are averaged and the resulting flavor ratio at Earth will be approximately $1 : 1 : 1$ [10, 37]. The typical energy of each neutrino follows $E_\nu \sim 1/4\; E_\pi \sim 1/20\; E_p$, so protons at the cosmic ray knee (few PeV) will create $\sim 100\,\text{TeV}$ neutrinos [11, 38].

1.3 Potential Sources of High-Energy Neutrinos

The Hillas diagram (Figure 1.4) shows a few classes of objects capable of accelerating cosmic rays to high energies. Here we consider Galactic and extragalactic objects in more detail.

1.3.1 Galactic Sources

Supernova Remnants (SNRs) are expanding shells of matter left over after a stellar explosion. The stellar material ejected from the supernova forms a shock wave that expands into interstellar space at thousands of kilometers per second for a duration of tens of thousands of years [39]. They are observed across the electromagnetic spectrum (Figure 1.6) [32, 34, 39]. Electrons are accelerated in the shock front via the Fermi process, producing radio and x-ray emission via synchrotron radiation. The $>$ MeV emission could originate from inverse-Compton scattering, bremsstrahlung, or neutral pion decay. While SNRs were one of the first proposed sources of cosmic rays [40], the hadronic origin of the gamma-ray emission in most SNRs is ambiguous at best. The exception are Fermi observations of SNRs interacting with molecular clouds [32]. SNRs are therefore predicted to be neutrino sources in which cosmic rays are accelerated in and interact near the shock front [41–46].

Pulsars and Pulsar Wind Nebulae (PWN) Pulsars are rapidly rotating, highly magnetized neutron stars. They emit beamed radiation along their spin axis, creating periodic, "pulsed" emission patterns when observed from Earth. They are observed in radio, x-rays, and gamma-rays [47]. The pulsar wind surrounds the neutron star and interacts with surrounding material to produce a shock front. A steady neutrino flux is predicted from hadrons accelerated near the neutron star surface or in the pulsar wind, and transient neutrino emission is also predicted when the pulsar is first created [48–52]. The extragalactic population of pulsars may also generate an observable neutrino flux [53].

Binaries/Microquasars Microquasars are binary systems in which a compact object accretes matter from a donor star. They often have relativistic jets and are characterized by luminous x-ray emission, which is often time-dependent or periodic. Some have been observed in TeV gamma-rays [54]. Internal shocks in the jet may accelerate protons to TeV – PeV energies via the Fermi process. Neutrinos can then be produced via $p\gamma$ interactions with synchrotron photons radiated by electrons accelerated in the jet or x-ray photons from the surrounding accretion disk [55–58].

Diffuse Galactic Emission Neutrinos can also be produced as cosmic rays diffuse through the Galactic disk. While Fermi acceleration predicts an E^{-2} energy spectrum at the source, the cosmic ray spectrum steepens to $\sim E^{-2.7}$ because propagation processes such as energy losses and advection attenuate the flux at higher energies. Neutrinos may be produced when these cosmic rays interact with the interstellar medium, creating a soft-spectrum flux coincident with the observed gamma rays emission within $\pm 2.5°$ of the Galactic latitude $b = 0$ [8, 59–62]. Diffuse gamma rays are also observed from large circular regions above and below the Galactic Center [63]. Dubbed the Fermi bubbles, the origin of emission from this region is still unclear. If the emission is due to hadronic interactions generated by star formation activity in the central region of the Galaxy, neutrino emission would be expected [64–69].

Dark Matter is a hypothesized form of matter that has yet to be detected, although there is significant evidence for its existence from galaxy rotation curves, gravitational lensing, and observations of the CMB [70]. Dark matter may accumulate at the center of astronomical bodies including the Earth, Sun, Galactic Center, and dwarf galaxies. Many dark matter models predict TeV – PeV particles that could produce neutrinos via decay or annihilation [71–73]. While many such neutrino sources would have large spatial extensions, some could appear as point sources. The analyses presented in this thesis were not optimized to discover dark matter but are sensitive to neutrino fluxes in the relevant energy range for some models.

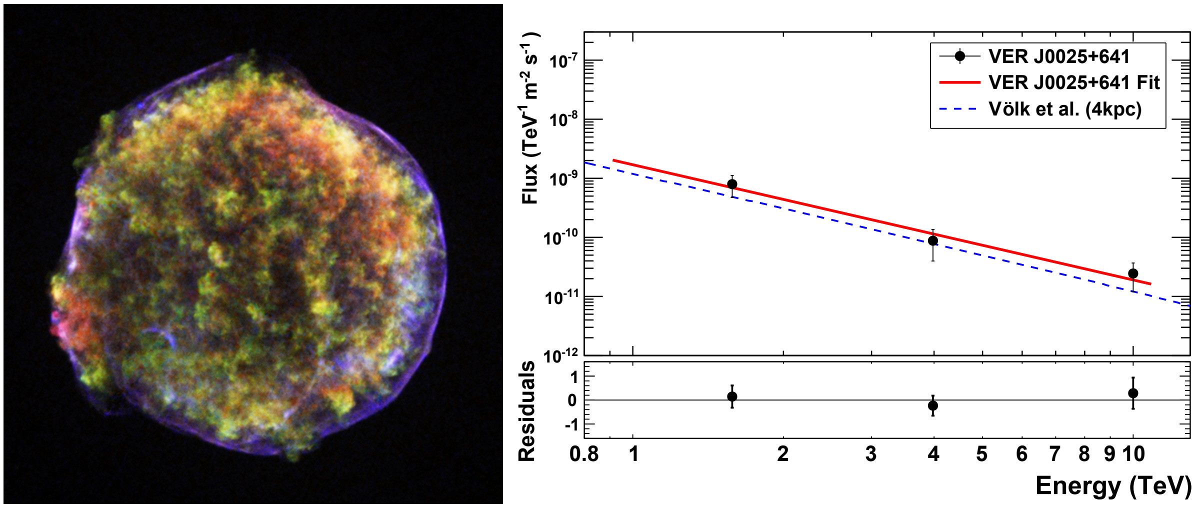

Figure 1.6: Electromagnetic observations of Tycho's supernova remnant. Left: The x-ray false color image from the Chandra observatory shows synchrotron emission from electrons accelerated in the expanding shock (blue). Image credit: NASA/CXC/Rutgers/J.Warren & J.Hughes et al. Right: TeV gamma-ray spectrum measured by VERITAS, with an $E^{-1.95}$ power-law fit. While the hadronic or leptonic origin of the gamma-rays cannot be determined unequivocally, the leptonic model requires a lower magnetic field than other observations [34] while the hadronic model from [74] is consistent with the data. Figure from [34].

1.3.2 Extragalactic Sources

Active Galactic Nuclei are extremely luminous galaxies with accretion disks surrounding the supermassive black hole at their centers. Many are observed to have relativistic collimated outflows called jets. They are observed across the electromagnetic spectrum and many have time-dependent emission with periods of enhanced activity lasting for days or weeks. Cosmic rays are hypothesized to be accelerated up to EeV energies in shocks formed either by infalling matter near the AGN core or by colliding matter in the jets [75, 76]. These cosmic rays may then interact with x-rays and other photons in the AGN or nearby, producing a flux of high-energy neutrinos and photons [77–82].

Starburst Galaxies have intense star formation activity thought to be triggered by galaxy mergers [83]. The elevated star formation rate endures for millions of years, leading to higher than average supernova rates. As discussed above, SNRs are likely sources of cosmic ray acceleration. Starburst galaxies may effectively act as calorimeters if this cosmic-ray population interacts with the interstellar medium, leading to neutrino production via pp interactions [33, 84–88]. The neutrino flux would likely have a cutoff in the PeV energy range due to the maximum energy of the SNRs.

Galaxy Clusters are hypothesized to accelerate cosmic rays in Mpc-scale shocks formed by accretion of matter onto the cluster or in termination shocks of galactic winds [89, 90]. Such cosmic rays could then create neutrinos and gamma rays after interacting with the inter-cluster medium or background photon population [91, 92]. While some galaxy clusters could be observed as point sources, many of the closest clusters have extents of a few degrees.

Gamma-Ray Bursts are the most luminous sources in the universe. These transients emit gamma-rays over milliseconds to hundreds of seconds, and are thought to be caused by massive star collapse or compact objects collisions [9]. This is theorized to create a relativistic fireball consisting of electrons, gamma-rays, and baryons [93]. As the fireball expands cosmic rays could be accelerated in strong shocks formed by colliding shells of plasma. Neutrinos are then produced when these cosmic rays interact with gamma rays inside the fireball. Neutrino production is predicted to be dominated by the Δ^+ resonance and peak in the PeV range [93–98]. So far, no neutrinos have been observed to be coincident with gamma-ray bursts, constraining many models [99].

GZK Neutrinos The cosmic-ray spectrum has a cutoff at 4×10^{19} eV. This is consistent with cosmic-ray absorption on the CMB via the GZK mechanism, in which cosmic rays lose energy via $p\gamma$ interactions at the Δ^+ resonance. This process also creates EeV neutrinos [100]. If the cosmic rays creating these neutrinos are energetic enough to not be deflected by intergalactic magnetic fields, GZK neutrinos point back to cosmic-ray sources. GZK neutrino fluxes depend on the cosmic-ray flux and composition and the CMB spectrum [101–103]. Most models predict hard-spectrum neutrino fluxes peaking at EeV energies, while a heavier cosmic ray composition would create a lower flux peaking at lower energies.

Chapter 2

High-Energy Neutrino Detection

Current observations and theories generate abundant opportunities for producing high-energy neutrinos, but actually detecting these particles is another matter. Since neutrinos only interact via the weak force, their cross-section is much smaller than other leptons. Expected diffuse fluxes of astrophysical neutrinos are small enough to require cubic-kilometer-scale detectors [78]. Here we review properties of neutrino interactions and their observational signatures.

2.1 Neutrino-nucleon Interactions

Neutrinos interact by exchanging a W or Z boson with other weakly-interacting particles. The interaction of neutrinos with nucleons is most relevant to the detection of astrophysical neutrinos. Neutrinos collide with the quarks comprising protons and neutrons. There are two main channels through which this occurs. Charged-current interactions involve the exchange of a W boson and produce a charged lepton of the same flavor as the neutrino. In neutral-current interactions the neutrino and nucleon exchange a Z boson, and no charged lepton is produced. Feynman diagrams of these processes are shown in Figure 2.1.

Figure 2.2 shows the total neutrino-nucleon cross-section as a function of neutrino energy. The cross-section is $\sim 7-10$ orders of magnitude smaller than the cross-section for pp collisions [104]. At higher neutrino energies, the interaction is dominated by scattering off sea quarks that carry a small fraction of the nucleon's total momentum (a low value of Bjorken x). The sea quark contribution increases at higher collision energies and lower

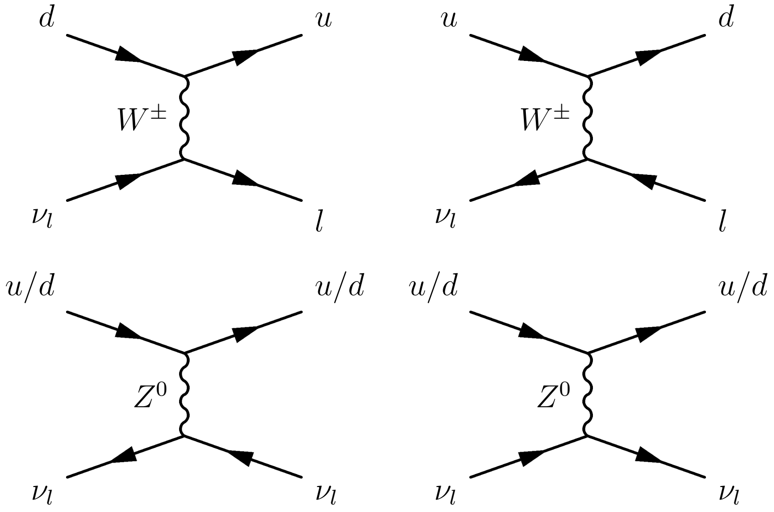

Figure 2.1: Feynman diagrams for neutrino-quark charged-current (top row) and neutral-current interactions (bottom row). Charged-current interactions create charged leptons accompanied by hadronic cascades, while neutral-current interactions only create the hadronic component.

values of Bjorken x, causing the total cross-section to increase as well. Below $10^4 - 10^5$ GeV, the cross-section is proportional to the incoming neutrino energy. Above this energy the momentum transfer of the interaction Q^2 is much greater than the W/Z boson mass. Since the cross-section is inversely proportional to the W/Z boson propagator, which goes as $Q^2 + M_{W/Z}^2$, the propagator reduces the cross-section at high energies [105].

While neutrino-nucleon interactions are the dominant detection channel for most high-energy neutrino detectors, interactions with electrons can also contribute. They are mostly subdominant because the electron mass is 1000 times smaller than the proton mass. However, when a 6.3 PeV $\bar{\nu}_e$ scatters off an electron, an “on-shell” W^- boson is produced via $\bar{\nu}_e + e^- \to W^-$. The cross-section is greatly enhanced by this resonance, dominating over the neutrino-nucleon cross-section by a factor of 300 [105]. This is known as the Glashow resonance [107], and only effects $\bar{\nu}_e$. In principle, a similar resonance occurs for ν_e scattering off positrons

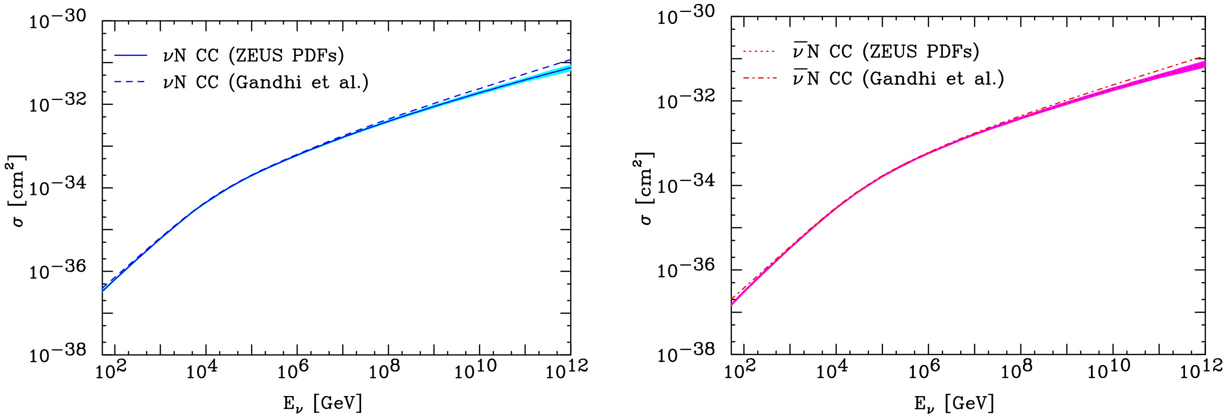

Figure 2.2: Neutrino-nucleon cross-section as a function of energy [105, 106]. The shaded band shows the uncertainty on the calculation from [106], which is $\sim$ 10% for neutrinos in IceCube's energy range. Figure from [106].

and ν_μ scattering off muons, but the neutrino detectors considered here only have nucleon and electron targets.

2.2 Detecting Charged-current ν_μ Interactions

Charged-current ν_μ interactions produce muons via $\nu_\mu(\bar{\nu}_\mu) + q \rightarrow \mu^\mp + q'$. These muons travel are of sufficient energy to in straight lines without being perturbed by the Earth's magnetic field. Muons radiate energy via continuous losses such as ionization and stochastic losses from bremsstrahlung, photo-nuclear interactions, and e^+e^- pair production. By placing an array of photosensors in a clear medium, these particles can be observed as linear, track-like light patterns, and are referred to as "tracks". Figure 2.3 shows the energy loss rate as a function of muon energy. At GeV energies, the energy loss rate is relatively constant and is dominated by ionization losses. At energies above $\sim$ 1 TeV stochastic loss mechanisms dominate and the loss rate is proportional to the muon energy. In ice, the energy loss rate can be parametrized as

$$-\frac{dE}{dx} = a + bE. \tag{2.1}$$

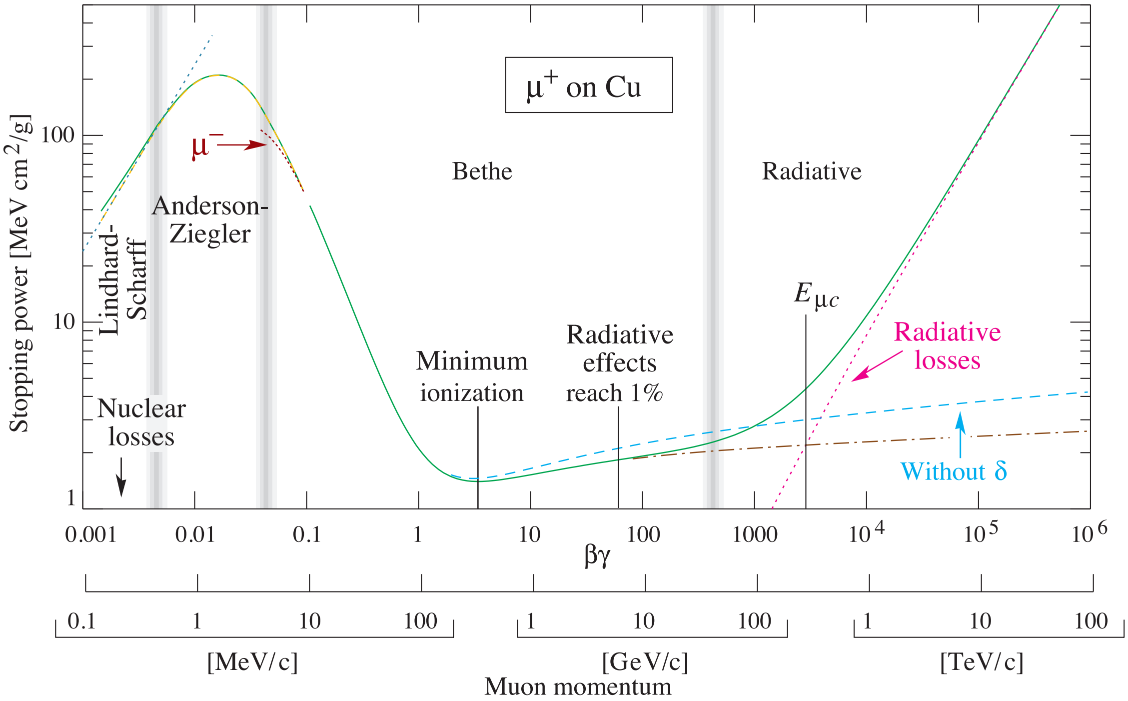

Figure 2.3: The "Bethe-Bloch" function describing muon energy loss as a function of muon energy. At GeV energies, energy loss is dominated by ionization and is mostly independent of energy. Above TeV energies, stochastic losses from e^+e^- pair production and bremsstrahlung dominate. The energy loss rate is proportional to the muon energy, allowing detectors to reconstruct the energy based on the amount of observed light. Figure from [104].

The first term represents the energy-independent loss rate due to ionization, where $a \approx 0.26$ GeV per meter of water-equivalent (mwe). The second term describes the stochastic loss rate, which is proportional to energy with $b \approx 3.6 \times 10^{-4}/$ mwe in ice [108]. With this energy loss rate, high-energy muons are able to travel through many kilometers of ice before dropping below the Cherenkov threshold (Figure 2.4). This means the effective detector volume for muon neutrinos is greatly enhanced by observing muons created outside the detector. If, however, the ν_μ interaction vertex is inside the detector volume, light can also be observed from the hadronic cascade created when the target nucleon is broken apart by the incident neutrino.

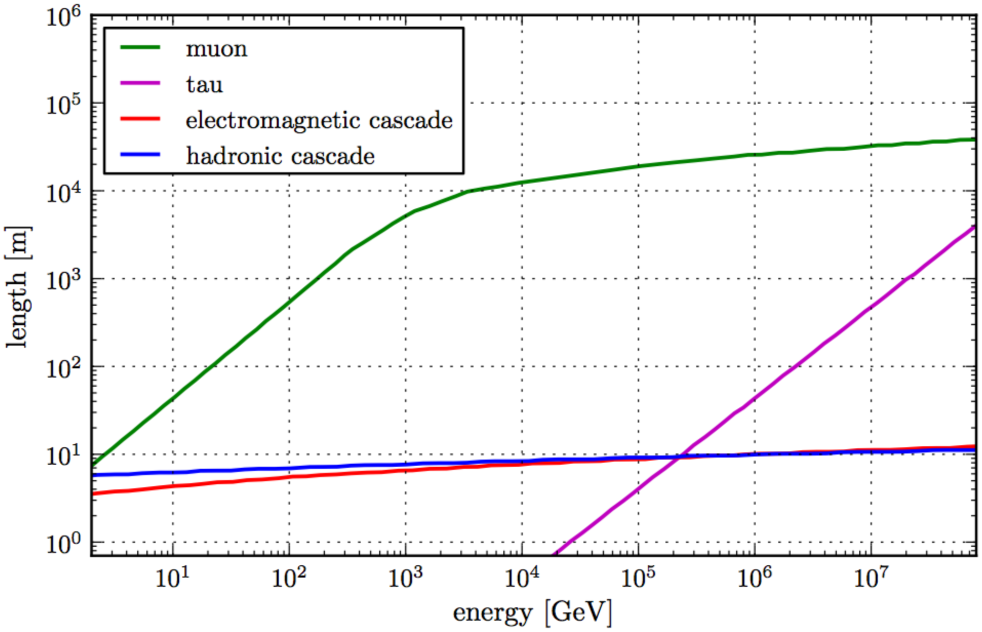

Figure 2.4: Mean length of charged particles in water as a function of energy. High-energy muons can travel tens of kilometers, while electromagnetic and hadronic cascades lose all energy over 10 m. Taus travel approximately 50 m for every PeV of energy. Figure from [109].

For most neutrino energies of interest, the neutrino-nucleon interaction is highly boosted in the forward direction and the outgoing muon is nearly collinear with the incident neutrino. Even if the neutrino interacts far outside the detector the direction of the muon is a good proxy for the neutrino arrival direction. The average opening angle between the muon and neutrino roughly follows $\sim 0.7^\circ \times (E/\mathrm{TeV})^{-0.7}$ [8].

2.3 Detecting Charged-current ν_e interactions

A charged-current electron neutrino interaction produces a free electron that initiates an electromagnetic cascade in the ice. An electron bremsstrahlung loss creates a gamma ray, which creates an e^+e^- pair. This process repeats until the e^+e^- pair drops below the Cherenkov threshold or the gamma ray drops below the pair production threshold. Almost the entire neutrino energy is deposited over a distance of $\sim$ 10 m (Figure 2.4). Part of the energy is also transferred to the struck nucleon, which initiates a hadronic cascade. The electromagnetic and hadronic cascades are not separable in a sparsely-instrumented detector such as IceCube.

Since all photons from the entire cascade are emitted over a $< 10\,\mathrm{m}$ path, an electromagnetic cascade appears as a spherical pattern of light in any detector instrumented with distance scales greater than $10\,\mathrm{m}$. These are referred to "cascade events" throughout this thesis. Additionally, since the Cherenkov emission is from many independent particles with overlapping Cherenkov cones, the angular emission profile is broader than the emission from muons [110].

2.4 Detecting Charged-current ν_τ interactions

Compared to muons, tau leptons have shorter lifetimes and lower energy loss rates. The shorter lifetime leads to short track lengths (Figure 2.4). A PeV tau will only travel $\sim 50\,\mathrm{m}$ before decaying. Taus decay to a tau neutrino and either a quark-antiquark pair or a lepton pair. The hadronic decay occurs with a branching ratio of 65%, while $\tau \rightarrow \mu\nu_\mu$ occurs 15% of the time [104]. At energies below a few hundred TeV, a charged-current ν_τ interaction usually appears as a cascade since the hadronic cascade from the neutrino vertex is not distinguishable from the hadronic cascade from the tau decay. This is indistinguishable from neutral-current interactions or charged-current ν_e interactions. If time structure from the two hadronic cascades is differentiable, "double pulses" may be observable in individual DOMs.

At higher energies, where the tau lepton propagates a resolvable distance, four interaction signatures are possible. A double-bang event occurs when both the ν_τ interaction and tau decay occur inside the detector and would appear as two cascades separated by a dim track. Due to the lower energy loss rate of taus (for example, the bremsstrahlung cross section is suppressed by the mass of the particle squared), they appear like muon tracks with less deposited energy. The large cascade energies and characteristic time difference between the cascades make the double-bang signature nearly background-free. However, it is likely that either the initial interaction or decay is outside the detector, creating a dim track preceded by or followed by a large cascade. This is referred to as a lollipop or inverse-lollipop signature. In the cases where the tau decays to a muon (15% branching ratio), a dim track appears to suddenly becomes much brighter.

2.5 Detecting Neutral-current ν_x interactions

Neutral-current interactions of all neutrino flavors create the same observational signature. The outgoing neutrino is not observed and the outgoing quark or anti-quark initiates a hadronic cascade. An electromagnetic component may also be created via the production of neutral pions, which decay to gamma-rays. On an event-by-event basis, hadronic cascades are indistinguishable from electromagnetic cascades for detectors with relatively sparse instrumentation density such as IceCube.

2.6 Cherenkov Radiation

High-energy neutrinos are ultimately detected via the charged particles they produce. These charged particles travel faster than the speed of light in the medium, generating radiation via the Cherenkov process. In a transparent medium, these photons are then observed by photosensors.

Charged particles disrupt the electromagnetic field in the medium through which they travel [112]. When these particles travel faster than the speed of light, a coherent shockwave of electromagnetic radiation is produced (Figure 2.5). This effect is analogous to the sonic boom created by an airplane traveling faster than the speed of sound and the wake created by a boat moving faster than the speed of water waves. Cherenkov light is emitted along a cone, with a characteristic angle

$$\cos\theta_c = \frac{1}{\beta n(\lambda)}. \tag{2.2}$$

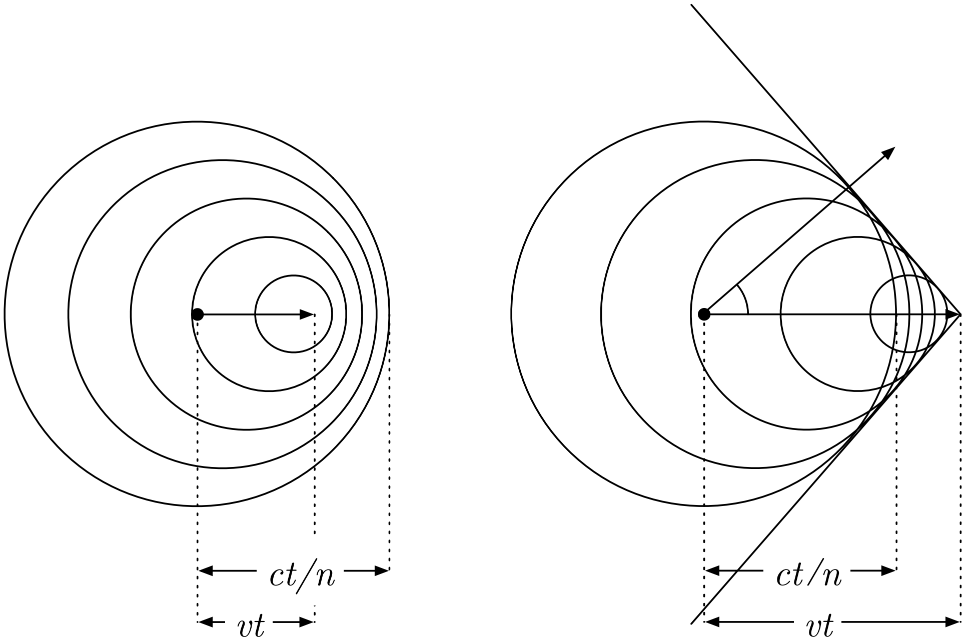

Figure 2.5: Diagram of Cherenkov radiation. A particle traveling faster than the speed of light in a medium generates coherent radiation. The radiation is emitted along a cone, with an angle determined by the particle speed and the speed of light in the medium. Image from [111].

where $\beta = v/c$ is the relative velocity of the particle and n is the index of refraction of the medium. For a relativistic charged particle traveling through ice, $\theta_c \approx 41°$. The photon yield as a function of wavelength is given by the Frank-Tamm formula [113]

$$\frac{d^2N}{dxd\lambda} = \frac{2\pi\alpha}{\lambda^2}\left(1 - \frac{1}{\beta^2 n^2(\lambda)}\right), \tag{2.3}$$

where α is the fine structure constant. The emission is peaked at shorter wavelengths, making Cherenkov light appear blue.

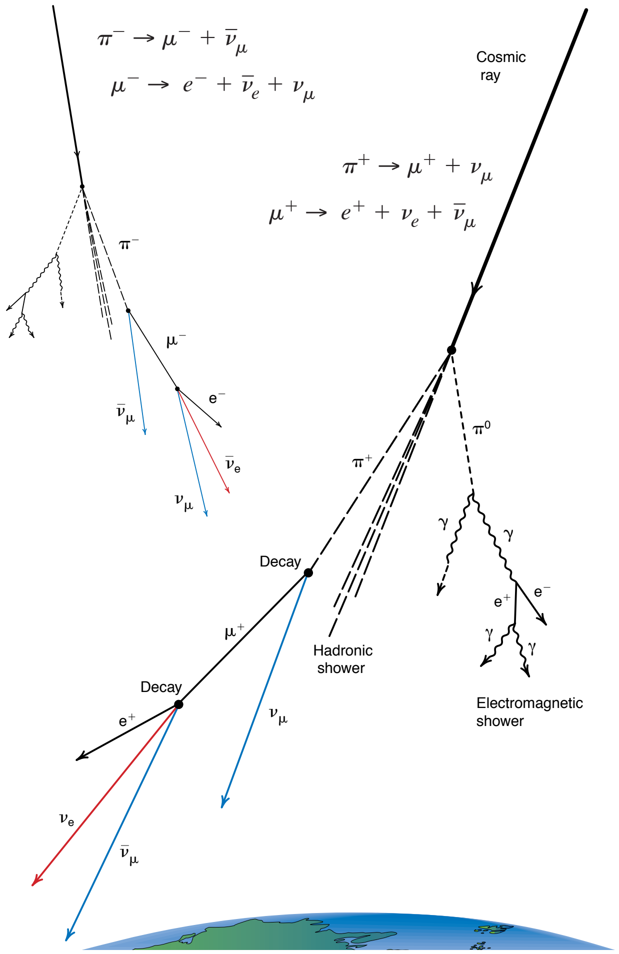

Figure 2.6: Diagram of a cosmic-ray air shower. The flux of muons and neutrinos from the hadronic component forms the dominant background for most astrophysical neutrino searches. Image from Los Alamos Science, 25, 1997.

2.7 Backgrounds to detecting astrophysical neutrinos

In most high-energy neutrino detectors, the interactions of astrophysical neutrinos are buried under a background of atmospheric muons and atmospheric neutrinos from cosmic-ray air showers. The flux of protons and higher charged nuclei hitting the atmosphere creates muons and neutrinos [114]. This process is the same process that governs the production of neutrinos in a source. Nucleon-nucleon collisions create hadronic and electromagnetic cascades. The electromagnetic component is often initiated by the production of neutral pions decaying to photons and is sustained by bremsstrahlung and e^+e^- pair production. However, as the radiation length of electrons in dense materials is tens of centimeters, the electromagnetic component does not penetrate to underground detectors. The hadronic component, however, creates a high flux of muons and neutrinos via charged-pion decay that can penetrate through kilometers of ice [114–116]. Figure 2.6 shows a schematic of a cosmic-ray air shower.

Chapter 3

The IceCube Neutrino Observatory

The previous chapter reviewed high-energy neutrino interactions, focusing on the interaction products and their unique observational signatures. This chapter details the technology and techniques implemented by the IceCube Neutrino Observatory to transform these interaction signatures into usable data.

The IceCube Neutrino Observatory is a cubic-kilometer-sized Cherenkov detector embedded in the ice at the geographic South Pole [117]. Optimized to detect neutrinos above TeV energies, it consists of 5160 photomultiplier tubes (PMTs) instrumented along 86 cables, called strings. Each PMT is housed in a digital optical module (DOM), consisting of a pressure-resistant sphere with digitization hardware and calibration LEDs [118, 119]. The DOMs detect Cherenkov photons emitted by charged leptons that traverse the detector. Each string consists of 60 DOMs spaced in 17 m intervals 1450 - 2450 m beneath the surface of the ice sheet. Strings are oriented vertically in the ice and are spaced 125 m apart. In the central, deep region of the detector, additional strings spaced ∼70 m apart form the DeepCore sub-array [120]. These strings contain high quantum efficiency DOMs spaced 7 m apart. A diagram of the detector is shown in Figure 3.1. Construction of the detector occurred over seven austral summers, and physics data was collected with each partial detector configuration. Figure 3.2 show's a bird's eye view of the detector, with the strings comprising each configuration highlighted.

The remainder of the chapter details each step of the data-taking process, explaining how the observational signal is transformed from photons emitted by a particle to digitized PMT

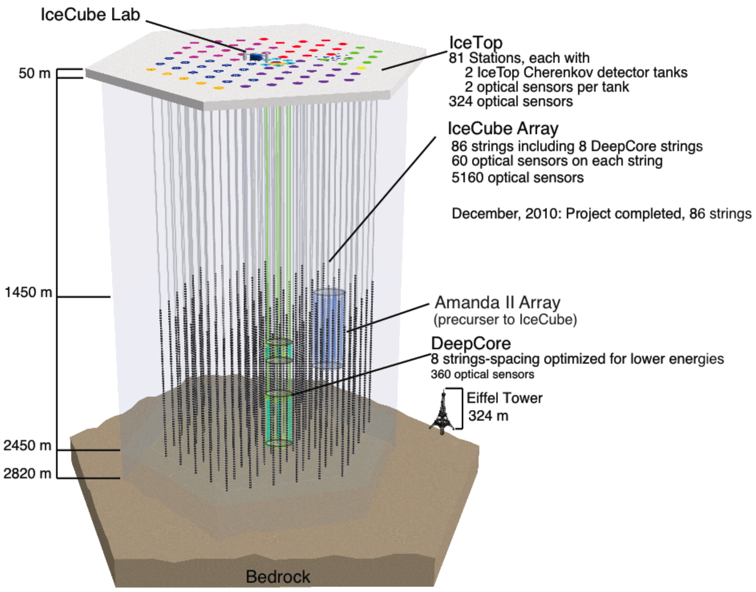

Figure 3.1: Diagram of the IceCube Neutrino Observatory. 60 DOMs are attached to each string, instrumenting ice between depths of 1450 – 2450 m. The DeepCore sub-array in the deep, central portion of the detector has a higher instrumentation density. The IceTop surface array consisting of DOMs in ice-filled tanks.

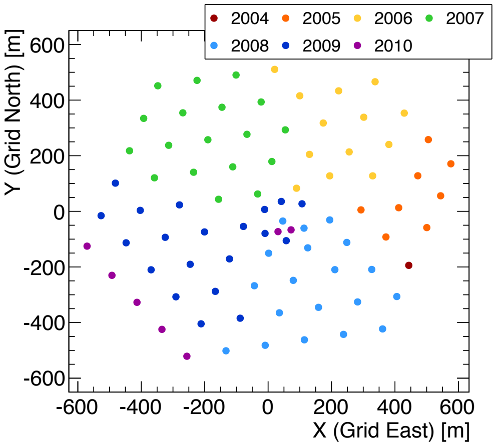

Figure 3.2: Bird's eye view of IceCube, with colors denoting the year each string was deployed in the ice. The 40-string configuration (IC40) includes all strings from 2004 - 2007. The 59- and 79-string configurations include additional strings installed in 2008 and 2009, respectively. IC86 is the complete detector with 86 strings.

pulses and triggered physics events. Basic analysis tools are also described, including event reconstruction techniques and detector simulation.

3.1 Optical Properties of the Glacial Ice

High-energy leptons travel through the ice and emit light via the processes described in Chapter 2, and observing these photons requires a transparent medium. The deep glacial ice at the South Pole is the clearest ice in the world, allowing photons to travel hundreds of meters from their point of emission to a PMT.

As photons travel through the ice, they can be scattered or absorbed. At depths above $\sim 1300\,\mathrm{m}$, the ice has high concentrations of air bubbles that restricts the scattering length to $\lesssim 5\,\mathrm{m}$ [121]. At greater depths, air bubbles are compressed by the increasing pressure and eventually disappear. In this regime, scattering and absorption are governed by the concentration of dust particles. Scattering processes wash out the time structure of observed photons, which is crucial for directional reconstruction of neutrino events. Absorption reduces the overall photon statistics available for any reconstruction and affects energy determination, which is directly correlated with the number of observed photons.

The optical properties of the ice have been measured using *in situ* calibration LEDs. A depth-dependent model of the photon scattering and absorption lengths is used to fit maximum-brightness flasher data. Additional parameters of the model include the shape of the distribution of photon scattering angles and the overall flasher brightness. The scattering and absorption lengths as a function of depth are shown in Figure 3.3, and the model itself is described in [122]. In the upper half of the detector, the typical scattering and absorption lengths are 25 m and 70 m, respectively. In the middle of the detector, a 100 m-thick dust layer is observed. This layer has been correlated with an interglacial period 65,000 years ago, in the Pleistocene era, and has absorption lengths as short as 20 m. Below this region, the ice becomes clearer, with scattering and absorption lengths as long as 70 m and 200 m, respectively.

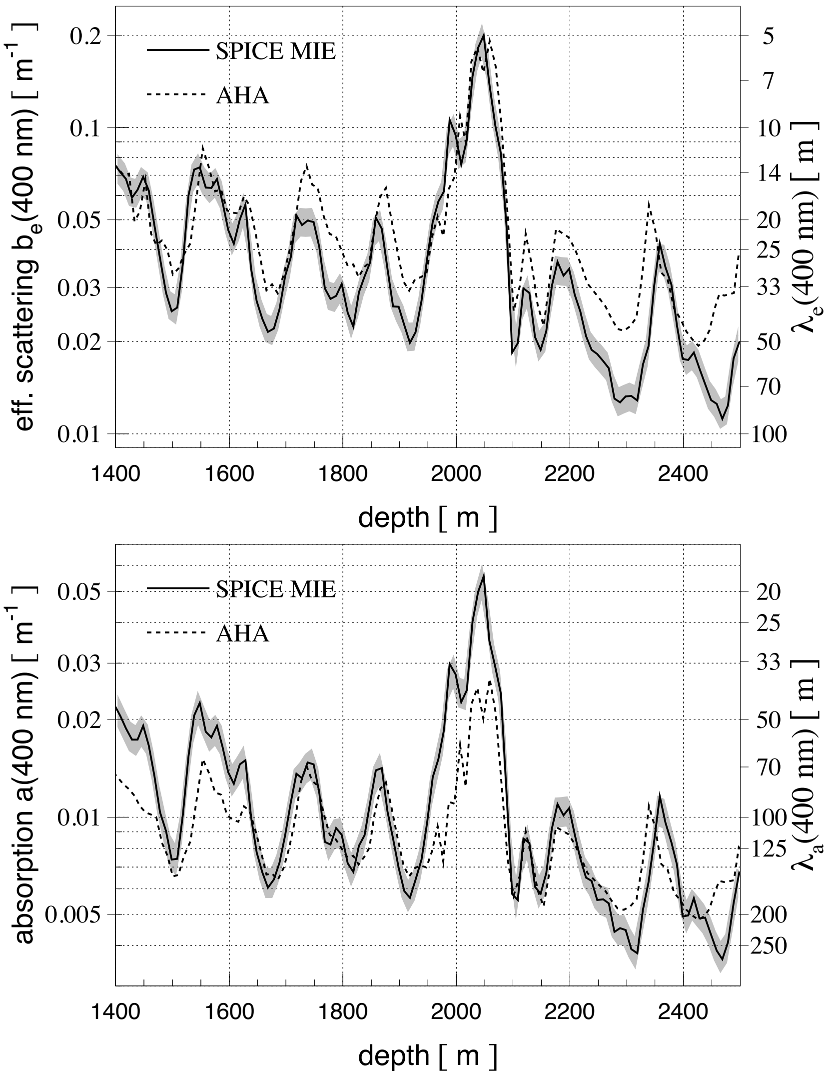

Figure 3.3: Optical properties of the deep glacial ice at the South Pole as a function of depth. The scattering (top) and absorption (bottom) lengths are shown for the current SPICE Mie ice model [122] as well as a previous model named AHA [121]. Scattering and absorption are highly correlated. The region of significantly increased scattering and absorption around a depth of 2050 m is due to a dense dust layer, and the ice below this layer is on average clearer than the ice in the top half of the detector.

The scattering and absorption lengths not only vary with depth but also with the (x,y) coordinate in the detector. This is because the ice layers are tilted. The borehole dust logger described in [123] mapped dust concentrations at various detector locations, creating a three-dimensional model of dust layer tilt, which is used when fitting the flasher data. More recent investigations have also found preliminary evidence for anisotropic scattering and absorption in the ice [124].

In the analyses presented in this thesis, the detector is simulated using the ice model described in [122], referred to as the SPICE Mie ice model. The model uncertainty in the scattering and absorption lengths are correlated, with the 1σ range corresponding to independent changes in the scattering and absorption coefficients of $+10\%$ and a correlated shift of -7.1% in both scattering and absorption. This is incorporated into the systematic error budget of each physics analysis by simulating the detector response with these varied ice properties.

3.2 The Digital Optical Module (DOM)

Photons are emitted as high-energy leptons travel through the detector, are scattered as they propagate through the Antarctic ice, and are finally observed when they hit a digital optical module (DOM). A diagram of a DOM is shown in Figure 3.4. Each DOM is an autonomous detector consisting of a photomultiplier tube (PMT), onboard digitization electronics, and calibration LEDs [119]. The DOM components are housed in a 0.5-inch thick glass pressure sphere that can withstand pressures up to 690 atm. Each DOM is attached to an IceCube string, enabling wired communication with the IceCube Lab (ICL) on the surface of the ice sheet.

Photon are detected with the ten-inch R7081-02 PMT from Hamamatsu Photonics, which is sensitive between 300 and 650 ns. The PMT has a quantum efficiency of 18% and a timing resolution of 2 ns [118]. In the DeepCore sub-array, R7081MOD PMTs are instead used, which have a 35% increased quantum efficiency compared to the standard IceCube

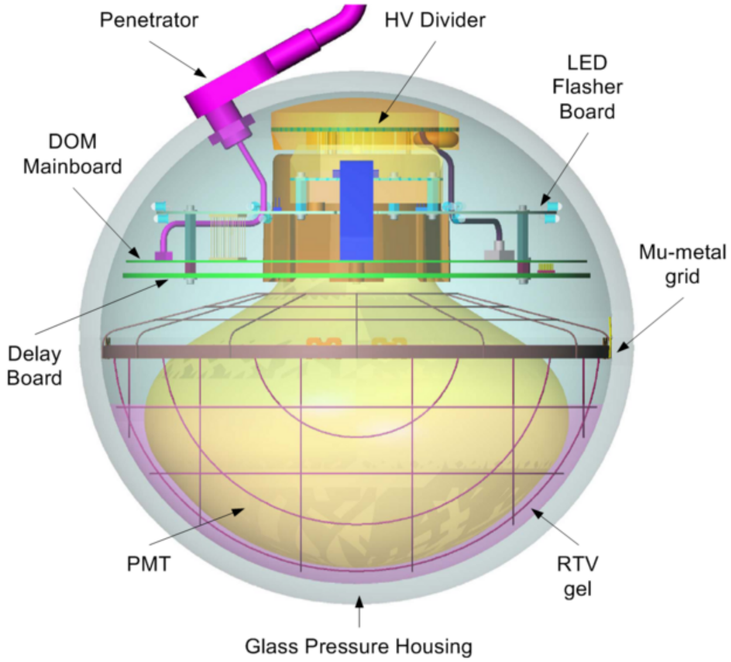

Figure 3.4: Diagram of a Digital Optical Module (DOM).

DOMs [120]. The single photoelectron (PE) response is an electrical pulse of amplitude $\sim 10\,\text{mV}$ and width $\sim 5\,\text{ns}$.

The DOM main board digitizes the PMT pulses using the Analog Transient Waveform Digitizer (ATWD) and the Fast Analog-to-Digital Converter (FADC) [119]. The ATWD samples the pulse at 3.3 ns intervals for 422 ns before digitizing, which takes 29 microseconds. This provides fine time resolution at the cost of substantial dead-time. Therefore, each DOM has two independent ATWDs operated in ping-pong mode. Each ATWD consists of three channels with different gains that provide digitized pulses over a large dynamic range. The ATWD initiates digitization when the PMT pulse crosses the discriminator threshold of 0.25 PE. The FADC digitizer offers a poorer sampling rate of 25 ns, but can readout $6.4\,\mu s$ pulses and has no dead-time.

The flasher board contains 12 LEDs capable of emitting pulses bright enough to be observed by DOMs on neighboring strings. Six LEDs point horizontally, while the other six are angle up at an angle of 42°. These can be flashed individually or together at varying brightnesses, and are used to measure ice properties, to simulate cascade-like events for reconstruction studies, and to calibrate the detector geometry.

3.3 Data Acquisition, Triggers, and Filters

When a PMT pulse crosses the 0.25 PE discriminator threshold, the DOM communicates this information to nearby DOMs to look for coincident hits. A hard local coincidence (HLC) hit is defined as two neighboring or next-to-neighboring DOMs on the same string triggering in a $1\,\mu$s time window. Trigger information from all DOM are sent, via the cable network, to surface computers located in the ICL. These machines sort hits from the entire array and form physics events based on the observed hit pattern.

DOM hits are first sent to DOMHubs. Each DOMHub computer sends power and operating commands to 60 in-ice DOMs via the DOM Readout (DOR) cards. The DOR card enables low-level communication with the DOMs, controlling tasks such as powering and starting DOMs, switching data-taking modes, and running time calibration software. Four DOMs on two twisted wire-pairs are connected to each DOR card with two DB9 connectors. In addition to the DOR cards and DOM power supply, each DOMHub contains its own power supply, a single-board computer to sort and process DOM hits, a hard drive, and one DOMHub Service Board (DSB) that distributes GPS timing to each DOM.

Accessing DOMHub hardware often requires removing an entire string from data taking. Disconnecting a hub can be a time-consuming process, because 15 DB9 connectors (with two screws each) are used to attach 60 DOMs to the DOMHub. To minimize detector downtime during hardware upgrades, a custom screwdriver, dubbed the DB8R, was developed and tested on-site at the South Pole. Among tools available to fasten DB9 connectors, the DB8R is truly peerless. It is a standard flat-head screwdriver with a thin aluminum sleeve enclosing the tip. This sleeve secures the screwdriver over the screw in the connector. Since the DB9 connectors are often difficult to access among the DOMHub cables, the DB8R enables efficient torquing while minimizing slippage. This reduced the risk of injury and accidents and improved the speed of DOMHub upgrades by a factor of two, greatly reducing detector downtime. Minimalistic, efficient, and robust, the DB8R is a paragon of Antarctic engineering.

In the ICL, DOMHubs communicate with other components of the data acquisition system (DAQ) to form physics events. Detector-wide trigger conditions must be satisfied for PMT pulses to be integrated into a physics event and passed forward for additional processing. While many triggers operate simultaneously in IceCube, the analyses presented here primarily use events with an eight-channel simple majority trigger (SMT8), which requires eight DOMs to have HLC hits within a $5\,\mu$s time window. If this criterion is satisfied, the DAQ reads out all hits on all DOMs in the $5\,\mu$s trigger window plus an additional $\pm\,10\,\mu$s readout window. Digitized waveforms from the ATWD and FADC are recorded for HLC hits, while isolated DOMs only transmit FADC waveforms to form soft local coincidence (SLC) hits.

The overall trigger rate for the full detector is $\sim 2500\,$Hz. The online filtering system, which runs in real-time on a computer cluster in the ICL, reduces the overall rate by a factor of ten. This software chain reconstructed PE arrival times from the observed PMT pulses, calculates basic event information, and applies criteria to select useful physics events. PE reconstruction, known as feature extraction, represented the full PMT pulses as a linear combination of PEs with specific charges and arrival times [125]. This information is used to calculate the total charge of an event and to reconstruct particle directions and energies. Events with desired properties are selected for transfer via satellite to data storage facilities in Madison, WI for further processing and analysis.

Over 20 filters run in real-time on the cluster in the ICL, each optimized to select either track-like events or shower-like events with different energies and properties. In the analyses presented in this thesis, the Muon and Extreme High-Energy (EHE) Filters are used. The EHE Filter selects events with more than 1000 observed photoelectrons. The muon filter selects track-like events using the reconstructed zenith direction, a variable describing the quality of the track fit, and the deposited charge. The Minimum Bias Filter, which randomly selects one out of 1000 triggered events, is also used for calibration purposes.

3.4 Reconstructing Particle Directions and Energies

The extracted times and charges of the observed photons form a pattern of hits for each event. The goal of reconstruction is to infer the direction and energy of the muon track or hadronic/electromagnetic cascade from this hit pattern. A number of algorithms exist to calculate these quantities, and they vary greatly in complexity, accuracy, and computing time. For most analyses, multiple algorithms are applied in a chain, using results from simple "first-guess" algorithms as a seed for more complex, computationally expensive techniques.

Directional reconstructions for muon tracks use the observed PEs to determine the direction (θ, ϕ) and position (x, y, z) of a linear track. Most muon energy reconstructions take a fixed direction and position as an input to reconstruct the energy in a single-dimensional fit, although more general algorithms fit the direction and energy simultaneously without assuming a specific event topology.

3.4.1 LineFit

This first-guess algorithm performs a least-squares fit to the location and time of each hit DOM. The least squares fit is modified to be robust against the effect of outlier hits by applying an Huber function [126]. The direction and position of the track is reconstructed by minimizing the function

$$\min_{t_0, \vec{x}_0, \vec{v}} \sum_{i=1}^{N} \phi(\rho_i(t_0, \vec{x}_0, \vec{v})), \tag{3.1}$$

where N is the total number of hit DOMs and the Huber penalty function $\phi(\rho)$ is defined as

$$\phi(\rho) \equiv \begin{cases} \rho^2 & \text{if } \rho < \mu \\ \mu(2\rho - \mu) & \text{if } \rho \geq \mu \end{cases} . \tag{3.2}$$

Here, $\rho_i(t_0, \vec{x}, \vec{v})$ is

$$\rho_i(t_0, \vec{x}_0, \vec{v}) = \|\vec{v}(t_i - t_0) + \vec{x}_0 - \vec{x}_i\|_2 \tag{3.3}$$

where $\vec{x}_i$ and t_i are the position and time of the ith hit, and $\vec{v}$ is the velocity of the muon track. The reconstructed track is defined to pass through point $\vec{x}_0$ at time t_0.

This algorithm models the muon as a plane wave of light traversing the detector. Hits relatively close to the track are likely to be muon-induced physics hits and are given quadratic weight in the loss function, as in a standard least squares fit. Hits far from the track, on the other hand, are more likely to be noise. Their weights in the loss function are reduced to a linear dependence to limit their impact on the result. The distance scale is set with the parameter μ, whose optimal value for simulated neutrinos was determined to be 153 m.

Since the loss function is solved analytically, this algorithm is extremely fast and, despite making large approximations in modeling the Cherenkov light, results in a median angular resolution of a few degrees.

3.4.2 Likelihood-based Angular Reconstruction - SPE and MPE

The single photoelectron (SPE) and multi photoelectron (MPE) likelihood reconstructions model the muon as a straight line traveling at the speed of light that continuously emits photons along the Cherenkov cone [127]. The times when the photons are expected to arrive at the DOMs depend on the distance between the track and the DOM and the scattering and absorption in the ice. Unlike the LineFit algorithm, the likelihood must be solved numerically to find the best-fit five parameter solution (θ, ϕ, x, y, z). The SPE log likelihood is defined as

$$\log \mathcal{L} = \sum_i \log p(\vec{x}_i|\vec{a}) \ , \tag{3.4}$$

where $\vec{a}$ consists of the track parameters (θ, ϕ, x, y, z). The probability distribution function (PDF) $p(\vec{x}_i|\vec{a})$ represents the probability the track $\vec{A}$ creates the observed hit $\vec{x}_i$. Here, the hit vector $\vec{x}_i = (x_i, y_i, z_i, t_i)$ consists of the position of the ith DOM and the time residual for the first hit on the ith DOM. The time residual is defined as the difference between the observed arrival time and the arrival time of a “direct” photon that is emitted at the Cherenkov angle and travels straight to the receiving DOM.

The minimum of $-\log \mathcal{L}$ is found using numerical minimizers such as Minuit [128]. For some events, especially those with large random noise fluctuations or with multiple muons in the detector at once, the likelihood space can be complex and the algorithm sometimes finds a local minimum. This can be avoided by exploring a larger portion of the likelihood space, in practice completed by repeating the SPE fit with different starting conditions.

Although $p(\vec{x}_i|\vec{a})$ is the PDF for *any* observed photon on a given DOM, the above equation only actually uses the arrival time of the *first* hit. This approximation is sufficient for lower energy events, but for events with many observed hits on each DOM the likelihood becomes distorted. If a given DOM has 100 observed photons, the distribution of the arrival time of the first photon is highly peaked around the direct speed-of-light time, while the arrival time distribution for any photon has a much larger spread. The MPE likelihood accounts for the total charge observed on each hit DOM by modifying $p(\vec{x}_i|\vec{a})$

$$p(\vec{x}_i|\vec{a}) \rightarrow N \cdot p(\vec{x}_i|\vec{a}) \cdot \left(\int_{t_i}^{\infty} p(\vec{x}|\vec{a}) dt \right)^{(N-1)}, \tag{3.5}$$

where N is the total number of observed photoelectrons on the ith DOM.

The statistical power of the likelihood description comes from the accuracy of $p(\vec{x}_i|\vec{a})$. Here we detail two approaches for determining these PDFs.

3.4.2.1 Approximate PDF Description using the Pandel Distribution

The Pandel distribution [129] is a form of the gamma distribution that provides a reasonably accurate description of the photon arrival time distribution. It is relatively fast to compute and can be integrated analytically, which are advantages since it needs to be computed oncer per DOM for each iteration of the likelihood minimization. The distribution is defined as [127]

$$p(t_i) \equiv \frac{1}{N(d)} \frac{\tau^{-(d/\lambda)} \cdot t_i^{(d/\lambda - 1)}}{\Gamma(d/\lambda)} \cdot e^{-\left(t_i \cdot \left(\frac{1}{\tau} + \frac{c_{\mathrm{medium}}}{\lambda_a}\right) + \frac{d}{\lambda_a}\right)} , \tag{3.6}$$

$$N(d) = e^{-d/\lambda_a} \cdot \left(1 + \frac{\tau \cdot c_{\mathrm{medium}}}{\lambda_a}\right)^{-d/\lambda} , \tag{3.7}$$

where c_{medium} is the speed of light in the ice, d is the perpendicular distance between the track and the DOM, λ_a is the average absorption length of the ice, and λ and τ are constants determined by simulation. The distribution is plotted for two distances in Figure 3.5.

3.4.2.2 Spline Parametrization of Detailed Ice Properties

While the Pandel distribution is a parametrization of the average photon timing distribution, it fails to capture many features observed in data, including the depth-dependent ice properties. An improvement is therefore to use a complete photon transport simulation using a depth-dependent model of scattering and absorption in the ice [122]. The arrival time of a photon is a function of the orientation and depth of the muon source and the displacement vector between the muon and the receiving PMT. Photons are simulated for different muon-receiver configurations, and the resulting timing distributions and overall light yields are tabulated [130,131]. These tabulated PDFs can be used directly in the likelihoods above. However, the finite binning of the tables creates numerical artifacts in the likelihood space that confuse the minimizer. Constructing finer-binned tables ameliorates this problem, but the amount of storage and memory required to access the tables increases with the binning, making this solution unfeasible.

An alternative approach is to fit a multi-dimensional spline surface to the arrival time distributions from the detailed photon propagation simulation. This is done using the photospline package [132], which provides an analytic parametrization of the tabulated PDFs. Like the Pandel distribution, this parametrization can be computed efficiently and integrated analytically, and the smooth surface does not create artifacts in the likelihood space like the

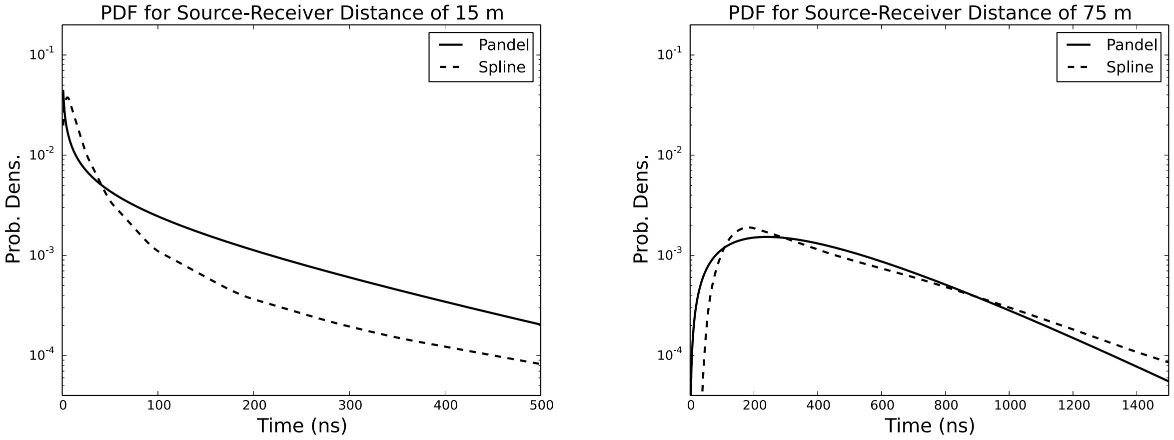

Figure 3.5: Photon timing distributions for muon angular reconstructions. The left plot shows the simulated timing distribution for a DOM placed 15 m from the muon, while the distribution for a 75 m distance is shown on the right. Both the Pandel function [129] and the spline parametrization are shown. The spline parametrization is a more accurate representation of the actual photon propagation.

binned PDFs. Unlike the Pandel distribution, the parametrization provides an accurate description of the photon timing distributions. These splines are used as PDFs in the MPE likelihood. A comparison between the spline function and the Pandel distribution is shown in Fig. 3.5. Using the spline-based PDF instead of the Pandel distribution in the likelihood leads to a 26% improvement in the median neutrino angular resolution at 30 TeV. This angular reconstruction is used for the point source analysis in Ch. 6 and Ch. 8; details if its performance can be found there.

3.4.3 MuEX Angular Reconstruction

The MuEX angular reconstruction is an iterative reconstruction that combines the MPE likelihood above with a bootstrapped sampling method. MuEX is usually applied with four iterations. Each iteration uses a bootstrapped pulse series extracted randomly from the measured pulses using a charge-weighted multinomial distribution, so high charge pulses are more likely to be selected than low ones. The MPE likelihood uses each of these bootstrapped pulse series with the Pandel distribution, modified to include depth-dependent ice properties, to reconstruct the position and direction of the track. The results of these four reconstructions are then averaged and used as a seed for one final reconstruction using the complete pulses. This process helps the minimizer avoid local minima, reducing the rate of misreconstructed background by 30%. It also improves the median neutrino angular resolution from 0.7° to 0.6° at 30 TeV.

3.4.4 Paraboloid Angular Uncertainty Estimator

To find neutrino point sources, it is important to have not only the reconstructed direction of each muon track but also an estimated uncertainty of the direction. Such an estimate can be acquired for each event individually using the likelihood space of the reconstruction [133, 134]. This is accomplished by calculated the profile likelihood in angular space around the minimum. 24 points in (θ, ϕ) are chosen around the best-fit direction, and at each point the likelihood is maximized in $(\vec{x},\vec{y},\vec{z})$. A paraboloid function is fit to the curve mapped out by the likelihood, from which the 1σ angular error range is determined. This is used for the point source analyses in Ch. 6 and 8.

3.4.5 MuEX Energy Reconstruction

After reconstructing the direction of a track, separate algorithms are usually applied to fit for the visible energy of the muon along its direction. The muon-based analyses in Ch. 6 and 8 use the MuEX algorithm. This energy reconstruction uses a Poissonian likelihood to compare the observed number of photoelectrons k to the expected light yield per unit energy Λ for a particle with energy E

$$\ln \mathcal{L} = k \ln (E\Lambda + \rho) - (E\Lambda + \rho) - \ln (k!) , \tag{3.8}$$

where ρ is the expected number of noise photons. The energy of this hypothetical particle is varied until the expected light yield $(E\Lambda+\rho)$ essentially matches the observed photoelectrons.

Here, the expected light yield per unit energy represents the light yield for a single muon that emits light continuously as it traverses the entire detector.

Similar to the time PDFs described above, the expected light yield is a function of the distance between the muon and the receiving DOM and the optical properties of the ice. MuEX calculates the light yield using an analytic approximation for light emitted at the Cherenkov angle from a line source. This parametrization describes both short-distance photon propagation, where scattering is sub-dominant, and the diffusive behavior dominant at large distances [125]. It also convolves the expected light yield with a probabilistic distribution to account for the stochastic light emission behavior of high-energy muons [125]. Similar to the directional reconstructions, this likelihood is minimized numerically, solving for the one free parameter E.

3.4.6 Millipede Energy Unfolding - Energy and Direction

The Poissonian likelihood in Eqn. 3.8 can be adapted to model multiple light-emitting particles. This is useful because a high energy muon emits most of its light in stochastic energy losses such as bremsstrahlung and photonuclear interactions. Instead of a single particle with constant light emission, a more realistic model of a high-energy muon is a linear chain of cascade-like energy losses with varying energies. The Millipede algorithm implements this model and solves for the energy of each hypothesis cascade via a linear unfolding:

$$\vec{k} - \vec{\rho} = \mathbf{\Lambda} \cdot \vec{E}, \tag{3.9}$$

where the observed photons on all DOMs $\vec{k}$ originate from energy losses $\vec{E}$, and the matrix $\mathbf{\Lambda}$ contains the predicted light yield at every point in the detector for every hypothesis source position.

For a given track location and direction, Millipede unfolds the energy loss distribution, returning the position and energy of each reconstructed loss. This is used in Ch. 6 to distinguish single muons from muon bundles, which have different energy loss distributions.

This algorithm can be expanded to also fit for the position and direction of the muon if the energy unfolding is repeated for different hypothesis tracks. This is a $5 + N$ parameter fit $(\theta, \phi, x, y, z, \vec{E})$, where N is the number of hypothesis energy losses representing the muon track (ie. the length of $\vec{E}$). Standard numerical minimizers have difficulty finding the global minimum in this high-dimensional space, so an angular grid scan is applied. The sky is divided into $\sim 10^5$ equal-area pixels using the HEALPix package [135], and at each pixel Millipede is applied. At each pixel, the direction of the muon is kept fixed and the position of the muon is varied with the energy losses being unfolded at each step. This is a computationally expensive process, taking $10^2 - 10^3$ CPU hours per event.

This brute-force scan finds the global minimum and provides a full-sky PDF describing the probability an event came from any direction in the sky. This is therefore a more accurate and comprehensive alternative to the Paraboloid algorithm for estimating angular uncertainties. This is used in Ch. 7 to reconstruct both tracks and cascades. For cascade events a track-like chain of hypothesis cascades is also formed, but the unfolding typically only solves for point like emission from a few adjacent losses, and the remaining are reconstructed to have zero energy.

3.5 Detector Simulation

To validate our understanding of the detector, the detector response to muons and neutrinos is simulated. The simulation generates observable leptons via fundamental interactions, tracks these leptons as they traverse the detector and radiate light, propagates the light through the ice to the DOMs, and simulates the PMT and detector electronics.

Two programs handle the event generation. The CORSIKA package [136] creates atmospheric muons, the dominant background at trigger level, by simulating cosmic ray nucleons interacting in the atmosphere above Antarctica. This uses the SIBYLL interaction model, although simulations with alternative interactions models were tested in Ch. 4. For each interaction, CORSIKA produces a list of final state particles with their relevant properties (position, direction, energy). To simulate neutrino interactions, software based on the

ANIS package [137] generates neutrinos, propagates them through the Earth, and simulates their interaction with ice molecules. Similar to the atmospheric muon simulation, the result is the final state particles and their properties. This software uses neutrino cross-sections from [105, 106] and generates events in a flexible weighted manner, in which the same events can be re-weighted to represent an atmospheric neutrino flux or an astrophysical flux. The particles produced by the neutrino or cosmic ray interactions are propagated through the ice using Muon Monte Carlo (MMC) [108]. MMC tracks leptons in the ice and bedrock, simulating all energy losses and secondaries. Both continuous energy losses and stochastic energy losses are simulated, resulting in the number of photons emitted from each interaction.

These photons are propagated through the ice using either Photonics [130] or PPC [131]. Both use the measured depth-dependent ice properties to simulate photon scattering and absorption. Photonics simulates a vast quantity of these photons in advance, storing the arrival times and photon yields at each detector location in look-up tables. These tables are then sampled to determine whether a photon emitted by a simulated particle is observed. This approach is efficient because a large number of photons are simulated only once, and then the relatively-fast look-up tables are used repeatedly. However, the table binning sacrifices accuracy in the simulation and can lead to artifacts in simulated PMT waveforms. This effect is minimized by fitting multi-dimensional splines to the look-up tables, as in Sec. 3.4. The smooth splines are then sampled without creating binning artifacts.

PPC takes the alternative approach of direct propagation, simulating scattering and absorption of each individual photon emitted by a lepton to determine if it hits a DOM. This is accurate but much slower than the lookup-table approach. However, the computing time is reduced by orders of magnitude by using GPUs. As each photon's path through the ice is independent, photons for a given event can be simulated in parallel on the many threads of the GPU. This makes direct photon propagation feasible for neutrinos below $\sim$1 PeV.

After the photon collides with a DOM, the PMT and detector components are simulated. The conversion of photons to PEs uses the single PE distribution measured in the lab. PMT jitter is introduced along with after-pulses and pre-pulses. A basic noise model is used to add random noise hits. Local coincidence and trigger conditions are applied just as for real detector data.

Chapter 4

Detector Calibration

The ability to reconstruct energies and directions of particles passing through IceCube depends crucially on the calibration of the detector. Reconstructions use detailed information on photon arrival times and total observed charge. Thus, much of detector calibration revolves around understanding how photons travel through the ice, and how efficient the DOM is at observing those photons.

The optical properties of the ice are described by a model that specifies the scattering and absorption lengths as a function of depth, and is described in Section 3.1 and Reference [122]. The efficiency of the PMTs was measured in controlled laboratory testing. Reference [118] describes the characterization of the timing and single photoelectron (SPE) response of the PMTs using LEDs and lasers, as well as a technique to measure the absolute efficiency of the PMT using Rayleigh scattered light from a laser. However, the bare PMT is not used directly in IceCube, but is packaged inside the DOM and placed in the ice. Properties of the DOM housing, string cable, and refrozen hole ice may affect the overall optical efficiency.

This chapter details two analyses that use in-ice muon data to complement the ice property and absolute calibration measurements described above. The first uses timing distributions to compare muon data to simulated muon data with various ice properties. This is not only a useful validation tool for the ice model, but it also provides a direct probe of ice properties that effect short distances, such as the scattering function and the properties of the refrozen hole ice. The second analysis uses low-energy single muons near the minimum-ionizing regime as a standard light source to measure the absolute optical efficiency of the DOMs *in situ*.

4.1 Verification of the optical properties of the ice using atmospheric muons

To investigate the accuracy of the ice model, an analysis was performed to compare atmospheric muon data with simulated muons. In the 2009 59-string detector configuration, atmospheric muons triggered IceCube at a typical rate of 1.8 kHz, creating a large data set for comparing muon data and simulated muons. For this study we simulated atmospheric muons using the CORSIKA air shower simulation package [136] coupled with IceCube detector simulation (see Section 3.5. To compare different ice models and photon propagation techniques, parameters effecting the photon propagation are varied in simulation, while all other settings remain fixed. For the majority of results presented here, photon propagation was simulated directly using PPC [131], although some datasets instead made use of lookup-tables using the Photonics package [130].

A relatively generic method to compare ice models and examine specific ice properties is the DeltaT distribution. DeltaT is defined as

DeltaT: the time difference between first hits on adjacent DOMs on the same string.

A positive DeltaT represents a photon that strikes the upper DOM followed by a photon observed by the DOM directly below (Figure 4.1). This method permits close investigation of basic photon timing without reconstructing the muon position, which requires knowledge of the ice properties. The distribution of DeltaT values for downgoing muon data taken with the 59-string detector configuration is shown in Fig. 4.2. The tails of this distribution consist of relatively long-lived photons and contain information about the bulk ice properties, such as scattering and absorption. On the other hand, the peak of the distribution consists of photons that travel from source to DOM with few scatters (i.e. direct photons), and is

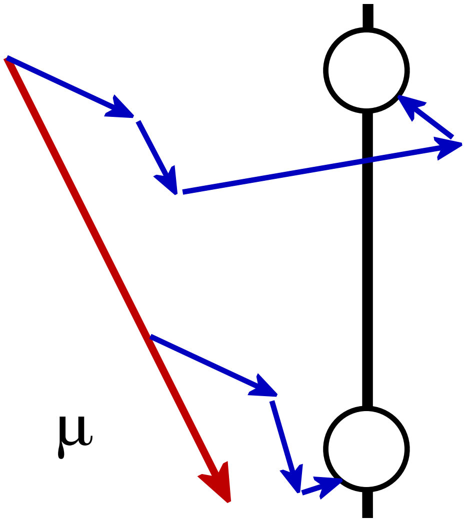

Figure 4.1: Diagram of muon hit timing on adjacent DOMs. DeltaT is defined as the time difference between first hits on adjacent DOMs on the same string. As the muon (red) travels through the ice, it emits Cherenkov photons (blue) which are scattered before hitting the DOM.

relatively invariant to the depth-dependent bulk ice properties. Figure 4.3 illustrates this relationship throughout all detector depths.

The detector response to atmospheric muons was simulating using different ice parameters to examine their effects on the shape and height of the peak in the DeltaT distribution. Figures 4.4, 4.5, 4.6, and 4.7 show the peak shape for data and various simulation models. The description of the ice denoted as SPICE2x was an intermediate model in this analysis, and is characterized by similar scattering and absorption lengths to those of the SPICE Mie model, which is the baseline model. In SPICE2x, a Henyey-Greenstein (HG) scattering function is used instead of a linear combination of the HG and SL functions. Additionally, SPICE2x has an average scattering angle of $g = \langle \cos\theta \rangle = 0.8$ instead of 0.9 (used in the final result), where θ is the scattering angle at each photon scatter. It also lacks the global flasher time offset parameter used in the fit of SPICE Mie. Additional datasets were generated using PPC to examine the effects of specific ice parameters on direct hits. The parameters

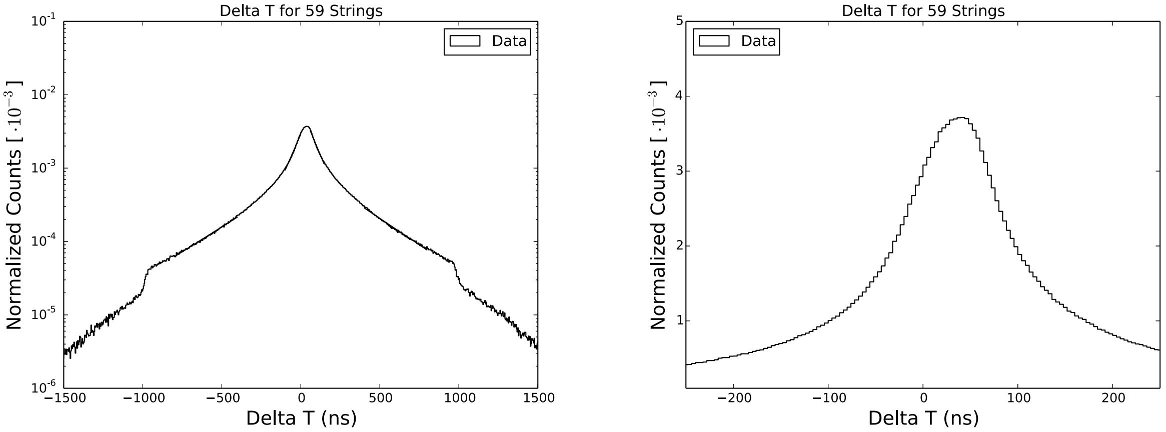

Figure 4.2: Left: DeltaT distribution for muon data. The cutoff at ± 1000 ns is due to the coincidence trigger window where data from a triggered DOM will only be read out if an adjacent or next-to-adjacent DOM also triggers within a time window of 1000 ns. Right: A zoom of the peak of the distribution. The peak is shifted towards positive times because it is dominated by direct photons from downgoing muons, which are detected first by the upper DOM and then the lower DOM. The shift roughly corresponds to the muon flight time between DOMs.

under consideration included the bulk ice scattering coefficient, the scattering parameter $g = \langle \cos\theta \rangle$, the density of air bubbles in hole ice, and the composition of the scattering function. These parameters were varied within the framework of both the SPICE2x ice model and the SPICE Mie ice model. In PPC, the hole ice description is specified by the DOM angular sensitivity function, and Figure 4.8 shows the three angular sensitivity functions used in these models. In all of the permutations of the ice properties examined, the only parameters that significantly changed the shape of the peak were the hole ice scattering, scattering function composition, and the time offset parameter.

Since atmospheric muons are often observed with multiple muons from the same air shower, the effect of muon multiplicity on DeltaT distributions was also studied. Two different approaches were used to isolate samples of single muons. The first method selected muons that stop in the detector, as stopping muons have a high probability of being single

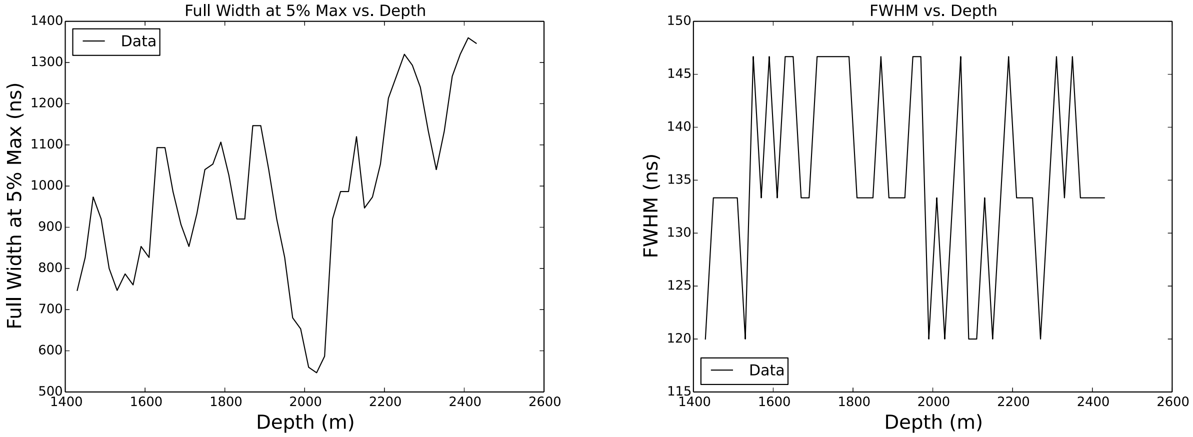

Figure 4.3: DeltaT distributions for DOMs binned in 20 m depths. Widths of the peaks and tails were extracted and plotted vs. depth for the entire detector. Left: The full width at 5% of the maximum, corresponding to the width of the tails, shows a strong depth dependence similar to the derived scattering and absorption parameters. Right: The full width at half maximum (FWHM) shows very little depth dependence. The FWHM was computed by multiplying the number of bins and the bin width, resulting in the discrete level structure in the plot.

muons. A sample of approximately 80% purity of single muons was achieved via this method. In the second approach, single muons were selected by searching for low energy tracks with long direct lengths, leading to a sample of approximately 75% purity of single muons. For each event sample, the resulting DeltaT distributions showed the same characteristics and trends as for the full dataset, thus eliminating muon multiplicity as being associated with the discrepancy in the number of direct hits between various ice models and the detector data.

4.2 Measuring the DOM efficiency using minimum-ionizing muons

While IceCube's PMTs have been calibrated in a laboratory setting [118], the actual efficiency of the full DOM in the ice may be affected by the DOM housing, the string cable,

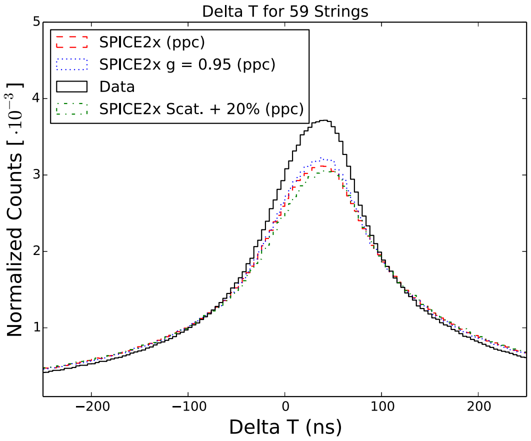

Figure 4.4: The peak region of the DeltaT distribution for the SPICE2x model shows a lack of direct photon hits compared to the data. Neither increasing the amount of forward scattering (g = 0.95) nor increasing the bulk ice scattering by 20% changes the peak height or shape.

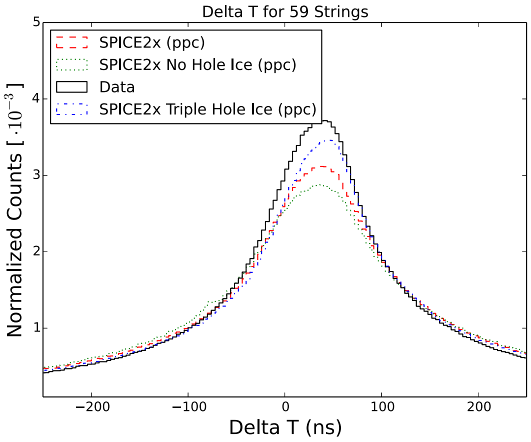

Figure 4.5: DeltaT distribution for hole ice models. The hole ice is modeled as a vertical column of ice with a higher concentration of air bubbles, resulting in a local scattering length of 50 cm. Simulations with no hole ice scattering and with three times the nominal hole ice bubble concentration are shown. Increased hole ice scattering is thought to increase the number of direct photon hits because more photons from downgoing muons are locally up-scattered into the downward-facing PMT, altering the angular sensitivity of the DOM.

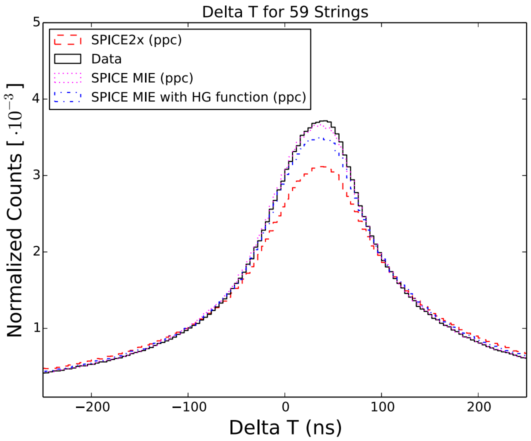

Figure 4.6: The peak region of the DeltaT distribution for SPICE Mie, comparing the full model ($f_{SL} = 0.45$) to the model with only the HG scattering function (i.e., setting $f_{SL} = 0$). The observed effect is thought to be caused by the higher probability of photons scattering through intermediate angles of $\approx 20° - 40°$. Even though the typical muon-to-DOM distance is small compared to the effective scattering length, photons are more likely to scatter at larger angles and therefore to be detected.

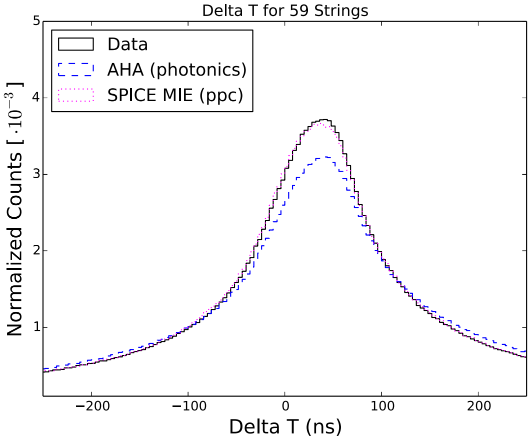

Figure 4.7: The peak region of the DeltaT distribution comparing the final SPICE Mie fit result to the previous model ([121]) and the muon data. The fit to the data is significantly improved with the SPICE Mie model.

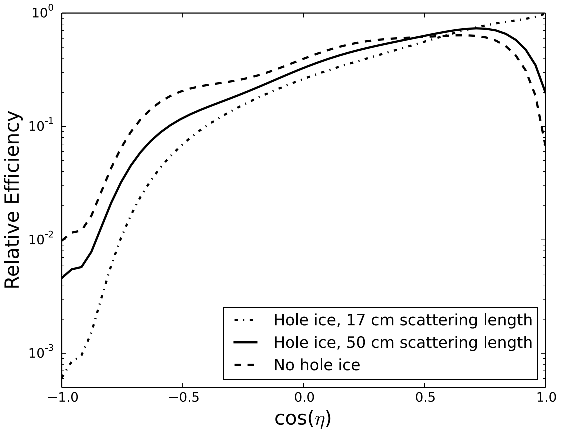

Figure 4.8: DOM angular efficiency curve for different hole ice models. The relative efficiency is shown as a function of $\cos(\eta)$, where η is the photon arrival angle with respect to the PMT axis. The model without hole ice, based on a lab measurement, is normalized to one at $\cos(\eta) = 1$. Decreasing the hole ice scattering length corresponds to less sensitivity to photons arriving at the DOM from below, but more sensitivity to photons originating from above.

and the refrozen hole ice. To better determine the impacts of these factors, this study used low-energy single muons to measure the efficiency of the optical modules *in situ*. Since this measures the observed charge for Cherenkov emitters passing through the ice, it also serves as a calibration of the absolute energy scale of the detector.

Minimum-ionizing muons, created in cosmic ray air showers, are well-suited for energy scale calibration because they have constant known light emission, are abundant, and leave well-defined tracks in the detector. We obtained a large sample of $\sim 100\,\text{GeV}$ single muons, reconstructed their positions and directions to high precision, and compared the observed PMT charges to expected values from Monte Carlo simulation. This was repeated for a number of different simulated DOM efficiencies, allowing the true DOM efficiency to be determined to high precision. The effect of various systematics, including properties of the bulk ice and the hole ice, were also assessed.

To isolate a sample of events we first required that events pass an SMT8 trigger. We then remove poorly-reconstructed events by cutting on track quality parameters, including the number of DOMs with direct hits and the fit quality of the MPE track reconstruction. We select low-energy single muons by searching for tracks that deposit little light in the outer strings and appear to stop in the detector fiducial volume. This is done using the finiteReco likelihood reconstruction, which reconstructs the muon endpoint and is described in [138]. Finally, we require the tracks to be inclined $40° - 70°$ with respect to the straight downgoing direction, to ensure the muon's Cherenkov cone is incident on the active side of our PMTs (Figure 4.9). A complete list of the cuts can be found in Table 4.1. These cuts provide a sample of 70,000 events in 30 days of data taken with IceCube in its 79-string configuration. Distributions of a few event variables for data and simulated atmospheric muons are shown in Figure 4.10. The muon bundle contamination and muon energies estimated from simulation are shown in Figure 4.11. Based on these studies, this sample consists of $> 95\%$ single muons with a median energy of 90 GeV at the detector center.

We then focus on a subset of IceCube DOMs in the deep part of the detector where the glacial ice is exceptionally clear (absorption lengths of $\sim 200\,\mathrm{m}$ [122]). The includes DOMs numbered 41 and above on all standard IceCube strings in the inner two rings of the detector, in addition to the central string. We explicitly do not include high quantum efficiency DeepCore DOMs, so all DOMs in the sample have the same approximate efficiency. We then group the DOMs according to their distance to the reconstructed track. To reduce potential correlations between the observed charge and the track reconstruction, we reconstruct the muon track excluding a specific DOM and then calculate the distance to this de-biased reconstruction. This was done in a five-fold iterative procedure, in which every 5th DOM was removed from the event, the event was reconstructed, and the charge and track-DOM distance of the removed DOMs was tabulated. The resolution of the angular reconstruction and the track-DOM distance is shown in Figure 4.12. These studies show this procedure successfully reconstructs the muon direction and the track-DOM distance within $\sim 2°$ and $\sim 10\,\mathrm{m}$ of the true direction and position, respectively.

Table 4.1: Single muon selection criteria for the DOM efficiency measurement.

Selection Criterion	Description
SMT8	Simple multiplicity trigger requiring at least 8 HLC hits.
$\mathrm{NCh}_{\mathrm{center}} \geq 1$	Require at least one hit DOM on the strings used in the analysis.
$40^\circ < \theta_{\mathrm{MPE}} < 70^\circ$	Cut on reconstructed zenith angle to select highly-inclined tracks, which can pass below the downward-facing DOMs.
$\mathrm{Rlogl} < 10$	Remove poor-quality events with high reduced log likelihoods.
$\mathrm{NDirC} > 5$	Remove poor-quality events that have 5 DOMs with direct hits or less. A direct hit is defined as arriving within [-15,75] ns of the speed-of-light time.
$\mathrm{NCh}_{\mathrm{Excluded}} > 20$	$\mathrm{NCh}_{\mathrm{Excluded}}$ is the # of hit DOMs on the outer strings, which are not included in the charge measurement.
$\mathrm{Z}_{\mathrm{Endpoint}} > -400\,\mathrm{m}$	Select for stopping muons. Z-coordinate of endpoint is reconstructed using finiteReco.
$\Delta d > 50\,\mathrm{m}$	Δd is the x-y distance from the reconstructed endpoint to the border of the detector.

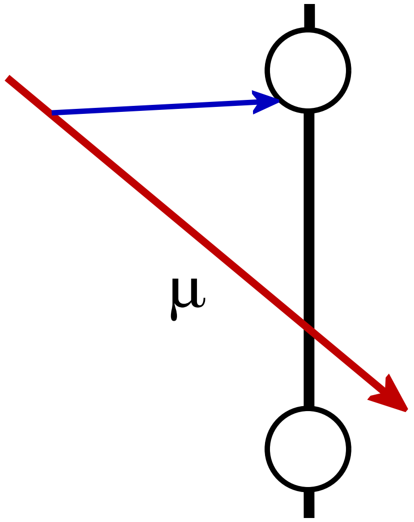

Figure 4.9: Diagram of track-DOM geometry used for the DOM efficiency analysis. Inclined tracks (red) are selected. DOMs are only selected if the muon travels underneath it, so Cherenkov photons (blue) are able to travel up into the active side of the DOM. This reduces the impact of scattering in the refrozen hole ice around the DOM.

To further isolate the measurement from systematic effects, only a sub-sample of DOMs was used in which the reconstructed track passes below the DOM and continues past the DOM for at least 100 m before stopping (as determined by the reconstructed endpoint). The DOMs were divided into bins based on their track-DOM distances, and the average charge per DOM was calculated. Figure 4.13 shows the charge histograms for two distance bins, and Figure 4.14 shows the average charge as a function of the track-DOM distance.

To measure the DOM sensitivity, we take the ratio of average charges for data and MC in each distance bin. This is repeated for detector simulations with DOM sensitivities varied from -10% to 30% in 10% intervals, and is shown in Figure 4.15. To determine the best-fit DOM efficiency for the data, the charges for track-DOM distances of less than 20m or greater than 80m are discarded. At small distances, the error on the reconstructed track-DOM distance is much larger than at other distances, while charge observed at large distances is more susceptible to discrepancies in modeling the light propagation in the ice. We average

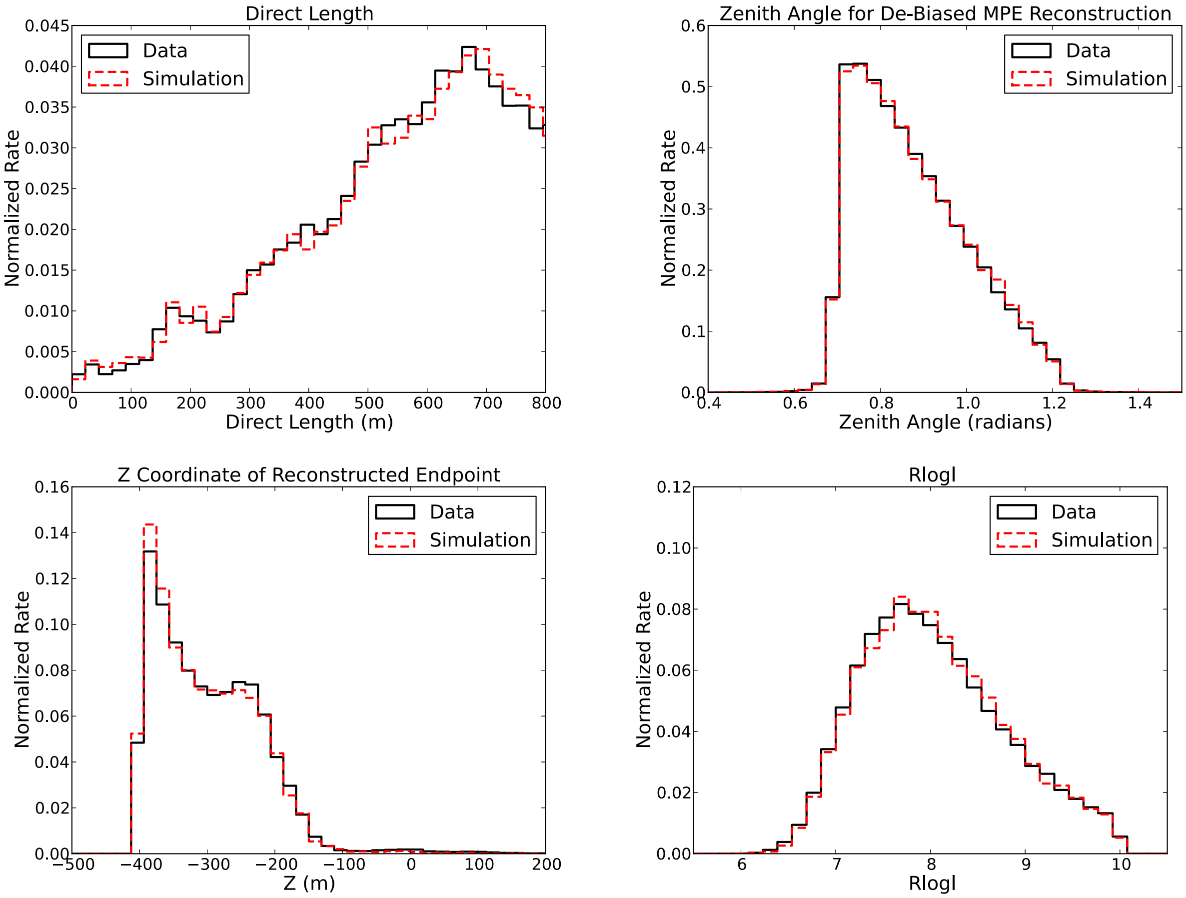

Figure 4.10: Distributions of a few event variables for data and atmospheric muon simulation. The total simulation rate is normalized to the data.

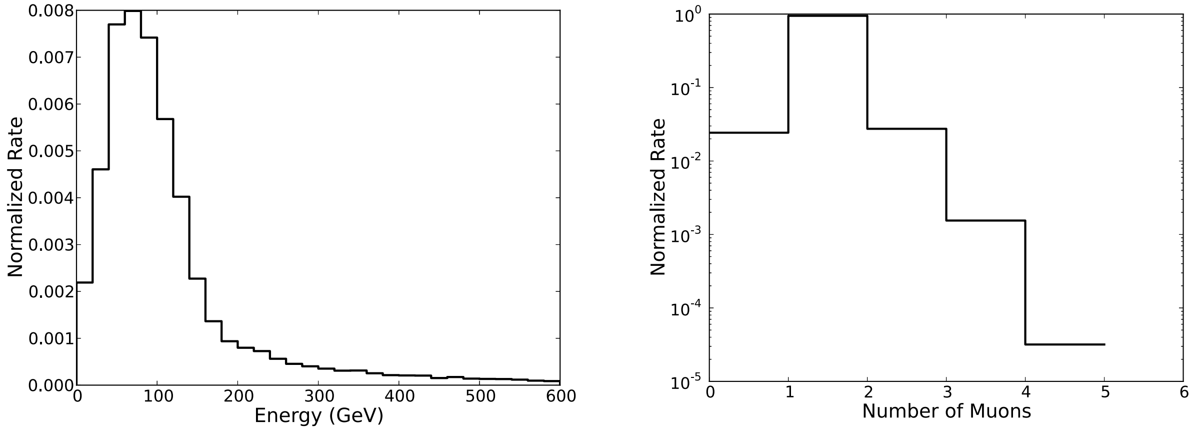

(a) (b)

Figure 4.11: (a) The total simulated energy of muons at the position of closest approach to the center of the detector, for events passing all event selection criteria. The median is 90 GeV. (b) The number of simulated muons per event passing within 140 m of each DOM used in the analysis. Only $\sim 2.5\%$ of DOMs used in the analysis have more than one muon nearby. The first bin represents mis-reconstructed events where the simulated muon was greater than 140 m from the DOM but was reconstructed to be closer.

the charge ratios in the 20-40 m, 40-60 m, and 60-80 m bins, and plot the average charge ratio as a function of simulated DOM efficiency (Figure 4.16). The response is linear over the entire range of simulated DOM efficiencies, and the intercept of the line with a charge ratio of 1.0 (corresponding to the observed data), determines the actual DOM efficiency. This is found to be 109.9%.

The uncertainty on the derived DOM efficiency is estimated to be ±3.0%. The statistical error only contributes ±0.94% uncertainty, because the charge ratio is fit over a wide range of simulated DOM efficiencies, which reduces the statistical uncertainty of the simulation. Uncertainties in a number of detector effects contribute to the DOM efficiency error bar. Their uncertainties were propagated through the entire analysis to estimate their effect on the derived DOM efficiency. The largest contribution is from the uncertain properties of

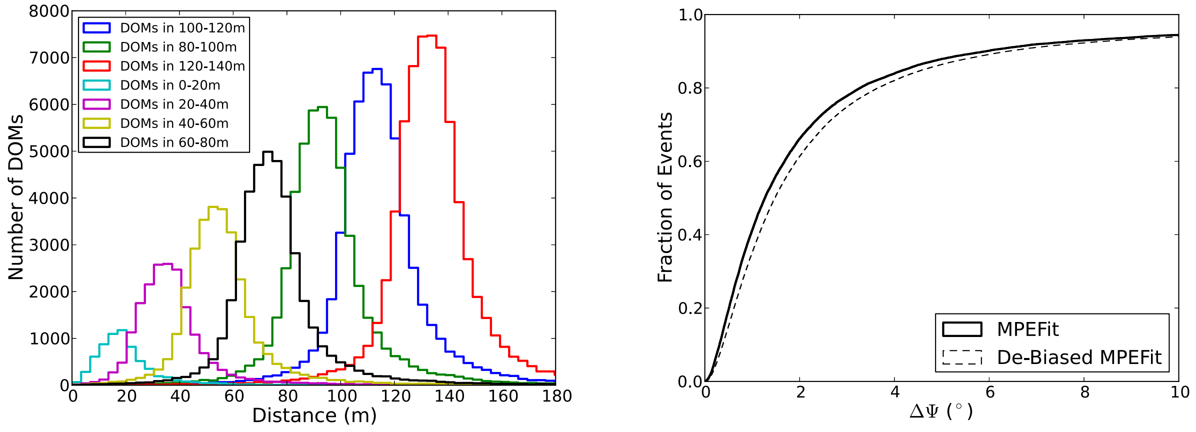

(a)

(b)

Figure 4.12: (a) The true distance between simulated muon tracks and DOMs, for different reconstructed distance ranges. The reconstruction performs well at all distances, although there is some systematic bias of muons being reconstructed closer to the DOM than reality. The bias is proportionally worst for distances $< 20\,\mathrm{m}$. (b) The accuracy of the directional reconstruction for simulated events when using all hit DOMS (solid line) and after excluding every 5th DOM (dashed line). This procedure does not cause the reconstruction accuracy to deteriorate significantly, and the median angular resolution is 1.5° for the de-biased reconstruction.

the refrozen ice in the hole immediately surrounding the DOMs. Studies from AMANDA suggested this column of ice has a high density of air bubbles, with a scattering length of 50 cm. More recent investigations with a controllable video camera embedded in the ice indicated the hole ice column may actually be relatively clear with an opaque central column of bubbles. To estimate the uncertainty on this parameter, we simulate hole ice models with scattering lengths of 30 cm and 100 cm. The corresponding uncertainty on the derived DOM efficiency was ±2.8%. The uncertainty on the muon bundle contamination in the sample was estimated using air shower simulations from three hadronic interaction models (SIBYLL [139], QGSJet [140], and EPOS [141]), and was found to have a ±0.5%

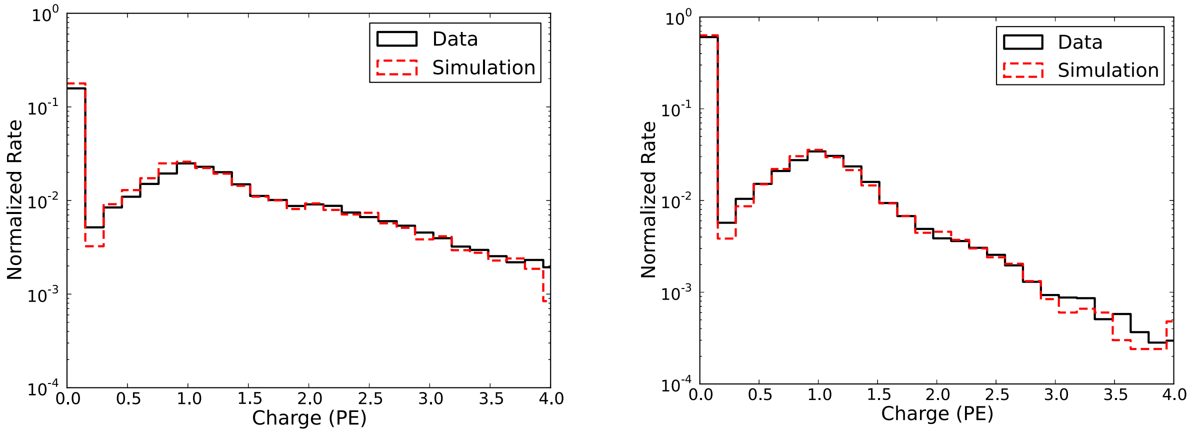

(a) (b)

Figure 4.13: Histogram of observed charges for DOMs (a) within 20-40 m of the reconstructed muon and (b) within 60-80 m. The single photoelectron and double photoelectron peaks can be seen, as well as a large number of DOMs observing no charge. At larger distances, the high-charge tail decays more steeply. Data and simulation show close agreement.

effect on the DOM efficiency. The uncertainty on the afterpulse and detector noise rates were also estimated to contribute ±0.09% and ±0.03%, respectively. Summing these uncertainties in quadrature produces the total uncertainty of ±3.0%.

There are two caveats to the results presented here. The first is the properties of the bulk ice can also effect the derived DOM efficiency. In most physics analyses in IceCube, the systematic uncertainties from the DOM efficiency and the bulk ice are assumed to be uncorrelated, and are summed in quadrature. With this measurement, however, these two uncertainties are correlated. To avoid double-counting these effects, the bulk ice was not included in the ±3.0% systematic uncertainty quoted above. Instead, three different ice models (corresponding to the accepted uncertainty range for the model described in [122]) were propagated through the analysis, and the change in the derived DOM efficiency was determined for each. This serves as a correlation coefficient that can be used to estimate systematic uncertainties for a physics analysis by simulating a change in ice model along with

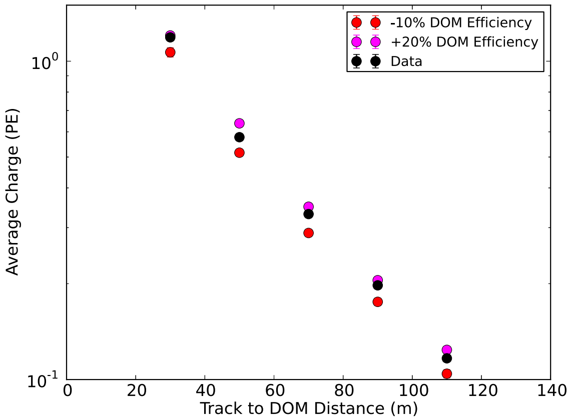

Figure 4.14: Average observed charge vs. distance from the DOM to the reconstructed muon track, shown for data as well as simulation with different DOM efficiencies. Due to the selection of minimum-ionizing, single muons, the observations are dominated by single photoelectrons.

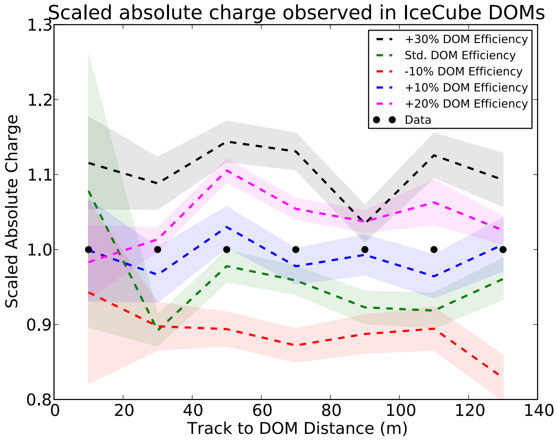

Figure 4.15: The average charge vs. track-DOM distance, normalized to the observed charge in data. Muon data and simulations of five different DOM efficiencies are shown. The observed charge is clearly above the nominal values, and appears consistent with the charge expected for a DOM efficiency increased by 10%.

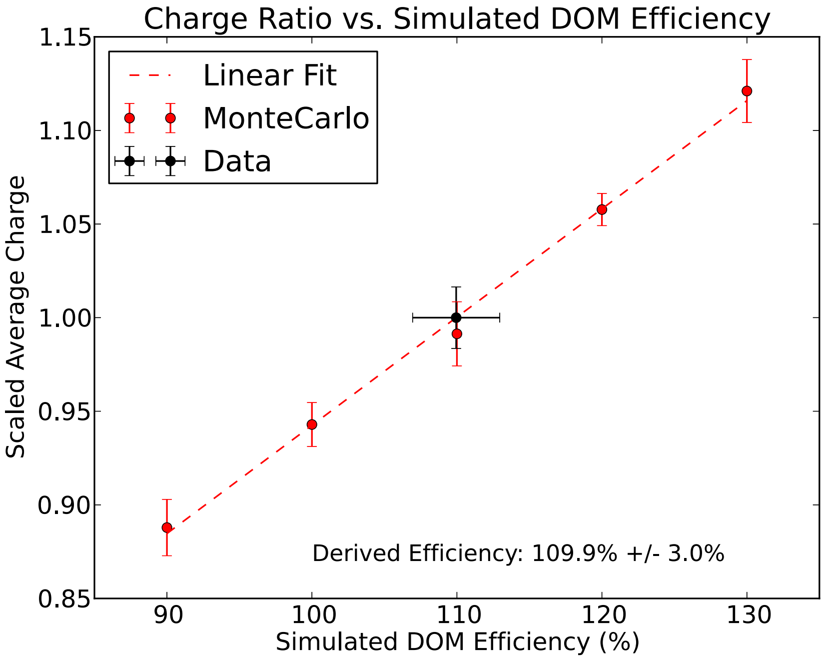

Figure 4.16: Scaled average charge as a function of the simulated DOM efficiency for five different simulations (red). The scaled average charge is the average of the scaled charges in the 20-40 m, 40-60 m, and 60-80 m distances bins in Figure 4.15. A linear function (dashed red line) fits the simulation trend. The scaled average charge for data, defined to be 1.0, is plotted on the line. The x-coordinate of this point corresponds to the derived DOM efficiency for the data, which is 109.9%. The horizontal error bar of 3.0% includes statistical and systematic uncertainties on the final derived quantity, added in quadrature.

a small change in the simulated DOM efficiency. The effective DOM efficiency for ice models with 10% increased scattering, 10% increased absorption, and 7.1% decreased scattering and absorption are 98.0%, 99.4%, and 101.0%, respectively.

The second caveat is while the peak of the single photoelectron (SPE) distribution for simulation lies directly at a charge of 1.0, the distribution in data is on average shifted to a charge of 1.022. This signifies one SPE in data is 2.2% higher than one SPE in simulation. Ideally, this would be fixed at the charge calibration stage; however, this was not possible at the time of this writing. As a result, the 109.9% DOM efficiency quoted above is a correction not only for the DOM efficiency but for this SPE shift as well. If the SPE shift is explicitly de-convolved from the data before fitting DOM efficiency, the derived DOM efficiency is 106.2% ± 3.2%. This is a more correct estimate of the efficiency of the DOM itself, while the number above is an effective DOM efficiency that is currently more useful for simulating the detector.

Chapter 5

Point Source Searches: Introduction

This thesis contains three separate analyses that search for point sources of astrophysical neutrinos. Each analysis uses a different event selection strategy to reduce the atmospheric backgrounds. They all apply the same unbinned maximum likelihood method to test different hypotheses of neutrino emission from different sources.

The first analysis uses a high-statistics sample of throughgoing muon tracks. It is sensitive to TeV – PeV neutrino sources in the northern hemisphere and 100 TeV – 100 PeV sources in the southern hemisphere. It is most sensitive in the northern hemisphere, where the atmospheric muon background is reduced by the Earth. The second analysis uses a small sample of high-energy contained-vertex events—events that interact inside the detector volume, most of which have cascade topologies. Compared to the throughgoing muon analysis, this search has a much lower background rate but a worse angular resolution. It is most sensitive in the southern hemisphere at energies $\gtrsim 50\,\mathrm{TeV}$. The third search extends the throughgoing muon analysis to lower energies in the southern hemisphere by selecting track events that start inside the detector volume. This utilizes similar techniques to the high-energy contained-vertex search, and greatly enhances the sensitivity to southern hemisphere sources below $\lesssim 1\,\mathrm{PeV}$. Fig. 5.1 shows the type of event used in each analysis and Table 5.1 summarizes the overall event rates.

The following three chapters detail the techniques and results for each analysis. The last chapter investigates the astrophysical implications of these results.

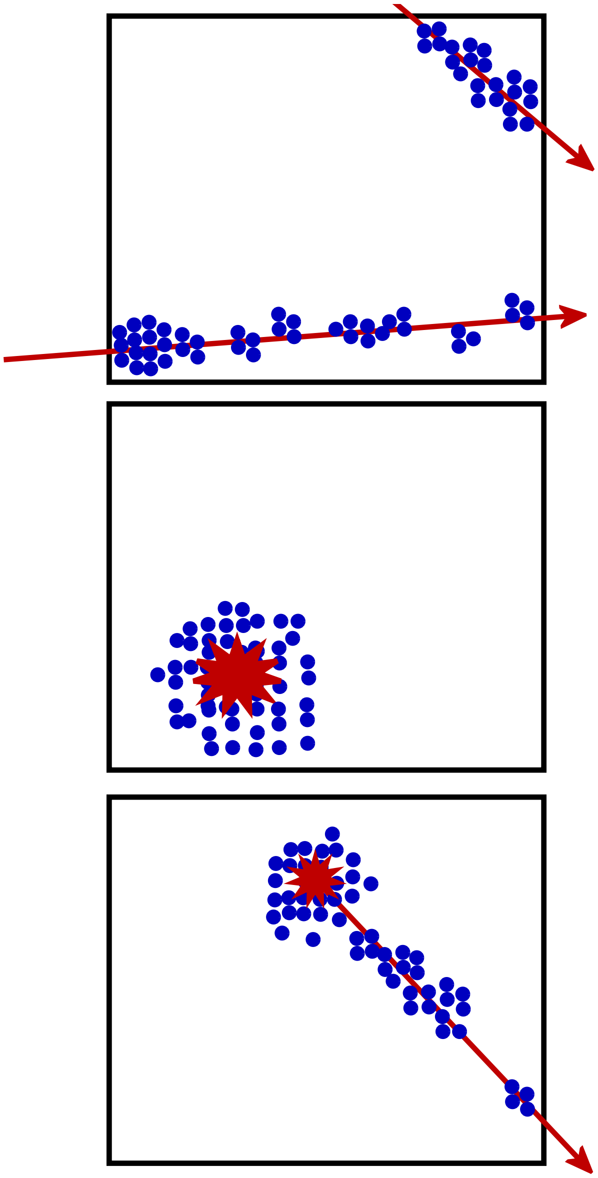

Figure 5.1: Diagram of event topologies used in each point source analysis. The top panel illustrates the upgoing and downgoing throughgoing muon tracks used in Ch. 6. The middle panel shows a cascade event, which is the dominant topology in the high-energy contained-vertex analysis in Ch. 7. The bottom panel shows medium-energy starting-track events from the southern hemisphere, used in Ch. 8. The black box represents IceCube, while particle interactions are shown in red and hit DOMs in blue.

Analysis	Live-time [days]	Event Topology	# Up-going	# Down-going
Throughgoing Muon	1372.4	Muon Tracks	177,544	215,113
High-Energy Contained-Vertex	988.5	Cascades, Starting Tracks	11	24
Medium-Energy Starting Track	988.5	Starting Tracks	0	549

Table 5.1: Summary of live-time and event numbers for each point source analysis. An event is defined as up-going if it has a zenith angle $> 85°$, since the overburden at these angles is sufficient to remove all atmospheric muons.

Chapter 6

Search for Point Sources using Four Years of Throughgoing Muon Data

This chapter describes an analysis for astrophysical neutrino emission from point-like sources using four years of throughgoing muon data. The analysis selects high-quality muon tracks and applies an un-binned maximum likelihood method to search for spatial clustering. The background for this search is dominated by atmospheric muons and atmospheric neutrinos in the southern and northern hemispheres, respectively. Both these populations of events are distributed isotropically across the sky and follow a softer spectra compared to most models of astrophysical sources. An astrophysical source would appear as an excess of high-energy muons coming from a specific location in the sky. The likelihood method, combined with the muon angular resolution of $< 1^\circ$, allows us to measure the position of the source and fit its flux and energy spectrum.

We start by describing the event selection for the most recent year of data, taken with the 86-string detector configuration. The first three years of data are from the 40-string, 59-string, and 79-string detector configurations, and the event selection for these years are fully explained in [133, 142]. This is followed by a description of the analysis method, a discussion of the hypotheses tested and the analysis sensitivity, and finally, the results.

6.1 Neutrino Event Selection

The event selection reduces the total rate of detected events by roughly six orders of magnitude to obtain a final sample suitable for the likelihood method. In each hemisphere, the backgrounds differ greatly. In the northern hemisphere, or upgoing region in IceCube's coordinate system, the Earth acts as a shield against cosmic ray muons. Atmospheric neutrinos, on the other hand, travel through the Earth without absorption and interact near the detector. On an event-by-event basis, these look identical to astrophysical neutrinos, and are an irreducible background. We expect $\sim 10^5$ such events per detector year, corresponding to an event rate on the order of mHz. However, we observe a kHz event rate triggerring the detector that appear to be upgoing events. The vast majority of these are muons from cosmic ray interactions in the atmosphere above Antarctica that are mis-reconstructed as upgoing. This is a reducible background, and the event selection in the northern hemisphere is dedicated to removing these events.

In the southern hemisphere, there is only 1.5 km of ice above the experiment to shield the detector from the kHz cosmic ray muon rate. Many of these events are indistinguishable from astrophysical neutrinos interacting in the ice above the detector. The goal of the event selection in this region is then to simply reduce the rate while keeping as high a signal efficiency as possible. This is done via quality cuts, energy cuts, and variables that distinguish atmospheric muon bundles from astrophysically-induced single muons.

The event selection first consists of a series of cuts that reduce the data rate by a factor of 30, called the Level 3 filter. Machine learning algorithms are then applied to discriminate between signal and background to obtain the final sample. At all stages, different variables and cuts are used in each hemisphere. For our purposes, the northern hemisphere extends 5° above the horizon, where the Earth and glacial ice still provide a shield from the cosmic ray background. The event selection is divided at this boundary for each stage.

6.1.1 Preliminary Data Reduction: The Level 3 Filter

The event selection starts with the 34 Hz of data (10 Hz upgoing, 24 Hz downgoing) that passed the Muon and Extreme High-Energy (EHE) Filters (see Section 3.3). At this level, the data in the upgoing region are dominated by events consisting of muons from multiple independent air showers passing through the detector at the same time ("coincident

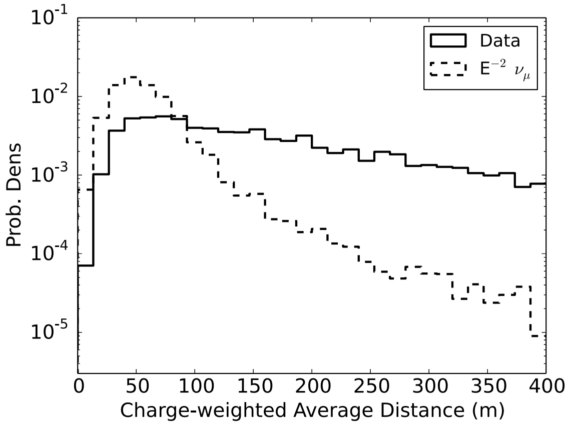

Figure 6.1: Charge-weighted average distance for data at filter level (solid) and simulated E^{-2} neutrinos (dashed). The charge-weighted average distance is calculated using the MPE reconstruction. Mis-reconstructed background events more often have large charge-weighted average distances.

events") and low-energy atmospheric muons from a single air shower that are reconstructed as upgoing. The data rate is reduced to 1.7 Hz using a sequence of pre-cuts, event splitting, and final cuts. This procedure is referred to as the Level 3 filter. After the cuts, advanced directional and energy reconstructions are applied to the remaining data.

The pre-cuts remove obvious poorly-reconstructed events and reduce the data rate sufficiently so event splitting can be applied. This is done using the total charge of the event and the charge-weighted distance parameter. The charge-weighted distance is defined as the average distance from the reconstructed track to the hit DOMs, weighted by the charge on each DOM (Fig. 6.1). By only keeping events with a charge-weighted distance of less than 90m or a total charge of greater than 100 photoelectrons (PE), we reduce the upgoing data rate from 10 Hz to 3 Hz while keeping 97% of simulated upgoing signal neutrinos (E^{-2} spectrum).

In the downgoing region, this cut is applied and the online muon filter is re-applied. Online, the muon filter uses a single-iteration SPE reconstruction to determine the zenith angle of the event. At Level 2, more advanced reconstructions are applied, and by using the MPE reconstruction many events that previously appeared to be upgoing now appear to be low-energy downgoing events. Reapplying the muon filter removes this background. The cumulative effect of these two cuts reduces the downgoing data rate from 24 Hz to 10 Hz while keeping 89% of simulated E^{-2} signal neutrinos. The majority of the signal that is removed in this region is relatively low-energy.

With the remaining 13 Hz of data, it is computationally affordable to apply an event splitting algorithm. Event splitting is used to identify coincident events by grouping PMT hits and assigning them to different hypothetical particles which may be traveling through the detector at the same time. We apply a clustering algorithm named Topological Splitter that identifies causally connected hits. Hits closer together than 300 m in the x-y plane, 255 m in depth, and 1000 ns in time are grouped together. This splitting algorithm not only identifies coincident events but also removes noise hits and afterpulses. Since it returns a new pulse series (or multiple pulse series) for each original event, we reconstruct these new pulse series with the Level 2 directional reconstruction chain (see Section 3.3). After splitting, 35% of data events that were originally upgoing are now reconstructed as downgoing, and are thrown away.

The effect of the splitting on simulated signal events is minimal. 6.8% of signal events that are not accompanied by a coincident event are split into one event consisting of the primary physics hits, and a separate event consisting of afterpulses and noise. The afterpulse/noise events are easily removed by quality cuts, and which is beneficial for correctly reconstructing the energies of bright events. On the other hand, 0.2% of signal events are incorrectly split into two separate physics events. This primarily happens for low-energy neutrinos, which can traverse large chunks of the detector without being observed. To safeguard against this pathology, split events that are reconstructed to be coming from the same direction (within 5°) are recombined into one event.

After splitting and reconstructing the new events, a series of quality cuts are applied to reduce the data rate to 1.7 Hz. The cut variables describe how well the track reconstruction fits the data. In most events, the MPE reconstruction is used to calculate these variables;

however, if this reconstruction did not converge, the SPE or LineFit reconstructions are used instead. The variables are:

NDir: The number of DOMs with a direct hit. A direct photon hit is defined as any observed photoelectron within [-15,250] ns of the speed-of-light time for a photon emitted by the muon at the Cherenkov angle. A larger number of direct hits signifies the track reconstruction is a better fit to the data, and is associated with signal events.

Direct Ellipse: This variable describes an ellipse in the NDir-LDir plane. LDir, or the direct length, is defined as the length along the reconstructed track between the first DOM with a direct hit and the last DOM with a direct hit. Signal events tend to have a higher number of direct hits and/or a longer direct length. An ellipse in this space efficiently removes events with short direct lengths and few direct hits.

Rlogl: The reduced log likelihood, Rlogl, is the best-fit negative log likelihood from the MPE reconstruction divided by the number of degrees of freedom of the fit, $-\log\mathcal{L}/(\mathrm{NCh}-5)$. NCh is the total number of hit DOMs. Track reconstructions us the first hit on each DOM and fit for 5 parameters (zenith,azimuth,x,y,z), so the fit has (NCh−5) degrees of freedom. Well-reconstructed tracks have lower Rlogl values, while mis-reconstructed background have higher values.

Plogl: It is observed that the Rlogl distribution is energy-dependent, with higher-energy tracks more likely to have a lower Rlogl. A tight cut on Rlogl therefore removes more low-energy signal than desired. To correct for this, the variable Plogl is defined as $-\log\mathcal{L}/(\mathrm{NCh}-3)$, which is observed to have better descrimination power between background and signal neutrinos with a softer E^{-3} spectrum.

In the upgoing region, events satisfying the following criteria are kept:

$$(\text{Direct Ellipse} > 2 \text{ and NDir} > 6) \text{ or Plogl} < 7.5 \text{ or Rlogl} < 8.3$$

In the downgoing region, additional cuts must be applied to reduce the higher background from high-energy atmospheric muon bundles. At this level the variable with the

Region	Event Type	Efficiency (%)	Rate (Hz)
Upgoing	Data	3.8	0.4
	$E^{-2}\ \nu_\mu$	91	–
	$E^{-3}\ \nu_\mu$	86	–
Downgoing	Data	5.4	1.3
	$E^{-2}\ \nu_\mu$	64	–
	$E^{-3}\ \nu_\mu$	25	–

Table 6.1: Signal and data efficiencies for the Level 3 filter.

most discrimination power is the energy of the event. After applying the cuts above to select well-reconstructed tracks, we then apply a zenith-dependent charge cut to remove low-energy events while keeping an equal event rate per solid angle. The final cut is:

$$\text{(Upgoing Cut) and } \log q > 0.27 + 13.62x - 27.62x^2 + 26.07x^3 - 9.21x^4$$

where x is the cosine of the zenith angle. Additionally, in both hemispheres all events with a deposited charge greater than 10^4 PE are kept, even if they failed other cuts. This avoids losing high-energy events due to a bad track reconstruction, as some studies have shown the MPE reconstruction performs worse on the highest energy events.

1.7 Hz of data pass these cuts (0.4 Hz upgoing, 1.3 Hz downgoing). The overall efficiency of the event selection is summarized in Table 6.1. For this data rate, computationally expensive reconstructions can be applied that are useful for the final event selection. These include the MuEX angular reconstruction, the SplineMPE reconstruction, and the Paraboloid angular uncertainty estimator, which are described in Section 3.4.

6.1.2 Final Event Selection

From the 1.7 Hz of remaining data, 4.8 mHz of events are selected for the final analysis sample. This is done separately for the upgoing and downgoing regions. In the northern sky the background is dominated by low-energy mis-reconstructed atmospheric muons. This can be mostly eradicated to isolate a sample of well-reconstructed up-going atmospheric neutrinos, which are an irreducible background for the astrophysical neutrino signal. In the southern sky, the background consists of high-energy muon bundles. This background more closely mimics the signal, and is much harder to eliminate. Therefore, the event selection in the south selects high-energy well-reconstructed events to reduce the data rate. For the first time, we also discriminate between muon bundles and single muons of the same energy deposition in order to enhance the signal efficiency.

In both regions the event selection uses a classification algorithm known as a Boosted Decision Tree (BDT). A decision tree is a series cuts that divide a data sample into different classes. It is a supervised training algorithm - given events pre-identified as signal or background and a series of variables or "features" to use in the event selection process, the decision tree learns how to classify the events. By optimizing the series of cuts on this known data, it determines the probability that a new unknown data event is signal or background, based on the values of its parameters. BDTs have previously been used for event selection in neutrino experiments [142, 143].

Decision trees are highly effective at classifying data, but they also suffer from overtraining. While decision trees are meant to exploit differences in statistical distributions that describe the data set, they can also find regions of the parameter space where the signal and background appear to be well-separated, due to chance fluctuations. In such a scenario, the decision tree's predictive power for new events will be overestimated. One common technique to reduce overtraining is boosting. In a BDT, a decision tree is formed usually the training data. The algorithm then tabulates which events it correctly classified and which it did not, and adjusts the relative weighting of the events to increase the importance of the misclassified events. This new re-weighted dataset is then used to train another decision tree. This process is repeated several hundred times. When a new, unknown event is then run through the BDT, its resulting score is a weighted sum of the results of all the trees. In this event selection, we use the pyBDT software package to train and apply our BDTs.

6.1.2.1 Northern Hemisphere

To best separate signal from background ratio, the northern sky is divided into two zenith regions. Due to neutrino absorption in the Earth, the straight upgoing region is mostly sensitive to neutrinos below 100 TeV while the region closer to the horizon is sensitive to a wider energy range. The first region extends from a zenith angle of 85° to 130° and the second covers 130° to 180°. In each region, one BDT is trained using E^{-2} Monte Carlo as signal and another BDT is trained using a softer $E^{-2.7}$ spectrum. The output scores from both are used in the final event selection. The following nine variables are used in the BDTs in both zenith regions:

Bayesian reconstruction likelihood ratio A 2-iteration SPE Fit is applied to the data, weighted with a prior describing the zenith distribution of atmospheric muon events. The reconstruction applies a strong prior probability of an event being downgoing. For mis-reconstructed events, a downgoing hypothesis often has the best overall likelihood when weighted with this prior, while true upgoing events are robust against such a weight. The likelihood ratio between the bayesian fit and the standard 2-iteration SPE fit is provided to the BDT.

Space angle between SplineMPE and LineFit The space angle between different reconstructions, which use very different algorithms and techniques, is used to estimate the stability of the reconstruction and the quality of the event. Compared to the LineFit, the SplineMPE reconstruction uses more detailed information on the photon timing distributions. It is also seeded with the MuEX angular reconstruction, which uses an iterative bootstrapping procedure to avoid local minima in the likelihood space, and therefore better reconstructs low-quality events. For signal-like events, these two algorithms usually reconstruct the events within a few degrees of each other, while these reconstructions can differ by 20° - 30° for background-like events.

Space angle between high-noise and standard MPE Fit This variable is similar to the one above, but uses the standard (Pandel-based) MPE reconstruction and a high-noise MPE fit. The MPE PDF includes a noise term to tolerate a low number of hits arriving randomly in time. By increasing the noise term by a factor of 10^5, the reconstruction more easily tolerates excess noise from random hits or a second muon in the detector. It often achieves a more accurate reconstruction when the standard MPE reconstruction fits for a local minimum. Therefore, the space angle between these two reconstructions can be large for poor-quality background events and small for signal-like events.

NDir The total number of DOMs with a "direct" photoelectron hit, defined as [-15,250] ns with respect to the speed-of-light time. The SplineMPE reconstruction defines the track position for the photon travel distance. Well-reconstructed events have a higher number of direct hits, indicating the reconstruction fits the data well.

Direct Length This variable is the maximum length along the reconstructed track between DOMs with direct hits. Signal-like events tend to have longer tracks and therefore longer direct lengths.

Muon speed from LineFit The LineFit reconstruction returns not only the direction and position of the muon track, but also its speed. For well-reconstructed events, this parameter is close to the speed of light, 0.299 m/ns, while poorly reconstructed events often have faster or slower speeds.

Reconstructed energy Most astrophysical neutrino fluxes are predicted to have a harder spectrum than atmospheric backgrounds. The MuEX energy reconstruction is used here (see Section 3.4).

COG$_Z$ The z-coordinate of the "center-of-gravity" of the event, or the average depth of hit DOMs. Since the background is dominated by mis-reconstructed atmospheric muons originating from above, they deposit most of their energy near the top of the detector.

Minimum zenith of split reconstructions A series of reconstructions are run in which the collection of hit DOMs in the event is split in half, and separate reconstructions are run on each half of the event. This is done by splitting the hit series in half in either space and time, producing four reconstructions - one for each half of the hit series, for both types of splitting. This technique identifies coincident events. It also identifies low-energy events where the reconstruction was distracted by a large cluster of noise hits. Well-reconstructed upgoing events are relatively robust against this splitting procedure, while background events often appear downgoing after such aggressive splitting. The zenith angle of the most downgoing of the four split reconstructions is used in the BDT.

The following variables are used only in the BDT in the horizontal region:

Rlogl This parameter was defined in Section 6.1.1. Here, the SplineMPE reconstruction provides the likelihood.

Angular uncertainty using Paraboloid The paraboloid algorithm [134] estimates the uncertainty of an angular reconstruction by fitting the profile likelihood around the minimum. Eight zenith and azimuth locations are sampled, and the remaining dimensions (vertex position) are fit independently at each point. A paraboloid function is fit to the likelihood shape, returning the one sigma contour in angular space. Here, the algorithm is applied to the MPE reconstruction.

The following variables are used only in the BDT for the vertical region:

Plogl This parameter was defined in Section 6.1.1. Here, the SplineMPE reconstruction provides the likelihood.

Angular uncertainty using MuEX Similar to paraboloid, this algorithm determines the uncertainty associated with an angular reconstruction. Both the direction and uncertainty are reconstructed using the iterative bootstrapping approach of MuEX (described in section 3.4). The angular uncertainty is defined as the median angular difference between each track reconstructed from the bootstrapped pulses and the final track fit using the complete pulse series.

Both these pairs of parameters strive to separate signal and background events in the same way, but the latter pair achieves slightly better separation power for lower-energy events, which dominate the vertical region.

Distributions of a few BDT input variables, for both background and signal, are shown in Figure 6.2. The resulting score distributions for each BDT in each region are shown in Figure 6.3. Cuts on the BDT output scores are optimized to achieve the best discovery potential for both E^{-2} and $E^{-2.7}$ signal spectra. The final cut keeps any event in the horizontal region with a score from either the hard-spectrum or soft-spectrum BDT of greater than 0.13, as well as any event in the vertical region with a score from either BDT greater than 0.11.

6.1.2.2 Southern Hemisphere

At an angle of more than 5° above the horizon, a pure neutrino sample cannot be isolated from the high-energy atmospheric muon bundles that mimic neutrinos. The background can be reduced by raising the energy threshold, applying quality cuts, and searching for signatures of single neutrinos while rejecting muon bundles.

Before training the BDT, the data are reduced by applying the IceTop veto. This parameter exploits IceTop, the water cherenkov array on the surface of the glacier above IceCube, by looking for surface hits from an air shower in coincidence with the muon observed in the ice. Figure 6.4 shows the distribution of hits observed in the surface array. The time range between -50 ns and 500 ns is used as the veto region, and any event with two or more IceTop hits in this interval is discarded, as it likely originates from a cosmic ray air shower. This cut is most effective at small zenith angles, where events are likely to pass close to IceTop, and reduces the total data rate in the southern hemisphere by 13%. The signal efficiency for this cut is estimated from the off-time data. Less than 2% of events have two or more random noise hits in a 550 ns off-time region, and would therefore be accidentally vetoed.

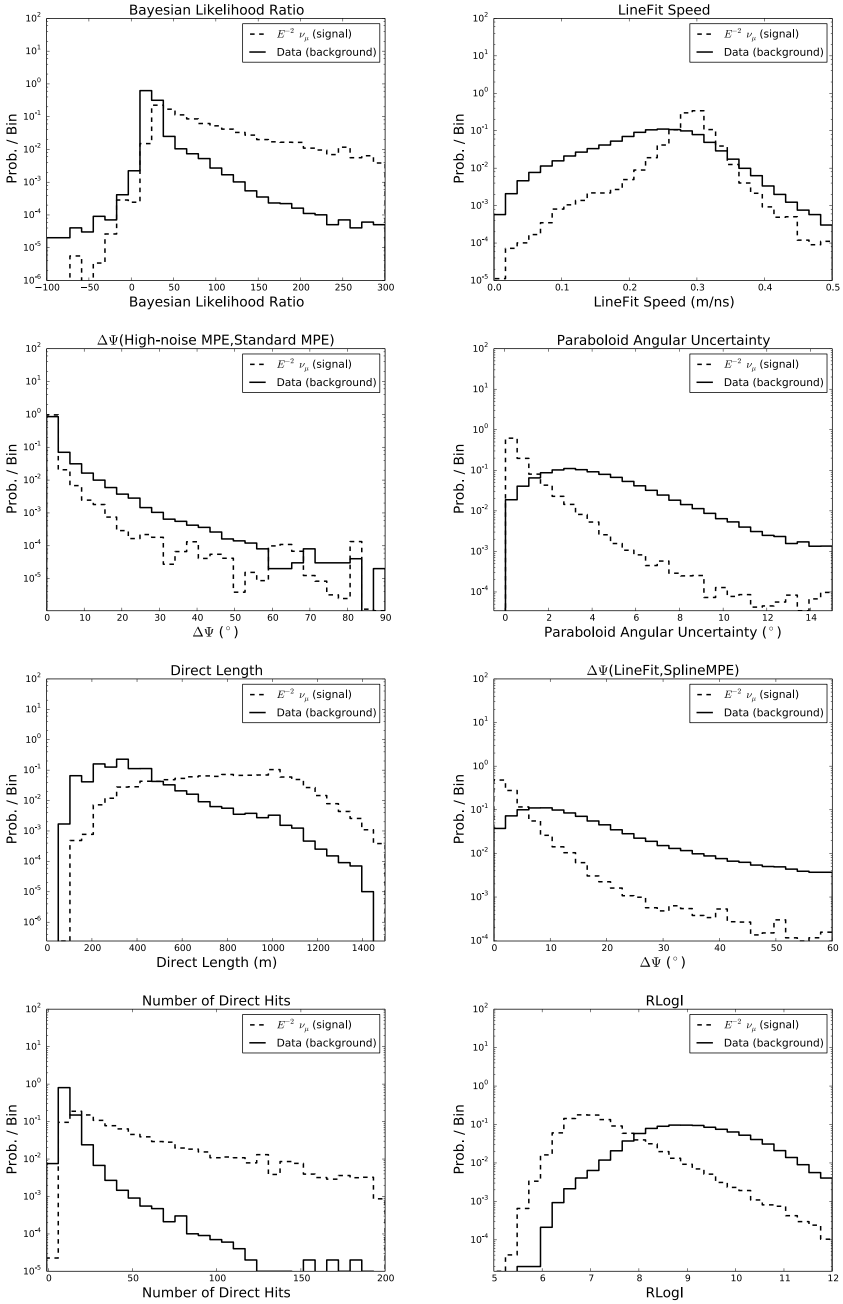

Figure 6.2: Distributions of BDT variables for signal and background in the horizontal region. Each plot shows the data (solid), representing the background, and simulated E^{-2} ν_μ for signal (dashed). The signal only includes events reconstructed within 5° of the true direction.

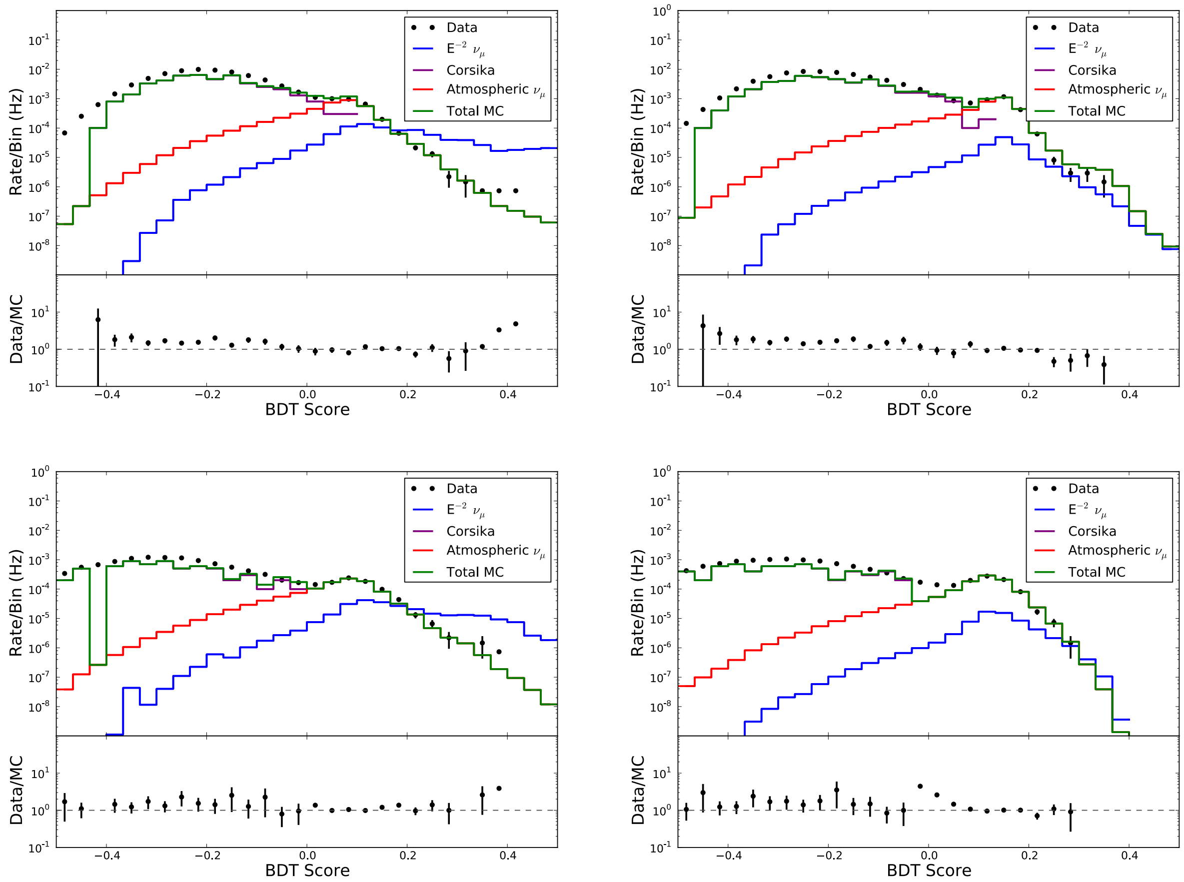

Figure 6.3: Distributions of BDT scores for the upgoing region. The upper two plots show the output scores for the BDTs trained for the horizontal region, while the lower two plots show the vertical region. The left plots show the BDTs trained with $E^{-2.0}$ ν_μ, while the right plots show the BDTs trained with $E^{-2.7}$ ν_μ. In each plot, the lower panel shows the ratio between the data and the sum of the simulations. For higher score values, the BDT becomes dominated by atmospheric neutrinos. At low scores, the data has an excess of events compared to the simulated backgrounds. The agreement improves greatly in the neutrino-dominated region.

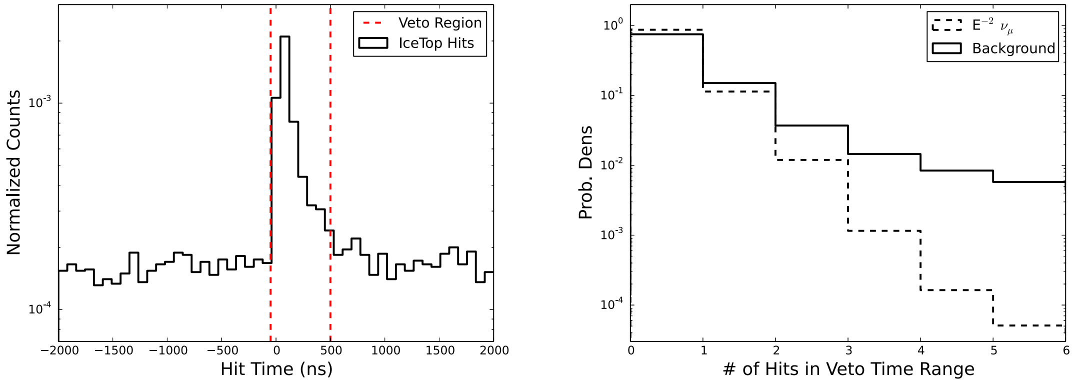

Figure 6.4: Hit distributions for the IceTop surface veto. The left plot shows the hit rate as a function of time with respect to the in-ice muon. Hits between -50 ns and 500 ns often originate from the atmospheric air shower accompanying the in-ice event, and are used as a veto. Hits beyond this time range, representing random noise hits, illustrate the effect of the veto on astrophysical neutrinos, which have no accompanying air shower. The right plot shows the efficiency of a cut on the number of veto hits for signal and background, both estimated from the data. Most astrophysical neutrinos have zero or one coincident IceTop hits, while background events are much more likely to have more than one veto hit.

One BDT is trained for the entire downgoing region using data to describe the background and E^{-2} neutrino simulation for signal. Eleven variables are used to train the BDT. The first six are also used in the northern hemisphere:

NDir

Direct Length

Rlogl

Angular Uncertainty using Paraboloid

Space Angle between high-noise and standard MPE Fit

COG_Z

The following two variables are geometrical quantities used to reject poor-quality events:

Separation The separation parameter measures the distance between the center-of-gravity of the first quartile and last quartile of hits.

COG squared radius The center-of-gravity radius is the distance in the x-y plane from the center of the detector to the average x-y position of the hit DOMs in the event. This parameter helps remove events that only pass near the edge or corner of the detector, which are harder to reconstruct accurately.

The last three variables exploit differences between single muons and muon bundles:

$\mathbf{N_{Early}}$ / $\mathbf{N_{Ch}}$

Energy loss likelihood ratio

Time residual likelihood ratio

High-energy single muons leave different charge deposition profiles in the detector compared to muon bundles of similar energies. Large muon bundles consist of many low-energy muons that typically lose energy at a constant rate as they traverse the detector. On the other hand, neutrinos only create high-energy single muons and therefore have relatively stochastic energy loss profiles. Photons from muons bundles are generally detected within a wide time range, due to the width of the bundle. Outlying muons can also be recognized by photon hits arriving at the DOM earlier than the speed-of-light time, as this time is calculated from the reconstruction at the center of the bundle. and narrower photon timing distributions. High-energy neutrino-induced muons, being single muons, have narrower time residual distributions. The identification of early hits is done using the $\mathrm{N_{Early}}$ / $\mathrm{N_{Ch}}$ variable. The subtler properties of the energy loss and timing distributions are quantified by a likelihood technique.

For each signature (energy losses, photon timing), a likelihood is constructed to make use of all relevant information - every reconstructed energy loss and every hit DOM. Probability tables of these observables are constructed for both the background (here represented by data) and the signal (simulated neutrinos weighted to an E^{-2} spectrum). For a given event and its observed data, the likelihood is calculated first using the signal PDFs and then the background PDFs, and the ratio of the log likelihoods is used as a discriminator.

More formally, the likelihood to describe the energy loss distribution is

$$\mathcal{L} = \prod_{\text{losses}} P(E_{\text{loss}}|E, L_{\text{loss}}). \tag{6.1}$$

The product is over all energy losses, and the probability P of an event with energy E having a loss of energy E_{loss} at a length L_{loss} along the track is looked up in a histogram constructed from either the data or simulated neutrinos. The size and location of each individual energy loss is calculated using Millipede, and the energy proxy E is chosen to be Millipede dE/dX, the total deposited energy reconstructed using Millipede divided by the track length. Figure 6.5 shows an example of an energy loss PDF. The signal distribution is centered on higher energies than the background, and has a larger variance. The likelihood is calculated twice, once using the signal PDFs and once using the background PDFs. The logarithm of the likelihood ratio,

$$\log_{10}\left(\frac{\mathcal{L}_S}{\mathcal{L}_B}\right), \tag{6.2}$$

is then used as a variable in the BDT, where $\mathcal{L}_S$ and $\mathcal{L}_B$ are the likelihoods calculated using the signal and background PDFs, respectively.

Similarly, the time residual likelihood is

$$\mathcal{L} = \prod_{\text{DOMs}} P(t_{\text{hit}}|E, d). \tag{6.3}$$

The product is over all hit DOMs, t_{hit} is the time residual for the first hit on a given DOM, d is the distance of closest approach between the given DOM and the reconstructed track, and E is again the event's energy proxy. To avoid potential systematic uncertainties in the modeling of the ice properties, only DOMs within 150 m of the track and with time

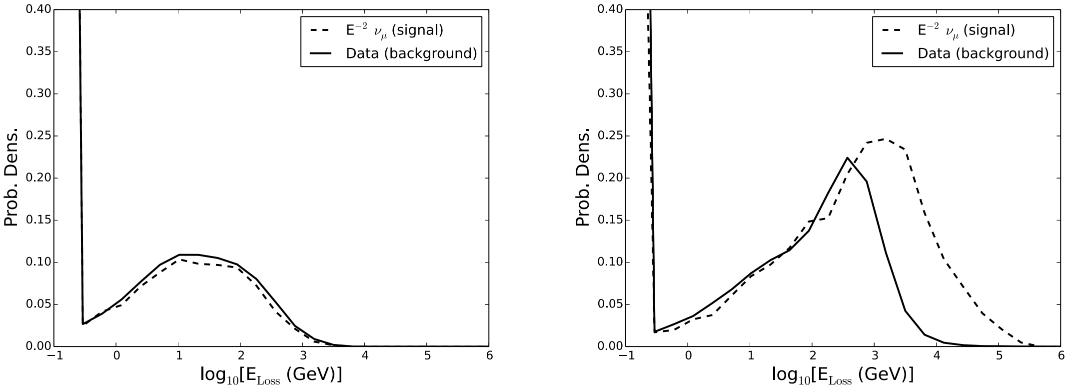

Figure 6.5: Probability distribution function for the energy loss likelihood. The left plot shows the distribution of energy losses occurring 400 m down the track. Both data and simulated signal tracks with a reconstructed dE/dX between 10^{-1} and $10^{0.8}$ are shown. These tracks are of low enough energy that single muons and muon bundles have very similar energy loss profiles. On the other hand, the right plot shows tracks with a reconstructed dE/dX between $10^{2.1}$ and 10^{3}. For events of this brightness, single muons are much more likely to have individual energy losses greater than 1 TeV at this distance along the track. In both plots, reconstructed energy losses of 0 are floored to 0.1 GeV.

residuals between -200 ns and 300 ns are included. Figure 6.6 shows an example of a time residual PDF. Similar to the energy loss likelihood, the time residual likelihood is calculated once using signal PDFs, once using background PDFs, and the log likelihood ratio is used as a variable in the BDT.

The distribution of BDT scores is shown in Figure 6.7. To obtain the final sample, a cut on BDT score is varied with zenith to select an equal event rate per solid angle. We also investigated a zenith-dependent energy cut, as was done in previous analyses [142], but found the cut on BDT score accepted more events at lower energies, leading to increased

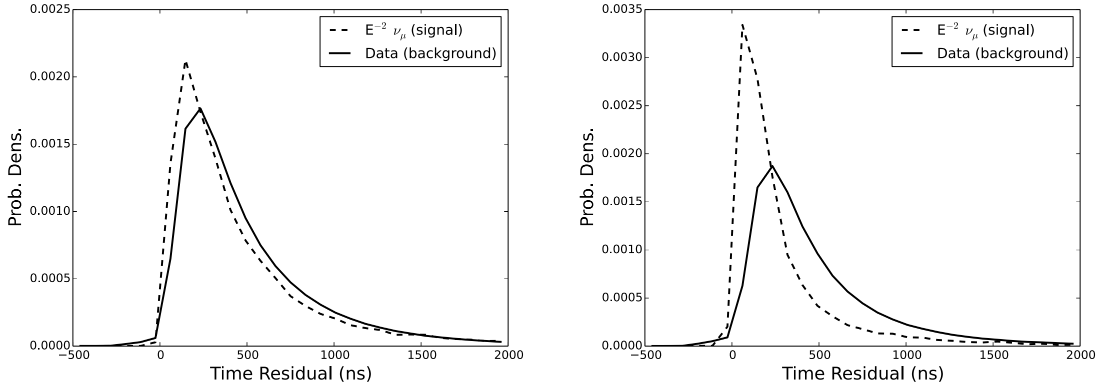

Figure 6.6: Probability distribution function for the time residual likelihood. The left plot shows the time residual distribution for hit DOMs 100 m from the reconstructed track. Both data and simulated signal tracks with a reconstructed dE/dX between $10^{0.8}$ and $10^{1.4}$ are shown. These tracks are of low enough energy that single muons and muon bundles have similar time residual distributions. On the other hand, the right plot shows tracks with a reconstructed dE/dX between $10^{2.1}$ and 10^{3}. For events of this brightness, muon bundles are much more likely to have early and late hits.

efficiency in this region. The final cut on the BDT score is described by the following piecewise function:

$$s > 0.07 \;\&\; \begin{cases} s > -0.303 + 5.805x - 24.592x^2 + 34.815x^3 & x < 0.24 \\ s > 0.171 - 0.055x - 0.044x^2 + 0.033x^3 + 0.087x^4 & \\ + 0.091x^5 + 0.041x^6 - 0.057x^7 - 0.193x^8 & 0.24 \leq x < 0.9 \\ s > -2.583 + 3.170x + 3.243x^2 - 3.790x^3 & x \geq 0.9 \end{cases} \tag{6.4}$$

where s is the BDT output score and x is the cosine of the zenith angle.

6.2 Characteristics and Performance of the Final Event Sample

The final data sample for the first year of operation of the 86-string detector has 138,322 events, of which approximately half are in the northern hemisphere. The livetime and rates

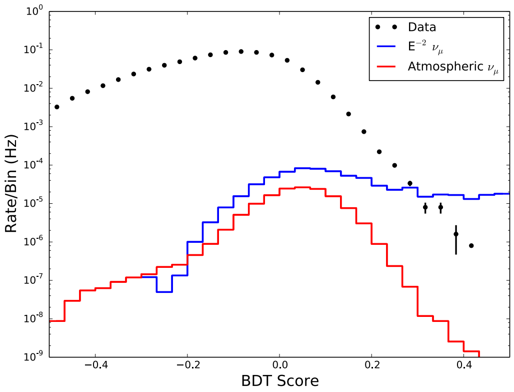

Figure 6.7: Distributions of BDT scores for the downgoing region. Since the properties of the signal (blue) and background (black) are similar to each other, the separation between the two classes is less significant than in the upgoing region. The majority of atmospheric neutrino events (red) are not distinguishable from atmospheric muons, and no BDT score achieves a high purity of atmospheric neutrinos.

for all four years of detector data are summarized in Table 6.2. The neutrino angular resolution is shown in Figure 6.8. The median angular resolution is $< 1^\circ$ for neutrinos with energies above 1 TeV, and approaches 0.3° at the highest energies. The neutrino effective area for this selection and the central 90% energy region for three signal spectra are shown in Figure 6.9. The effective area is the largest near the horizon. Far below the horizon high-energy neutrinos suffer from absorption in the Earth. Above the horizon the cuts necessary to remove the background remove a significant portion of the lower-energy signal. As a result the analysis is most sensitive to all energies near the horizon, while in the southern hemisphere the sensitivity rapidly deteriorates at lower energies.

Distributions of a few observables for northern hemisphere data and atmospheric neutrino simulation can be found in Figure 6.10. Both the rate and shape of most distributions agree quite well, although there are some discrepancies in a few variables, including the reconstructed energy.

no. of strings	dates	live-time [days]	atm. νs	# up-going	# down-going
40	4/6/2008 - 5/20/2009	375.5	40/day	14,121	22,779
59	5/20/2009 - 5/31/2010	348.1	120/day	43,339	64,230
79	5/31/2010 - 5/13/2011	316.2	180/day	50,857	59,009
86	5/13/2011 - 5/15/2012	332.6	210/day	69,227	69,095

Table 6.2: Summary for four different IceCube configurations for point source analyses. The fourth column shows the expected atmospheric neutrino rate from simulation [115], while the fifth and sixth columns contain numbers of up- and down-going data events at final selection level. The upgoing data are dominated by atmospheric neutrinos, while data in the downgoing region are dominated by atmospheric muons.

6.3 Point Source Analysis Method

To search for point sources, we look for spatial clustering of events around individual points in the sky using an un-binned maximum likelihood. We follow the technique used in [144] and [142]. This method has a number of advantages. It correctly incorporates probabilistic information about each event's position and angular uncertainty. Compared to a binned search, this uses a more precise treatment of the detector angular resolution that ultimately leads to an enhanced sensitivity. Information about each event's energy is also included in the likelihood, which improves sensitivity to a wide range of source spectra as well as enabling the likelihood to explicitly fit for the spectral shape of the source. Additionally, significances are estimated by repeating each hypothesis tests on data sets randomized in right ascension, which provides robust p-values that are largely independent of detector systematic uncertainties.

We first describe the likelihood and test statistic formulation, and then discuss the detector observables the likelihood uses, the sensitivity of the analysis, and the specific hypothesis tests we apply.

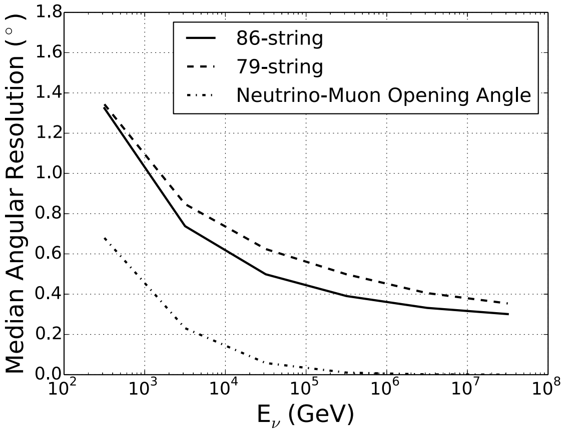

Figure 6.8: Median neutrino angular resolution (angle between reconstructed muon track and neutrino direction) as a function of neutrino energy for simulated northern hemisphere event samples from the 86-string (solid) and 79-string (dashed) detector configurations. The improvement is due to the SplineMPE reconstruction algorithm. At 30 TeV, the 40 and 59 string event selections (not shown) give angular resolutions of $\sim 0.8°$ and $\sim 0.75°$, respectively [142]. The dash-dotted line shows the median kinematic opening angle between the neutrino and muon.

6.3.1 Likelihood and Test Statistic

The likelihood is defined as

$$\mathcal{L}(\gamma, n_s) = \prod_j \mathcal{L}^j(\gamma, n_s^j) = \prod_j \prod_{i \in j} \left[\frac{n_s^j}{N^j} \mathcal{S}_i^j + \left(1 - \frac{n_s^j}{N^j}\right) \mathcal{B}_i^j \right], \tag{6.5}$$

where $\mathcal{B}_i$ is the background PDF and $\mathcal{S}_i$ is the signal PDF. The likelihood is a function of two fit parameters - n_s, the number of signal neutrino events originating from the point source, and γ, the astrophysical neutrino spectral index of a source with a power law spectrum. This likelihood combines data from different detector configurations, using independent PDFs for each data set. The outer product is over j datasets. Here, we combine four years of detector data, so j represents one of {IC40, IC59, IC79, IC86}. The inner product is over the N total events in each dataset.

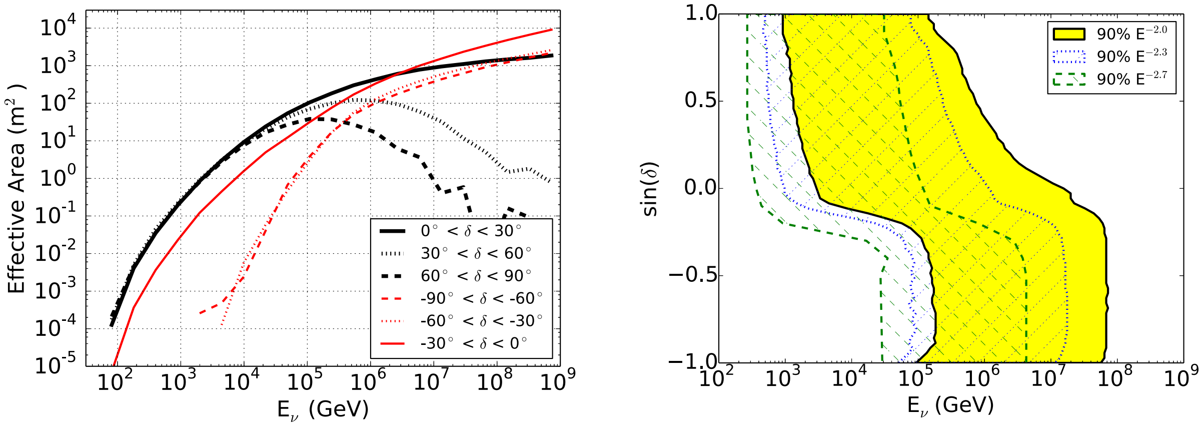

(a)

(b)

Figure 6.9: (a) Neutrino effective area for the 86-string detector as a function of primary neutrino energy for six declination bands. The effective area is the average of the area for ν_μ and $\bar{\nu_\mu}$. (b) Central 90% energy region for simulated neutrino events as a function of declination. This defines the region where the upper limits for E^{-2}, $E^{-2.3}$, and $E^{-2.7}$ source spectra are valid.

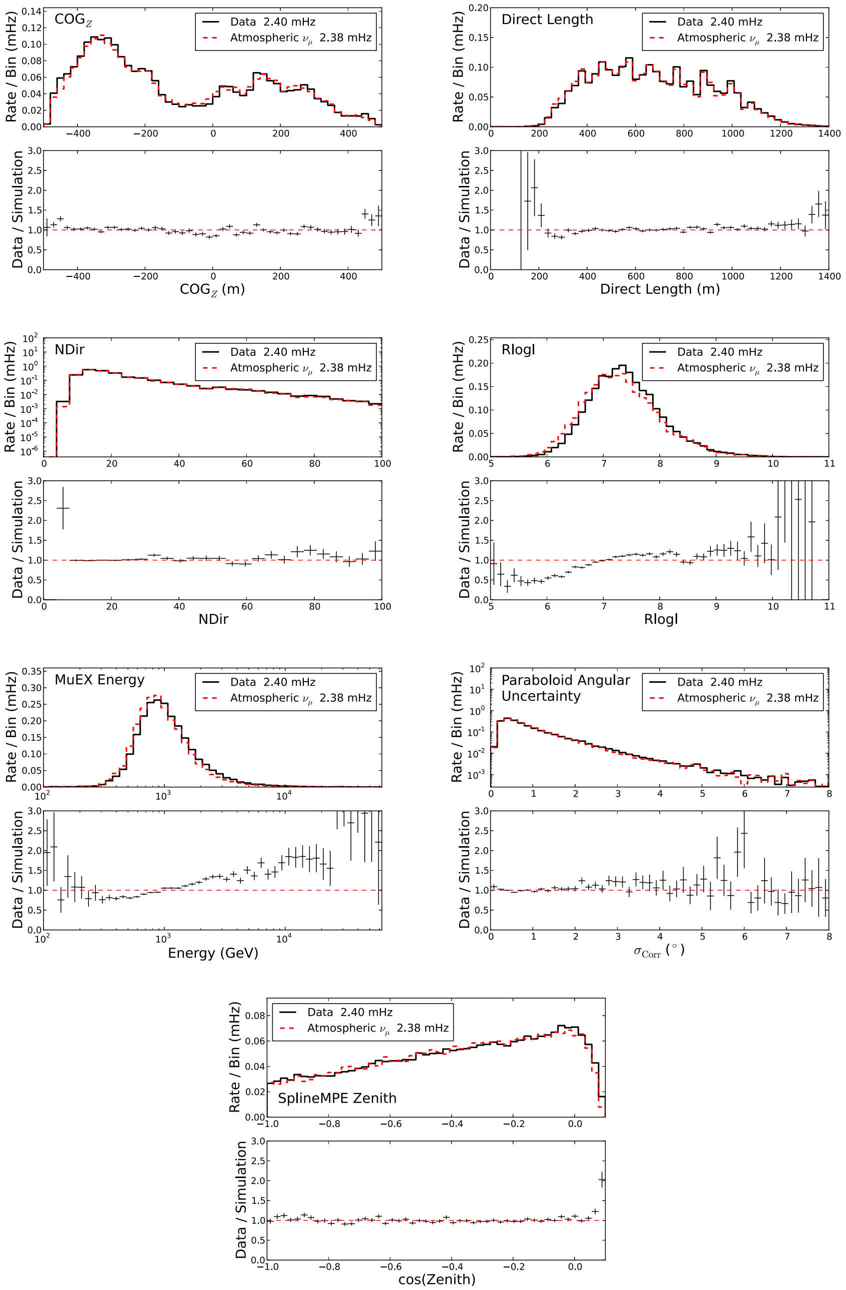

Figure 6.10: Comparison of data and simulation at neutrino level for the Northern Hemisphere. In each plot, the top panel shows the distribution of the variable, while the bottom panel shows the ratio between the data and the simulation. The simulation represents atmospheric muon neutrinos according to the model from [115].

The signal PDF $\mathcal{S}_i$ incorporates both directional and energy information about each individual event by multiplying independent spatial and energy PDFs:

$$\mathcal{S}_i^j = S_i^j(|\vec{x}_i - \vec{x}_s|, \sigma_i)\mathcal{E}_i^j(E_i, \delta_i, \gamma). \tag{6.6}$$

The spatial PDF is defined as a two-dimensional gaussian,

$$S_i^j(|\vec{x}_i - \vec{x}_s|, \sigma_i) = \frac{1}{2\pi\sigma_i^2} e^{-\frac{|\vec{x}_i - \vec{x}_s|^2}{2\sigma_i^2}}, \tag{6.7}$$

centered on the source position with a standard deviation that corresponds to each individual event's estimated angular uncertainty. The energy PDF for signal is the normalized energy distribution for neutrinos simulated from a power law distribution. It is a function of the event's energy and the source spectral index γ. Since the detector acceptance changes changes with declination, the energy PDF is also a function of the event's declination δ_i. Figure 6.11 shows the energy PDF for sources with different spectral indices.

The background PDF $\mathcal{B}_i$ is also a product of spatial and energy terms,

$$\mathcal{B}_i^j = B_i^j(\delta_i)\mathcal{E}_i^j(E_i, \delta_i). \tag{6.8}$$

It is constructed using the spatial and energy distributions of the data. $B_i^j(\delta_i)$ is the event density per unit solid angle as a function of declination. This quantity is independent of right ascension because IceCube, being situated at the South Pole, has uniform acceptance in right ascension. $\mathcal{E}_i^j(E_i, \delta_i)$ is the normalized energy distribution for data events at a declination δ_i.

The likelihood is a function of only a single spectral index γ and total number of signal events at each location at the sky. As this search focuses on time-independent point sources, the spectral index is not allowed to vary independently for each data set. Likewise, the total number of signal events is a fit parameter, but the division of n_s into a n_s^j for each year of data is fixed according to the detector acceptance in each year. Figure 6.12 shows the relative efficiency of each detector year for different source spectra.

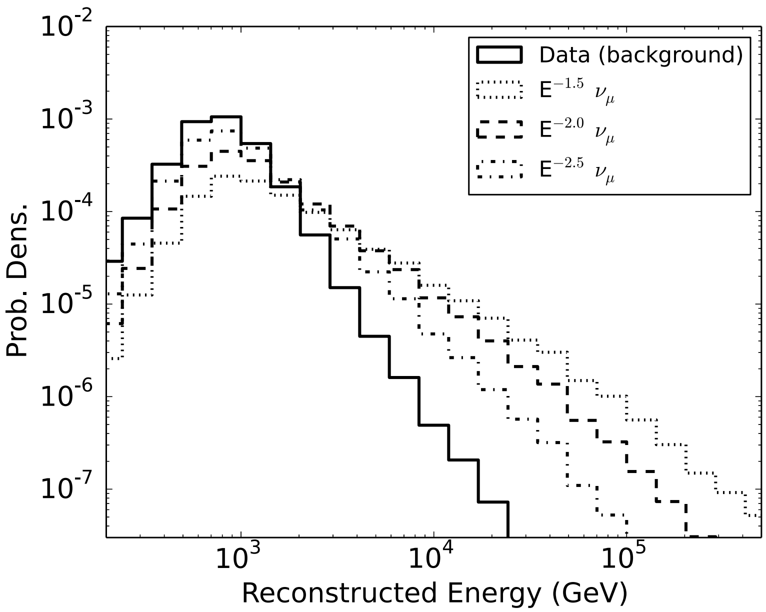

Figure 6.11: Energy probability density function for the point source likelihood, at a declination of 30°. The background distribution (given by the data) and distributions for three simulated astrophysical neutrino spectra are shown.

After maximizing the likelihood at a specific location in the sky, and determining the best fit number of signal events $\hat{n}_s$ and spectral index $\hat{\gamma}$, the test statistic (TS) is defined as the log likelihood ratio between the null and alternative hypothesis. In our case, the null hypothesis is that all events are generated from the background distribution, ie. $n_s = 0$. The alternative hypothesis is a point source of strength $\hat{n}_s$ and spectral index $\hat{\gamma}$ exists at the tested location. The TS is calculated via:

$$\mathrm{TS} = 2\log\left[\frac{\mathcal{L}(\hat{n}_s, \hat{\gamma})}{\mathcal{L}(n_s = 0)}\right]. \tag{6.9}$$

Here, we only fit for upward fluctuations by constraining $n_s \geq 0$. Additionally, we constrain γ to be between -1 and -4. The significance of an observation is determined by compared the TS to the TS distribution from data sets randomized in right ascension. The TS distribution for randomized data sets represents the probability a given observation

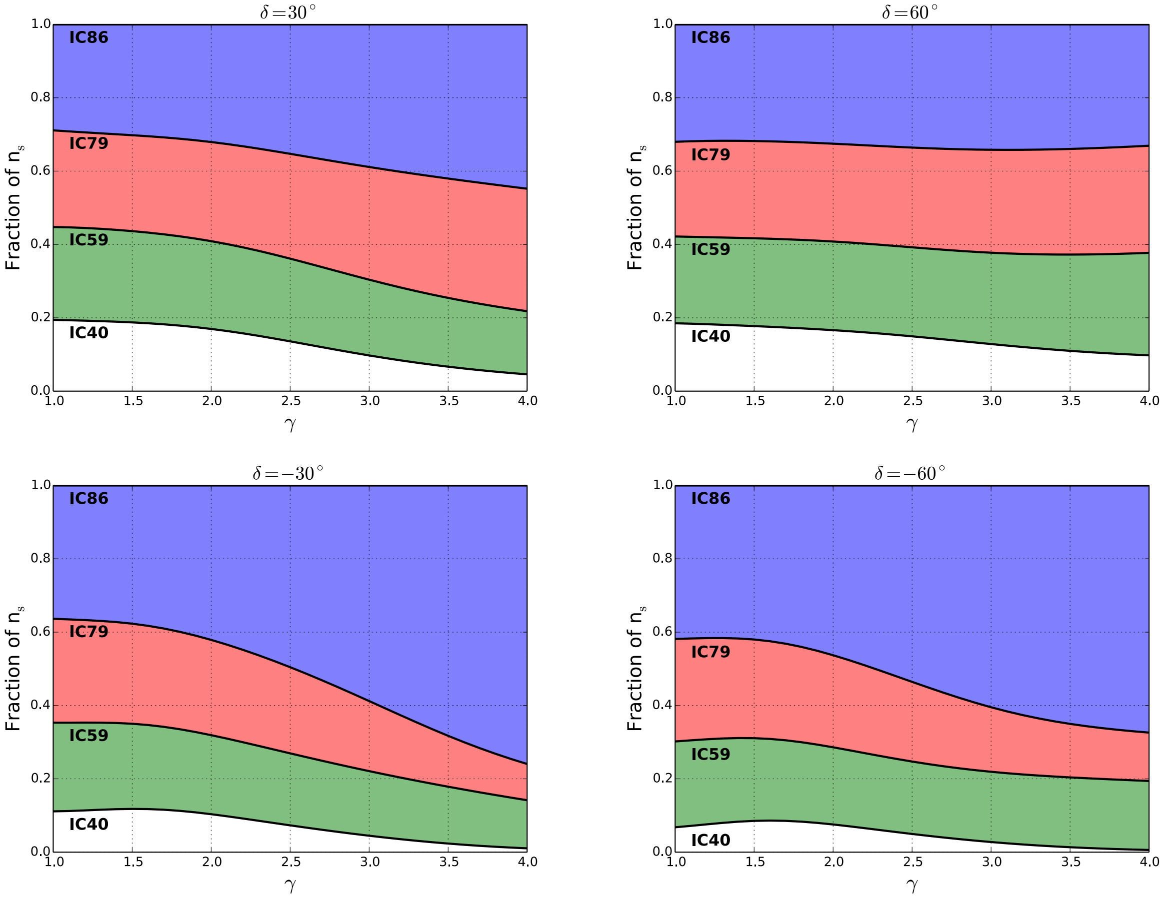

Figure 6.12: Fraction of signal events expected in each detector year, for four different declinations. In the northern hemisphere (top two panels) the signal fraction is relatively independent of spectral index, with IC86 contributing approximately 1/3 of the total signal. In the southern hemisphere the fraction of signal events in each data set exhibits a strong energy dependence. The improved event selection in IC86 leads it to contribute > 50% of the expected signal for E^{-3} spectra and softer in this region.

could occur by random chance with the given data. For large sample sizes, this distribution approximately follows a chi-squared distribution, where the number of degrees of freedom corresponds to the difference in the number of free parameters between the null hypothesis and the alternate hypothesis [145]. Since both n_s and γ float freely for the alternate hypothesis but are fixed for the null hypothesis, the number of degrees of freedom is 2. Figure 6.13 shows the TS distribution for randomized data sets.

6.3.2 Observables used in the Likelihood

The likelihood requires three pieces of information about each event: its location, its angular uncertainty, and its reconstructed energy. Besides the event selection, the performance of the analysis is due to the precision with which these three observables are known.

The direction and angular uncertainty are obtained using the SplineMPE reconstruction, which is discussed in Section 3.4. An estimate of the angular uncertainty is obtained using the paraboloid algorithm [134], which fits a 2D paraboloid to the profile likelihood around the minimum. The performance of this algorithm is evaluated using simulated signal events. For an ideal estimator, the estimated angular uncertainty would contain the true simulated direction in 68% of cases. The pull, defined as the ratio between the true reconstruction error and the estimated reconstruction error, should follow a 2D gaussian distribution projected into a 1D plane, with a unit median and standard deviation. However, when paraboloid is applied to simulated neutrinos, the median pull is often offset from one. It more often underestimates the angular uncertainty, with the bias becoming worse at higher energies. Since this behavior degrades the performance of the likelihood search, we apply a correction function to return the median pull to one at all energies. This function is derived from the simulation, and is shown in Figure 6.14.

The last ingredient for the likelihood is the energy proxy. While it is possible to use simple parameters such as the total deposited charge or total number of hit DOMs for each event, the sensitivity of the analysis can be improved by using likelihood-based energy reconstructions. In this analysis we use MuEX as the energy proxy, which is described in

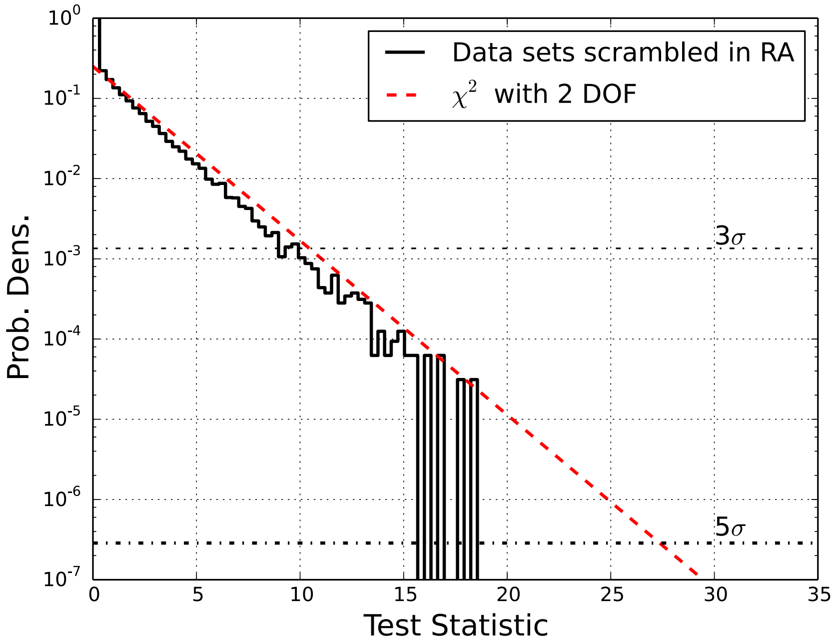

Figure 6.13: Test statistic distribution for randomized data sets. The chi-squared approximation agrees well with the data. The test statistic values required for 3σ and 5σ rejection of the null hypothesis are denoted by the intersection of the horizontal lines with the red curve. Here, the chi-squared approximation is divided by 2, since under-fluctuations are not allowed in the point source fit.

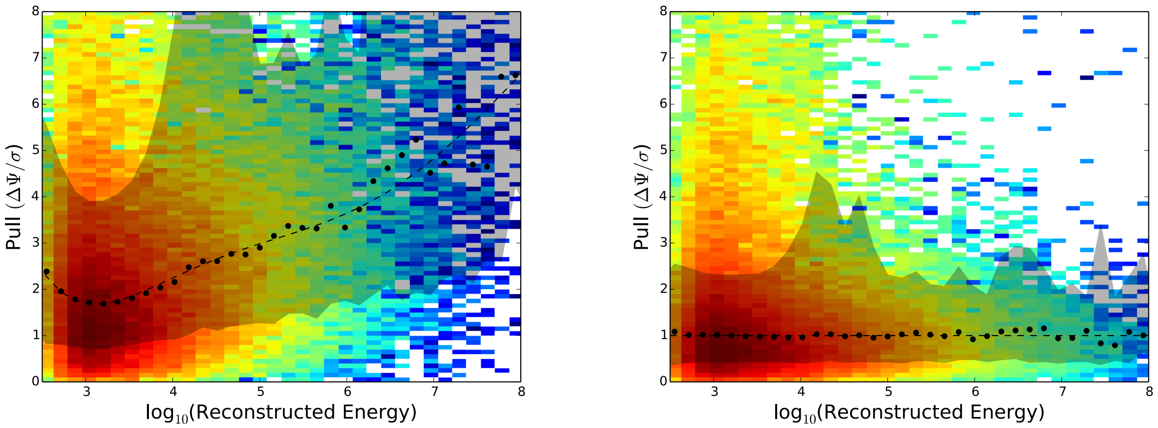

Figure 6.14: Pull distributions for the paraboloid angular uncertainty estimator. The plot on the left shows the pull as a function of reconstructed energy (MuEX). The black points are the median pull at each energy, and the gray shaded area denotes the central 68% of the distribution. The pull is defined as the ratio between the true reconstruction error from simulation and the reconstruction error estimated using paraboloid. The estimated uncertainty often underestimates the reconstruction error at higher energies, resulting in a larger pull. A polynomial is fit to the median of the distribution (dashed line). The right plot shows the pull distribution after the estimated angular uncertainties for each event are corrected by the polynomial function. The distribution is now centered at a pull of one (dashed line) at all energies.

Section 3.4 as well as [125]. Other algorithms, including the truncated mean algorithm [146], were also testing but did not improve performance.

6.3.3 Sensitivity and Discovery Potential

To estimate the performance of the analysis, we simulate point sources of various strengths and observe the analysis response. Two metrics are used - the discovery potential and the sensitivity.

The discovery potential corresponds to the point source flux that required for a 5σ discovery. Pseudo-experiments are generated with randomized data, and signal events drawn from an astrophysical spectrum are injected into the data set. For each pseudo-experiment, the likelihood is maximized and the test statistic computed at the location of the injected point source. The number of signal events is adjusted until 50% of pseudo-experiments receive a test statistic that is greater than the 5σ discovery threshold. In other words, half the pseudo-experiments result in a TS greater than ~ 27.5, above which only 0.00003% of background-only pseudo-experiments are expected.

The sensitivity corresponds to the flux level at which 90% of pseudo-experiments receive a p-value less than 0.5. 90% of randomized data sets with signal injected at this level obtain a TS above the median background-only test statistic. This corresponds to the median upper limit the analysis produces in the absence of a signal.

The discovery potential as a function of energy and declination is shown in Fig. 6.15 and Fig. 6.17, respectively. Compared to the 3-year point source analysis [142], the addition of the first year of data from the completed detector, including improved reconstruction and background rejection techniques leads, to a $40 - 50\%$ improvement in the discovery potential. Larger gains are achieved at energies below 1 PeV in the southern hemisphere.

6.3.4 Hypothesis Tests Performed

With the likelihood framework described above, we complete two searches for point sources. The first searches for evidence of a neutrino point source anywhere in the sky.

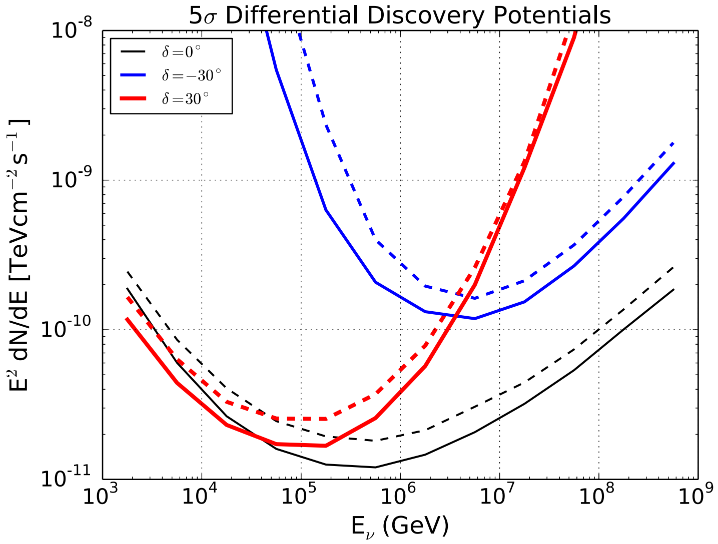

Figure 6.15: Discovery flux as a function of the neutrino energy at 5σ confidence level, for three different declinations (solid lines). Point sources with an E^{-2} spectrum are simulated over a half-decade in energy, and the flux in each bin required for discovery forms the curve above. Results from the previous analysis with 3 years of the data are shown with dashed lines.

This test is independent of any prior information on locations of potential sources, and is therefore a relatively model-independent search. The likelihood is evaluated in each direction in the sky, in steps of 0.1° × 0.1° within the declination range -85° to +85°. Beyond this declination range, the phase space in right ascension is reduced and the scrambling technique no longer effectively estimates the statistical significance of an observation. At each location, the likelihood fits for the source strength n_s and spectral index γ.

The final result of this test is the location, fit information, and p-value of the most significant fluctuation (the "hottest spot"). As this analysis has substantially different sensitivities in either hemisphere, the hottest spot in each hemisphere ($\delta < -5°$, $\delta \geq 5°$) is reported. Since every location in the sky is considered in this search, the number of effective trials is very high and is related to the angular resolution. To correct for the trial factor, this same test is repeated on an ensemble of scrambled data sets and the probability of observing a spot more significant than the final result by random chance is obtained.

The second hypothesis test searches for neutrino emission from a catalog of candidate sources. These sources are selected based on observations from other wavelengths (x-rays, gamma-rays, etc.) or astrophysical models predicting neutrino emission. This technique reduce the large number of effective trials associated with scanning the entire sky. It is also is useful for communicating and reporting results, as the sky map contains significant information of interest beyond the hottest spot. The source list contains 44 sources chosen *a priori*. Similar to the all-sky search, the most significant source from each hemisphere is reported, and the chance probability of such a correlation occurring is estimated by repeating the test on data sets randomized in right ascension.

6.3.5 Systematic Uncertainties

In the analyses described here, the background is estimated by scrambling the detector data in right ascension. This technique provides a p-value independent of both theoretical uncertainties on the fluxes of atmospheric backgrounds as well as systematic uncertainties in the detector simulation. The p-values are therefore robust against most sources of systematic error. However, upper limits and analysis sensitivities are calculated by simulating the detector response to astrophysical neutrinos. Detector uncertainties including the optical properties of the ice and the absolute efficiency of the optical modules can affect the reported sensitivities and upper limits.

The magnitude of the systematic uncertainty is estimated by repeating the sensitivity calculation using signal simulation with varied properties. Ref. [142] and [133] contain a detailed discussion of all relevant systematic uncertainties. The dominant sources of uncertainty were found to be the absolute efficiency of the DOMs and the properties of the glacial ice. The analysis using three years of data was estimated to have a total systematic uncertainty of 18%. Since 65% of the data used here is the same as the three-year analysis and the techniques for the new event selection and analyses are similar, the systematic uncertainty on the four year sample is about the same. However, the added year of data utilizes the new SplineMPE track reconstruction, which is more sensitive to uncertainties in the optical properties of the ice. We re-evaluate the effect of the ice properties on the analysis for the 2011-2012 data, finding a corresponding systematic uncertainty of +16%/-8%. This is incorporated into the overall systematic uncertainty by averaging it with the ice model effect from the previous years. The resulting overall systematic uncertainty on the quoted sensitivities and upper limits is 21%.

6.4 Results

Figure 6.16 shows the result of the all-sky scan for point sources in terms of significance at each location in the sky. The most significant deviation in the northern sky has a pre-trial p-value of 4.81×10^{-6}, and is located at 29.25° r.a. and 10.55° dec. At this location, the best fit values of the number of source events, $\hat{n}_s$, and signal spectral index, $\hat{\gamma}$, are 43.0 and 2.88, respectively. In the southern sky, the most significant deviation has a pre-trial p-value of 6.81×10^{-6} and is located at 347.95° r.a. and $-57.75°$ dec. Here, the best fit values of $\hat{n}_s$ and $\hat{\gamma}$ are 13.0 and 3.95, respectively. After accounting for the trial factor associated with

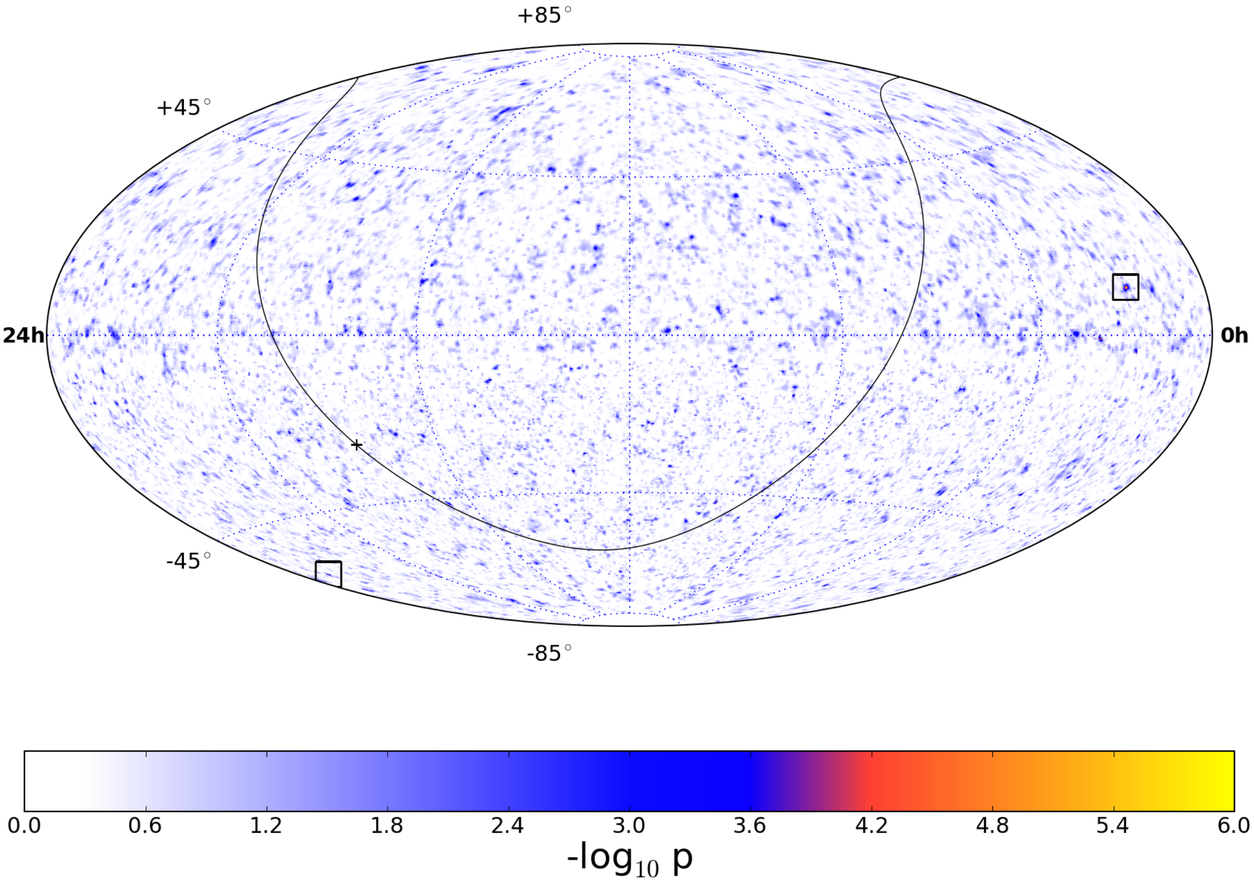

Figure 6.16: Pre-trial significance skymap in equatorial coordinates (J2000) of the all-sky point source scan for the combined four year data sample. The black line indicates the Galactic plane, and the black plus sign indicates the Galactic Center. The most significant fluctuation in each hemisphere is indicated with a square marker.

scanning the sky for the most significant spots, the post-trial p-values are 0.23 for the spot located in the northern sky and 0.44 for the spot located in the southern sky.

The search for neutrino emission from an *a priori* list of 44 candidate sources produced the results shown in Tables 6.3 and 6.4. In the northern sky, 1ES 0229+200 has the strongest upward fluctuation. The pre-trial p-value of such a fluctuation is 0.053, but after considering the random chance of observing such a fluctuation in any of the sources, the post-trial p-value is 0.61. In the southern sky, PKS 0537-441 has the strongest upward fluctuation, with a pre-trials p-value of 0.083 and a post-trials p-value of 0.33. Upper limits on the E^{-2} muon neutrino flux for 90% confidence level (C.L.) from each source are listed in the table, and are shown along with the analysis sensitivity in Figure 6.17.

No evidence for neutrino emission from point sources have been found in the first four years of IceCube data, and the results presented here are compatible with the background-only hypothesis. These searches are quite model-independent. The event selection was optimized for a wide energy range, and the hypothesis tests searched for emission anywhere in the sky.

Increased sensitivity to more specific models and source classes can be gained by including more model-dependent information in the likelihood. A number of hypothesis tests used this same data sample to search for emission from targeted source catalogs [147], while others used different techniques to search for multiple point sources in the entire sky or in the Cygnus region [148]. The catalog-based analyses searched for neutrinos associated with blazars and AGN, galaxy clusters, starburst galaxies, supernova remnants, molecular clouds interacting with supernova remnants, pulsar wind nebulae, and TeV gamma ray sources observed by Milagro [147]. These searches use a stacking technique, in which the likelihood is modified to include signal contributions from numerous spatially-separated sources. While this increases the total flux required for discovery, the flux per source is significantly reduced [133, 147]. In all cases, the observations were consistent with the background only hypothesis. The most significant result came from the stacking of six TeV gamma ray sources observed by Milagro, where the likelihood fit 51.4 signal events with a soft $E^{-3.95}$ spectrum, resulting in a p-value of 0.02. While this is compatible with the background-only hypothesis, it is intriguing because a large upwards fluctuation was observed in this same catalog in an *a posteriori* search using the 40-string IceCube data set. In [147], this year of data was explicitly removed to avoid bias, and a modest overfluctuation is again observed with the three additional years of data. While the best-fit $E^{-3.95}$ spectrum is softer than most astrophysical models, a hard-spectrum source with a cutoff could lead to a soft-spectrum best-fit. The upper limit from this observation is still a factor of 1.95 above the model flux predicted in [149]. More data is needed to tell whether this correlation is just a chance fluctuation or the start of a signal.

The data and analysis technique described here can also be modified to search for time-dependent neutrino sources. Many astrophysical objects have time-dependent emission in other wavelengths. Gamma-ray bursts emit a large flux of gamma-rays over second or sub-second intervals. Blazars are observed to have enhanced gamma-ray emission over periods of days to weeks. X-ray binaries, including microquasars, exhibit periodic emission. Searches for flaring neutrino emission, either triggered by other observatories or un-triggered, have been completed using the data sample presented here. No evidence of any time-dependent emission has been found [150].

Table 6.3: Results for Galactic objects on the *a priori* search list.

Category	Source	r.a. [°]	dec. [°]	p-value	$\hat{n}_S$	$\hat{\gamma}$	B_{1°	$\Phi^{90\%}_{\nu_\mu+\bar{\nu}_\mu}$
SNR	TYCHO	6.36	64.18	–	0.0	–	17.8	2.06
	Cas A	350.85	58.81	–	0.0	–	17.8	1.70
	IC443	94.18	22.53	0.35	4.6	3.9	27.8	1.38
HMXB /mqso	LSI +63 303	40.13	61.23	–	0.0	–	17.8	1.95
	Cyg X-3	308.11	40.96	0.42	3.7	3.9	21.5	1.70
	Cyg X-1	299.59	35.20	0.18	8.9	3.9	23.4	2.33
	HESS J0632+057	98.25	5.80	0.14	13.4	3.4	37.0	1.37
	SS433	287.96	4.98	–	0.0	–	37.6	0.65

Continued on next page

Table 6.3 – *Continued from previous page*

Category	Source	r.a. [°]	dec. [°]	p-value	$\hat{n}_S$	$\hat{\gamma}$	B_{1°	$\Phi^{90\%}_{\nu_\mu+\bar{\nu}_\mu}$
Star Formation Region	Cyg OB2	308.08	41.51	–	0.0	–	21.0	1.36
pulsar/ PWN	MGRO J2019+37	305.22	36.83	–	0.0	–	23.1	1.23
	Crab Nebula	83.63	22.01	0.44	4.4	3.9	27.8	1.15
	Geminga	98.48	17.77	–	0.0	–	30.7	0.92
Galactic Center	Sgr A*	266.42	-29.01	–	0.0	–	36.6	8.11
Not identified	MGRO J1908+06	286.98	6.27	–	0.0	–	36.4	0.71

Note. – Sources are grouped according to their classification as High-Mass X-ray binaries or micro-quasars (HMXB/mqso), SNRs, Pulsar Wind Nebulas (PWNs), star formation regions and unidentified sources. The p-value is the pre-trial probability of compatibility with the background-only hypothesis. The $\hat{n}_S$ and $\hat{\gamma}$ columns give the best-fit number of signal events and spectral index of a power-law spectrum. When $\hat{n}_S = 0$, no p-value or $\hat{\gamma}$ are reported. The eighth column gives the number of background events in a circle of 1° around the search coordinates. The last column shows the upper limits based on the classical approach [152] for an E^{-2} flux normalization of $\nu_\mu + \bar{\nu}_\mu$ flux in units of $10^{-12}\,\mathrm{TeV}^{-1}\mathrm{cm}^{-2}\mathrm{s}^{-1}$.

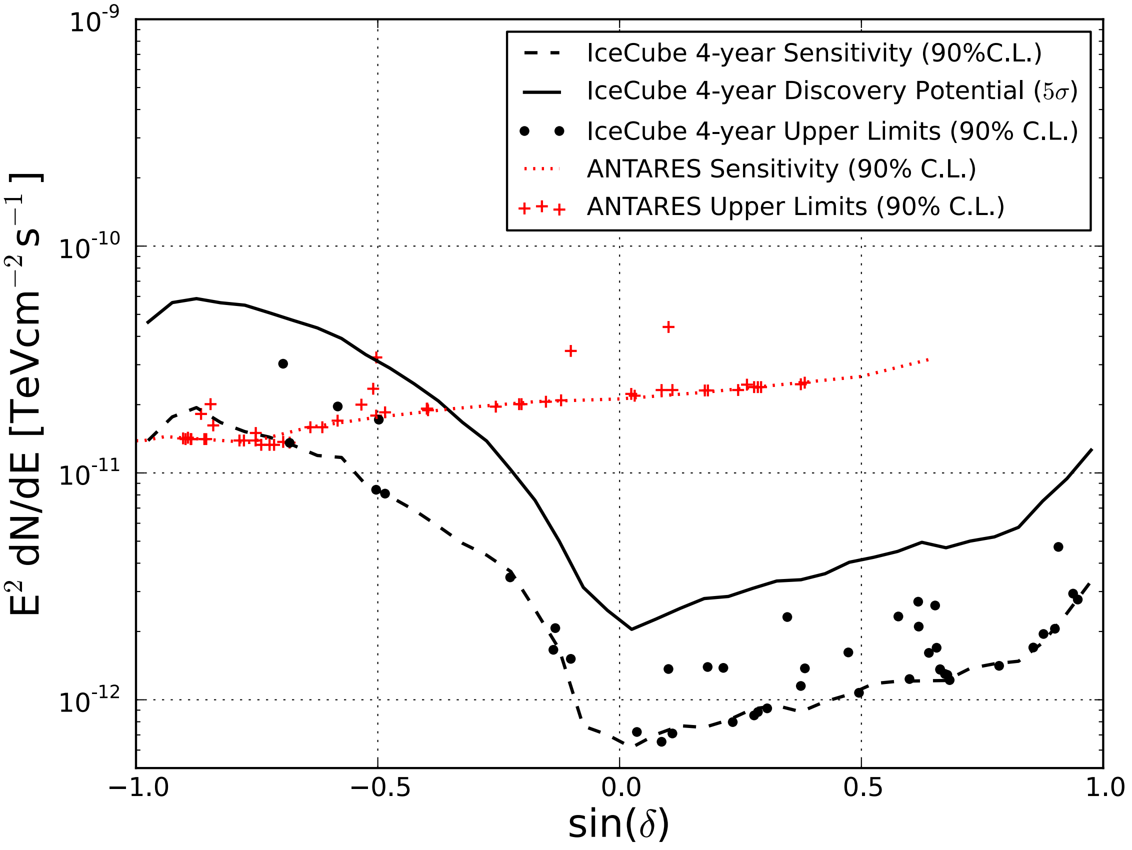

Figure 6.17: Muon neutrino upper limits with 90% C.L. evaluated for the 44 sources (dots), for the combined four years of data (40, 59, 79, and 86 string detector configurations). The solid black line is the flux required for 5σ discovery of a point source emitting an E^{-2} flux at different declinations while the dashed line is the median upper limit or sensitivity also for a 90% C.L. The ANTARES sensitivities and upper limits are also shown [151]. For sources in the southern hemisphere, ANTARES constrains neutrino fluxes at lower energies than this work.

Table 6.4: Results for extragalactic objects on the *a priori* search list.

Category	Source	r.a. [°]	dec. [°]	p-value	$\hat{n}_S$	$\hat{\gamma}$	B_{1°	$\Phi^{90\%}_{\nu_\mu+\bar{\nu}_\mu}$
BL Lac	S5 0716+71	110.47	71.34	–	0.0	–	16.5	2.77
	1ES 1959+650	300.00	65.15	0.083	9.8	3.2	17.7	4.72
	1ES 2344+514	356.77	51.70	–	0.0	–	19.1	1.41
	3C66A	35.67	43.04	–	0.0	–	20.5	1.220
	H 1426+428	217.14	42.67	–	0.0	–	20.8	1.29
	BL Lac	330.68	42.28	–	0.0	–	20.8	1.30
	Mrk 501	253.47	39.76	0.45	3.2	3.7	22.1	1.61
	Mrk 421	166.11	38.21	0.26	3.8	1.9	22.4	2.10
	W Comae	185.38	28.23	0.34	1.4	1.6	25.9	1.62
	1ES 0229+200	38.20	20.29	0.053^a	16.0	3.7	28.6	2.32
	PKS 0235+164	39.66	16.62	–	0.0	–	31.4	0.88
	PKS 2155-304	329.72	-30.23	–	0.0	–	37.0	8.43
	PKS 0537-441	84.71	-44.09	0.083^b	6.3	3.9	35.2	30.03
FSRQ	4C 38.41	248.81	38.13	0.12	10.6	2.8	22.4	2.71
	3C 454.3	343.49	16.15	–	0.0	–	31.4	0.85
	PKS 0528+134	82.73	13.53	–	0.0	–	32.3	0.80
	PKS 1502+106	226.10	10.49	0.21	6.1	2.3	33.2	1.39
	3C 273	187.28	2.05	0.45	3.2	2.6	38.9	0.72
	3C279	194.05	-5.79	–	0.0	–	33.5	1.51
	QSO 2022-077	306.42	-7.64	0.45	1.3	2.0	34.1	2.07
	PKS 1406-076	212.24	-7.87	–	0.0	–	34.1	1.66
	QSO 1730-130	263.26	-13.08	–	0.0	–	37.1	3.46
	PKS 1622-297	246.53	-29.86	0.13	6.2	2.7	36.6	17.17

Continued on next page

Table 6.4 – *Continued from previous page*

Category	Source	r.a. [°]	dec. [°]	p-value	$\hat{n}_S$	$\hat{\gamma}$	B_{1°	$\Phi^{90\%}_{\nu_\mu+\bar{\nu}_\mu}$
	PKS 1454-354	224.36	-35.65	0.2	5.4	3.9	35.6	19.64
Starburst	M82	148.97	69.68	–	0.0	–	16.3	2.94
Radio Galaxies	NGC 1275	49.95	41.51	–	0.0	–	21.0	1.36
	Cyg A	299.87	40.73	0.18	1.8	1.5	21.5	2.60
	3C 123.0	69.27	29.67	–	0.0	–	25.7	1.07
	M87	187.71	12.39	0.26	8.8	3.9	32.4	1.38
	Cen A	201.37	-43.02	–	0.0	–	35.5	13.57

Note. – Sources are grouped according to their classification as BL Lac objects, Radio Galaxies, Flat-Spectrum Radio Quasars (FSRQ) and Starburst galaxies. The p-value is the pre-trial probability of compatibility with the background-only hypothesis. The $\hat{n}_S$ and $\hat{\gamma}$ columns give the best-fit number of signal events and spectral index of a power-law spectrum. When $\hat{n}_S = 0$, no p-value or $\hat{\gamma}$ are reported. The eighth column gives the number of background events in a circle of 1° around the search coordinates. The last column shows the upper limits based on the classical approach [152] for an E^{-2} flux normalization of $\nu_\mu + \bar{\nu}_\mu$ flux in units of $10^{-12}\,\mathrm{TeV}^{-1}\ \mathrm{cm}^{-2}\mathrm{s}^{-1}$.

[a,b] Most significant p-value in the northern and southern skies, respectively, among all Galactic and extragalactic objects on the *a priori* search list.

Chapter 7

Search for Point Sources using Three Years of High-Energy Contained-Vertex Event Data

7.1 Introduction

The point source analysis described in the previous chapter used a high statistics sample of through-going muons. This represents the traditional strategy for neutrino telescopes [147,151], and has a number of benefits. Muon tracks can be reconstructed to high precision, reducing the effective background per bin on the sky and allowing for the identification of the source object in the presence of a signal. Using through-going tracks also boosts the detector effective area by including neutrinos that interact many kilometers away from the fiducial volume.

However, requiring a track-like topology restricts the analysis to only use the charged-current ν_μ interaction channel. Many models of astrophysical neutrino emission predicts a flux with a 1:1:1 ν_e:ν_μ:ν_τ flavor ratio at the Earth [11]. The vast majority of ν_e and ν_τ interactions leave shower-like signatures in our detector, and NC ν_μ interactions appear as showers as well. Above $\sim 100\,\mathrm{TeV}$, as much as 80% of the total 1:1:1 astrophysical flux appears as showers in IceCube. A point source search using an event sample with both tracks and showers can therefore gain a substantial fraction of the signal.

Here, we present an all-sky, all-flavor point source analysis using three years of high-energy contained-vertex events. By selecting bright events that start inside the detector, the background can be reduced to isolate a sample of only dozens of events, which are mostly astrophysical neutrinos. While shower events have substantially worse angular resolution than muons, the low overall background rates improves sensitivity to point sources of lower fluxes and lower energies in the southern hemisphere.

The analysis searches for astrophysical sources by testing for spatial clustering using an un-binned maximum likelihood method. Model-independent searches for clustering in any part of the sky are performed, as well as targeted searches for correlation with known gamma-ray sources. We first give an overview of the event selection, event sample, and the evidence for an astrophysical component of the flux. This is described in detail in [12, 13]. We then describe the point source analysis method and the results from each hypothesis test performed.

7.2 Event Selection

The event selection reduces the background by selecting for events with interaction vertices inside the detector's fiducial volume. It focuses on energies above $\sim 60\,\mathrm{TeV}$, where the backgrounds can be reduced by relatively simple cuts and potential astrophysical signal begins to dominate. Atmospheric muons are identified and vetoed by light deposited in the outer layers of the detector at the beginning of the event. Figure 7.1 shows the detector split into the inner fiducial volume and the outer veto layer. For sufficiently high-energy events, an entering muon track reliably produces hits in the veto region. We required that each event have fewer than three of its first 250 observed PE detected in the veto region. In addition, we required that the event produce at least 6000 PE overall to ensure that statistical fluctuations in the light yield were low enough for entering muons to reliably produce light in the veto region. This event selection rejects 99.999% of the muon background above 6000 PE (7.2). It also removes 70% of atmospheric neutrinos [153] in the southern hemisphere, due to both the charge cut and a property of the background known as the self-veto. Since atmospheric neutrinos are produced in atmospheric air showers, they are often accompanied by muons from the same air shower. In the southern hemisphere, IceCube can detect both components. While the atmospheric neutrino may interact inside IceCube without leaving

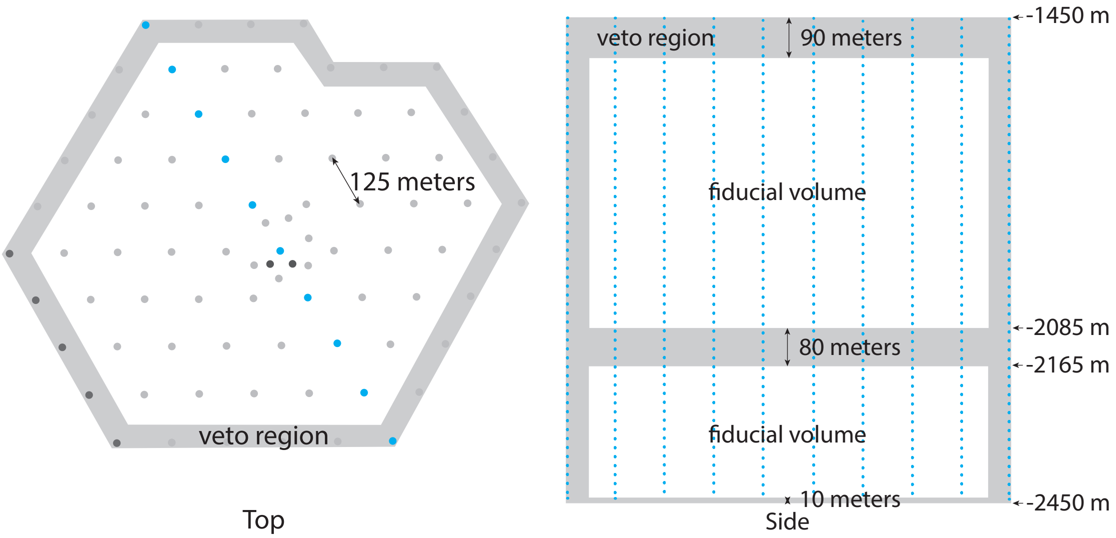

Figure 7.1: Diagram of the 86-string configuration of IceCube. The 79-string configuration, also used in this analysis, is missing the dark gray strings in the bottom left corner for the 2010-2011 season. The side view (right) shows a cross-section of the detector indicated in the top view (left) in blue. Events producing first light in the veto region (shaded area) were discarded as entering tracks (usually from cosmic ray muons entering the detector). Most background events are nearly vertical, requiring a thick veto cap at the top of the detector. The horizontal veto layer from 2085 - 2165 m removes highly inclined events entering the detector in the large dust layer [122], where they could potentially go undetected by the outer strings. Figure from [12].

light in the veto region, the accompanying muon will deposit light in the veto region, causing the entire event to be vetoed. This becomes more effective at higher neutrino energies, since higher-energy neutrinos are likely to be accompanied by more numerous and higher-energy muon bundles, which are less likely to underfluctuation and sneak through the veto region [154].

This event selection not only sufficiently removes the vast majority of the background, but also retains nearly all astrophysical neutrino events interacting within the fiducial volume

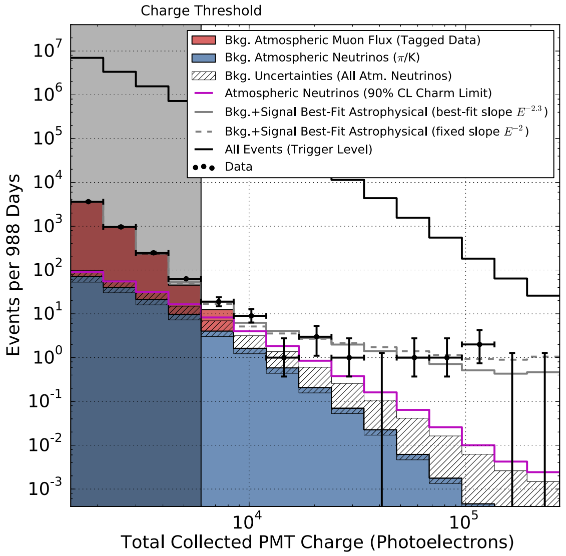

Figure 7.2: Distribution of deposited charge. Muons at higher total charges are less likely to pass the veto layer undetected, causing the muon background (red, estimated from data) to fall faster than the overall trigger rate (uppermost line). The data events in the unshaded region, at charge > 6000, are the events reported in this work, with error bars indicating 68% Feldman-Cousins intervals. The best-fit $E^{-2.3}$ astrophysical spectrum (gray line) and atmospheric neutrino flux (blue) are shown, along with current experimental uncertainties on the atmospheric neutrino background (hatched). The magenta line shows the experimental 90% CL upper bound on the atmospheric neutrino flux from charmed meson decays from [155]. Figure from [13].

at energies above a few hundred TeV. This selection is largely independent of neutrino flavor, event topology, or arrival direction. No event quality parameters or topology characteristics are used to select events - as long as its interaction vertex is inside the fiducial volume, it does not matter how the event behaves after starting. Figure 7.3 shows the neutrino effective area and effective target mass. For charged-current ν_e events, the selection criteria is fully efficient above 200 TeV. Since charged-current ν_μ interactions create a high-energy muon that often leaves the detector with a significant proportion of its energy, the energy threshold is highest for this channel.

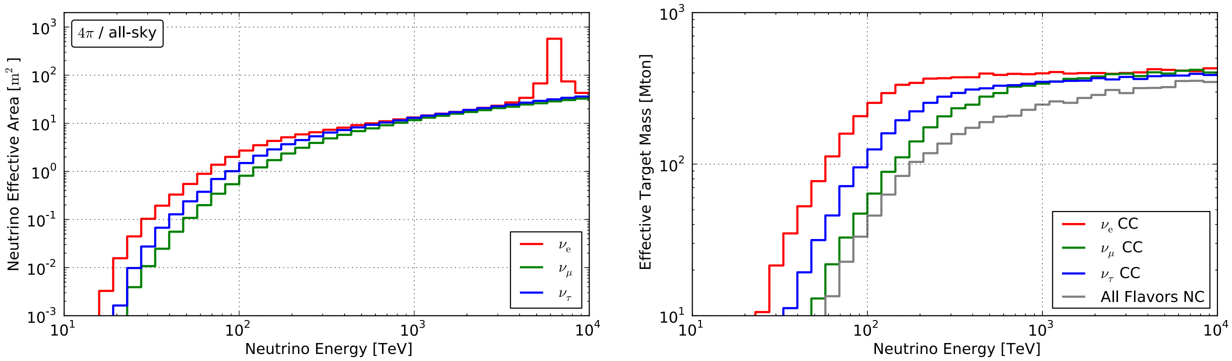

Figure 7.3: Left: Neutrino effective areas for each flavor assuming an equal flux of neutrinos and antineutrinos and averaged over all arrival angles. At 6.3 PeV, resonant W production on atomic electrons increases sensitivity to $\bar{\nu}_e$. The effective area includes effects from attenuation of neutrinos in the Earth [106], relevant at energies above 100 TeV. Right: Effective target mass as a function of energy. The deposited energy threshold in this search causes bias against ν_μ and ν_τ at low energies, as secondaries from charged-current interactions can carry a portion of the total interaction energy out of the detector. For ν_e charged-current events, where all the neutrino energy is visible in the detector, full efficiency is reached above 100 TeV. Figure from [12].

This analysis uses three years of data, covering IC79, IC86-I, and IC86-II. In the 988 days of livetime, 37 events passed the cuts. Two of these events are obvious backgrounds. One has hits in IceTop that arrive at the time expected from an atmospheric air shower in coincidence with the in-ice muon. The other is an obvious coincident event, with two muons from different air showers in the detector within the trigger window. For the point source analysis, both these events were removed, leaving a final sample of 35 events. Table 7.1 lists the energies, times, directions, and angular uncertainties of the events.

ID	Dep. Energy (TeV)	Time (MJD)	Decl. (deg.)	R.A. (deg.)	Med. Ang. Error (deg.)	Event Topology
1	$47.6^{+6.5}_{-5.4}$	55351.3222143	-1.8	35.2	16.3	Shower
2	117^{+15}_{-15}	55351.4659661	-28.0	282.6	25.4	Shower
3	$78.7^{+10.8}_{-8.7}$	55451.0707482	-31.2	127.9	$\lesssim 1.4$	Track
4	165^{+20}_{-15}	55477.3930984	-51.2	169.5	7.1	Shower
5	$71.4^{+9.0}_{-9.0}$	55512.5516311	-0.4	110.6	$\lesssim 1.2$	Track
6	$28.4^{+2.7}_{-2.5}$	55567.6388127	-27.2	133.9	9.8	Shower
7	$34.3^{+3.5}_{-4.3}$	55571.2585362	-45.1	15.6	24.1	Shower
8	$32.6^{+10.3}_{-11.1}$	55608.8201315	-21.2	182.4	$\lesssim 1.3$	Track
9	$63.2^{+7.1}_{-8.0}$	55685.6629713	33.6	151.3	16.5	Shower
10	$97.2^{+10.4}_{-12.4}$	55695.2730461	-29.4	5.0	8.1	Shower
11	$88.4^{+12.5}_{-10.7}$	55714.5909345	-8.9	155.3	16.7	Shower
12	104^{+13}_{-13}	55739.4411232	-52.8	296.1	9.8	Shower
13	253^{+26}_{-22}	55756.1129844	40.3	67.9	$\lesssim 1.2$	Track
14	1041^{+132}_{-144}	55782.5161911	-27.9	265.6	13.2	Shower
15	$57.5^{+8.3}_{-7.8}$	55783.1854223	-49.7	287.3	19.7	Shower
16	$30.6^{+3.6}_{-3.5}$	55798.6271285	-22.6	192.1	19.4	Shower
17	200^{+27}_{-27}	55800.3755483	14.5	247.4	11.6	Shower
18	$31.5^{+4.6}_{-3.3}$	55923.5318204	-24.8	345.6	$\lesssim 1.3$	Track
19	$71.5^{+7.0}_{-7.2}$	55925.7958619	-59.7	76.9	9.7	Shower
20	1141^{+143}_{-133}	55929.3986279	-67.2	38.3	10.7	Shower

Table 7.1 – continued from previous page

ID	Dep. Energy (TeV)	Time (MJD)	Decl. (deg.)	R.A. (deg.)	Med. Ang. Error (deg.)	Event Topology
21	$30.2\,^{+3.5}_{-3.3}$	55936.5416484	-24.0	9.0	20.9	Shower
22	$220\,^{+21}_{-24}$	55941.9757813	-22.1	293.7	12.1	Shower
23	$82.2\,^{+8.6}_{-8.4}$	55949.5693228	-13.2	208.7	$\lesssim 1.9$	Track
24	$30.5\,^{+3.2}_{-2.6}$	55950.8474912	-15.1	282.2	15.5	Shower
25	$33.5\,^{+4.9}_{-5.0}$	55966.7422488	-14.5	286.0	46.3	Shower
26	$210\,^{+29}_{-26}$	55979.2551750	22.7	143.4	11.8	Shower
27	$60.2\,^{+5.6}_{-5.6}$	56008.6845644	-12.6	121.7	6.6	Shower
28	$46.1\,^{+5.7}_{-4.4}$	56048.5704209	-71.5	164.8	$\lesssim 1.3$	Track
29	$32.7\,^{+3.2}_{-2.9}$	56108.2572046	41.0	298.1	7.4	Shower
30	$129\,^{+14}_{-12}$	56115.7283574	-82.7	103.2	8.0	Shower
31	$42.5\,^{+5.4}_{-5.7}$	56176.3914143	78.3	146.1	26.0	Shower
32	—	56211.7401231	—	—	—	Coincident
33	$385\,^{+46}_{-49}$	56221.3424023	7.8	292.5	13.5	Shower
34	$42.1\,^{+6.5}_{-6.3}$	56228.6055226	31.3	323.4	42.7	Shower

Table 7.1 – continued from previous page

ID	Dep. Energy (TeV)	Time (MJD)	Decl. (deg.)	R.A. (deg.)	Med. Ang. Error (deg.)	Event Topology
35	2004^{+236}_{-262}	56265.1338677	−55.8	208.4	15.9	Shower
36	$28.9^{+3.0}_{-2.6}$	56308.1642740	−3.0	257.7	11.7	Shower
37	$30.8^{+3.3}_{-3.5}$	56390.1887627	20.7	167.3	$\lesssim 1.2$	Track

Table 7.1: Properties of the 37 high-energy contained-vertex events. Deposited energies and angular uncertainties include statistical and systematic uncertainties. Events 28 and 32 have coincident hits in the IceTop surface array, implying that they are almost certainly produced in cosmic ray air showers. Table from [13].

7.3 Reconstruction

The vertex position, direction, and energy loss pattern of each event is reconstructed simultaneously using the millipede reconstruction (see Section 3.4). The result of the reconstruction used in the clustering analysis is a full sky likelihood map. For each direction in the sky, this provides the likelihood describing how well a hypothesis particle from this direction fits the observed PMT pulses. This map can be normalized to form a PDF describing the event's arrival direction.

This computationally-expensive process is completed by splitting the sky into pixels. The likelihood at each pixel can then be maximized independently. For each pixel, the likelihood minimizer scans across the (x, y, z) coordinates of the vertex position, unfolding the energy loss pattern at each step and assuming the event direction corresponding to the pixel direction. The position of the pixels are determined using HEALPix [135], which provides bins of equal solid angle covering the entire sky. For cascade events, the sky is partitioned into 49,152 independent pixels, corresponding to a pixel resolution of $\sim 0.9°$. For track events, which can be reconstructed to less than 1°, the likelihood scan is repeated with a finer binning around the maximum, corresponding to a $\sim 0.1°$ resolution.

Systematic uncertainties, such as our knowledge of the ice properties and DOM efficiency, can affect the width and shape of the likelihood space. To account for this in the analysis, each track and cascade map is smoothed by 1° and 10°, respectively. Examples of full-sky likelihood maps for two events are shown in Figure 7.4.

7.4 Evidence for Astrophysical Origin of the Events

The observation of 37 high-energy contained-vertex events represents a large excess over the expected background rate of atmospheric muons and atmospheric neutrinos. The rate of atmospheric muons that do not leave hits in the veto region can be estimated from data. By using an outer region of the detector to tag muon events and an inner region to measure their detection efficiency, the muon background is estimated to be 8.4 ± 4.2 events in the

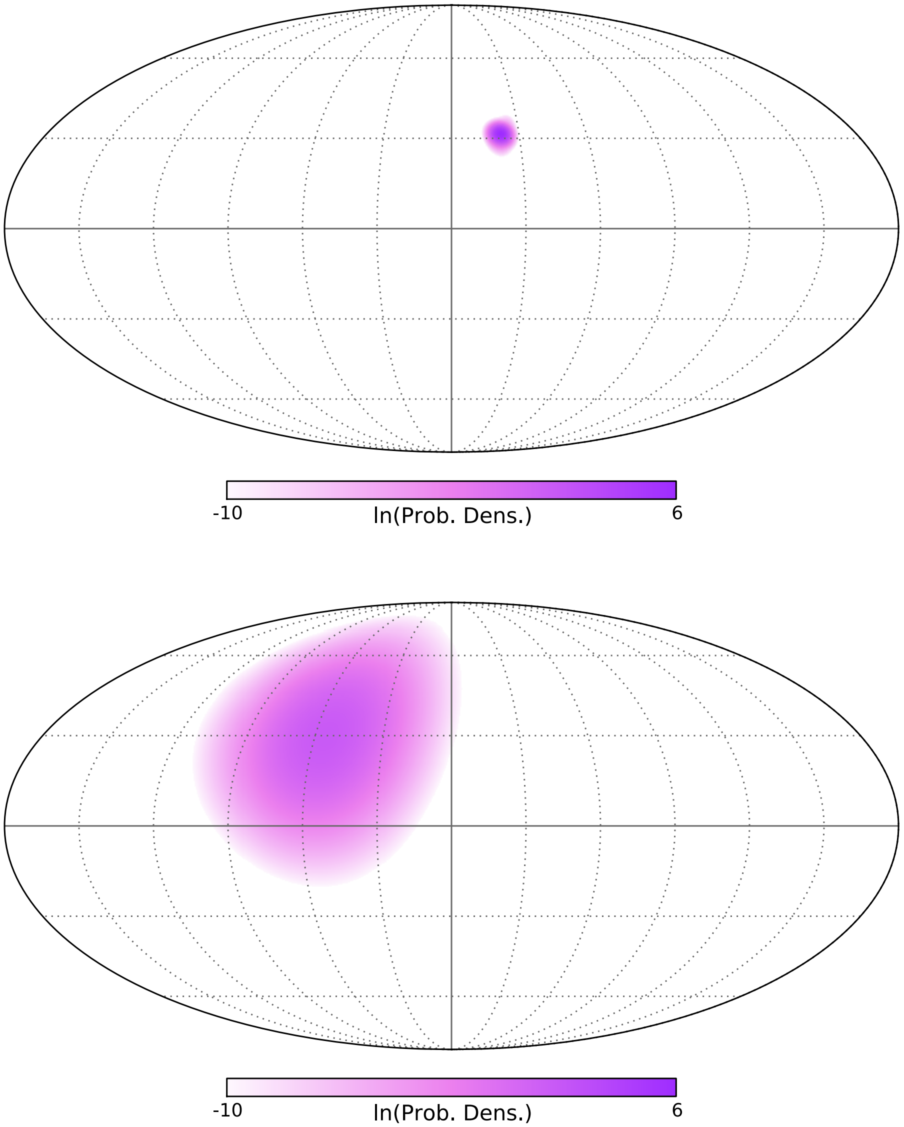

Figure 7.4: Examples of likelihood maps for track and cascade events, in local detector coordinates. The top panel shows the normalized and smoothed likelihood map for Event 3, a highly-localized track event. The bottom panel is the map for Event 10, a cascade event.

three year sample. This technique, which is independent of Monte Carlo simulation, provides a robust background estimate with no systematics - the error bar is purely statistical. The atmospheric neutrino background is estimated to produce $6.6^{+5.9}_{-1.6}$ events in the entire sample. This is estimated using a parametrization of the atmospheric neutrino flux that is consistent with previous IceCube measurements of the northern hemisphere ν_μ spectrum [115,155,156]. The uncertainty on this estimate is dominated by the ν_μ flux from charmed meson decays, which has never been experimentally measured. Lesser contributions include uncertainties on the nuclear composition of cosmic rays and models of hadronic interactions, as well as detector systematics such as the efficiency of the DOMs.

Besides the total excess of events, the event distribution in energy and zenith angle as well as the event topologies provide compelling evidence for an astrophysical component. The majority of the backgrounds would yield an excess of low-energy tracks. The flux of conventional atmospheric muons and neutrinos falls as $E^{-3.7}$, and the atmospheric neutrino flux from charmed meson decays would follow a $E^{-2.7}$ energy spectrum. The data, however, appear to have a much harder energy spectrum and are dominated by high-energy shower events instead of tracks.

Additionally, at these energies atmospheric neutrino backgrounds are suppressed in the southern hemisphere. Since atmospheric neutrinos are produced in air showers alongside high-energy muons, these accompanying muons will be observable at depth and would serve to identify any atmospheric event upon entering the detector. However, the observed excess in data is dominated by higher-energy events in the southern hemisphere, which is incompatible with any flux of atmospheric origin. This atmospheric neutrino suppression is a distinctive and generic feature of any neutrinos originating in cosmic ray interactions in the atmosphere - it does not matter whether the neutrinos originate from decays of pions and kaons or charmed mesons. As long as they are created in atmospheric air showers, their flux will be reduced by the self-veto.

Figure 7.5 shows the distribution of observed energies compared with the expectations from simulations, and Figure 7.6 shows the the declination for events that deposit 60 TeV or more inside the detector. A poissonian likelihood is used to fit the observed energy and declination distributions to a combination of background muons, conventional atmospheric neutrinos, atmospheric neutrinos from charmed meson decay, and an isotropic 1:1:1 astrophysical flux. The fit includes events with $60\,\mathrm{TeV} < E_{dep} < 3\,\mathrm{PeV}$. For an E^{-2} astrophysical flux, the best-fit flux normalization is $E^2\phi(E) = 0.95 \pm 0.3 \times 10^{-8}\mathrm{GeV cm^{-2} s^{-1} sr^{-1}}$. This represents a 5.7σ departure from the null hypothesis, in which the astrophysical flux normalization is forced to 0 and the flux of atmospheric neutrinos from charmed meson decays is allowed to float to 3.6 times the current 90% CL upper limit from IceCube's northern hemisphere ν_μ measurements [155]. Allowing the spectral index of the astrophysical spectrum to float in the fit returns a best-fit astrophysical flux of $E^2\phi(E) = 1.5 \times 10^{-8}(E/100\mathrm{TeV})^{-0.3}\mathrm{GeV cm^{-2} s^{-1} sr^{-1}}$.

7.5 Analysis Method

An un-binned maximum likelihood method is used to search for emission from point-like and extended sources, closely following the likelihood model from Section 6.3. A linear combination of point source signal and isotropic background populations is used to model the data. The likelihood function is defined as [144]:

$$\mathcal{L}(n_s, \vec{x}_s) = \prod_{i=1}^{N} \Big[\frac{n_s}{N}\mathcal{S}_i(\vec{x}_s) + (1 - \frac{n_s}{N})\mathcal{B}_i\Big], \tag{7.1}$$

where $\mathcal{B}_i$ is the background PDF, $\mathcal{S}_i$ is the signal PDF, N is the total number of events, and n_s is number of signal events. The likelihood is maximized with respect to n_s for a source position $\vec{x}_s$. While previous searches used a gaussian profile to model the signal PDF (Sec. 6.3), here $\mathcal{S}_i(\vec{x_s})$ is the value of the full-sky reconstruction map for the ith event, evaluated at the source position $\vec{x_s}$. Additionally, since there are only 35 data events being used in the likelihood, the declination distribution of the data can not be used to model the background PDF. Ideally, a robust high-statistics simulation of the detector response to atmospheric muons, atmospheric neutrinos, and diffuse astrophysical neutrinos would

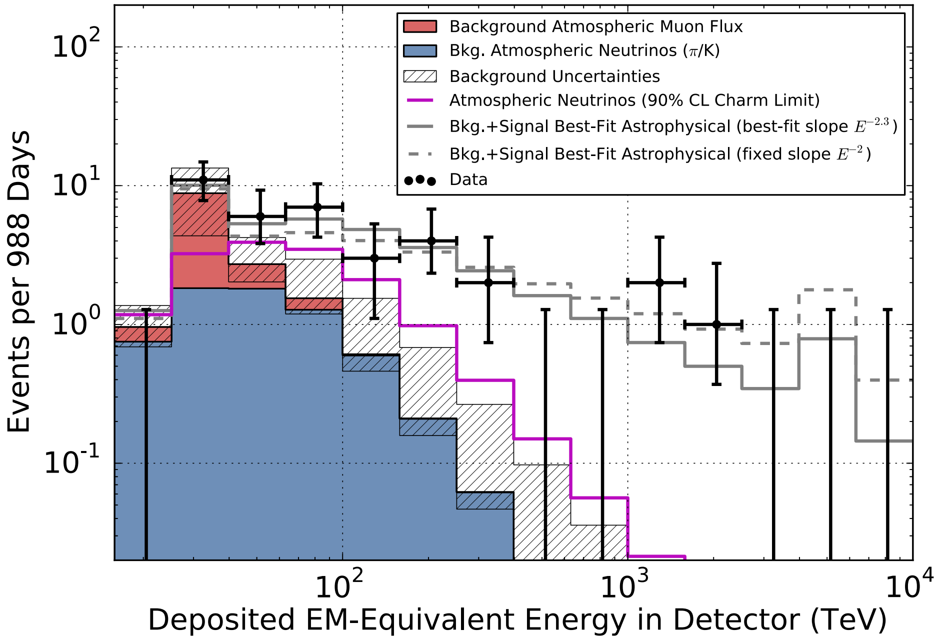

Figure 7.5: Distribution of reconstructed deposited energies for observed events with predictions. The hashed region shows uncertainties on the sum of all backgrounds. The muon template (red) is derived from simulation and scaled to match the total measured background rate. The gray line shows the sum of the background distributions and the best-fit E^{-2} (dashed line) and $E^{-2.3}$ (solid line) astrophysical fluxes. Figure from [13].

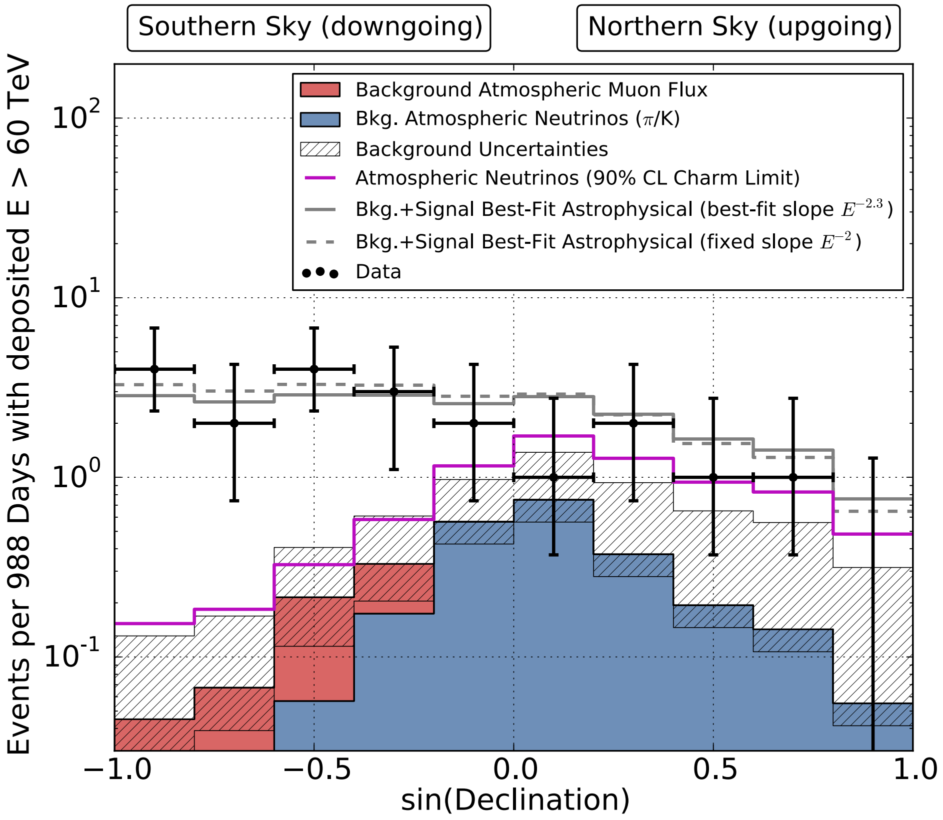

Figure 7.6: Distribution of reconstructed declination angles for observed events with deposited energies greater than 60 TeV. This represents the events used in the fit, and removes the majority of cosmic ray muon background (red). In the southern hemisphere, the background rate is suppressed because atmospheric neutrinos are vetoed by accompanying muons from the same air shower. The large excess of events in this region is well fit by an astrophysical component. In the northern hemisphere, the event rate decreases because part of the flux is absorbed when traversing the Earth. Figure from [13].

provide the background PDF. Technical and computational constraints prevented this from being possible, so $\mathcal{B}_i$ is instead approximated as isotropic and defined as $1/4\pi$. Since all p-values are calculated from datasets randomized in right ascension, the final result is robust against minor mis-modeling of the background PDF. Investigations of both an isotropic background PDF and a PDF based on simulation also showed this approximation did not significantly change the analysis sensitivity.

Four independent searches were completed using this likelihood with different signal hypotheses. The following sections outline each hypothesis test.

7.5.1 Search using All-Sky Likelihood Scan

Similar to Section 6.3, an all-sky likelihood scan was performed. This analysis considers all positions in the sky equally, and is therefore a relatively model-independent search for point sources. The likelihood is evaluated at every point in the sky, fitting for the number of signal events n_s independently at each point. We define the test statistic (TS) as

$$\mathrm{TS} = 2 \ln \frac{\mathcal{L}(\hat{n}_s, \hat{\vec{x}}_s)}{\mathcal{L}(n_s = 0, \hat{\vec{x}}_s)} \tag{7.2}$$

where $\hat{\vec{x}}_s$ is the position in the sky with the greatest test statistic, or the "hottest spot". The final p-value is evaluated by repeating this procedure on data sets randomized in right ascension, and calculating the percentage of scrambled data sets with a TS greater than or equal to the observed TS. This method produces a skymap of the likelihood fit result (the "local TS") at each individual point in the sky.

We repeat this test twice - once for all events in the sample, and once only for the cascade events. Separating the cascade events is necessary because the likelihood is biased towards single well-resolved muon tracks. Tracks receive high weights in the likelihood due to their $\lesssim 1°$ angular resolution. This small angular resolution leads to a different effective trial factor for tracks and cascades when evaluating the likelihood at every location in the sky. There are many more uncorrelated locations of hypothesis sources for the likelihood to test. For 15°-wide cascades, on the other hand, there are fewer independent locations on the sky. The likelihood does not appropriately deal with this difference in effective trial factors, necessitating completing the test for all events and cascades separately.

7.5.2 Search using Marginalization

To solve this problem of different effective trial factors for tracks and cascades, we apply an additional all-sky test using a marginalization technique that appropriately combines both event topologies in the same statistical test. We define the marginal likelihood as

$$\mathcal{L}(n_s) = \int\limits_{\vec{x}_s} \prod_{i=1}^{N} \Big[\frac{n_s}{N}\mathcal{S}_i(\vec{x}_s) + (1 - \frac{n_s}{N})\mathcal{B}_i\Big] P(\vec{x}_s) d\vec{x}_s, \tag{7.3}$$

where the integral is over all possible source locations and $P(\vec{x}_s)$ is a bayesian prior on the source position. This technique is analogous to that commonly used in all-sky scans for flaring neutrino sources [157]. Here, we use a uniform prior for the source position to remain agnostic about the location of the source.

For a given value of n_s, we evaluate the integrand of the above equation at every point in the sky, or every pixel in the healpix map. The integration is then simply the sum of the likelihood map, including the factors defining the priors and the pixel size. We repeat this procedure for all values of n_s from 0 to N to find the value of n_s that maximizes the likelihood. Our TS is defined as

$$\mathrm{TS} = 2 \ln \frac{\mathcal{L}(\hat{n}_s)}{\mathcal{L}(n_s = 0)}, \tag{7.4}$$

which is similar to the TS for the all-sky scan except here it is independent of the source position $\vec{x}_s$. We estimate the significance of the result by repeating this procedure for data sets randomized in right ascension, and finding the fraction of scrambles producing a test statistic greater than or equal to the observed TS.

This search differs from the all-sky likelihood scan in the number of fit parameters and the interpretation of the results. Here we only fit for one parameter (n_s) instead of two (n_s, $\vec{x}_s$). The source position $\vec{x}_s$ is "marginalized out" in the integration process. As a result, multiple regions of the skymap can contribute to the test statistic. This method returns one p-value, which measures the degree of clustering anywhere in the sky. It also returns a skymap of the likelihood at every location in the sky. However, since the same $\hat{n}_s$ is used to evaluate the likelihood at every point, it only shows the contribution of each part of the sky to the final test statistic.

The procedure improves the sensitivity to a wider range source scenarios. While the marginalization and all-sky scan methods have the same sensitivity to a source producing a 1:1:1 ratio of $\nu_\mu : \nu_e : \nu_\tau$, the marginalization method is more sensitive to a source producing only cascades. Since every location in the sky contributes to the TS in the marginalization method, it is more sensitive to multiple sources spaced throughout the sky. The marginalization search is therefore a more general method to answer the question "are there any point sources anywhere in the sky?" However, the method does not provide information about where the source is, or even the flux of the source (since multiple regions of the sky contribute to $\hat{n}_s$). Given an actual source, the all-sky scan still provides a better answer to the questions"where is the point source, and what is its flux?" The marginalization search is therefore a complementary test to the all-sky scan for discovering the first neutrino point sources. In the presence of a strong signal, both methods are equally sensitive.

7.5.3 Galactic Plane Search

Besides the general clustering tests listed above, we also search for neutrino emission from known gamma-ray sources The first search is for clustering along the galactic plane. The likelihood (Equation 7.1) is modified to only include regions of each event's spatial PDF that overlap with the galactic plane. The likelihood becomes

$$\mathcal{L}(n_s) = \prod_{i=1}^{N} \Big[\frac{n_s}{N} \sum_{j}^{n_{bins}} \frac{W(\vec{x}_j)\mathcal{S}_i(\vec{x}_j)}{n_{bins}} + (1 - \frac{n_s}{N})\mathcal{B}_i \Big]. \tag{7.5}$$

$W(\vec{x}_j)$ is a weight defining the galactic plane region. We model the galactic plane as a bar extending ±2.5° around galactic latitude = 0, with equal weights at all locations within the bar. The ±2.5° corresponds to the width of the galactic plane seen with high-energy gamma-ray observations [62]. $W(\vec{x}_j)$ is set to zero for every pixel outside this bar. This test produces one p-value for all events. Removing the track events is not necessary for this test, since we are not scanning the sky for the hottest spot.

While this search is motivated by gamma-ray observations, neutrino emission from galactic objects or from cosmic ray interactions with diffuse galactic dust and photons may not be spatially coincident with the gamma-rays. We therefore apply a search along the galactic plan with a free-floating width. We repeat the test above for widths of ±2.5° to ±30°, in steps of 2.5°. The width that maximizes the likelihood is chosen as the best fit, and the p-value is calculated by repeating the same test on scrambled data sets, thus including the trial factor for scanning across many plane widths.

7.5.4 Source List Search

Similar to Section 6.3, we also search for neutrino emission correlated with an *a priori* list of potential sources. This source list includes objects with observed gamma-ray emission or promising neutrino emission models. This search reduces the trial factor associated with scanning every location in the sky. It is also is useful for communicating and reporting results, as the sky map contains significant information of interest beyond the hottest spot.

We construct the catalog using pre-defined source lists from previous IceCube and ANTARES analyses. The IceCube list consists of the 44 sources used in Section 6.3, while the ANTARES source list is taken from [151]. The IceCube list focuses mostly on northern hemisphere sources, as that is where the throughgoing muon analysis is most sensitive. Since ANTARES is in the northern hemisphere, they select more southern hemisphere sources. Since the contained-vertex event sample is sensitive to a similar energy range throughout the entire sky, we combine both source lists for full-sky coverage. We search for neutrino emission associated with any of these sources, with a few modifications:

- If any source appears in both lists, only include it once.

- If any sources are within $< 1^\circ$ of each other, average their positions, since this is not resolvable with the angular resolution of these events.
- Remove the source ”IceCube hotspot” from the ANTARES list, since this is not a source.

Significances are estimated with data sets randomized in right ascension. For each source, a pre-trial p-value is formulated by constructing the distribution of TS values from scrambles trials for all sources on the list in each hemisphere. The fraction of random trials for all sources resulting in a TS greater than or equal to the observed value for a specific source is the pre-trial p-value for that source. The highest significance source in the northern and southern hemispheres are also reported, and the post-trial p-value is computed by finding the fraction of scrambled data sets whose most significant source has a greater TS than the observed.

7.6 Analysis Performance

The sensitivity of the point source analysis as a function of declination is shown in Figure 7.7. Estimating the sensitivity for this analysis is complicated by the event reconstruction techniques used. Obtaining a full-sky likelihood map using millipede is too computationally expensive to apply it to a large ensemble of simulated signal events, which are needed to determine the sensitivity. To overcome this, a toy Monte Carlo simulation was used. We approximate likelihood maps for tracks and showers as von Mises’ distributions with 1° and 13° (the median angular resolution of cascades in the data) widths, respectively. These are injected at a given location in the sky, offset by a reconstruction error that is sampled from the distribution. Events are injected from an astrophysical flux witha 1:1:1 flavor ratio. The estimated 90% CL sensitivity flux corresponds to an average of ~ 2.5 injected events, as expected for a poisson process with almost zero background.

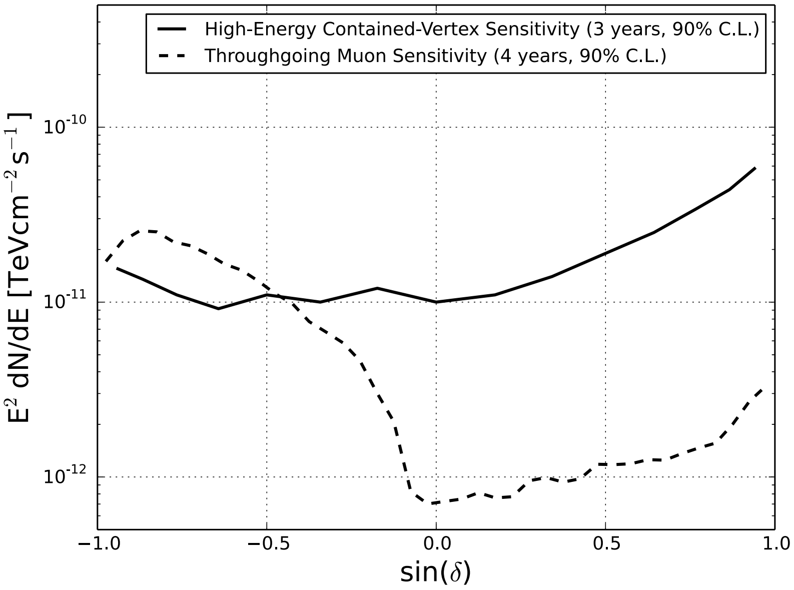

Figure 7.7: Sensitivity vs. declination for an E^{-2} point source flux ending at 10 PeV. The three year contained-vertex analysis is shown as the solid line. In the southernmost quarter of the sky, this search represents a factor of two improvement in point source sensitivity compared to the muon analysis of Ch. 6 (dashed). In the northern hemisphere, this search is not competitive because the event containment requirement vastly reduces the detector effective area.

7.7 Results

No hypothesis test yielded statistically significant evidence of clustering or correlations. For the all-sky clustering test with all events, the location with the highest test statistic was 127.3° r.a. and −31.0° dec., where a single track partially overlaps a shower event (Fig. 7.8 and 7.9). At this point the likelihood fits for 2.3 signal events, resulting in a TS of 11.4. The post-trial p-value, estimated by the proportion of scrambled data sets that produced locations with equal or greater TS, was 84% (Fig. 7.10). For the all-sky clustering test with shower-like events only, the location with the highest TS was 279.1° r.a. and −19.2° dec, where the likelihood fits for 5.3 signal events with a TS of 12.0. Five cascade events in the first two years of data are clustered around this location. This includes an event of 1 PeV deposited energy, which has a best-fit direction only a few degrees away from the galactic center. However, no events in the third year of data were strongly correlated with this region. 7.2% of data sets randomized in right ascension resulted in a TS greater than or equal to the observed TS (Fig. 7.10).

When using the marginalized likelihood, the best-fit global n_s was 3.3 events, resulting in a TS of 0.3. Fig. 7.11 shows the best-fit marginalized skymap. Compared to the all-sky likelihood scan, the best fit number of signal events is higher because the fit gave an increased weight to the cascade cluster. A TS greater than or equal to the observed value was found in 28% of scrambled data sets.

Tests for correlated emission with known gamma-ray sources also resulted in no statistically significant result. For the source list, the most significant source in the northern hemisphere was the Galactic supernova remnant W44. Here, the likelihood fit for $\hat{n}_s = 2.5$, resulting in a 1% pre-trial p-value. After accounting for the trial factor associated with looking at 38 sources, the post-trial p-value was estimated to be 28%. In the southern hemisphere, the most significant source was the Galactic x-ray binary LS 5039. This location, near the center of the cluster of shower events, received a $\hat{n}_s = 4.9$. This corresponds to a pre-trial p-value of 0.2% and an 8% post-trial p-value. Tables 7.2 and 7.3 list the complete source list results, for Galactic and extragalactic objects, respectively.

Correlation with the galactic plane was also not significant. The test for emission from a galactic plane with a fixed width of ±2.5° returned a best-fit number of signal events of 1.9 and a p-value of 24%. When letting the width float freely, the best fit was ±7.5° with 8.2 signal events. 1% of scrambled data sets had a TS greater or equal to that observed, and after accounting for the trial factor associated with varying the plane width, the post-trial p-value was estimated to be 2.8% (Fig. 7.12). Existing gamma-ray observations provide little motivation for neutrino emission associated with the galactic plane of this angular extent [61, 62].

This work focused on search for time-independent neutrino sources. These events have also been used to search for evidence of time-dependent sources. No evidence of event time clustering was found [13], and a search for correlations of the contained-vertex events with gamma-ray bursts was also consistent with the background-only hypothesis [158].

While no significant clustering or correlation was observed, the interpretation of this skymap is markedly different from the results in Ch. 6. Unlike the throughgoing muon data, the majority of events in this sample are astrophysical neutrinos. In fact, over 80% of the cascade events are expected to be of astrophysical origin [13]. Although the current data do not allow identification of specific sources, each astrophysical event does in fact point back to its source.

Beyond the statistical tests performed here, there is much to learn from the properties of the angular distribution of these events. While we cannot exclude a Galactic or extragalactic origin of this flux, the high galactic latitudes of many events (Fig. 7.9) suggest an extragalactic component. Exceptions may be made for local large diffuse sources (e.g. the Fermi bubbles [67] or the galactic halo [159, 160]), but these models typically can explain only a fraction of the data. Additionally, the large spatial separation between events suggests no single source dominates the observed flux. Including information from throughgoing muon point source analysis can strengthen this constraint. Chapter 9 pursues this line of thought in more detail to place constraints on the minimum number of sources contributing to this flux.

Ultimately, more data are needed to identify astrophysical objects associated with these events. An additional few years of data will result in a stronger statement about the mild correlation with the Galactic plane and mild significance of cascade events near the Galactic center. Additionally, much sensitivity can be gained by expanding the contained-vertex event selection to lower energies. This strategy has been pursued in detail, and Chapter 8 presents an analysis that uses a similar event selection with a lower-energy threshold to search for southern hemisphere point sources.

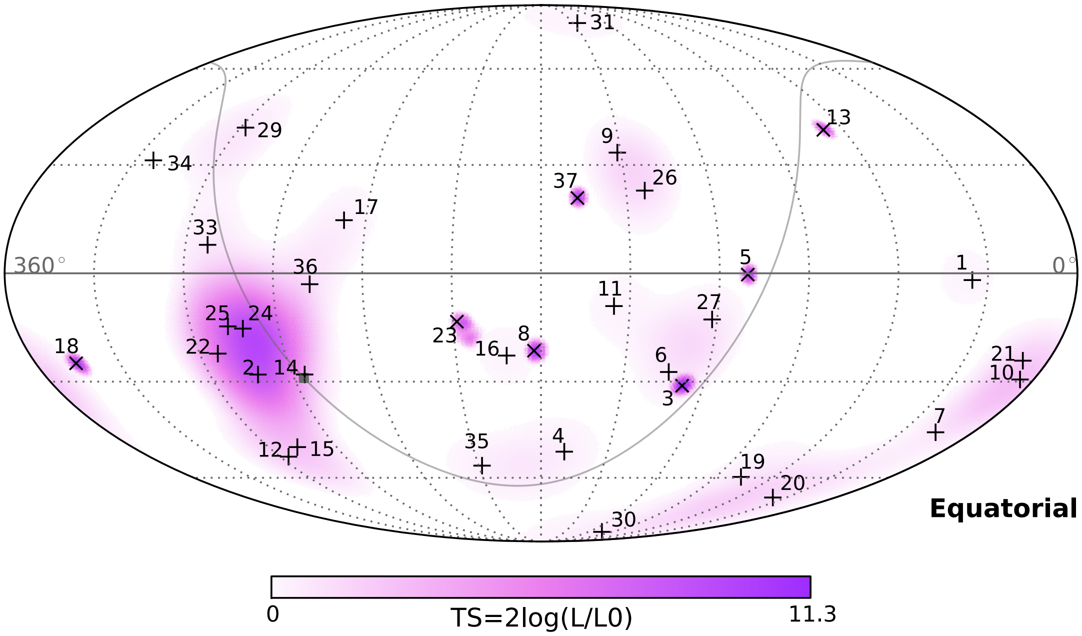

Figure 7.8: Arrival directions of the events in equatorial coordinates (J2000). Shower-like events are marked with + and those containing muon tracks with ×. Event IDs match those in Table 7.1 and are time ordered. The grey line denotes the galactic plane. The color map shows the test statistic (TS) for the point source clustering test at each location. No significant clustering was observed.

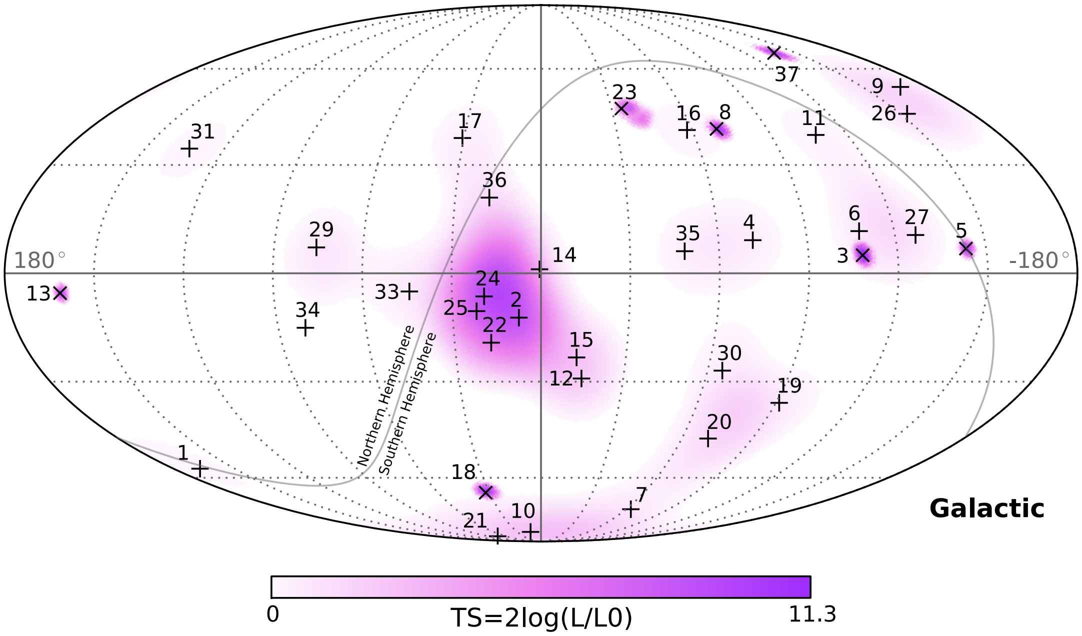

Figure 7.9: Arrival directions of the events in Galactic coordinates. Shower-like events are marked with + and those containing muon tracks with ×. Event IDs match those in Table 7.1 and are time ordered. The grey line denotes the equatorial plane. The color map shows the test statistic (TS) for the point source clustering test at each location. No significant clustering was observed.

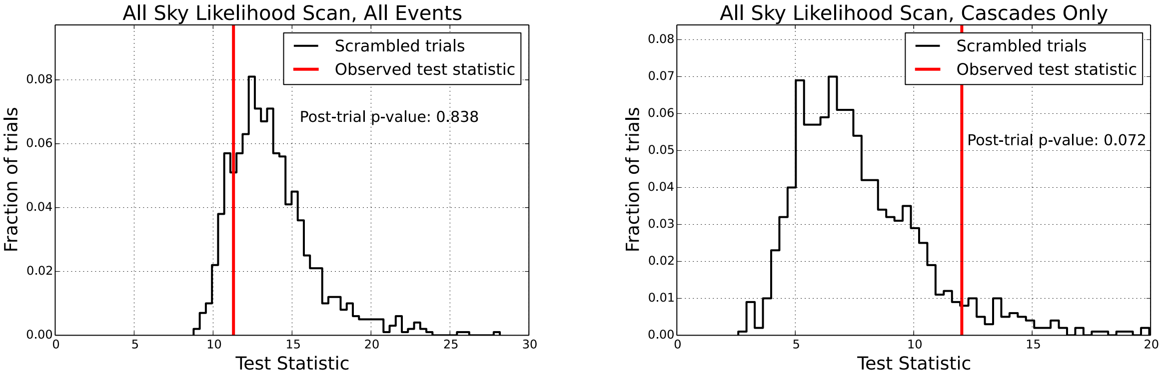

Figure 7.10: Distribution of TS results for scrambled data sets for the all-sky likelihood scan using all events (left) and cascade events only (right). In each, the vertical red line denotes the observed TS. Using these distributions, the post-trial p-values for the all-sky scan were estimated to be 84% and 7.2% when using all events and only shower events, respectively.

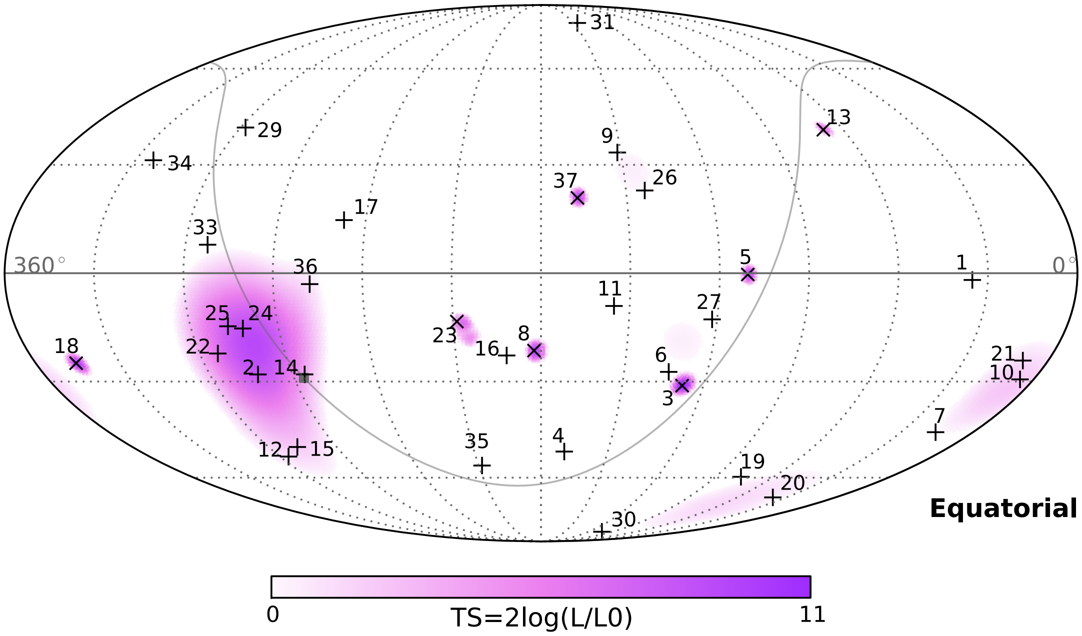

Figure 7.11: Color map of TS value at each location for the best-fit marginalized likelihood ($\hat{n}_s = 3.3$), in equatorial coordinates (J2000). Arrival directions of shower and track events are marked with + and ×, respectively. Event IDs match those in Tab. 7.1 and are time ordered. The grey line denotes the galactic plane.

Category	Source	RA (°)	Dec (°)	$\hat{n}_s$	p-value
SNR	TYCHO	6.36	64.18	0.0	–
	Cas A	350.85	58.82	0.0	–
	IC443	94.18	22.53	0.0	–
	W51C	290.75	14.19	0.7	0.05
	W44	284.04	1.38	2.5	0.01
	W28	270.43	-23.34	4.3	0.01
	RX J1713.7-3946	258.25	-39.75	0.0	–
	RX J0852.0-4622	133.0	-46.37	0.0	–
	RCW 86	220.68	-62.48	0.3	0.41
XB/mqso	LSI 303	40.13	61.23	0.0	–
	Cyg X-3	308.10	41.23	0.8	0.05
	Cyg X-1	299.59	35.20	1.0	0.03
	HESS J0632+057	98.24	5.81	0.0	–
	SS433	287.96	4.98	1.5	0.02
	LS 5039	276.56	-14.83	4.9	0.002
	GX 339-4	255.7	-48.79	0.0	–
	Cir X-1	230.17	-57.17	0.0	–
Star Formation Region	Cyg OB2	308.10	41.23	0.8	0.05
Pulsar/PWN	MGRO J2019+37	305.22	36.83	0.9	0.04
	Crab Nebula	83.63	22.01	0.0	–
	Geminga	98.48	17.77	0.0	–
	HESS J1912+101	288.21	10.15	0.8	0.04
	Vela X	128.75	-45.6	0.0	–
	HESS J1632-478	248.04	-47.82	0.0	–
	HESS J1616-508	243.78	-51.40	0.0	–

Table 7.2 – continued from previous page

Category	Source	RA (°)	Dec (°)	$\hat{n}_s$	p-value
Pulsar/PWN	HESS J1023-575	155.83	-57.76	0.2	0.44
	MSH 15-52	228.53	-59.16	0.06	0.48
	HESS J1303-631	195.74	-63.52	0.8	0.28
	PSR B1259-63	195.74	-63.52	0.8	0.28
	HESS J1356-645	209.0	-64.5	0.5	0.35
Galactic Center	Sgr A*	266.42	-29.01	3.1	0.04
Not Identified	MGRO J1908+06	286.99	6.27	1.3	0.03
	HESS J1834-087	278.69	-8.76	4.7	0.01
	HESS J1741-302	265.25	-30.2	2.5	0.07
	HESS J1503-582	226.46	-58.74	0.2	0.45
	HESS J1507-622	226.72	-62.34	0.1	0.47

Table 7.2: Catalog of 36 Galactic sources, grouped according to their classification as supernova remnants (SNR), X-ray binaries or microquasars (XB/mqso), pulsar wind nebulae (PWN), star formation regions, and unidentified sources. The post-trial p-values for the entire catalog in the northern and southern hemispheres were 28% and 8%, respectively. For each source, the pre-trial p-value was estimated by repeating the source catalog search with the data randomized in right ascension. The fraction of test statistic (TS) values from all individual sources that were greater than or equal to the observed TS determined the pre-trial p-value. The best-fit # of signal events ($\hat{n}_s$) is the result of the likelihood fit at each individual source. When $\hat{n}_s = 0$, no p-value is reported. Since many sources are spatially close together relative to the angular resolution, adjacent sources often receive similar fit results. For sources separated by less than 1°, their positions are averaged and they are treated as one source.

Category	Source	RA (°)	Dec (°)	$\hat{n}_s$	p-value
BL Lac	S5 0716+71	110.47	71.34	0.0	–
	1ES 1959+650	300.00	65.15	0.0	–
	1ES 2344+514	356.77	51.70	0.0	–
	3C66A	35.67	43.04	0.0	–
	H 1426+428	217.14	42.67	0.0	–
	BL Lac	330.68	42.28	0.0	–
	Mrk 501	253.47	39.76	0.0	–
	Mrk 421	166.11	38.21	0.0	–
	W Comae	185.38	28.23	0.0	–
	1ES 0229+200	38.20	20.29	0.0	–
	PKS 0235+164	39.66	16.62	0.0	–
	VER J0648+152	102.2	15.27	0.0	–
	RGB J0152+017	28.17	1.79	0.1	0.15
	1ES 0347-121	57.35	-11.99	0.0	–
	1ES 1101-232	165.91	-23.49	0.0	–
	PKS 2155-304	329.72	-30.22	0.0	–
	H 2356-309	359.78	-30.63	1.8	0.08
	PKS 0548-322	87.67	-32.27	0.0	–
	PKS 0426-380	67.17	-37.93	0.0	–
	PKS 0537-441	84.71	-44.08	0.0	–
	PKS 2005-489	302.37	-48.82	1.5	0.11
FSRQ	4C 38.41	248.82	38.14	0.0	–
	3C 454.3	343.50	16.15	0.0	–
	PKS 0528+134	82.74	13.53	0.0	–
	PKS 1502+106	226.10	10.52	0.0	–
	3C 273	187.28	2.05	0.0	–

Table 7.3 – continued from previous page

Category	Source	RA (°)	Dec (°)	$\hat{n}_s$	p-value
FSRQ	3C279	194.05	-5.79	0.0	–
	HESS J1837-069	279.41	-6.95	4.5	0.01
	QSO 2022-077	306.42	-7.64	0.4	0.44
	PKS 1406-076	212.24	-7.87	0.0	–
	PKS 0727-11	112.58	-11.7	0.4	0.39
	QSO 1730-130	263.26	-13.08	3.3	0.03
	PKS 0454-234	74.27	-23.43	0.0	–
	PKS 1622-297	246.53	-29.86	0.0	–
	PKS 1454-354	224.36	-35.65	0.0	–
Starburst	M82	148.97	69.68	0.07	0.15
Radio Galaxies	NGC 1275	49.95	41.51	0.0	–
	Cyg A	299.87	40.73	0.9	0.03
	3C 123.0	69.27	29.67	0.0	–
	M87	187.71	12.39	0.0	–
	Cen A	201.37	-43.02	0.03	0.49
Seyfert	ESO 139-G12	264.41	-59.94	0.0	–

Table 7.3: Catalog of 42 extragalactic sources, grouped according to their classification as BL Lac objects, Radio galaxies, Flat Spectrum Radio Quasars (FSRQ), Starburst galaxies, and Seyfert galaxies. A description of the information in the table can be found in Table 7.2.

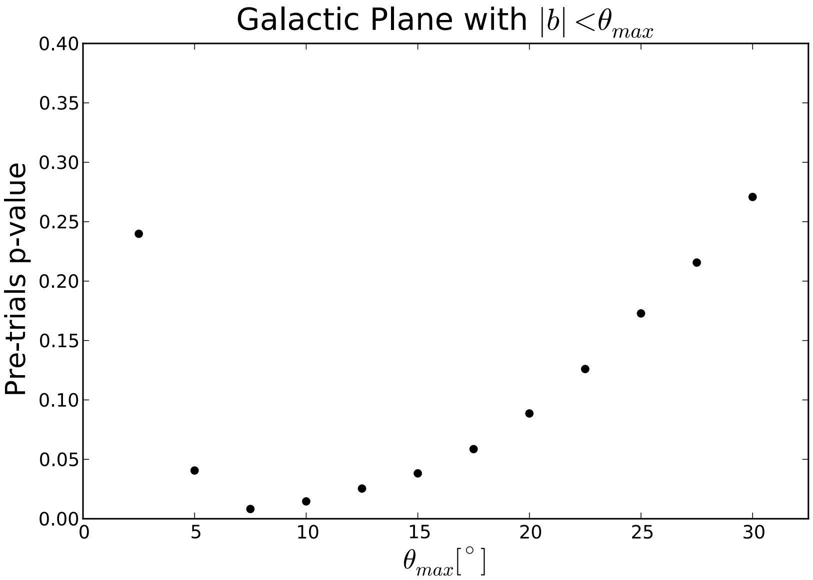

Figure 7.12: Pre-trial p-value vs. width of galactic plane hypothesis. The width of the galactic plane is varied from ±2.5° to ±30° in steps of 2.5°. For each width, the pre-trial p-value is calculated by comparing the maximized likelihood to that from scrambled datasets. All results are consistent with the background-only hypothesis.

Chapter 8

Search for Point Sources using Three Years of Medium-Energy Starting Track Events

8.1 Introduction

This chapter describes a point source analysis focused on reducing IceCube's energy threshold in the southern hemisphere. The southern hemisphere is a difficult region for IceCube because of the 2.5 kHz background rate from atmospheric muons. This background can be reduced by selecting well-reconstructed high-energy throughgoing tracks (as in Ch. 6), at the cost of a significantly reduced sensitivity below 1 PeV. An alternative strategy, pursued in Ch. 7, removed the atmospheric muon background by selecting high-energy events that start inside the detector. This succeeded in removing the vast majority of the background, providing a signal-dominated sample. However, most these events were cascades with an angular resolution of $\sim 15°$, which are not ideal for isolating specific astrophysical objects or sky locations as the sources.

Yet, the science potential for sub-PeV sources in the southern sky remains strong. The majority of the galactic plane is in the southern hemisphere, where astrophysical objects are predicted to accelerate cosmic rays to ~ 3 PeV, corresponding to a maximum neutrino energy of ~ 200 TeV [11]. Additionally, gamma ray telescopes observe many galactic sources with cutoffs in the $1-10$ TeV range [32,161,162]. If these gamma rays are produced hadronically, the sources should be TeV neutrino emitters as well. Even more intriguing, the high-energy contained vertex search was dominated by southern hemisphere events, including a cluster of cascades near the galactic center. While not statistically significant, it clearly deserves further study.

Here we describe an analysis that strives to lower the energy threshold in the southern sky by selecting charged-current ν_μ events that start inside the detector. Compared to the high-energy contained-vertex event search, the ν_μ effective area below $\sim 200\,\mathrm{TeV}$ is enhanced, increasing the expected rate of signal events with $< 1^\circ$ pointing resolution. Compared to the throughgoing muon analysis, the background rate is reduced by a factor of 400 while retaining similar angular and energy resolution. This selection provides a near independent sample of events, which are combined with the throughgoing muon data in a joint likelihood fit.

We first outline the event selection and properties of the final sample. We then briefly review the point source analysis technique, which is identical to that in Sec. 6.3, and verify the performance of our reconstructions on starting track events. Sensitivities and discovery potentials for various source spectra are shown, and then the results of two hypothesis tests are presented. We conclude with a discussion of the properties of the highest energy starting track event, which comprises the hottest spot in the skymap.

8.2 Event Selection and Performance of the Final Sample

The starting track event selection is applied to three years of detector data - one year of data from the 79-string detector configuration, and the first two years of data from the completed 86-string detector. The event selection uses veto techniques and energy information to isolate a sample of a few hundred events. Five cuts are applied.

The first cut removes events with hits on the outer layer of the detector, identical to the method in Sec. 7.2. The veto region is defined as the outer strings, the top 90 m of the detector, the bottom 10 m, and a 60 m layer of DOMs in the dust layer. Events with more than 3 PE in the veto region before the event start time (defined as the time at which 250 PE has accumulated) are removed. The second cut removes events with total deposited charge less than 1500 PE, a significantly lower threshold than the 6000 PE requirement used in Sec. 7.2. This leaves ~ 3900 events per year, 97% of which are reconstructed downgoing and appear to be atmospheric muons.

The third and fourth cuts use the direction of the reconstructed track. We select only downgoing events with a zenith angle $< 85°$. Due to the containment requirement, the effective area in the northern sky is significantly reduced compared to the throughgoing muon analysis, so starting events in the upgoing region do not improve the point source sensitivity. The zenith angle is obtained from the spline-based MPE fit (SplineMPE), as in Sec. 6.3. We then require the space angle between the LineFit and SplineMPE reconstructions to be less than 42°. This removes coincident muon events as well as cascade events, both of which are undesired backgrounds. Coincident muons originate from the atmosphere and can dilute astrophysical signal. Cascade events, while normally considered signal, cannot be reconstructed with the track-based algorithms used in this analysis. Without pointing resolution, they are simply high-energy events originating from random directions, which also dilutes the significance of a signal. The agreement between the LineFit and SplineMPE reconstructions removes 77% of cascade events while removing only 5% of well-reconstructed ($\Delta\Psi < 5°$) charged-current ν_μ events.

The final selection criterion is a two-dimensional cut on the reconstructed muon energy and the position of the event vertex. Unlike neutrinos with contained interaction vertices, atmospheric muon events accumulate at low energies and almost always deposit energy near the border of the detector. Many background events leave evidence of an incoming muon near the detector border without triggering the 3 PE outer layer veto. Higher energy events are more likely to emit observable light near the border, while lower energy events can sometimes pass by one or two string layers without being detected. For each event, we reconstruct the energy loss pattern using the Millipede reconstruction (see Sec. 3.4), and calculate the distance from the first non-zero, contained energy loss to the border of the detector. Figure 8.1 shows distributions of this vertex distance versus reconstructed muon

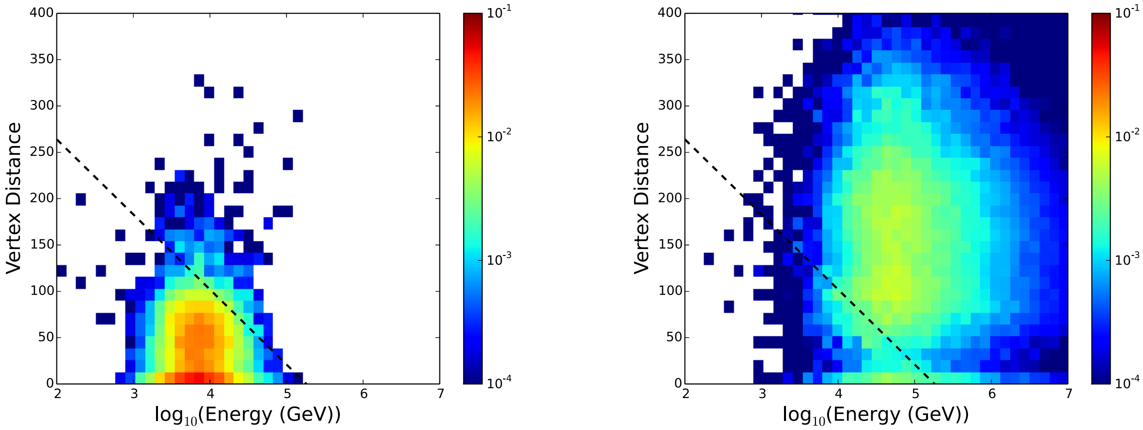

Figure 8.1: Vertex distance vs. reconstructed muon energy for data (left) and E^{-2} ν_μ signal (right). The muon energy is reconstructed using MuEX. Both event samples have all cuts applied except the final energy-dependent containment cut. The data, dominated by low-energy background, often deposits energy near the detector border. Astrophysical neutrinos, on the other hand, often have higher energies and interact uniformly throughout the detector. Events lying above the black dashed line are kept.

energy for data and simulated signal events. A linear cut is applied, optimized to achieve the highest $S/\sqrt{B}$ ratio:

$$\text{Vertex Distance} > -81 * \log_{10}(\text{MuEX}) + 426. \tag{8.1}$$

This cut keeps 91% of the E^{-2} ν_μ signal while only keeping 5% of the background-dominated data.

In the three years of data, 549 events satisfy the selection criteria. Plots comparing data to simulation, before the final linear cut on vertex distance and energy, are shown in Figure 8.2. Applying the complete event selection to simulated neutrinos produces the effective area and energy distribution shown in Figure 8.3, and the neutrino angular resolution using the SplineMPE reconstruction is shown in Figure 8.4.

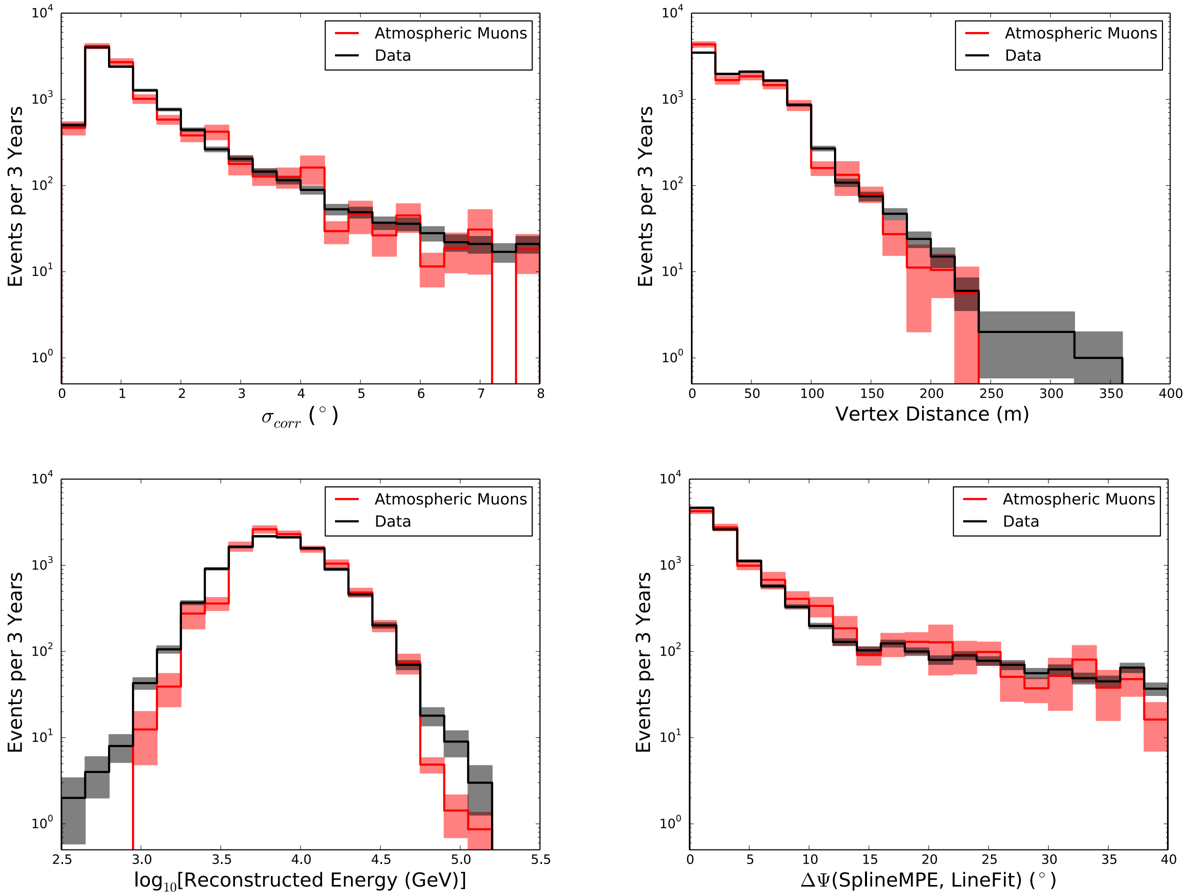

Figure 8.2: Comparison of data (black) and simulated atmospheric muons (red) for the starting track sample, before the final cut. At the final level, too few data events and simulated events remain to effectively compare the two. The error bands represents the 1σ statistical uncertainty for each. Clockwise from the upper left, the distributions show the corrected angular uncertainty estimate from paraboloid [134], the distance from the first reconstructed energy loss to the border of the detector, the space angle between the LineFit and SplineMPE reconstructions, and the reconstructed muon energy using MuEX. Since the atmospheric simulation only contains single muons, without contributions from muon bundles, the simulation was normalized to the overall data rate. The shapes of these distributions show excellent agreement between data and simulation.

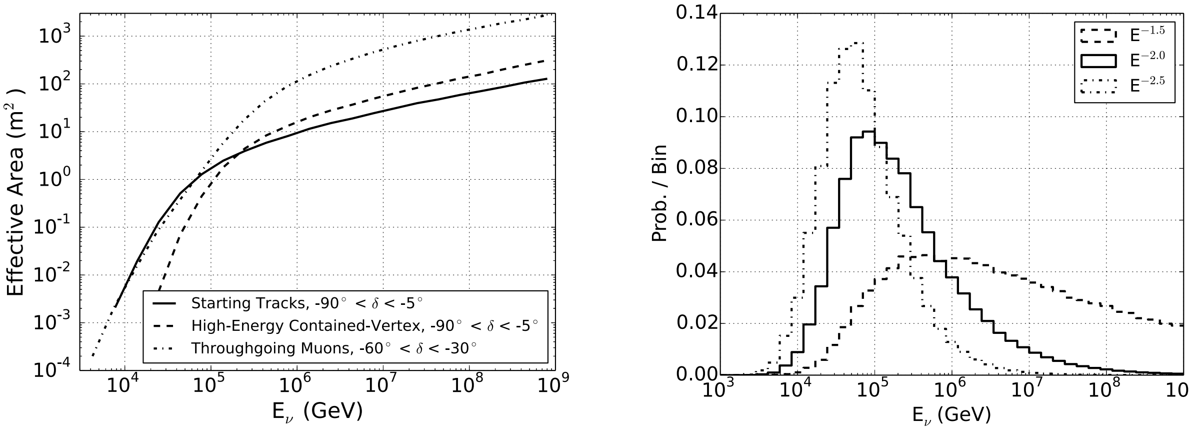

Figure 8.3: Left: Neutrino effective area for charged current ν_μ events passing the starting track selection criteria (solid line). Compared to the high-energy contained-vertex ν_μ event selection from Ch. 7 (charged and neutral current interactions, dashed line), lowering the charge threshold increases the effective area below $\sim 200\,\mathrm{TeV}$. Compared to the throughgoing muon event selection from Ch. 6 (dash-dotted line), the starting track selection has slightly higher detector acceptance below $\sim 75\,\mathrm{TeV}$, but a much lower acceptance at higher energies due to the containment requirement. Right: Normalized distribution of primary neutrino energies for simulated events passing the starting track selection criteria, for three different astrophysical spectra. For E^{-2} and softer spectra, the majority of the signal is below 1 PeV.

8.3 Analysis Method and Performance

We search for point sources using an un-binned maximum likelihood method that combines the three year starting track data sample with the four year sample of throughgoing muons from Ch. 6. The likelihood is identical to that used in Ch. 6:

$$\mathcal{L}(\gamma, n_s) = \prod_j \mathcal{L}^j(\gamma, n_s^j) = \prod_j \prod_{i \in j} \left[\frac{n_s^j}{N^j} \mathcal{S}_i^j + \left(1 - \frac{n_s^j}{N^j}\right) \mathcal{B}_i^j \right]. \tag{8.2}$$

The first product is over the different data sets j, where j denotes data from one of {IC40, IC59, IC79, IC86-I, Starting Track Sample}. Although the starting track sample includes

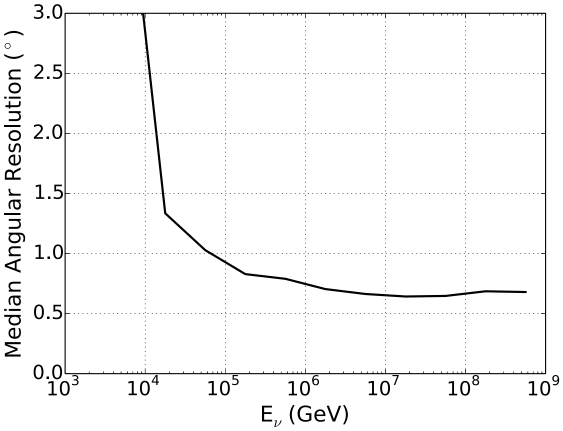

Figure 8.4: Angular resolution as a function of neutrino energy for simulated charged current ν_μ events, for the SplineMPE reconstruction. The median angular resolution is $< 1°$ above 65 TeV.

data from three different detector years, the event selection and detector response is constant for the entire period, so they are combined in one PDF in the likelihood. As before, the PDFs describe the spatial and energy distributions of the signal and background. We fit for two parameters - n_s, the number of neutrino events originating from the point source, and γ, the neutrino spectral index for a source with a power law spectrum. Figure 8.5 shows the fraction of signal events expected in each data set. The starting track event sample contributes a larger fraction of the expected signal for softer spectrum sources at larger southerly declinations. The test statistic (TS) is defined as

$$\mathrm{TS} = 2\log\left[\frac{\mathcal{L}(\hat{n}_s, \hat{\gamma})}{\mathcal{L}(n_s = 0)}\right]. \tag{8.3}$$

As in Ch. 6, pre-trial significances are estimated by approximating the TS distribution as a χ^2 distribution with two degrees of freedom, for the two fit parameters n_s and γ.

Since data from the same period of detector operation are used in both the starting track sample and the throughgoing muon sample, we must ensure the data sets do not overlap. To avoid such correlations, we remove events from the throughgoing muon sample

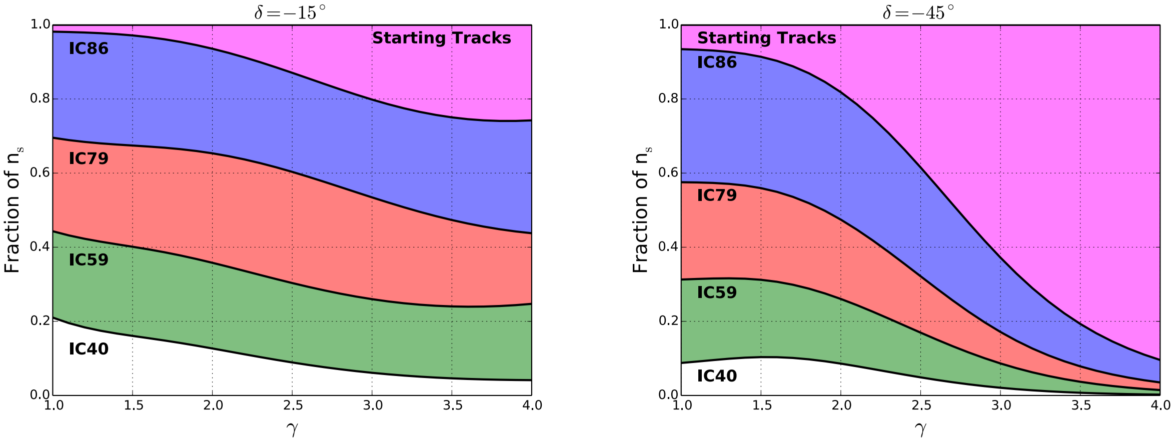

Figure 8.5: Fraction of signal events expected in each event sample. Near the horizon (left), the starting track sample only contributes 5% - 25% of the expected signal flux. At large southerly declinations (right), the majority of the signal is expected to arrive in the starting track sample. Note that this plot only shows the detector acceptance for signal - since the starting track sample has a much lower background rate than the other samples, its impact on the analysis sensitivity is further enhanced.

that also pass the selection criteria defined here. This is applied to both the data and the simulated signal. Only five data events appear in both samples, and are therefore removed from the throughgoing muon sample. At 100 TeV, 15% of simulated signal events pass the selection criteria for both the throughgoing muon and starting track analyses, and are therefore removed from the throughgoing muon simulation. This overlap reduces to $< 5\%$ above 1 PeV.

The likelihood method requires three observables: a reconstructed direction, an estimated angular uncertainty, and an energy. The same techniques used in the throughgoing muon analysis are applied here. The SplineMPE reconstruction provides the direction (Fig. 8.4), and MuEX is used for the energy proxy (Figure 8.6). The angular uncertainty is estimated using the paraboloid algorithm [134], which must be corrected for energy-dependent biases using simulation. The paraboloid pull as a function of energy is shown in Figure 8.7.

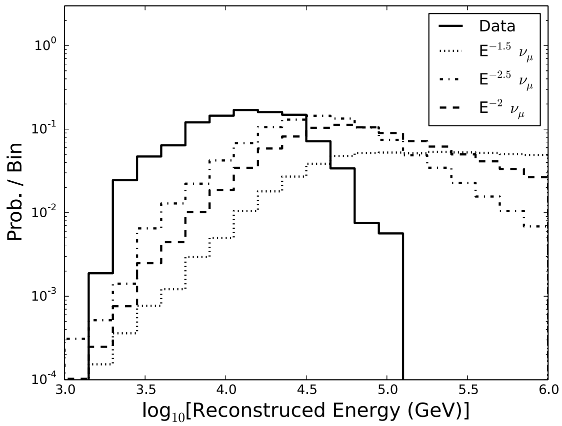

Figure 8.6: Distribution of reconstructed muon energy (MuEX) for data and three astrophysical source spectra. MuEX effectively discriminates between higher energy astrophysical signal and lower energy atmospheric background. The performance of Millipede was also investigated, but led to a worse discovery potential compared to MuEX.

The discovery potential of this analysis is defined as the source flux required to observe a 5σ discovery in 50% of simulated pseud-experiments. Figure 8.8 shows the discovery potential for different source spectra, compared to the throughgoing muon analysis. For a point source with an unbroken E^{-2} spectrum, the high-energy events in the throughgoing muon sample dominate the likelihood, and adding the starting track sample only improves the discovery potential by 10% - 50%. For sources with low-energy cutoffs, however, the starting track sample dominates the likelihood and leads to large improvements. The largest increase is for fluxes below a $\sim$ few PeV at large southerly declinations. Below a declination of $-30°$, the starting track sample improves the E^{-2} discovery potential for fluxes ending at 1 PeV and 100 TeV by roughly a factor of 3 and 20, respectively. As the starting track event selection only extends to a declination of $-5°$, the analysis is unchanged with respect to the throughgoing muon analysis above this declination.

Using the likelihood described here, we perform two hypothesis tests to search for point sources. The first is the model-independent all-sky likelihood scan, in which the likelihood is maximized independently at each location in the sky on a $0.1° \times 0.1°$ grid. This is identical to

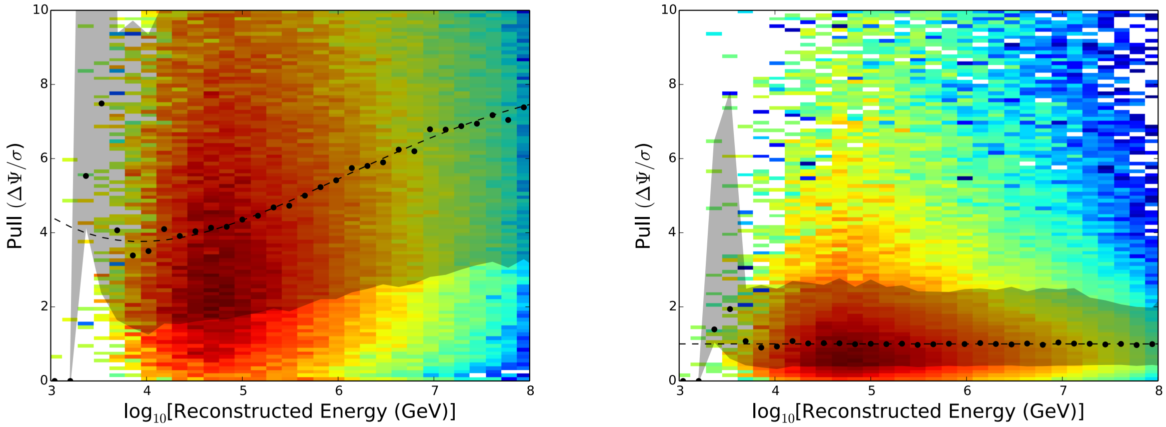

Figure 8.7: Pull distributions for the paraboloid angular uncertainty estimator for the starting track sample. The pull is defined as the true angular resolution divided by the estimated resolution from paraboloid. MuEX provides the reconstructed energy. While the energy dependence is similar to previous data samples, the median pull has a greater offset from one, especially at lower energies (left). This is due to the event topology. The reconstruction likelihood assumes bare muon light without stochastic losses (see Sec. 3.4), while light originating from stochastic losses has a different arrival time profile. Therefore, the estimator deviates from the truth for events with large stochastic losses, such as starting tracks. The pull is corrected by fitting a 4th order polynomial (dashed line) to the median pull in each energy slice (dots). The right plot shows the pull after applying the correction function.

Ch. 6, except we restrict the source to a declination between -85° and -5°. The final result of this test is the location, best-fit parameters, and p-value of the most significant fluctuation (the “hottest spot”). The final post-trial p-value is obtained by repeating this same test on an ensemble of data sets randomized in right ascension.

To reduce the large number of effective trials associated with scanning the entire sky, the second hypothesis test searches for neutrino emission from a catalog of candidate sources. These sources are selected based multi-wavelength electromagnetic observations (x-rays, gamma-rays, etc.) or astrophysical models predicting neutrino emission. We apply the exact same catalog used in the southern hemisphere in Ch. 7. This list contains 38 *a priori*

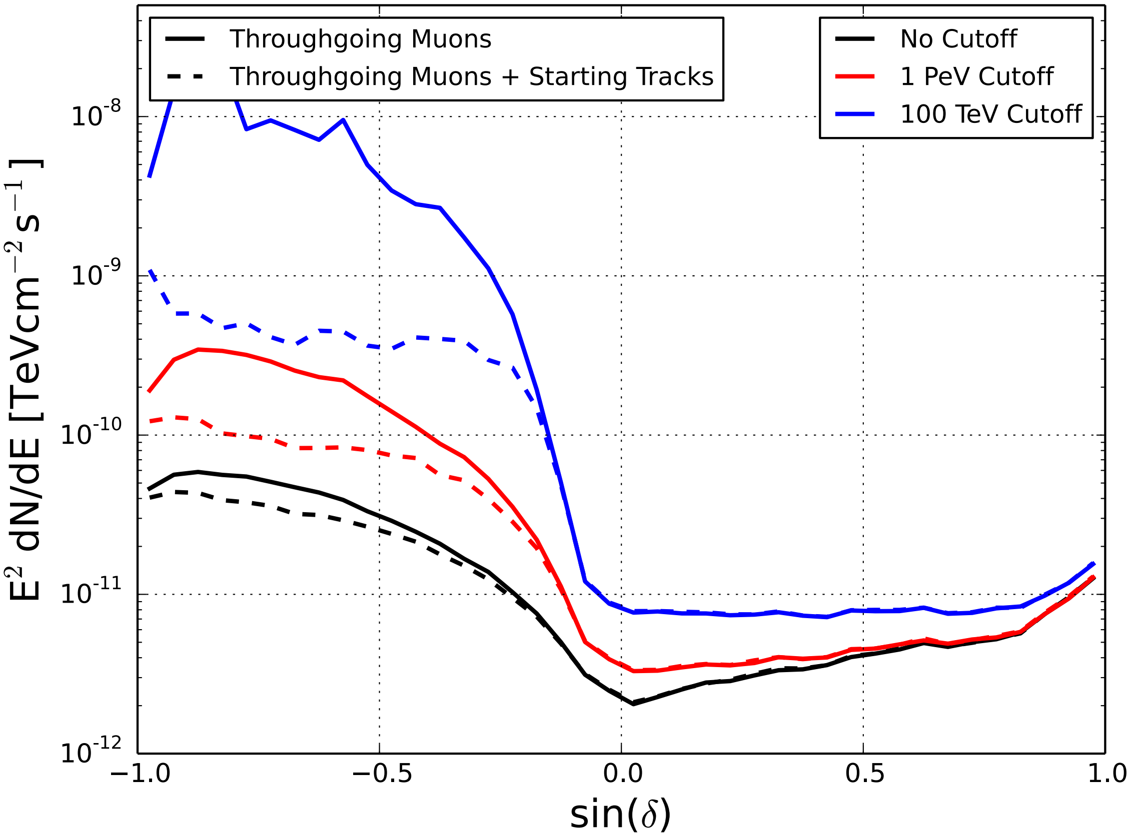

Figure 8.8: Discovery potential vs. declination for point sources with E^{-2} fluxes and three different energy cutoffs. Fluxes ending (with hard cutoffs) at 100 TeV (blue), 1 PeV (red), and 1 EeV (black) are shown. The solid lines illustrate the performance of the standard throughgoing muon analysis (Ch. 6), while the results from combining the throughgoing muon sample with the starting track sample are represented with dashed lines. The starting track analysis improves the discovery potential by a factor of $\sim 5-20$ for fluxes ending at 100 TeV and a factor of $\sim 2-3$ for fluxes ending at 1 PeV.

selected sources from previous IceCube (Sec. 6.3) and ANTARES [151] analyses. Similar to the all-sky search, the source with the most significant p-value is reported, and the chance probability of such a correlation occurring is estimated by repeating the test on scrambled data sets.

This background estimation technique provides p-values independent of both theoretical uncertainties on the fluxes of atmospheric backgrounds as well as systematic uncertainties in the detector simulation. However, upper limits and analysis sensitivities are calculated by simulating the detector response to astrophysical neutrinos, and are therefore subject to these uncertainties. The impact of detector uncertainties on the analysis performance was estimated using simulation. The systematic uncertainties associated with the ice properties and DOM absolute efficiency were estimated to have a 16% and 15% effect on the analysis sensitivity. Summing these uncorrelated errors in quadrature, we find the overall systematic uncertainty on the quoted sensitivities and upper limits to be 22%, very similar to that found in Ch. 6.

8.4 Results

The skymap of pre-trials p-values is shown in Figure 8.9. In the northern hemisphere, the map is identical to that in Ch. 6. In the southern hemisphere, the results are for the starting track sample combined with the throughgoing muon data. The skymap appears sparser because while there are only 549 observed starting track events, the majority of signal for a soft spectrum would appear in this sample (Fig. 8.5). The absence of events places a strong constraint on the likelihood and causes it to often fit underfluctuations where no starting track events are present. Closer to the horizon, this constraint is loosened because a smaller percentage of signal is expected from the starting track sample, and the skymap appears similar to the northern hemisphere.

The location of the most significant pre-trial p-value is 301.15° r.a. and $-34.15°$ dec., where one starting track event is coincident with a small cluster of throughgoing muon events. The likelihood fits for 6.97 signal events with a relatively hard energy spectrum of $E^{-2.15}$,

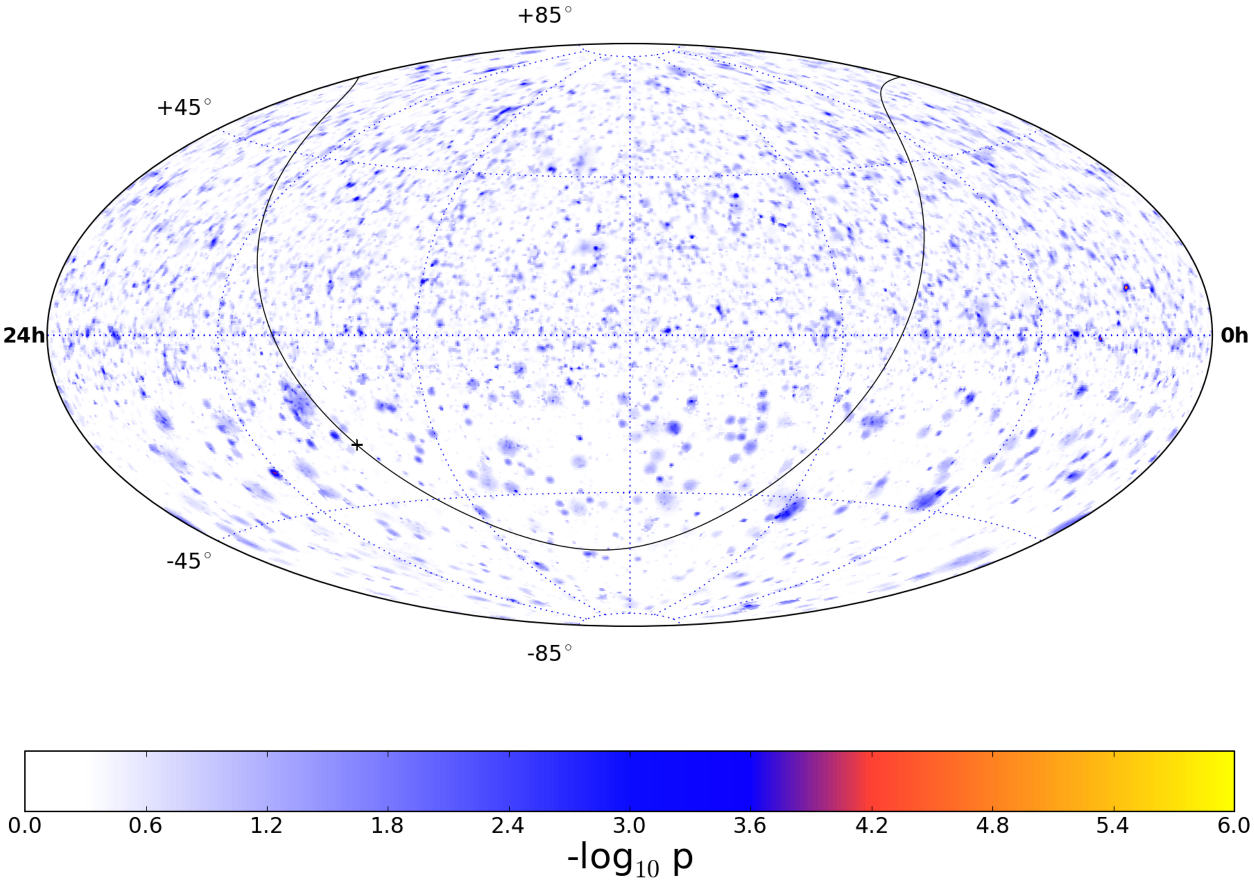

Figure 8.9: Pre-trial significance skymap in equatorial coordinates (J2000) of the point source scan for the starting track sample combined with the throughgoing muon sample. The black line indicates the Galactic plane, and the black plus sign indicates the Galactic Center. The map in the northern hemisphere is identical to that in Ch. 6. In the southern hemisphere, the most significant fluctuation is located at 301.15° r.a. and −34.15° dec.

resulting in a pre-trial p-value of 9.3×10^{-5}. However, a location with equal or greater significance is observed in 97% of scrambled skymaps.

Results for emission correlated with the *a priori* source list are shown in Table 8.1. The source with the strongest upward fluctuation is the Galactic x-ray binary LS 5039. The likelihood fit 3 signal events from this location, with a softer E^{-3} spectral index, resulting in a pre-trial p-value of 0.10. After accounting for the trial factor associated with the 38 sources on the list, the post-trial p-value is 0.76.

Figure 8.10 show the 90% confidence level upper limits on the E^{-2} neutrino flux from each source as a function of declination. Also shown is the sensitivity of this analysis to a few different source spectra, along with recent results from ANTARES [151]. For an unbroken E^{-2} spectrum, this search has the lowest sensitivity for sources anywhere in the sky. IceCube is now also the most sensitive experiment in 70% of the sky for sources only emitting below 1 PeV, and is a factor of 5-10 above the ANTARES sensitivity for sources with fluxes ending at 100 TeV.

Galactic Sources

Category	Source	RA (°)	Dec (°)	$\hat{n}_s$	$\hat{\gamma}$	p-value	$\Phi^{90\%}_{\nu_\mu+\bar{\nu}_\mu}$
SNR	W28	270.43	-23.34	0.0	–	–	6.0
	RX J1713.7-3946	258.25	-39.75	0.0	–	–	10.4
	RX J0852.0-4622	133.0	-46.37	0.0	–	–	11.7
	RCW 86	220.68	-62.48	2.3	2.0	0.28	23.0
XB/mqso	LS 5039	276.56	-14.83	3.0	2.9	0.10	7.4
	GX 339-4	255.7	-48.79	1.7	1.9	0.41	17.0
	Cir X-1	230.17	-57.17	0.0	–	–	12.6
Pulsar/PWN	Vela X	128.75	-45.6	0.8	2.9	0.44	16.9
	HESS J1632-478	248.04	-47.82	0.0	–	–	11.6
	HESS J1616-508	243.78	-51.40	0.0	–	–	12.4
	HESS J1023-575	155.83	-57.76	0.5	1.7	0.46	17.8
	MSH 15-52	228.53	-59.16	0.0	–	–	12.9
	HESS J1303-631	195.74	-63.52	0.0	–	–	12.6
	PSR B1259-63	195.74	-63.52	0.0	–	–	12.6
	HESS J1356-645	209.0	-64.5	0.0	–	–	12.4
Galactic Center	Sgr A*	266.42	-29.01	0.0	–	–	7.6
Not Identified	HESS J1834-087	278.69	-8.76	0.0	–	–	2.0
	HESS J1741-302	265.25	-30.2	0.0	–	–	8.1
	HESS J1503-582	226.46	-58.74	0.0	–	–	13.2
	HESS J1507-622	226.72	-62.34	0.0	–	–	13.5

Extragalactic Sources

Category	Source	RA (°)	Dec (°)	$\hat{n}_s$	$\hat{\gamma}$	p-value	$\Phi^{90\%}_{\nu_\mu+\bar{\nu}_\mu}$
BL Lac	1ES 0347-121	57.35	-11.99	0.0	–	–	2.9
	1ES 1101-232	165.91	-23.49	0.0	–	–	5.9

Table 8.1 – continued from previous page

Category	Source	RA (°)	Dec (°)	$\hat{n}_s$	$\hat{\gamma}$	p-value	$\Phi^{90\%}_{\nu_\mu+\bar{\nu}_\mu}$
	PKS 2155-304	329.72	-30.22	0.0	–	–	7.9
	H 2356-309	359.78	-30.63	0.0	–	–	8.2
	PKS 0548-322	87.67	-32.27	0.0	–	–	8.7
	PKS 0426-380	67.17	-37.93	0.0	–	–	10.3
	PKS 0537-441	84.71	-44.08	0.0	–	–	11.2
	PKS 2005-489	302.37	-48.82	0.0	–	–	11.8
FSRQ	3C279	194.05	-5.79	0.0	–	–	1.3
	HESS J1837-069	279.41	-6.95	0.0	–	–	1.4
	QSO 2022-077	306.42	-7.64	0.9	1.9	0.46	1.9
	PKS 1406-076	212.24	-7.87	6.3	2.6	0.10	3.3
	PKS 0727-11	112.58	-11.7	4.7	3.4	0.18	4.7
	QSO 1730-130	263.26	-13.08	2.4	3.9	0.28	4.9
	PKS 0454-234	74.27	-23.43	0.0	–	–	5.8
	PKS 1622-297	246.53	-29.86	4.1	2.5	0.19	14.3
	PKS 1454-354	224.36	-35.65	0.0	–	–	9.4

Table 8.1 – continued from previous page

Category	Source	RA (°)	Dec (°)	$\hat{n}_s$	$\hat{\gamma}$	p-value	$\Phi^{90\%}_{\nu_\mu+\bar{\nu}_\mu}$
Radio Galaxies	Cen A	201.37	-43.02	0.0	–	–	11.5
Seyfert	ESO 139-G12	264.41	-59.94	0.0	–	–	12.4

Table 8.1: Results for objects on the *a priori* source list for the starting track analysis. Galactic sources are grouped according to their classification as High-Mass X-ray binaries or micro-quasars (HMXB/mqso), SNRs, Pulsar Wind Nebulas (PWNs), star formation regions and unidentified sources. Extragalactic sources are grouped according to their classification as BL Lac objects, Radio Galaxies, Flat-Spectrum Radio Quasars (FSRQ) and Starburst galaxies. The p-value is the pre-trial probability of compatibility with the background-only hypothesis. The $\hat{n}_S$ and $\hat{\gamma}$ columns give the best-fit number of signal events and spectral index of a power-law spectrum. When $\hat{n}_S = 0$, no p-value or $\hat{\gamma}$ are reported. The last column shows the upper limits based on the classical approach [152] for an unbroken E^{-2} flux normalization of $\nu_\mu + \bar{\nu}_\mu$ flux in units of $10^{-12}\,\mathrm{TeV}^{-1}\ \mathrm{cm}^{-2}\mathrm{s}^{-1}$.

8.4.1 Discussion on the Starting Track Event at the Hottest Spot

While the largest upward fluctuation in the skymap was consistent with the background-only hypothesis, indicating no evidence of a neutrino point source, a single starting track event was the main contributor to the likelihood at this location. Here we describe an *a posteriori* investigation of this event.

A visualization of this event is shown in Figure 8.11. The event appears to be a high-energy ν_μ interacting inside the detector volume. The reconstructed vertex of this event is 286 m inside the detector, and in the direction of the track the event passes through three layers of strings without depositing any observable evidence. The reconstructed muon energy

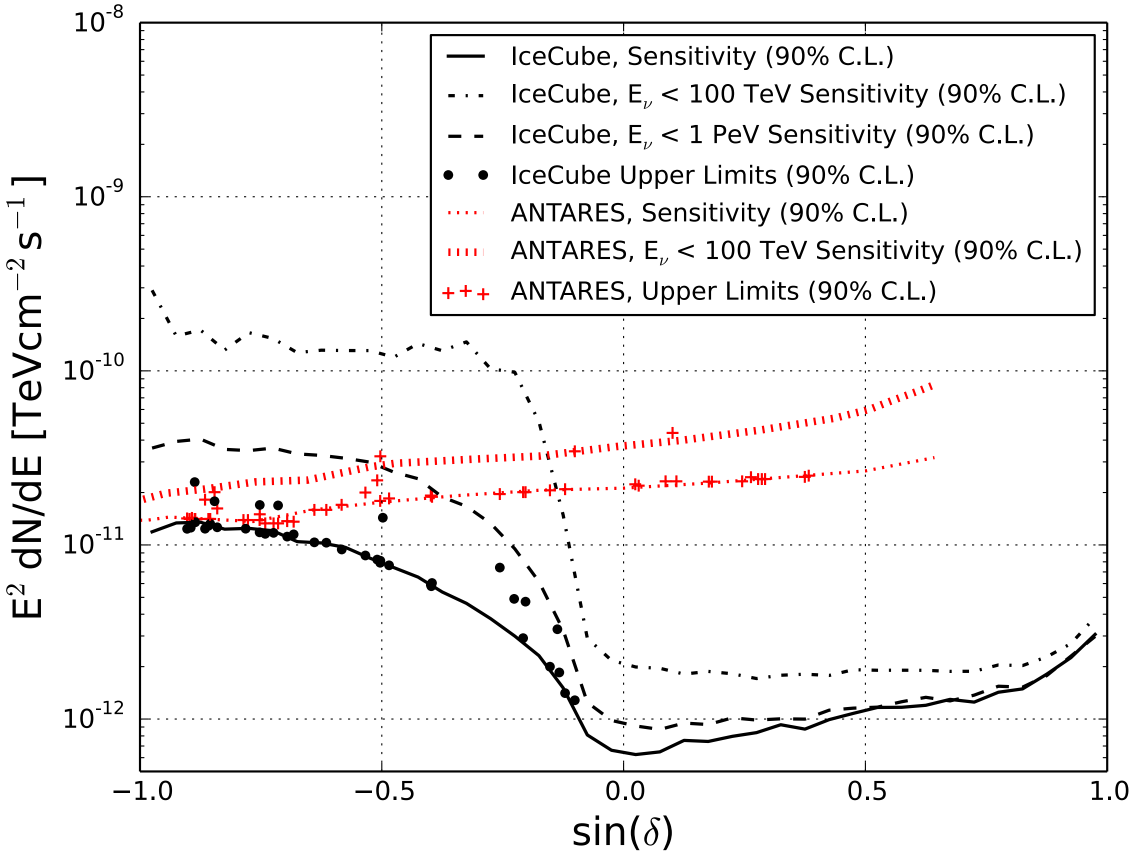

Figure 8.10: Muon neutrino upper limits with 90% C.L. evaluated for the 38 sources (dots), for the starting track sample combined with the throughgoing muon sample. The solid black line is the median 90% C.L. upper limit or sensitivity for a point source emitting an unbroken E^{-2} spectrum. The sensitivity to E^{-2} spectra ending at 1 PeV and 100 TeV are shown in the black dashed and dash-dotted lines, respectively. The ANTARES upper limits and sensitivities in two energy ranges are shown in red [151].

from MuEX is 124 TeV. This is consistent with the results from Millipede, which reconstructed a deposited energy of 84 TeV inside the detector (Figure 8.12). The reconstructed direction of the event, using SplineMPE, was determined to be 301.7° r.a. and $-34.4°$ dec. (corresponding to a zenith angle of 55.7°) with an estimated angular uncertainty of 0.6°. Its arrival time in MJD is 56093.1796492.

At this energy and zenith angle, the expected atmospheric ν_μ background is greatly suppressed by the self-veto effect. Since atmospheric neutrinos are produced in air showers, they are accompanied by atmospheric muons. At high energies, these muons easily propagate through the ice sheet to reach IceCube. Such muons often deposit light in the outer layers of the detector, triggering the veto and causing the entire event (neutrino and muon) to fail the event selection. In the *a posteriori* analysis described here, we calculate the total expected background rate for events with similar observed properties.

Figure 8.13 shows the neutrino energy distribution for simulated atmospheric ν_μ with a similar reconstructed muon energy. The self-veto passing rate from [154], for the observed zenith angle, is also shown. At these energies, the self-veto suppresses the atmospheric flux by a factor of 5 - 100. To calculate the total expected background rate, we generate a probability density function for background atmospheric ν_μ as a function of reconstructed zenith and energy. This includes both atmospheric neutrinos from pion and kaon decays using the model from [115] as well as neutrinos from decays of charmed mesons [116], both corrected to account for the knee in the cosmic ray spectrum [163]. We construct an equivalent probability density function for E^{-2} astrophysical ν_μ. With the observed event's reconstructed zenith angle and energy, we determine the signal to background ratio for this event. The total background rate from atmospheric ν_μ is then the expected rate of simulated events with a higher signal to background ratio. This includes lower-energy neutrinos at less-inclined zenith angles, where the self-veto effect is stronger, as well as higher-energy neutrinos closer to the horizon, where the self-veto is less powerful but the event energy distinguishes it from background. Figure 8.14 shows the PDF for the astrophysical signal and atmospheric ν_μ

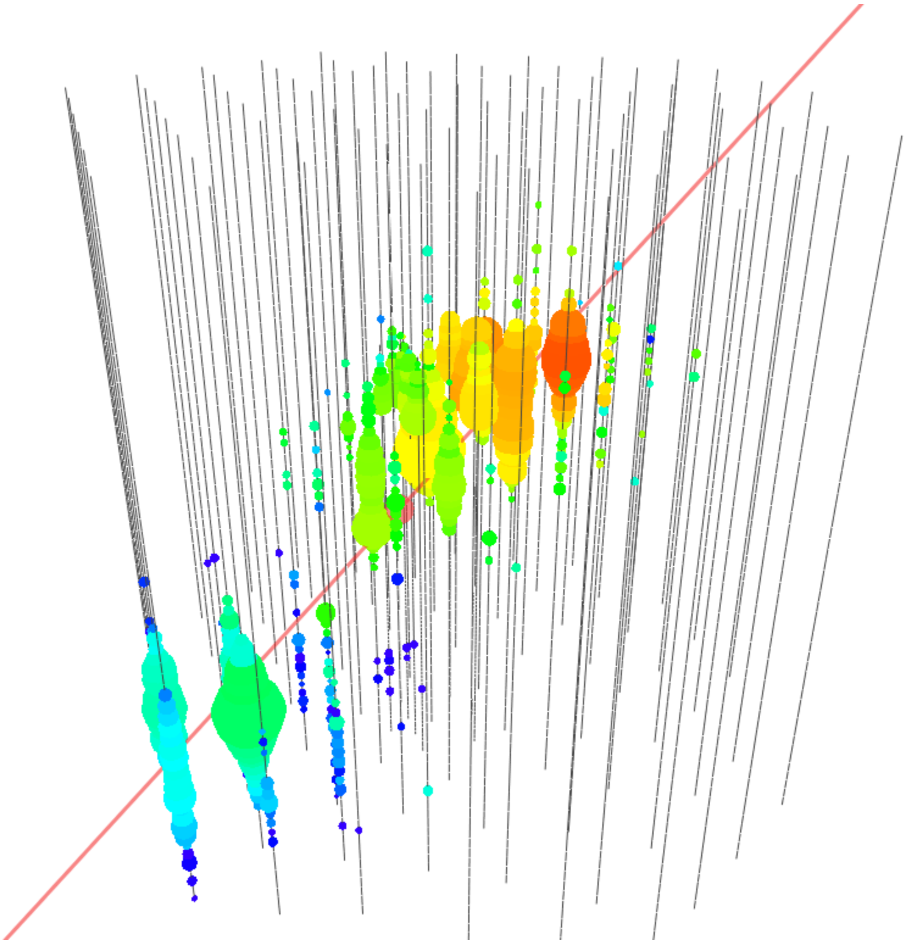

Figure 8.11: Event view of the starting track event. Gray lines show the position of IceCube strings. Colored circles show DOMs with observed charge, with red circles representing DOMs with earlier photon hits and blue representing DOMs with later hits. The size of the circles represents the amount charge observed on each DOM. The red line is the position and direction of the reconstructed track.

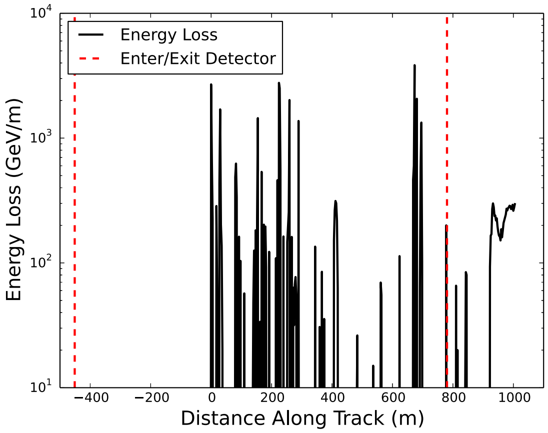

Figure 8.12: Energy loss profile for the highest energy starting track event. Millipede reconstructs the energy loss by placing a hypothesis cascade every 2.5 m along the track. Zero deposited energy is reconstructed along the first ~ 450 m of track length inside the detector. The first non-zero energy loss, representing the interaction vertex, contains 7 TeV. The largest energy loss occurs ~ 700 m after the vertex, where 9 TeV is deposited in a single cascade. The total reconstructed deposited energy inside the detector is 84 TeV.

background. The total rate of such atmospheric events is 0.0022 in three years of livetime. This event therefore represents a 2.8σ fluctuation above the background-only hypothesis.

We also considered the probability the observed event is an atmospheric muon, but this was determined to be a subdominant background. Atmospheric muons between 10 TeV and 1 PeV were simulated with similar directions and detector locations to the observed event. The Monte Carlo procedure sampled muon directions in a $6^\circ \times 6^\circ$ box around the event's reconstructed direction, and these muons were aimed at a 40 m × 20 m cylinder centered on the position of the event's reconstructed vertex. Out of 2×10^8 simulated events, none with similar reconstructed energies and vertex positions passed the event selection criteria. No event with a reconstructed muon energy $>$ 100 TeV traveled more than ~ 80 m inside the detector without depositing significant charge. The effective livetime of this simulation is 3×10^4 years at a muon energy of 10 TeV, increasing to 3×10^7 years at 100 TeV. In the data sample presented here, we would therefore expect $<$ 0.0001 atmospheric muon events that

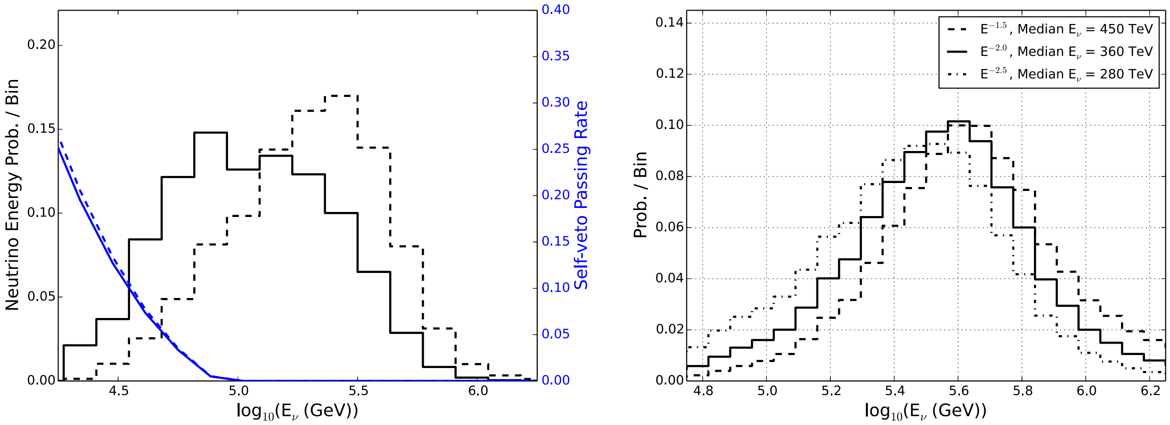

Figure 8.13: Probability distribution for the primary neutrino energy of the observed starting track event. The left plot shows the neutrino energy of simulated atmospheric ν_μ events from pion/kaon decays (solid) and charmed meson decays (dashed) [115, 116, 156, 163]. Only events with reconstructed muon energies within 25% of the observed event's energy are included. The self-veto probability from [154] is also shown. For the pion/kaon flux, neutrinos from approximately half of the expected energy range would be vetoed by accompanying muons $> 99.99\%$ of the time. The right plot shows the expected neutrino energy of astrophysical neutrinos with similar reconstructed energies, for three source spectra. If this event is astrophysical, the most probable neutrino energy for an E^{-2} source is 360 TeV.

appear similar to the observed event. Atmospheric muons therefore represent a subdominant background, and including them in the significance calculation does not change the result.

While the background hypothesis has trouble explaining the observed event, it is consistent with expected astrophysical signal. The best-fit astrophysical neutrino flux measured in **??** would produce 4.1 starting track events in this data set, including 1.0 event with reconstructed muon energies at or above 124 TeV. Figure 8.13 shows the distribution of primary neutrino energies for simulated signal events with reconstructed energies similar to the observed event. If this event originates from an astrophysical flux, it was likely generated by a few hundred TeV ν_μ.

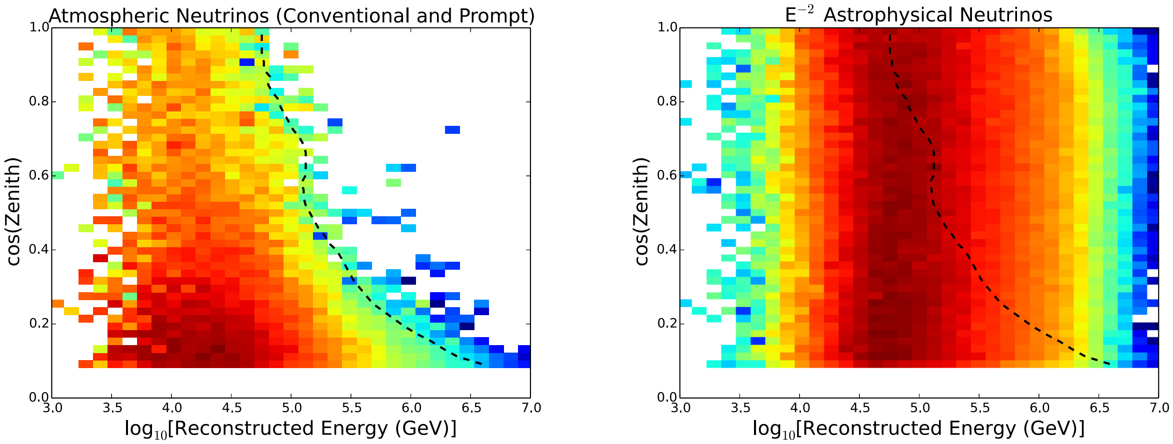

Figure 8.14: Astrophysical signal and atmospheric ν_μ background PDFs for the observed starting track event. The left plot shows the PDF as a function of reconstructed zenith angle (SplineMPE) and reconstructed energy (MuEX) for atmospheric neutrinos following the models from [115,116,156,163]. This includes the self-veto probability from [154] for each event. The right plot shows the same PDF for E^{-2} astrophysical neutrinos. The likelihood ratio between the signal and background hypothesis is calculated for the observed event, and the dashed line denotes the zenith-energy contour with this likelihood ratio. Events to the right of this contour are more "signal-like" than the observed event. The sum of the atmospheric neutrino expectations in this region is 0.0022 events in three years of livetime.

It is important to note the 2.8σ significance calculated here represents the chance probability that this event originates from an atmospheric flux. It does not include any information about spatial clustering of this event with others, or the correlation of this event with known astrophysical sources. As there is no significant evidence for clustering nor correlation, this event does not represent a neutrino point source. Instead, it is likely the most astrophysical-like well-localized neutrino event found by IceCube so far. If this event is astrophysical, it points back to its location of production within 0.6°.

Future IceCube analyses will build on the work presented here to increase sensitivity to fainter and lower energy sources. This can be achieved by extending the event selection to lower energies using enhanced veto techniques. This analysis used a veto independent of reconstructed direction coupled with a high charge threshold. A veto that exploits reconstructed directions while lowering the charge threshold could isolate a sample with more low-energy signal events and similar background rates. An alternative approach would be to tighten the event selection to select only well-contained starting track events with energies $\gtrsim 50\,\mathrm{TeV}$. This could lead to a small but pure sample of astrophysical tracks that are essentially background free. The cascade channel may also provide opportunities to search for spatial clustering of events. Since the background from atmospheric ν_e is substantially lower than atmospheric ν_μ, a cascade event selection could extend to lower energies than considered here.

Observations by ANTARES [151], the current mediterranean neutrino telescope, as well as future kilometer- and multi-kilometer-scale telescopes planned for both the mediterranean [164] and the South Pole, can further investigate the location of the highest energy starting track event to search for sources. Follow-up observations by optical, x-ray, and gamma-ray observatories could also elucidate the origin of this event and future track events of clear astrophysical origin, which, given the evidence for the astrophysical neutrino flux, will continue to be observed.

Chapter 9

Astrophysical Implications of Point Source Results

The previous chapters presented three different analyses searching for neutrino emission from astrophysical sources. While no statistically significant evidence of a point source was found, the resulting sensitivities and upper limits are the most stringent for sources with an E^{-2} spectrum located anywhere in the sky.

This chapter compares these null results with neutrino emission models, observations of sources in high-energy gamma-rays, and measurements of the diffuse astrophysical neutrino flux. We first consider the implications of these analyses for neutrino emission from individual sources, taking a model-dependent approach in which constraints are placed on specific neutrino flux models. We also present a more model-independent, multi-messenger approach, in which neutrino limits are converted into "neutrino-derived" limits on hadronic gamma-rays. These are then directly compared to gamma-ray observations. Insight can also be gained by comparing point source limits with the measured diffuse flux of astrophysical neutrinos [12, 13]. We first present model-independent constraints on the number of sources contributing to the diffuse flux. With additional model assumptions, constraints on the density of uniformly-distributed sources are also made and compared to known source classes.

9.1 Constraints on Single Sources

9.1.1 Model-dependent Tests for Specific Sources

The E^{-2} flux model, used widely for constructing upper limits in the previous chapters, is a baseline model for hadron acceleration in strong shocks [26]. However, neutrino fluxes from many sources are predicted to have different spectral slopes and energy cutoffs. Here we survey the existing literature and set upper limits on flux models for a few different sources.

Supernova remnants (SNRs) and pulsar wind nebulae (PWN) have long been hypothesized to be sources of Galactic cosmic rays and, therefore, high-energy neutrino emitters. In Figure 9.1, we consider three models for neutrino emission from the Crab Nebula, a Galactic PWN 2 kpc from Earth. The Crab Nebula is one of the brightest objects in the gamma-ray sky, and is often referred to as the standard candle of gamma-ray astronomy. In [51], the authors predict hadrons will be accelerated in the pulsar wind via the resonant cyclotron absorption model, which creates a flux of TeV - PeV neutrinos when the nuclei in the wind interact with surrounding photon and matter fields. The most optimistic model, with the highest effective target density and relativistic velocity of the pulsar wind, is excluded at 90% C.L (black line). The blue line shows the predicted neutrino flux from [50,165], in which nuclei are accelerated near the surface of the neutron star and interact with x-ray emission from the stellar surface. This model is also excluded by current IceCube observations. The green line corresponds to the model from [43], in which the gamma-ray flux is assumed to originate from neutral pion decay. The IceCube limit is a factor of 1.75 above the model, which mainly predicts neutrino emission below 10 TeV. With a few more years of data, IceCube will likely be able to corroborate or exclude this neutrino emission model for the Crab Nebula as well.

Figure 9.2 shows neutrino predictions and IceCube upper limits for three Galactic SNRs in the northern hemisphere. In [44], the authors derive the neutrino emission assuming the gamma-ray emission at energies $>$ GeV originates from pp interactions in the SNR. For G40.5-0.5, the SNR predicted to have the highest flux, the neutrino upper limit is a factor of three above the model. For IC443 and Cassiopeia A, where gamma-ray telescopes measure softer spectra, the neutrino upper limits are a factor of 10-100 above the models.

In the southern hemisphere, upper limits on models from SNRs and PWN are a factor of ~ 1000 above predictions. Figure 9.3 shows predictions for the SNR RXJ1713.7-3946 and the PWN Vela X. In both cases, the models are taken from [43], in which the gamma-ray

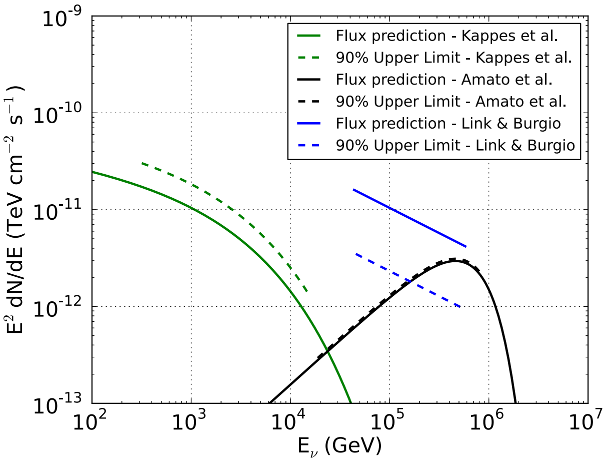

Figure 9.1: Flux predictions (solid) for three models of neutrino emission from the Crab Nebula, with their associated 90% C.L. upper limits (dashed) for an energy range containing 90% of the signal. Both the model from Amato *et al.* [51] and the most optimistic model from Link & Burgio [50, 165] are now excluded at 90% confidence level. For the gamma-ray based model from Kappes *et al.* [43], the upper limit is a factor of 1.75 above the prediction.

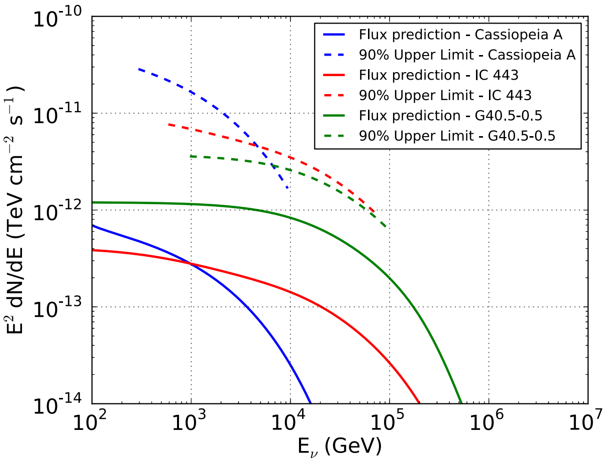

Figure 9.2: Flux predictions (solid) and upper limits (dashed) for three Galactic supernova remnants in the norther hemisphere. The neutrino models, based of fitted gamma-ray observations, are from [44]. For the source with the highest predicted flux, G40.5-0.5, the upper limit is a factor of three above the model.

emission is assumed to be originate from *pp* interactions. As both sources are observed to have gamma-ray cutoffs near 1 TeV, the predicted neutrino emission in IceCube's optimal energy range in the southern hemisphere is greatly reduced.

Predicted neutrino emission from the Galactic Center is also shown in Figure 9.3. The Galactic Center is a complex astrophysical region. It is home to the bright radio source Sagittarius A^*, thought to be a supermassive black hole at the center of the Milky Way that has also been observed in x-rays and gamma-rays [167,168]. The extended region around the black hole also harbors significant starburst activity [64,169]. Both these phenomena make the Galactic Center an interesting candidate neutrino source. Additionally, five of the first 28 high-energy astrophysical neutrino candidate events observed by IceCube originate near the Galactic Center, including an event with $\sim$ PeV energy [12]. A number of models predict a high-energy neutrino flux from this region, many normalizing the flux to the observed astrophysical events [11,149,170,171].

The most optimistic predictions are excluded by the muon-based point source analyses presented in this thesis. In [149] the authors predict an E^{-2} neutrino point source with a normalization of 6×10^{-11} $\mathrm{TeV^{-1}cm^{-2}s^{-1}}$ at 1 TeV, eight times greater than the Galactic Center upper limit presented in Ch. 8. Even if the neutrino spectrum does not continue above 1 PeV, this analysis is sensitive to a Galactic Center flux two times lower than this model. A point source of this strength is therefore ruled out at 90% C.L., although an extended source can still evade detection. On the other hand, models based on gamma-ray observations predict lower fluxes. The IceCube upper limit is a factor of 200 above the gamma-ray based model flux from [42] (blue line in Fig. 9.3).

Unidentified TeV gamma-ray sources are also predicted to be sources of high-energy astrophysical neutrinos. In [166], the authors assume these objects are Galactic hypernova remnants capable of producing neutrinos up to PeV energies. As in [42], they derive the neutrino emission from gamma-ray observations, and also assume the neutrino spectrum extends to 1 PeV. Figure 9.4 shows the predicted neutrino flux for three unidentified TeV gamma-ray sources in the southern hemisphere, along with the IceCube upper limits. For

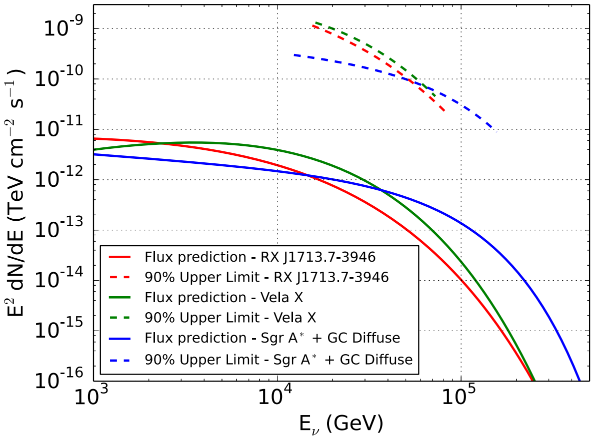

Figure 9.3: Flux predictions (solid) and upper limits (dashed) for three Galactic sources in the southern hemisphere. For each source, the models use the observed gamma-ray spectra to calculate the corresponding neutrino emission [42, 43], which is a factor of $\sim 100 - 1000$ below IceCube's upper limits.

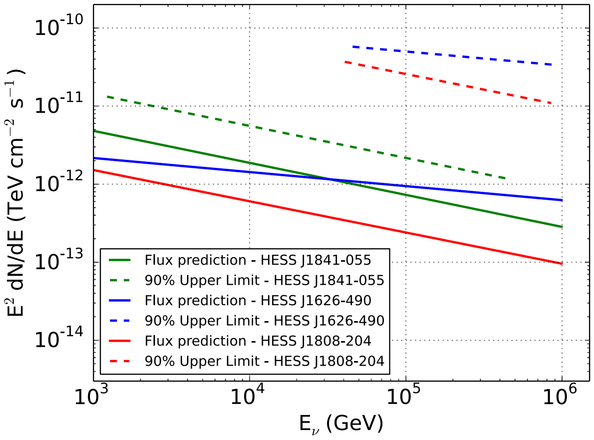

Figure 9.4: Flux predictions (solid) and upper limits (dashed) for three unidentified TeV gamma-ray sources in the southern hemisphere [166]. As HESS J1841-055 is close to the horizon, where the Earth still shields the detector from the atmospheric muon background, the limit is only a factor of 3 above the model. For the other two sources considered, the upper limits are a factor of $\sim 50 - 100$ above the predictions.

sources near the horizon (green), the upper limit is a factor of 3 above the prediction. For sources at larger southerly declinations, where the starting track analysis contributes the most to the sensitivity, and the upper limits are a factor of $\sim 50-100$ above the predictions.

For some of the objects investigated here, IceCube can exclude certain models of particle acceleration and neutrino emission. In many cases, the current data cannot probe the predicted flux levels, and we must await future data or improved analysis techniques to confirm or exclude these models.

9.1.2 Constraints on Hadronic Emission from Gamma-ray Sources

Many models considered in the previous section were based on gamma-ray observations. By fitting the observed gamma-ray spectra and assuming all or a fraction of those gamma-rays originate from neutral pion decay, the corresponding neutrino flux from charged pion decay can be predicted. Instead of setting upper limits on this predicted neutrino flux, it's possible to present IceCube's upper limits in terms of the gamma-ray flux directly. By assuming a basic *pp* interaction model, the flux in gamma rays and neutrinos can be related via [38, 42]

$$E_\gamma^2 \frac{d\Phi_\gamma}{dE_\gamma} \simeq 2E^2_{\nu_\mu+\bar{\nu}_\mu} \frac{d\Phi_{\nu_\mu+\bar{\nu}_\mu}}{dE_{\nu_\mu+\bar{\nu}_\mu}}, \tag{9.1}$$

where $E_\gamma \simeq 2E_{\nu_\mu+\bar{\nu}_\mu}$ and $\Phi_{\nu_\mu+\bar{\nu}_\mu}$ refers to the sum of the muon neutrino and antineutrino flux. This formula is used to convert IceCube's neutrino limits to "neutrino-derived" gamma-ray limits, which are then compared to gamma-ray observations. At energies where the observed flux is greater than the limit, the fraction of gamma-rays originating from hadronic interactions can be constrained. We use differential neutrino limits for this exercise, so the results do not require any assumed gamma-ray spectral shape.

In Figure 9.5, gamma-ray observations of Galactic SNRs Cassiopeia A and IC443 are presented alongside neutrino-derived gamma-ray limits. For both objects, the gamma-ray flux peaks near 1 GeV and steepens substantially before reaching TeV energies, where IceCube

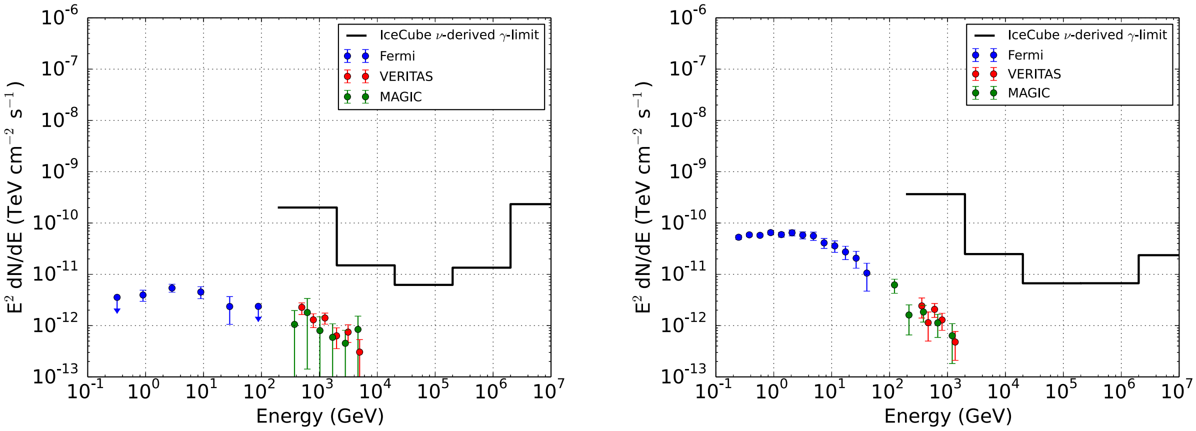

Figure 9.5: Neutrino-derived limit on hadronic gamma-ray production in two Galactic SNRs. The left plot shows gamma-ray observations of Cassiopeia A [172–174] compared to IceCube's upper limit, calculated by converting the neutrino flux to a gamma-ray flux. The right plot shows the same for IC443 [175–177]. For both sources, the neutrino limit is not strong enough to constrain the hadronic gamma-ray fraction.

is most sensitive. Therefore, no constraint on the hadronic fraction of the gamma-ray flux can be made.

This exercise is repeated for extragalactic objects such as blazars and active galactic nuclei (AGN). However, for extragalactic objects at large enough distances, the high-energy gamma-ray flux is attenuated because photons interact with the cosmic microwave background and the extragalactic background light (EBL) as they travel from the source to Earth [9,36,178]. The absorption as a function of the photon energy and the redshift of the source is shown in Figure 9.6. Here we use the EBL model from [36] to infer the gamma-ray flux at the source for objects with well-measured redshifts.

Figure 9.7 shows the gamma-ray spectrum at Earth for blazar 1ES1959+650 and the inferred, de-absorbed spectrum at the source. Although 1ES1959+650 is only at a redshift of 0.048, the flux at 10 TeV is likely five times higher at the source than at Earth. Since the steady-state emission (circle markers) is below the neutrino-derived gamma-ray limits, current IceCube data cannot constrain the origin of the gamma-ray flux. However, like many

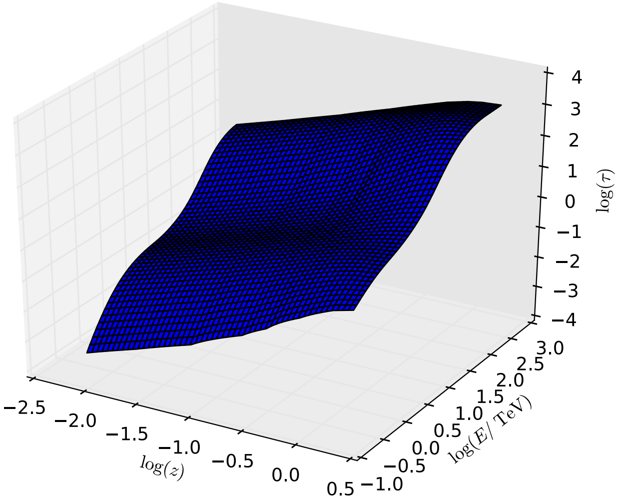

Figure 9.6: Photon absorption by the EBL as a function of the source redshift and photon energy, for the model from [36]. The photon flux at energy E from a source at redshift z is suppressed by the factor $e^{-\tau}$.

blazars, 1ES1959+650 has significant time-dependent emission. Most notably, in 2002 the Whipple and HEGRA telescopes observed an "orphan" flare in which enhanced TeV emission was not correlated with time-dependent x-ray or radio emission [179]. Such a phenomenon is difficult to explain with leptonic emission mechanisms [180]. Unfortunately, this flare occurred before IceCube began operating, but if a similar flare occurs in the future we will likely either observe coincident neutrinos or constrain the origin of the gamma-ray emission.

Figure 9.8 shows the derived gamma-ray flux at the source for blazar Markarian 421 and the AGN Centaurus A. Similar to 1ES1959+650, Markarian 421 has extremely variable emission. The steady state gamma-ray flux is a factor of ~ 3 below the time-integrated limits. The emission during a number of flares, which occurred before IceCube operated, surpass the level of the neutrino-derived limit shown here. As the flux in these flares are only sustained for short periods of time, they cannot be directly compared to these limits.

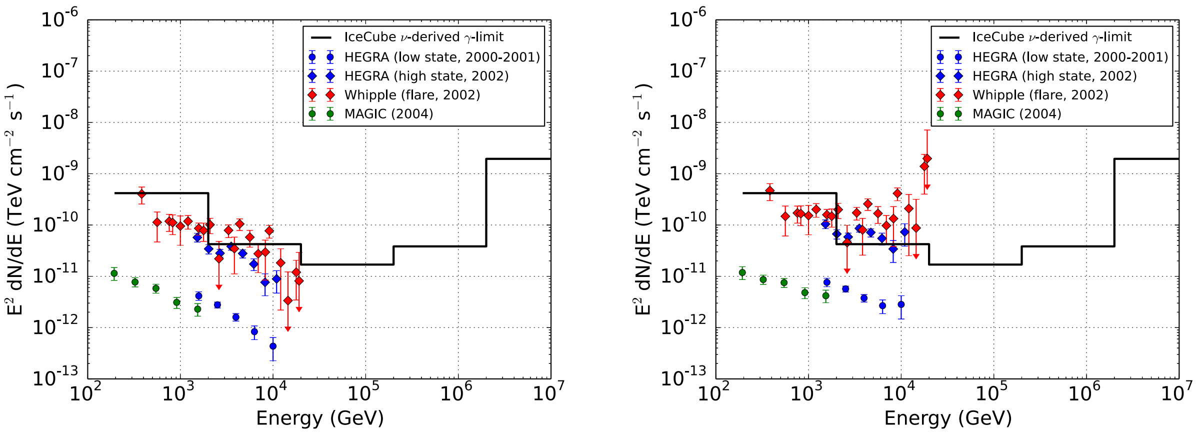

Figure 9.7: Neutrino-derived limit on hadronic gamma-ray production in 1ES_1959+650, with and without extinction from the EBL. The left plot shows the gamma-ray observations at Earth [181–183]. The right plot shows the gamma-ray data after being de-absorbed using the EBL model from [36], representing the gamma-ray flux at the source.

However, a time-dependent analysis, in which neutrino emission with a specific time profile is tested, may constrain the origin of similar-sized gamma-ray flares from Markarian 421 in the future [184]. For Centaurus A, an AGN in the southern hemisphere, IceCube limits only cover energies above ∼ 10 TeV. No gamma-ray measurements are present at these energies. On one hand, extrapolating the lower energy measurements to higher energies suggests more neutrino data is required before any constraints can be made. On the other hand, the lack of gamma-ray measurements indicate the neutrino-derived limits likely provide the strongest constraint on hadronic emission from Centaurus A at ∼PeV energies.

This investigation shows that, for a small selection of extragalactic sources, IceCube limits are approaching the same level as gamma-ray observations. While no constraints on the origin of the gamma-ray flux can be made at this time, with three more years of data IceCube will likely either begin observing astrophysical neutrinos or constraining the fraction of gamma-rays from hadronic emission. Additionally, emission during flaring states surpasses the time-integrated limits presented here. This suggests time-dependent neutrino searches may be sensitive enough to detect neutrinos from these flares if they are hadronic.

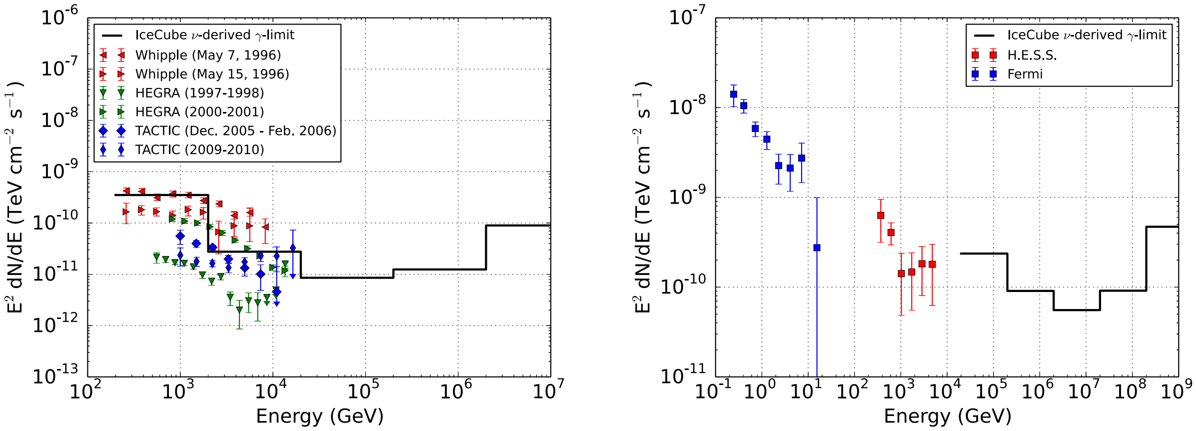

Figure 9.8: Neutrino-derived limits on hadronic gamma-ray production in Markarian 421 (left) and Centaurus A (right). The EBL de-absorption effect has been applied to the gamma-ray observations [185–191], so the data points show the inferred emission at the source.

As of this writing, no evidence of time-dependent neutrino emission has been found with IceCube [150, 184].

For all sources considered, we assumed gamma-rays were produced via pp interactions. If $p\gamma$ interactions are instead the dominant emission mechanism, the neutrino-derived gamma-ray limits would move up by a factor of two [38]. Additionally, the constraints on extragalactic objects do depend on the assumed EBL absorption model. Recent EBL measurements by Fermi [178] constrain the parameter space for these models, and the model used here is in the allowed region. While alternative models may give slightly different results, the general conclusions found here are unlikely to change significantly.

9.2 Constraints on Populations of Sources

While point source analyses are only beginning to probe the source strengths expected from individual objects, the diffuse astrophysical neutrino flux is observed at a much higher total flux level. The best-fit astrophysical neutrino flux from the high-energy contained vertex analysis is $E^2\phi(E) = 1.5 \times 10^{-8}(E/100\mathrm{TeV})^{-0.3}$ GeVcm^{-2}s^{-1}sr^{-1} [13], and analyses sensitive to a wider energy range show a preference towards softer spectra [192].

Whatever sources produce these neutrinos, their fluxes must be lower than the point source limits presented here. This condition provides a relatively model-independent constraint on the total number of sources contributing to the diffuse flux, and the following section calculates this constraint for different allowed diffuse spectra. If the diffuse flux originates from a single class of extragalactic objects, model-dependent constraints on the allowed source density can also be made. This is explored in the final section.

9.2.1 Model-independent Constraints on the Total Number of Sources

As mentioned in Ch. 7, the spatial distribution of astrophysical events suggests no single source dominates the diffuse flux and a substantial portion of the flux is likely extragalactic. Using point source upper limits, we estimate the minimum number of sources comprising the isotropic diffuse flux. Figure 9.9 shows the point source sensitivity in muons (throughgoing and starting) for three different energy spectra, compared to the diffuse flux level integrated over the entire sky. The ratio between these two values represents the minimum number of sources required to populate the diffuse flux while obeying the point source limits. In the southern hemisphere, the median sensitivity is only a few times lower than the total diffuse flux. In this region, only a few sub-threshold sources could explain the entire flux and still be consistent with the observed skymap. However, in the northern hemisphere, the median sensitivity is two orders of magnitude below integrated diffuse flux level. Therefore, we use the skymap above $\delta > -5^\circ$ to calculate the minimum allowed number of sources, under the assumption the observed diffuse flux is isotropic.

For a diffuse flux normalization ϕ^D, multiplying by the solid angle Ω covering $-5^\circ < \delta < 85^\circ$ gives the total diffuse flux integrated over the northern hemisphere, in point source flux

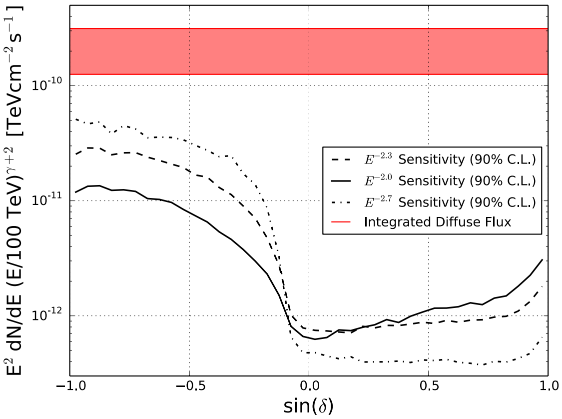

Figure 9.9: Point source sensitivity compared to the total diffuse flux level. The y-axis is the point source flux normalization at 100 TeV, and the curves show the sensitivity to sources with three different spectral slopes. The red band covers the allowed range of the diffuse flux normalization measured by [13], integrated over 4π—in other words, the point source flux if the entire diffuse flux originates from a single source. Throughout the entire sky, the point source sensitivity is below the diffuse flux level, indicating multiple sources must contribute to the diffuse flux.

units. This flux is created by N point sources each contributing ϕ_i^{PS}, where each ϕ_i^{PS} must be lower than the point source upper limit ϕ_i^{UL} at the location of the hypothetical source:

$$\phi^D \Omega = \sum_{i=1}^{N} \phi_i^{\mathrm{PS}} \qquad (\phi_i^{\mathrm{PS}} \leq \phi_i^{\mathrm{UL}}). \tag{9.2}$$

We first assume each of the hottest spots in the observed point source skymap is an actual source, with a flux just below the analysis upper limit. We calculate an upper limit at each of the hottest spots, assuming all sources have no extension and have the same spectral slope with no cutoff. These limits are subtracted from the total integrated diffuse flux budget, starting with the largest, to determine the minimum number of sources. To impose a certain degree of isotropy, the diffuse flux is divided equally among ten zenith bands, and hotspots in each band are considered separately. For an unbroken E^{-2} spectrum, 21 sources or more are required to comprise the diffuse flux while obeying the 90% C.L. point source upper limits.

By assuming the true point source are coincident with the skymap locations with the largest upward fluctuations, this constraint only considers a very small amount of phase space. This requirement is likely unrealistic, as sources could exist at many other locations in the sky while still generating an isotropic flux. Moreover, upper limits are statistical tests, just like p-values, and using the largest upper limits out of thousands of tested locations requires a trial penalty. To account for these effects, we create toy simulations of sources distributed isotropically, calculate point source flux upper limits at each hypothetical source location (using the skymap and likelihood analysis), and use Equation 9.2 to estimate the minimum number of sources. Since determining the upper limit at every location in the sky is computationally expensive, we form a distribution of upper limits by calculating the upper limit at 2000 isotropically distributed locations. For each ensemble, bootstrapped samples are drawn from this distribution to generate a population of sources consistent with both the observed diffuse flux and the point source upper limits. We repeat this procedure 10^4 times to generate a distribution of the potential minimum number of allowed sources.

Figure 9.10 shows histograms of the minimum number of allowed sources for the best-fit E^{-2} and $E^{-2.3}$ diffuse fluxes. Since the calculation uses 90% C.L. point source upper limits, the median of this histogram represents the 90% C.L. limit on the minimum number of sources contributing to the diffuse flux.

This calculation can be repeated for each combination of normalization and spectral slope within the measured uncertainties of the diffuse flux. Figure 9.11 shows the limit on the minimum number of sources for diffuse flux normalizations and spectral slopes allowed by [193]. Softer spectra require a greater number of sources because of the interplay between the diffuse and point source analyses. Most the statistical power of the diffuse flux measurements is due to events above 100 TeV. For the 1σ flux region from [13], the fluxes are effectively anchored at a few hundred TeV. With a normalization fixed at this energy, softening the spectrum leads to more observed events below a few hundred TeV. However,

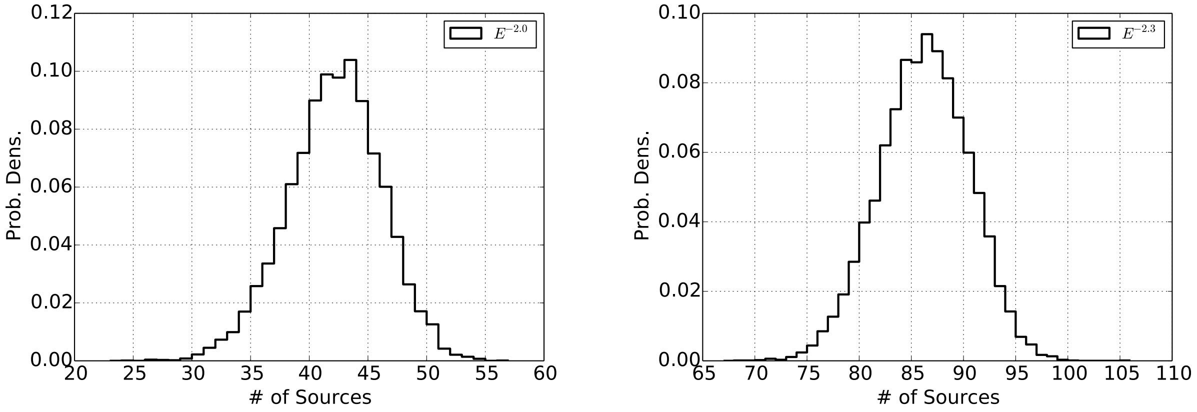

Figure 9.10: Normalized distribution of the number of sources per ensemble required to be consistent with the measured diffuse neutrino flux. Ensembles with sources emitting E^{-2} (left) and $E^{-2.3}$ (right) spectra are shown. Entries in the left side of each histogram corresponds to sources placed at random locations that had more upward fluctuations than average, corresponding to weaker upper limits on the point source flux and therefore a lower constraint on the minimum number of sources. Entries in the right side of each histogram, on the other hand, represent ensembles where more locations with underfluctuations were randomly chosen, resulting in a larger number of hypothetical sources to populate the diffuse flux.

the point source analysis in the northern hemisphere is most sensitive at lower energies (see Fig. 6.15), leading to a larger number of sources required to explain softer diffuse fluxes. This effect is also seen in Fig. 9.9.

These calculations assume the diffuse flux is created by isotropically distributed sources with no spatial extension that emit neutrinos following unbroken power law spectra. If the diffuse flux is present at higher levels in the southern sky than the northern sky, fewer sources would be allowed to comprise the flux in the North while the enhanced southern-sky flux would remain largely unconstrained. A smaller ensemble of spatially extended sources or sources with a spectral cutoff would also be allowed by current point source limits. If all assumed sources had 0.5° extensions, the constraints on the number of sources would be

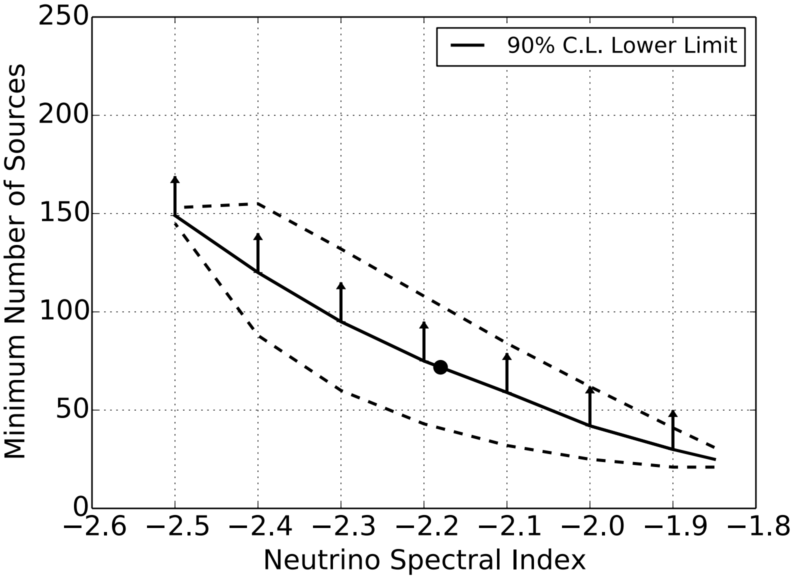

Figure 9.11: Minimum number of required sources for all realizations of the measured diffuse flux allowed at 1σ. The diffuse analysis in [193] provide an allowed region for the flux normalization and spectral slope. Each normalization/slope corresponds to a minimum number of sources determined by the point source analysis. The black marker denotes the minimum number of sources allowed for the best-fit diffuse flux, and the solid line shows the constraint for each spectral slope allowed by [193], using the best-fit normalization at each slope. The dashed lines illustrate how the constraint changes if the flux normalization is instead at the edge of the 1σ range allowed by [193]. If the diffuse flux has a softer spectrum, more sources are required to maintain consistency with the point source skymap.

weakened by $\sim 40\%$. Likewise, if all sources followed an E^{-2} spectrum with an exponential cutoff at 3 PeV, the constraints would be weakened by $\sim 20 - 30\%$. Additionally, we have assumed an equal partition of the diffuse flux into each neutrino flavor, and allowing ν_e or ν_τ to dominate the flavor ratio would also weaken these constraints.

However, there is at least some experimental evidence in favor of each of these assumptions. The diffuse flux is observed at similar levels in both the northern and southern hemisphere as well as in the muon and cascade channels [13, 192, 193], supporting isotropically distributed sources with a 1 : 1 : 1 flavor partition. Figure 9.11 uses the diffuse flux measured using muons in the Northern Hemisphere [193] and is therefore directly comparable to the point source limits. While an E^{-2} spectrum with a $\sim$ PeV cutoff is allowed by the measurement in [13], a softer spectrum with no cutoff is preferred, and measurements in [192] support this. Large contributions to the flux from extended sources, especially very large local sources, are still possible. However, many astrophysical events are reconstructed to originate from high galactic latitudes, and the diffuse flux is observed at similar levels in both hemispheres. Both these facts suggest a significant extragalactic component, and most extragalactic source classes would appear as point sources.

It is also important to note these calculations do not assume any specific distributions for the flux, luminosity, or distance of the sources. Sources are not required to have equal fluxes, or follow a specific luminosity distribution; their fluxes are only constrained by the observed point source upper limits. Therefore, this investigation does not require the diffuse flux to originate from a single source class.

9.2.2 Constraints on the Density of Uniformly Distributed Sources

The analysis presented above can be extended using a description of the distribution of sources throughout the universe and the luminosities of these objects. This type of investigation has been pursued as a means of constraining the density of neutrino sources [194–197], and similar work has been done in the context of the sources of the ultra-high energy cosmic rays [198, 199].

Here we apply this type of model to IceCube point source analyses. We assume the total diffuse neutrino flux is split among a class of extragalactic objects that appear as point sources and emit neutrinos at a constant rate. If these objects are distributed uniformly throughout the universe and have equal luminosities, the closest source will have the highest point source flux. For a given source density of uniformly distributed, equal luminosity sources, the observed diffuse flux determines the expected flux of the brightest source. Ref. [194] finds the flux of the brightest source ϕ^{PS} is probabilistic, following the distribution

$$p_1(\phi^{\mathrm{PS}}) \simeq \frac{3}{2}\frac{1}{\phi^{\mathrm{PS}}}\left(\frac{\phi(\hat{r})}{\phi^{\mathrm{PS}}}\right)^{\frac{3}{2}} \exp\left(-\frac{\phi(\hat{r})}{\phi^{\mathrm{PS}}}\right)^{\frac{3}{2}}. \tag{9.3}$$

The term $\phi(r)$ is the flux of a point source located at a radius r, which for $r \leq H_0^{-1}$ can be approximated as

$$\phi(r) \simeq \frac{H_0}{f_{\mathrm{sky}} 4\pi r^2 \xi_z \mathcal{H}_0} \times \phi^D, \tag{9.4}$$

where ϕ^D is the total diffuse flux, f_{sky} is the fraction of the sky visible to the detector, and $\mathcal{H}_0$ is the source density in Mpc^{-3} [194]. The variable $\hat{r}$ is defined as the radius of a sphere in which we expect a single source:

$$1 = \mathcal{H}_0 \times \frac{4}{3}\pi\hat{r}^3. \tag{9.5}$$

The flux of the source is probabilistic. For a generic source class, the distance to the closest source is not known *a priori*. Therefore, a given source density corresponds to a range of distances where the closest source is likely to exist, and hence a range of fluxes. By setting the 90% C.L. point source sensitivity to the median expected flux from Eqn. 9.3, we can explore the source densities to which IceCube is sensitive. Figure 9.12 shows IceCube's sensitivity to the source density as a function of the declination angle of the closest source, for a source class with an E^{-2} spectrum. Similar to the previous section, we restrict our region of interest to the northern hemisphere ($\delta > -5^\circ$), corresponding to $f_{\mathrm{sky}} = 0.54$ in [194]. The parameter ξ_z defines the redshift evolution for the spatial distribution of the sources. For an E^{-2} spectrum, $\xi_z = 2.4$ for sources following the star formation rate (such as starburst galaxies), while $\xi_z = 3.6$ for AGN [194].

For a class of rare sources characterized by a low source density, the total neutrino flux is split among a relatively small number of sources. While on average the closest source will be far away (hundreds of Mpc for densities of $< 10^{-7}\text{Mpc}^{-3}$), it will still have a high flux because the flux is split among only a few sources. For common sources with a high source density, the closest source is much closer to Earth. However, since the total diffuse flux is split equally (in luminosity) among all sources of this class, the closest source has a faint flux that is harder for IceCube to detect. The sensitivity of the current analysis partially encompasses the source density of blazars, but probing source densities corresponding to starburst galaxies will require significantly more data.

In this model, the source density detectable by IceCube depends on the normalization and spectrum of the total diffuse flux, the fraction of that flux originating from a single extragalactic source class, and the cosmological evolution of this source class. Figure 9.13 shows the sensitivity for different spectral indices. Current point source analyses are sensitive to a larger parameter space if the diffuse flux follows a softer spectrum, similar to the behavior seen in the model-independent analysis in the previous section. On the other hand, if a large fraction of the diffuse flux is Galactic rather than extragalactic (Fig. 9.13, right panel), the range of source densities currently in reach is reduced.

Another assumption of this investigation is that all sources have the same luminosity, a condition rarely realized in the universe. The impact of a more realistic luminosity distribution was explored in [194], where the authors found the flux expected from the closest source increased if the luminosity function was logarithmic instead of a simple delta function. Approaching the problem in a similar manner, we apply the luminosity function of Flat Spectrum Radio Quasars (FSRQs) detected by Fermi [200], finding the distribution of point source fluxes for the closest source increases by a factor of ~ 2.3. This corresponds to roughly a factor of ten increase in source density sensitivity. This makes sense because rarer, brighter sources dominate the behavior of the model. More luminous but rare distant sources are more likely to be detected than closer, dimmer sources. If the closest source is sampled from the tail of the luminosity function, it is more likely to be detected. If instead it has a below average luminosity, one of the next closest sources may be more luminous,

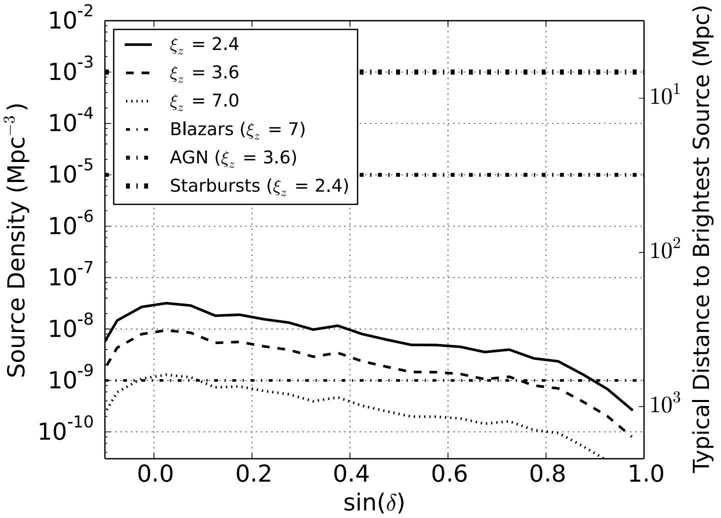

Figure 9.12: IceCube's sensitivity to the density of extragalactic sources comprising the diffuse flux, as a function of the declination angle of the closest source (curves). The ξ_z parameter describes the redshift evolution of the source class. Higher values of ξ_z indicates a stronger evolution with more sources at large distances, which reduces the flux of the closest source and weakens IceCube's source density sensitivity. For comparison, the source density for blazars, AGN, and starburst galaxies are shown as horizontal lines, with their corresponding ξ_z values in the legend.

becoming the brightest source. Similar behavior is observed in simulation-based studies of the sources of ultra-high energy cosmic rays [199].

This exercise is useful to explore IceCube's sensitivity to source classes with general properties. However, for a specific, known source class, a more direct and robust method of discovering neutrino emission is via a stacking analysis, such as those carried out in [133, 142, 147]. The blazar stacking analyses presented in [147] find no evidence of neutrino emission from blazars. The upper limits on the neutrino flux originating from the objects considered are already > 10 times lower than the total diffuse flux. Because blazars are so rare, this constrains the total contribution of this source class. The Fermi telescope has resolved $\sim 50\%$ of the total gamma-ray flux from FSRQs [200]. The upper limits from

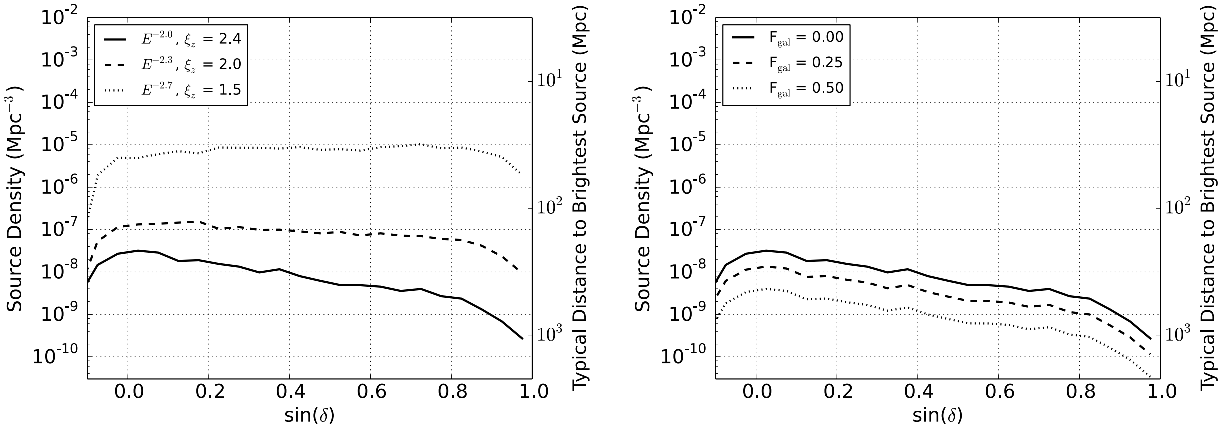

Figure 9.13: Source density sensitivity for different source spectra (left) and different Galactic flux contributions (right). The softer diffuse spectra allowed by the high-energy observations lead to more events at TeV energies, where the point source analysis is sensitive. This increases the source density sensitivity for softer spectra. On the other hand, if a substantial portion of the diffuse flux is Galactic, the total flux budget for extragalactic sources is reduced, weakening the source density sensitivity. In both plots, the source evolution is assumed to follow the star formation rate.

blazar stacking analyses therefore provide a more direct constraint on the proportion of the diffuse flux originating from this source class, assuming basic relationships between neutrino and gamma-ray fluxes. Similarly, the starburst analysis in [147] results in an upper limit > 10 times lower than the diffuse flux level. However, this analysis only utilizes the closest, brightest $\sim$ 100 starburst galaxies. This analysis cannot constrain the total contribution from this source class because starburst galaxies are extremely common and the diffuse neutrino flux could originate from distant starbursts not included in the catalog. Future data from IceCube or a next-generation neutrino telescope may be required to identify the dominant source class, especially if the flux originates from extragalactic objects with high source densities.

Chapter 10

Conclusion

This thesis presented results from three searches for astrophysical neutrino emission from point-like sources. The first analysis applied improved background rejection and event reconstruction techniques to a sample of throughgoing muon tracks. This search was sensitive to TeV – PeV sources in the northern hemisphere and PeV – EeV sources in the southern hemisphere. The second analysis searched for clustering among a sample of high-energy contained-vertex events. This sample, dominated by cascades with $\sim 15^\circ$ angular resolution, contains clear evidence for an astrophysical component of the flux. These events were used to search for clustering anywhere in the sky as well as for emission correlated with the Galactic Plane or a pre-defined source catalog. The third analysis used starting track events to search for point sources, combining the strengths of muon angular resolution and contained-vertex background rejection to target sources emitting below ~PeV energies in the southern hemisphere. This led to a factor of $2 - 10$ improvement in sensitivity for such sources.

All results were consistent with the background-only hypothesis, and no statistically significant evidence for a neutrino point source was found. The resulting upper limits are the most stringent to date for E^{-2} neutrino emission from sources anywhere in the sky, and some flux models for individual sources are now excluded. The analyses have also reached sensitivities comparable to gamma-ray measurements. However, for the majority of sources considered, IceCube is not yet probing flux levels that inform the origin of gamma-ray observations. By comparing the point source limits to the observed diffuse astrophysical

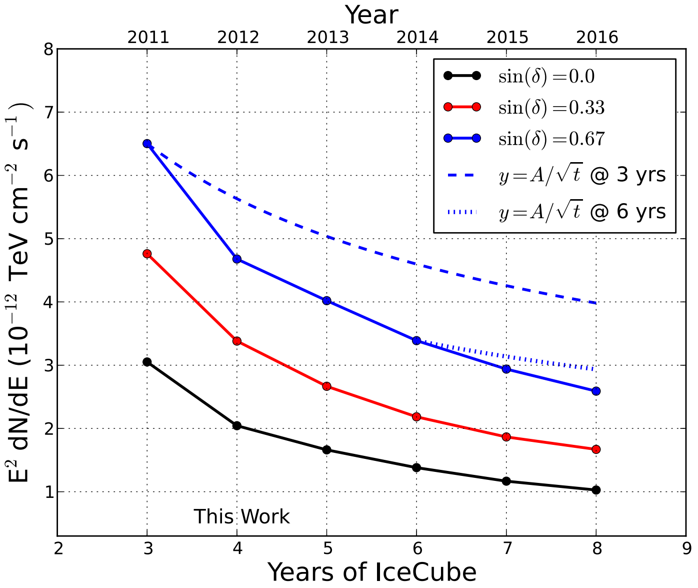

Figure 10.1: IceCube's point source discovery potential as a function of years of data-taking. Since the background rate is relatively low, especially at high energies, the significance improves faster than the $\sqrt{t}$ limit (dashed, dotted lines). Adding four more years of data will lead to a discovery potential two times lower than the analyses presented in this thesis.

neutrino flux, we also constrain the minimum number of neutrino sources and investigate the properties of potential source populations contributing to the diffuse flux.

Additionally, one of the highest energy starting tracks likely originates from a few 100 TeV astrophysical neutrino. While this event alone does not constitute a point source, it is the most significant individual event yet observed that is also well-localized on the sky.

The sources of the high-energy astrophysical neutrinos and the high-energy cosmic rays remain a mystery. Theoretical efforts have shed significant insight on the types of objects capable of generating the observed neutrino flux, and searches targeting these specific models will lead to improved sensitivity. Much will also be gained by simply analyzing more data. IceCube is now in a stable running mode with all 86-strings. As of this writing, two years of data beyond those presented here are already available, waiting to be analyzed. Figure 10.1 shows the estimated point source discovery potential as a function of IceCube's livetime,

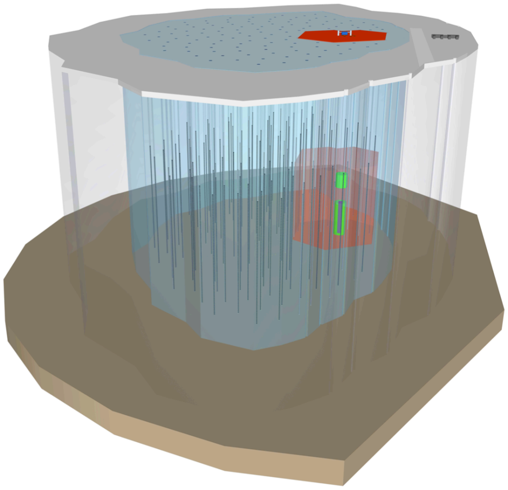

Figure 10.2: Artist's conception of a high-energy extension to IceCube. 120 strings placed 300 m apart (blue) are added to the 86-string IceCube array (red). Such a detector would have a significantly enhanced effective volume above ∼100 TeV.

which will improve by a factor of two In the next 4 years. As shown in Ch. 9, this improvement will either confirm or exclude a number of models. Efforts to improve background rejection and event reconstruction are also underway, and will improve the sensitivity beyond the estimates shown here, especially in the southern hemisphere.

While IceCube's observation of diffuse astrophysical neutrinos marks the start of high-energy neutrino astronomy, future detectors are likely necessary to study neutrino sources in detail. Construction has recently begun on KM3NeT, a cubic kilometer detector in the Mediterranean Sea. This instrument is predicted to reach the sensitivity required to observe TeV Galactic sources in the southern hemisphere. Emission from the SNR RXJ1713-3947, for example, is likely to be observed at 3σ (5σ) after 3.5 (9) years of operation [164].

Extensions to IceCube are also under investigation. The Precision IceCube Next Generation Upgrade (PINGU) is a proposed experiment to extend IceCube/DeepCore to lower energies [201]. Compared to DeepCore, PINGU will have a smaller string spacing and increased photocathode coverage. The primary science goals include determining the neutrino mass hierarchy and studying of neutrino oscillations, dark matter, and supernovae neutrinos.

At high energies, work has focused on developing a detector with a larger string spacing to increase the effective volume. Such an experiment could include an additional ~ 100 strings spaced 240 m apart to increase the muon effective area by a factor of $3-5$ (Figure 10.2). Such a detector, optimized for $\gtrsim 100\,\mathrm{TeV}$ energies, would enable a precision measurement of the diffuse energy spectrum using cascades while astrophysical sources could be identified with tracks. An enhanced surface array could also veto downgoing muon backgrounds, increasing expected signal rates and potentially providing a background-free data sample in the southern hemisphere. The observation of the first high-energy astrophysical neutrinos is a milestone for neutrino astronomy, and innovative techniques will continue to be required to discover the origin of this flux.

LIST OF REFERENCES

[1] W. Pauli. In *Rapports du Septieme Conseil de Physique Solvay*, Gauthier-Villars,Paris, 1934.

[2] C. L. Cowan, Jr., F. Reines, F. B. Harrison, H. W. Kruse, and A. D. McGuire. Detection of the Free Neutrino: A Confirmation. *Science*, 124:103–104, July 1956. `doi:10.1126/science.124.3212.103`.

[3] C. Spiering. Towards high-energy neutrino astronomy. A historical review. *European Physical Journal H*, 37:515–565, August 2012. `arXiv:1207.4952`, `doi:10.1140/epjh/e2012-30014-2`.

[4] John N. Bahcall and R. Davis. Solar Neutrinos - a Scientific Puzzle. *Science*, 191:264–267, 1976. `doi:10.1126/science.191.4224.264`.

[5] Y. Fukuda et al. Evidence for oscillation of atmospheric neutrinos. *Phys.Rev.Lett.*, 81:1562–1567, 1998. `arXiv:hep-ex/9807003`, `doi:10.1103/PhysRevLett.81.1562`.

[6] Q.R. Ahmad et al. Direct evidence for neutrino flavor transformation from neutral current interactions in the Sudbury Neutrino Observatory. *Phys.Rev.Lett.*, 89:011301, 2002. `arXiv:nucl-ex/0204008`, `doi:10.1103/PhysRevLett.89.011301`.

[7] W. D. Arnett, J. N. Bahcall, R. P. Kirshner, and S. E. Woosley. Supernova 1987A. *Annu. Rev. Astron. Astrophys.*, 27:629–700, 1989. `doi:10.1146/annurev.aa.27.090189.003213`.

[8] J. G. Learned and K. Mannheim. High-Energy Neutrino Astrophysics. *Annual Review of Nuclear and Particle Science*, 50:679–749, 2000. `doi:10.1146/annurev.nucl.50.1.679`.

[9] F. Halzen and D. Hooper. High-energy neutrino astronomy: the cosmic ray connection. *Reports on Progress in Physics*, 65:1025–1078, July 2002. `arXiv:astro-ph/0204527`, `doi:10.1088/0034-4885/65/7/201`.

[10] Julia K. Becker. High-energy neutrinos in the context of multimessenger physics. *Phys.Rept.*, 458:173–246, 2008. `arXiv:0710.1557`, `doi:10.1016/j.physrep.2007.10.006`.

[11] Luis A. Anchordoqui, Vernon Barger, Ilias Cholis, Haim Goldberg, Dan Hooper, et al. Cosmic Neutrino Pevatrons: A Brand New Pathway to Astronomy, Astrophysics, and Particle Physics. *Journal of High Energy Astrophysics*, 1-2:1–30, 2014. `arXiv:1312.6587`, `doi:10.1016/j.jheap.2014.01.001`.

[12] M.G. Aartsen et al. Evidence for High-Energy Extraterrestrial Neutrinos at the IceCube Detector. *Science*, 342(6161):1242856, 2013. `arXiv:1311.5238`, `doi:10.1126/science.1242856`.

[13] M.G. Aartsen et al. Observation of High-Energy Astrophysical Neutrinos in Three Years of IceCube Data. 2014. `arXiv:1405.5303`.

[14] V. F. Hess. Über Beobachtungen der durchdringenden Strahlung bei sieben Freiballonfahrten. *Phys. Z.*, 13:1084–1091, 1912.

[15] Antoine Letessier-Selvon and Todor Stanev. Ultrahigh Energy Cosmic Rays. *Rev.Mod.Phys.*, 83:907–942, 2011. `arXiv:1103.0031`, `doi:10.1103/RevModPhys.83.907`.

[16] J. J. Beatty and S. Westerhoff. The Highest-Energy Cosmic Rays. *Annual Review of Nuclear and Particle Science*, 59:319–345, November 2009. `doi:10.1146/annurev.nucl.58.110707.171154`.

[17] K. Kotera and A. V. Olinto. The Astrophysics of Ultrahigh-Energy Cosmic Rays. *Annual Review of Astron and Astrophys*, 49:119–153, September 2011. `arXiv:1101.4256`, `doi:10.1146/annurev-astro-081710-102620`.

[18] A. M. Hillas. The Origin of Ultra-High-Energy Cosmic Rays. *Annu. Rev. Astron. Astrophys.*, 22:425–444, 1984. `doi:10.1146/annurev.aa.22.090184.002233`.

[19] P. Abreu et al. Anisotropy and chemical composition of ultra-high energy cosmic rays using arrival directions measured by the Pierre Auger Observatory. *JCAP*, 1106:022, 2011. `arXiv:1106.3048`, `doi:10.1088/1475-7516/2011/06/022`.

[20] R.U. Abbasi et al. Indications of Intermediate-Scale Anisotropy of Cosmic Rays with Energy Greater Than 57 EeV in the Northern Sky Measured with the Surface Detector of the Telescope Array Experiment. *Astrophys.J.*, 790:L21, 2014. `arXiv:1404.5890`, `doi:10.1088/2041-8205/790/2/L21`.

[21] R.U. Abbasi et al. First observation of the Greisen-Zatsepin-Kuzmin suppression. *Phys.Rev.Lett.*, 100:101101, 2008. `arXiv:astro-ph/0703099`, `doi:10.1103/PhysRevLett.100.101101`.

[22] Kenneth Greisen. End to the cosmic-ray spectrum? *Phys. Rev. Lett.*, 16:748–750, Apr 1966. URL: `http://link.aps.org/doi/10.1103/PhysRevLett.16.748`, `doi:10.1103/PhysRevLett.16.748`.

[23] G. T. Zatsepin and V. A. Kuz'min. Upper Limit of the Spectrum of Cosmic Rays. *Soviet J. Exp. Theor. Phys.*, 4:78, August 1966.

[24] E. Fermi. On the Origin of the Cosmic Radiation. *Phys. Rev.*, 75:1169–1174, Apr 1949. `doi:10.1103/PhysRev.75.1169`.

[25] A. R. Bell. The non-linear self-regulation of cosmic ray acceleration at shocks. *Monthly Notices of the Royal Astronomical Society*, 225(3):615–626, 1987. `doi:10.1093/mnras/225.3.615`.

[26] M. Longair. *High Energy Astrophysics*. Cambridge University Press, 2011.

[27] M A Malkov and L O'C Drury. Nonlinear theory of diffusive acceleration of particles by shock waves. *Reports on Progress in Physics*, 64(4):429, 2001. URL: `http://stacks.iop.org/0034-4885/64/i=4/a=201`.

[28] Luis Anchordoqui, Thomas Cantzon Paul, Stephen Reucroft, and John Swain. Ultrahigh-energy cosmic rays: The State of the art before the Auger Observatory. *Int.J.Mod.Phys.*, A18:2229–2366, 2003. `arXiv:hep-ph/0206072`, `doi:10.1142/S0217751X03013879`.

[29] R. Abbasi et al. Measurement of the Anisotropy of Cosmic Ray Arrival Directions with IceCube. *Astrophys.J.*, 718:L194, 2010. `arXiv:1005.2960`, `doi:10.1088/2041-8205/718/2/L194`.

[30] B. Bartoli et al. Medium scale anisotropy in the TeV cosmic ray flux observed by ARGO-YBJ. *Phys.Rev.*, D88(8):082001, 2013. `arXiv:1309.6182`, `doi:10.1103/PhysRevD.88.082001`.

[31] G. R. Farrar, R. Jansson, I. J. Feain, and B. M. Gaensler. Galactic magnetic deflections and Centaurus A as a UHECR source. *J. Cosmol. Astropart. Phys.*, 1:23, January 2013. `arXiv:1211.7086`, `doi:10.1088/1475-7516/2013/01/023`.

[32] M. Ackermann et al. Detection of the Characteristic Pion-Decay Signature in Supernova Remnants. *Science*, 339(6121):807–811, February 2013. `arXiv:1302.3307`, `doi:10.1126/science.1231160`.

[33] Tova M. Yoast-Hull, J.S. Gallagher III, Ellen G. Zweibel, and John E. Everett. Active Galactic Nuclei, Neutrinos, and Interacting Cosmic Rays in NGC 253 and NGC 1068. *Astrophys.J.*, 780:137, 2014. `arXiv:1311.5586`, `doi:10.1088/0004-637X/780/2/137`.

[34] V.A. Acciari, E. Aliu, T. Arlen, T. Aune, M. Beilicke, et al. Discovery of TeV Gamma Ray Emission from Tycho's Supernova Remnant. *Astrophys.J.*, 730:L20, 2011. `arXiv:1102.3871`, `doi:10.1088/2041-8205/730/2/L20`.

[35] E.G. Berezhko and H.J. Volk. Theory of cosmic ray production in the supernova remnant rx j1713.7-3946. *Astron.Astrophys.*, 2006. `arXiv:astro-ph/0602177`.

[36] A. Franceschini, G. Rodighiero, and M. Vaccari. Extragalactic optical-infrared background radiation, its time evolution and the cosmic photon-photon opacity. *Astron. Astrophys.*, 487:837–852, September 2008. `arXiv:0805.1841`, `doi:10.1051/0004-6361:200809691`.

[37] H. Athar, M. Jezabek, and O. Yasuda. Effects of neutrino mixing on high-energy cosmic neutrino flux. *Phys.Rev.*, D62:103007, 2000. `arXiv:hep-ph/0005104`, `doi:10.1103/PhysRevD.62.103007`.

[38] Markus Ahlers and Kohta Murase. Probing the Galactic Origin of the IceCube Excess with Gamma-Rays. 2013. `arXiv:1309.4077`.

[39] S. P. Reynolds. Supernova Remnants at High Energy. *Annu. Rev. Astron. Astrophys.*, 46:89–126, September 2008. `doi:10.1146/annurev.astro.46.060407.145237`.

[40] W. Baade and F. Zwicky. Cosmic Rays from Super-novae. *Proceedings of the National Academy of Science*, 20:259–263, May 1934. `doi:10.1073/pnas.20.5.259`.

[41] J. Alvarez-Muniz and F. Halzen. Possible high-energy neutrinos from the cosmic accelerator RX J1713.7-3946. *Astrophys.J.*, 576:L33–L36, 2002. `arXiv:astro-ph/0205408`, `doi:10.1086/342978`.

[42] Matthew D. Kistler and John F. Beacom. Guaranteed and Prospective Galactic TeV Neutrino Sources. *Phys.Rev.*, D74:063007, 2006. `arXiv:astro-ph/0607082`, `doi:10.1103/PhysRevD.74.063007`.

[43] Alexander Kappes, Jim Hinton, Christian Stegmann, and Felix A. Aharonian. Potential Neutrino Signals from Galactic Gamma-Ray Sources. *Astrophys.J.*, 656:870–896, 2007. `arXiv:astro-ph/0607286`, `doi:10.1086/508936,10.1086/518161`.

[44] Matthias Mandelartz and Julia Becker Tjus. A statistical study of Galactic SNR source spectra detected at >GeV energies. 2013. `arXiv:1301.2437`.

[45] Vincenzo Cavasinni, Dario Grasso, and Luca Maccione. TeV Neutrinos from Super-Nova Remnants embedded in Giant Molecular Clouds. *Astropart.Phys.*, 26:41–49, 2006. `arXiv:astro-ph/0604004`, `doi:10.1016/j.astropartphys.2006.04.009`.

[46] F. Vissani, F. Aharonian, and N. Sahakyan. On the detectability of high-energy galactic neutrino sources. *Astroparticle Physics*, 34:778–783, May 2011. `arXiv:1101.4842`, `doi:10.1016/j.astropartphys.2011.01.011`.

[47] Patrizia A. Caraveo. Gamma-ray pulsar revolution. *Annual Review of Astronomy and Astrophysics*, 52(1), 2014. `arXiv:1312.2913`, `doi:10.1146/annurev-astro-081913-035948`.

[48] W. Bednarek and R.J. Protheroe. Gamma-rays and neutrinos from the Crab Nebula produced by pulsar accelerated nuclei. *Phys.Rev.Lett.*, 79:2616–2619, 1997. `arXiv:astro-ph/9704186`, `doi:10.1103/PhysRevLett.79.2616`.

[49] Pasquale Blasi, Richard I. Epstein, and Angela V. Olinto. Ultrahigh-energy cosmic rays from young neutron star winds. *Astrophys.J.*, 533:L123, 2000. `arXiv:astro-ph/9912240`, `doi:10.1086/312626`.

[50] Bennett Link and Fiorella Burgio. TeV mu neutrinos from young neutron stars. *Phys.Rev.Lett.*, 94:181101, 2005. `arXiv:astro-ph/0412520`, `doi:10.1103/PhysRevLett.94.181101`.

[51] Elena Amato, Dafne Guetta, and Pasquale Blasi. Signatures of high energy protons in pulsar winds. *Astron.Astrophys.*, 402:827–836, 2003. `arXiv:astro-ph/0302121`, `doi:10.1051/0004-6361:20030279`.

[52] K. Fang, K. Kotera, and A. V. Olinto. Newly Born Pulsars as Sources of Ultrahigh Energy Cosmic Rays. *Astrophys. J.*, 750:118, May 2012. `arXiv:1201.5197`, `doi:10.1088/0004-637X/750/2/118`.

[53] Ke Fang, Kumiko Kotera, Kohta Murase, and Angela V. Olinto. A decisive test for the young pulsar origin of ultrahigh energy cosmic rays with IceCube. 2013. `arXiv:1311.2044`.

[54] F. Aharonian et al. Discovery of very high energy gamma-rays associated with an x-ray binary. *Science*, 309:746–749, 2005. `arXiv:astro-ph/0508298`, `doi:10.1126/science.1113764`.

[55] C. Distefano, D. Guetta, E. Waxman, and A. Levinson. Neutrino flux predictions for known galactic microquasars. *Astrophys.J.*, 575:378–383, 2002. `arXiv:astro-ph/0202200`, `doi:10.1086/341144`.

[56] Hugo R. Christiansen, Mariana Orellana, and Gustavo E. Romero. High-energy neutrino emission from x-ray binaries. *Phys.Rev.*, D73:063012, 2006. `arXiv:astro-ph/0509214`, `doi:10.1103/PhysRevD.73.063012`.

[57] Diego F. Torres and Francis Halzen. LS I +61 303 as a potential neutrino source on the light of MAGIC results. *Astropart.Phys.*, 27:500–508, 2007. `arXiv:astro-ph/0607368`, `doi:10.1016/j.astropartphys.2007.02.004`.

[58] N. Sahakyan, G. Piano, and M. Tavani. Hadronic Gamma-Ray and Neutrino Emission from Cygnus X-3. *Astrophys.J.*, 780:29, 2014. `arXiv:1310.7805`, `doi:10.1088/0004-637X/780/1/29`.

[59] John F. Beacom and Julian Candia. Shower power: Isolating the prompt atmospheric neutrino flux using electron neutrinos. *JCAP*, 0411:009, 2004. `arXiv:hep-ph/0409046`, `doi:10.1088/1475-7516/2004/11/009`.

[60] G. Ingelman and M. Thunman. Particle production in the interstellar medium. 1996. `arXiv:hep-ph/9604286`.

[61] M. Ackermann et al. Fermi-LAT Observations of the Diffuse Gamma-Ray Emission: Implications for Cosmic Rays and the Interstellar Medium. *Astrophys.J.*, 750:3, 2012. `arXiv:1202.4039`, `doi:10.1088/0004-637X/750/1/3`.

[62] A.A. Abdo, B. Allen, T. Aune, D. Berley, E. Blaufuss, et al. A Measurement of the Spatial Distribution of Diffuse TeV Gamma Ray Emission from the Galactic Plane with Milagro. *Astrophys.J.*, 688:1078–1083, 2008. `arXiv:0805.0417`.

[63] M. Su, T. R. Slatyer, and D. P. Finkbeiner. Giant Gamma-ray Bubbles from Fermi-LAT: Active Galactic Nucleus Activity or Bipolar Galactic Wind? *Astrophys. J.*, 724:1044–1082, December 2010. `arXiv:1005.5480`, `doi:10.1088/0004-637X/724/2/1044`.

[64] E. Carretti, R. M. Crocker, L. Staveley-Smith, M. Haverkorn, C. Purcell, B. M. Gaensler, G. Bernardi, M. J. Kesteven, and S. Poppi. Giant magnetized outflows from the centre of the Milky Way. *Nature*, 493:66–69, January 2013. `arXiv:1301.0512`, `doi:10.1038/nature11734`.

[65] Roland M. Crocker, Geoffrey V. Bicknell, Ettore Carretti, Alex S. Hill, and Ralph S. Sutherland. A Revised Nuclear Star Formation Driven, Hadronic Model for the Fermi Bubbles. 2013. `arXiv:1312.0692`.

[66] C. Lunardini and S. Razzaque. High Energy Neutrinos from the Fermi Bubbles. *Physical Review Letters*, 108(22):221102, June 2012. `arXiv:1112.4799`, `doi:10.1103/PhysRevLett.108.221102`.

[67] Cecilia Lunardini, Soebur Razzaque, Kristopher T. Theodoseau, and Lili Yang. Neutrino Events at IceCube and the Fermi Bubbles. 2013. `arXiv:1311.7188`.

[68] Yutaka Fujita, Yutaka Ohira, and Ryo Yamazaki. The Fermi Bubbles as a Scaled-up Version of Supernova Remnants. *Astrophys.J.*, 775:L20, 2013. `arXiv:1308.5228`, `doi:10.1088/2041-8205/775/1/L20`.

[69] S. Adrian-Martinez et al. A Search for Neutrino Emission from the Fermi Bubbles with the ANTARES Telescope. *Eur.Phys.J.*, C74:2701, 2014. `arXiv:1308.5260`, `doi:10.1140/epjc/s10052-013-2701-6`.

[70] Gianfranco Bertone, Dan Hooper, and Joseph Silk. Particle dark matter: Evidence, candidates and constraints. *Phys.Rept.*, 405:279–390, 2005. `arXiv:hep-ph/0404175`, `doi:10.1016/j.physrep.2004.08.031`.

[71] V. Gammaldi, J.A.R. Cembranos, A. de la Cruz-Dombriz, R.A. Lineros, and A.L. Maroto. Gamma-ray and neutrino fluxes from Heavy Dark Matter in the Galactic Center. 2014. `arXiv:1404.2067`.

[72] Anindya Datta, Daniele Fargion, and Barbara Mele. SUSY resonances from UHE neutralinos in neutrino telescopes and in the sky. *JHEP*, 0509:007, 2005. `arXiv:hep-ph/0410176`, `doi:10.1088/1126-6708/2005/09/007`.

[73] Brian Feldstein, Alexander Kusenko, Shigeki Matsumoto, and Tsutomu T. Yanagida. Neutrinos at IceCube from Heavy Decaying Dark Matter. *Phys.Rev.*, D88(1):015004, 2013. `arXiv:1303.7320`, `doi:10.1103/PhysRevD.88.015004`.

[74] H. J. Völk, E. G. Berezhko, and L. T. Ksenofontov. Internal dynamics and particle acceleration in Tycho's SNR. *Astron. Astrophys.*, 483:529–535, May 2008. `arXiv:0803.1403`, `doi:10.1051/0004-6361:20079337`.

[75] P. L. Biermann and P. A. Strittmatter. Synchrotron emission from shock waves in active galactic nuclei. *Astrophys. J.*, 322:643–649, November 1987. `doi:10.1086/165759`.

[76] D. Kazanas and D. C. Ellison. The central engine of quasars and active galactic nuclei Hadronic interactions of shock-accelerated relativistic protons. *Astrophys. J.*, 304:178–187, May 1986. `doi:10.1086/164152`.

[77] F. W. Stecker, C. Done, M. H. Salamon, and P. Sommers. High-energy neutrinos from active galactic nuclei. *Phys. Rev. Lett.*, 66:2697–2700, May 1991. URL: `http://link.aps.org/doi/10.1103/PhysRevLett.66.2697`, `doi:10.1103/PhysRevLett.66.2697`.

[78] Eli Waxman and John N. Bahcall. High-energy neutrinos from astrophysical sources: An Upper bound. *Phys.Rev.*, D59:023002, 1999. `arXiv:hep-ph/9807282`, `doi:10.1103/PhysRevD.59.023002`.

[79] K. Mannheim. Possible production of high-energy gamma-rays from proton acceleration in the extragalactic radio source Markarian 501. *Science*, 279:684, 1998. `arXiv:astro-ph/9803241`, `doi:10.1126/science.279.5351.684`.

[80] W. Essey, O. E. Kalashev, A. Kusenko, and J. F. Beacom. Secondary Photons and Neutrinos from Cosmic Rays Produced by Distant Blazars. *Physical Review Letters*, 104(14):141102, April 2010. `arXiv:0912.3976`, `doi:10.1103/PhysRevLett.104.141102`.

[81] Oleg E. Kalashev, Alexander Kusenko, and Warren Essey. PeV neutrinos from intergalactic interactions of cosmic rays emitted by active galactic nuclei. *Phys.Rev.Lett.*, 111(4):041103, 2013. `arXiv:1303.0300`, `doi:10.1103/PhysRevLett.111.041103`.

[82] Kohta Murase, Yoshiyuki Inoue, and Charles D. Dermer. Diffuse Neutrino Intensity from the Inner Jets of Active Galactic Nuclei: Impacts of External Photon Fields and the Blazar Sequence. *Phys.Rev.*, D90:023007, 2014. `arXiv:1403.4089`, `doi:10.1103/PhysRevD.90.023007`.

[83] J. C. Mihos and L. Hernquist. Gasdynamics and Starbursts in Major Mergers. *Astrophys. J.*, 464:641, June 1996. `arXiv:astro-ph/9512099`, `doi:10.1086/177353`.

[84] B. C. Lacki, T. A. Thompson, E. Quataert, A. Loeb, and E. Waxman. On the GeV and TeV Detections of the Starburst Galaxies M82 and NGC 253. *Astrophys. J.*, 734:107, June 2011. `arXiv:1003.3257`, `doi:10.1088/0004-637X/734/2/107`.

[85] Abraham Loeb and Eli Waxman. The Cumulative background of high energy neutrinos from starburst galaxies. *JCAP*, 0605:003, 2006. `arXiv:astro-ph/0601695`, `doi:10.1088/1475-7516/2006/05/003`.

[86] Kohta Murase, Markus Ahlers, and Brian C. Lacki. Testing the Hadronuclear Origin of PeV Neutrinos Observed with IceCube. *Phys.Rev.*, D88(12):121301, 2013. `arXiv:1306.3417`, `doi:10.1103/PhysRevD.88.121301`.

[87] Gustavo E. Romero and Diego F. Torres. Signatures of hadronic cosmic rays in starbursts? High-energy photons and neutrinos from NGC 253. *Astrophys.J.*, 586:L33–L36, 2003. `arXiv:astro-ph/0302149`, `doi:10.1086/374654`.

[88] Tova M. Yoast-Hull, John E. Everett, J.S. Gallagher, and Ellen G. Zweibel. Winds, Clumps, and Interacting Cosmic Rays in M82. *Astrophys.J.*, 768:53, 2013. `arXiv:1303.4305`, `doi:10.1088/0004-637X/768/1/53`.

[89] H. J. Völk, F. A. Aharonian, and D. Breitschwerdt. The Nonthermal Energy Content and Gamma-Ray Emission of Starburst Galaxies and Clusters of Galaxies. *Space Science Reviews*, 75:279–297, January 1996. `doi:10.1007/BF00195040`.

[90] Francesco Miniati, Dongsu Ryu, Hyesung Kang, T.W. Jones, Renyue Cen, et al. Properties of cosmic shock waves in large scale structure formation. *Astrophys.J.*, 542:608–621, 2000. `arXiv:astro-ph/0005444`, `doi:10.1086/317027`.

[91] Kohta Murase, Susumu Inoue, and Shigehiro Nagataki. Cosmic Rays Above the Second Knee from Clusters of Galaxies and Associated High-Energy Neutrino Emission. *Astrophys.J.*, 689:L105, 2008. `arXiv:0805.0104`, `doi:10.1086/595882`.

[92] Brandon Wolfe, Fulvio Melia, Roland M. Crocker, and Raymond R. Volkas. Neutrinos and Gamma Rays from Galaxy Clusters. *Astrophys.J.*, 687:193–201, 2008. `arXiv:0807.0794`, `doi:10.1086/591723`.

[93] Peter Meszaros. Gamma-Ray Bursts. *Rept.Prog.Phys.*, 69:2259–2322, 2006. `arXiv:astro-ph/0605208`, `doi:10.1088/0034-4885/69/8/R01`.

[94] Dafne Guetta, D. Hooper, J. Alvarez-Muniz, F. Halzen, and E. Reuveni. Neutrinos from individual gamma-ray bursts in the BATSE catalog. *Astropart.Phys.*, 20:429–455, 2004. `arXiv:astro-ph/0302524`, `doi:10.1016/S0927-6505(03)00211-1`.

[95] Eli Waxman and John Bahcall. High energy neutrinos from cosmological gamma-ray burst fireballs. *Phys. Rev. Lett.*, 78:2292–2295, Mar 1997. URL: `http://link.aps.org/doi/10.1103/PhysRevLett.78.2292`, `doi:10.1103/PhysRevLett.78.2292`.

[96] M. Ahlers, M. C. Gonzalez-Garcia, and F. Halzen. GRBs on probation: Testing the UHE CR paradigm with IceCube. *Astroparticle Physics*, 35:87–94, September 2011. `arXiv:1103.3421`, `doi:10.1016/j.astropartphys.2011.05.008`.

[97] S. Hümmer, P. Baerwald, and W. Winter. Neutrino Emission from Gamma-Ray Burst Fireballs, Revised. *Physical Review Letters*, 108(23):231101, June 2012. `arXiv:1112.1076`, `doi:10.1103/PhysRevLett.108.231101`.

[98] Kohta Murase and Kunihito Ioka. TeVPeV Neutrinos from Low-Power Gamma-Ray Burst Jets inside Stars. *Phys.Rev.Lett.*, 111(12):121102, 2013. `arXiv:1306.2274`, `doi:10.1103/PhysRevLett.111.121102`.

[99] R. Abbasi et al. An absence of neutrinos associated with cosmic-ray acceleration in γ-ray bursts. *Nature*, 484:351–353, 2012. `arXiv:1204.4219`, `doi:10.1038/nature11068`.

[100] V. S. Beresinsky and G. T. Zatsepin. Cosmic rays at ultra high energies (neutrino?). *Physics Letters B*, 28:423–424, January 1969. `doi:10.1016/0370-2693(69)90341-4`.

[101] David Seckel and Todor Stanev. Neutrinos: The Key to UHE cosmic rays. *Phys.Rev.Lett.*, 95:141101, 2005. `arXiv:astro-ph/0502244`, `doi:10.1103/PhysRevLett.95.141101`.

[102] K. Kotera, D. Allard, and A. V. Olinto. Cosmogenic neutrinos: parameter space and detectabilty from PeV to ZeV. *J. Cosmol. Astropart. Phys.*, 10:13, October 2010. `arXiv:1009.1382`, `doi:10.1088/1475-7516/2010/10/013`.

[103] M. Ahlers and F. Halzen. Minimal cosmogenic neutrinos. *Phys. Rev. D*, 86(8):083010, October 2012. `arXiv:1208.4181`, `doi:10.1103/PhysRevD.86.083010`.

[104] J. Beringer et al. Review of Particle Physics (RPP). *Phys.Rev.*, D86:010001, 2012. `doi:10.1103/PhysRevD.86.010001`.

[105] Raj Gandhi, Chris Quigg, Mary Hall Reno, and Ina Sarcevic. Ultrahigh-energy neutrino interactions. *Astropart.Phys.*, 5:81–110, 1996. `arXiv:hep-ph/9512364`, `doi:10.1016/0927-6505(96)00008-4`.

[106] A. Cooper-Sarkar and S. Sarkar. Predictions for high energy neutrino cross-sections from the ZEUS global PDF fits. *Journal of High Energy Physics*, 1:75, January 2008. `arXiv:0710.5303`, `doi:10.1088/1126-6708/2008/01/075`.

[107] Sheldon L. Glashow. Resonant scattering of antineutrinos. *Phys. Rev.*, 118:316–317, Apr 1960. URL: `http://link.aps.org/doi/10.1103/PhysRev.118.316`, `doi:10.1103/PhysRev.118.316`.

[108] Dmitry Chirkin and Wolfgang Rhode. Propagating leptons through matter with muon monte carlo (mmc). 2004. `arXiv:arXiv:hep-ph/0407075`.

[109] C. Kopper. *Performance Studies for the KM3NeT Neutrino Telescope*. PhD thesis, Friedrich-Alexander-Universität Erlangen-Nürnberg, 2010.

[110] C. Wiebusch. *The Detection of Faint Light in Deep Underwater Neutrino Telescopes*. PhD thesis, RWTH Aachen University, 1995.

[111] J. van Santen. Markov-chain monte-carlo reconstruction for cascade-like events in icecube. Master's thesis, Humboldt-Universität zu Berlin, 2010.

[112] P. A. Čerenkov. Visible radiation produced by electrons moving in a medium with velocities exceeding that of light. *Phys. Rev.*, 52:378–379, Aug 1937. URL: `http://link.aps.org/doi/10.1103/PhysRev.52.378`, `doi:10.1103/PhysRev.52.378`.

[113] I. Frank and I. Tamm. Coherent radiation of fast electrons in a medium. *Doklady Akad. Nauk SSSR*, 14:107, 1937.

[114] T. Gaisser. *Cosmic Rays and Particle Physics*. Cambridge University Press, 1991.

[115] M. Honda, T. Kajita, K. Kasahara, S. Midorikawa, and T. Sanuki. Calculation of atmospheric neutrino flux using the interaction model calibrated with atmospheric muon data. *Physical Review D*, 75(4):043006, February 2007. `arXiv:arXiv:astro-ph/0611418`, `doi:10.1103/PhysRevD.75.043006`.

[116] R. Enberg, M. H. Reno, and I. Sarcevic. Prompt neutrino fluxes from atmospheric charm. *Physical Review D*, 78(4):043005, August 2008. `arXiv:0806.0418`, `doi:10.1103/PhysRevD.78.043005`.

[117] A. Achterberg et al. First Year Performance of The IceCube Neutrino Telescope. *Astropart.Phys.*, 26:155–173, 2006. `arXiv:astro-ph/0604450`, `doi:10.1016/j.astropartphys.2006.06.007`.

[118] R. Abbasi et al. Calibration and Characterization of the IceCube Photomultiplier Tube. *Nucl.Instrum.Meth.*, A618:139–152, 2010. `arXiv:1002.2442`, `doi:10.1016/j.nima.2010.03.102`.

[119] R. Abbasi et al. The IceCube Data Acquisition System: Signal Capture, Digitization, and Timestamping. *Nucl.Instrum.Meth.*, A601:294–316, 2009. `arXiv:0810.4930`, `doi:10.1016/j.nima.2009.01.001`.

[120] R. Abbasi et al. The Design and Performance of IceCube DeepCore. *Astropart.Phys.*, 35:615–624, 2012. `arXiv:1109.6096`, `doi:10.1016/j.astropartphys.2012.01.004`.

[121] M. Ackermann et al. Optical properties of deep glacial ice at the South Pole. *Journal of Geophysical Research (Atmospheres)*, 111:13203, July 2006. `doi:10.1029/2005JD006687`.

[122] M.G. Aartsen et al. Measurement of South Pole ice transparency with the IceCube LED calibration system. *Nucl.Instrum.Meth.*, A711:73–89, 2013. `arXiv:1301.5361`, `doi:10.1016/j.nima.2013.01.054`.

[123] M.G. Aartsen et al. South Pole Glacial Climate Reconstruction from Multi-Borehole Laser Particulate Stratigraphy. *Journal of Glaciology*, 59(218):1117, 2013. `doi:10.3189/2013JoG13J068`.

[124] M.G. Aartsen et al. The IceCube Neutrino Observatory Part VI: Ice Properties, Reconstruction and Future Developments. 2013. `arXiv:1309.7010`.

[125] M.G. Aartsen et al. Energy Reconstruction Methods in the IceCube Neutrino Telescope. *JINST*, 9:P03009, 2014. `arXiv:1311.4767`, `doi:10.1088/1748-0221/9/03/P03009`.

[126] M.G. Aartsen, R. Abbasi, Y. Abdou, M. Ackermann, J. Adams, et al. Improvement in Fast Particle Track Reconstruction with Robust Statistics. *Nucl.Instrum.Meth.*, A736:143–149, 2014. `arXiv:1308.5501`, `doi:10.1016/j.nima.2013.10.074`.

[127] J. Ahrens et al. Muon track reconstruction and data selection techniques in AMANDA. *Nucl.Instrum.Meth.*, A524:169–194, 2004. `arXiv:astro-ph/0407044`, `doi:10.1016/j.nima.2004.01.065`.

[128] F. James and M. Roos. Minuit - a system for function minimization and analysis of the parameter errors and correlations. *Computer Physics Communications*, 10:343–367, December 1975. `doi:10.1016/0010-4655(75)90039-9`.

[129] D. Pandel. Bestimmung von Wasser- und Detektorparametern und Rekonstruktion von Myonen bis 100 TeV mit dem Baikal-Neutrinoteleskop NT-72. Diploma Thesis, Humboldt-Universität zu Berlin, 1996.

[130] Johan Lundberg, P. Miocinovic, T. Burgess, J. Adams, S. Hundertmark, et al. Light tracking for glaciers and oceans: Scattering and absorption in heterogeneous media with Photonics. *Nucl.Instrum.Meth.*, A581:619–631, 2007. `arXiv:astro-ph/0702108`, `doi:10.1016/j.nima.2007.07.143`.

[131] Dmitry Chirkin. Photon tracking with GPUs in IceCube. *Nucl.Instrum.Meth.*, A725:141–143, 2013. `doi:10.1016/j.nima.2012.11.170`.

[132] Nathan Whitehorn, Jakob van Santen, and Sven Lafebre. Penalized Splines for Smooth Representation of High-dimensional Monte Carlo Datasets. *Comput.Phys.Commun.*, 184:2214–2220, 2013. `arXiv:1301.2184`, `doi:10.1016/j.cpc.2013.04.008`.

[133] R. Abbasi et al. Time-Integrated Searches for Point-like Sources of Neutrinos with the 40-String IceCube Detector. *Astrophys.J.*, 732:18, 2011. `arXiv:1012.2137`, `doi:10.1088/0004-637X/732/1/18`.

[134] Till Neunhoffer. Estimating the angular resolution of tracks in neutrino telescopes based on a likelihood analysis. *Astropart.Phys.*, 25:220–225, 2006. `arXiv:astro-ph/0403367`, `doi:10.1016/j.astropartphys.2006.01.002`.

[135] K. M. Gorski et al. HEALPix – a Framework for High Resolution Discretization, and Fast Analysis of Data Distributed on the Sphere. *Astrophys. J.*, 622:759–771, 2005. `arXiv:astro-ph/0409513`, `doi:10.1086/427976`.

[136] D. Heck, J. Knapp, J.N. Capdevielle, G. Schatz, and T. Thouw. CORSIKA: A Monte Carlo Code to Simulate Extensive Air Showers. Technical Report FZKA 6019, Forschungszentrum Karlsruhe, 1998.

[137] Askhat Gazizov and Marek P. Kowalski. ANIS: High energy neutrino generator for neutrino telescopes. *Comput.Phys.Commun.*, 172:203–213, 2005. `arXiv:astro-ph/0406439`, `doi:10.1016/j.cpc.2005.03.113`.

[138] J. P. Huelss. *Search for Neutrinos from the Direction of the Galactic Center with the IceCube Neutrino Telescope.* PhD thesis, RWTH Aachen University, 2010. URL: `http://www.physik.rwth-aachen.de/fileadmin/user_upload/www_physik/Institute/Inst_3B/Forschung/IceCube/publications/diss_JPH.pdf`.

[139] Ahn, E.-J. and others. Cosmic-Ray Interaction Event Generator SIBYLL 2.1. *Phys. Rev. D*, 80:094003, 2009. `arXiv:0906.4113`, `doi:10.1103/PhysRevD.80.094003`.

[140] S. Ostapchenko. Monte carlo treatment of hadronic interactions in enhanced pomeron scheme: Qgsjet-ii model. *Phys. Rev. D*, 83:014018, Jan 2011. URL: `http://link.aps.org/doi/10.1103/PhysRevD.83.014018`, `doi:10.1103/PhysRevD.83.014018`.

[141] T. Pierog and K. Werner. Muon production in extended air shower simulations. *Phys. Rev. Lett.*, 101:171101, Oct 2008. URL: `http://link.aps.org/doi/10.1103/PhysRevLett.101.171101`, `doi:10.1103/PhysRevLett.101.171101`.

[142] M.G. Aartsen et al. Search for Time-independent Neutrino Emission from Astrophysical Sources with 3 yr of IceCube Data. *Astrophys.J.*, 779:132, 2013. `arXiv:1307.6669`, `doi:10.1088/0004-637X/779/2/132`.

[143] Byron P. Roe, Hai-Jun Yang, Ji Zhu, Yong Liu, Ion Stancu, et al. Boosted decision trees, an alternative to artificial neural networks. *Nucl.Instrum.Meth.*, A543:577–584, 2005. `arXiv:physics/0408124`, `doi:10.1016/j.nima.2004.12.018`.

[144] J. Braun, J. Dumm, F. de Palma, C. Finley, A. Karle, and T. Montaruli. Methods for point source analysis in high energy neutrino telescopes. *Astroparticle Physics*, 29:299–305, May 2008. `arXiv:0801.1604`, `doi:10.1016/j.astropartphys.2008.02.007`.

[145] S. S. Wilks. The large-sample distribution of the likelihood ratio for testing composite hypotheses. *The Annals of Mathematical Statistics*, 9(1):60–62, 03 1938. URL: `http://dx.doi.org/10.1214/aoms/1177732360`, `doi:10.1214/aoms/1177732360`.

[146] R. Abbasi et al. An improved method for measuring muon energy using the truncated mean of dE/dx. *Nucl.Instrum.Meth.*, A703:190–198, 2013. `arXiv:1208.3430`, `doi:10.1016/j.nima.2012.11.081`.

[147] M.G. Aartsen et al. Searches for Extended and Point-like Neutrino Sources with Four Years of IceCube Data. 2014. `arXiv:1406.6757`.

[148] M.G. Aartsen et al. Searches for small-scale anisotropies from neutrino point sources with three years of IceCube data. 2014. `arXiv:1408.0634`.

[149] M.C. Gonzalez-Garcia, F. Halzen, and V. Niro. Reevaluation of the Prospect of Observing Neutrinos from Galactic Sources in the Light of Recent Results in Gamma Ray and Neutrino Astronomy. *Astropart.Phys.*, 57-58:39–48, 2014. `arXiv:1310.7194`, `doi:10.1016/j.astropartphys.2014.04.001`.

[150] M. G. Aartsen et al. Long Term Search for Flaring Neutrino Sources with the IceCube Detector. *Astrophys. J.in Prep*, 2014.

[151] S. Adrian-Martinez et al. Search for Cosmic Neutrino Point Sources with Four Year Data of the ANTARES Telescope. *Astrophys.J.*, 760:53, 2012. `arXiv:1207.3105`, `doi:10.1088/0004-637X/760/1/53`.

[152] J. Neyman. Outline of a theory of statistical estimation based on the classical theory of probability. *Phil. Trans. Royal Soc. London, Series A*, 236:333–80, 1937.

[153] Stefan Schonert, Thomas K. Gaisser, Elisa Resconi, and Olaf Schulz. Vetoing atmospheric neutrinos in a high energy neutrino telescope. *Phys.Rev.*, D79:043009, 2009. `arXiv:0812.4308`, `doi:10.1103/PhysRevD.79.043009`.

[154] Thomas K. Gaisser, Kyle Jero, Albrecht Karle, and Jakob van Santen. A generalized self-veto probability for atmospheric neutrinos. *Phys.Rev.*, D90:023009, 2014. `arXiv:1405.0525`, `doi:10.1103/PhysRevD.90.023009`.

[155] M.G. Aartsen et al. Search for a diffuse flux of astrophysical muon neutrinos with the IceCube 59-string configuration. *Phys.Rev.*, D89:062007, 2014. `arXiv:1311.7048`, `doi:10.1103/PhysRevD.89.062007`.

[156] T. K. Gaisser. Atmospheric leptons. the search for a prompt component. In *European Physical Journal Web of Conferences*, volume 52 of *European Physical Journal Web of Conferences*, page 9004, June 2013. `arXiv:1303.1431`, `doi:10.1051/epjconf/20125209004`.

[157] Jim Braun, Mike Baker, Jon Dumm, Chad Finley, Albrecht Karle, et al. Time-Dependent Point Source Search Methods in High Energy Neutrino Astronomy. *Astropart.Phys.*, 33:175–181, 2010. `arXiv:0912.1572`, `doi:10.1016/j.astropartphys.2010.01.005`.

[158] M.G. Aartsen et al. Model Independent Search For GRB Neutrinos Interacting Inside IceCube. In *Proc. of the 33rd ICRC*, 2013. `arXiv:1309.6979`.

[159] Yang Bai, Ran Lu, and Jordi Salvado. Geometric Compatibility of IceCube TeV-PeV Neutrino Excess and its Galactic Dark Matter Origin. 2013. `arXiv:1311.5864`.

[160] A. M. Taylor, S. Gabici, and F. Aharonian. Galactic halo origin of the neutrinos detected by IceCube. *Phys. Rev. D*, 89(10):103003, May 2014. `arXiv:1403.3206`, `doi:10.1103/PhysRevD.89.103003`.

[161] F. Aharonian et al. A detailed spectral and morphological study of the gamma-ray supernova remnant rx j1713.7-3946 with h.e.s.s. *Astron.Astrophys.*, 449:223–242, 2006. `arXiv:astro-ph/0511678`, `doi:10.1051/0004-6361:20054279`.

[162] A. Abramowski, F. Acero, F. Aharonian, A.G. Akhperjanian, G. Anton, et al. Probing the extent of the non-thermal emission from the Vela X region at TeV energies with H.E.S.S. *Astron.Astrophys.*, 548:A38, 2012. `arXiv:1210.1359`, `doi:10.1051/0004-6361/201219919`.

[163] M. G. Aartsen et al. Search for a diffuse flux of astrophysical muon neutrinos with the IceCube 59-string configuration. *Phys. Rev. D*, 89(6):062007, March 2014. `arXiv:1311.7048`, `doi:10.1103/PhysRevD.89.062007`.

[164] P. Bagley et al. *KM3NeT Technical Design Report for a Deep-Sea Research Infrastructure Incorporating a Very Large Volume Neutrino Telescope.* KM3NeT Consortium, 2011. `http://km3net.org/TDR/TDRKM3NeT.pdf`.

[165] Bennett Link and Fiorella Burgio. Flux predictions of high-energy neutrinos from pulsars. *Mon.Not.Roy.Astron.Soc.*, 371:375–379, 2006. `arXiv:astro-ph/0604379`, `doi:10.1111/j.1365-2966.2006.10665.x`.

[166] D.B. Fox, K. Kashiyama, and P. Mszars. Sub-PeV Neutrinos from TeV Unidentified Sources in the Galaxy. *Astrophys.J.*, 774:74, 2013. `arXiv:1305.6606`, `doi:10.1088/0004-637X/774/1/74`.

[167] Nicolas M. Barrire, John A. Tomsick, Frederick K. Baganoff, Steven E. Boggs, Finn E. Christensen, et al. NuSTAR Detection of High-energy X-Ray Emission and Rapid Variability from Sagittarius A* Flares. *Astrophys.J.*, 786:46, 2014. `arXiv:1403.0900`, `doi:10.1088/0004-637X/786/1/46`.

[168] F. Acero et al. Localising the VHE gamma-ray source at the Galactic Centre. *Mon.Not.Roy.Astron.Soc.*, 402:1877–1882, 2010. `arXiv:0911.1912`, `doi:10.1111/j.1365-2966.2009.16014.x`.

[169] Tova M. Yoast-Hull, J.S. Gallagher, and Ellen G. Zweibel. The Cosmic Ray Population of the Galactic Central Molecular Zone. 2014. `arXiv:1405.7059`.

[170] Soebur Razzaque. The Galactic Center Origin of a Subset of IceCube Neutrino Events. *Phys.Rev.*, D88:081302, 2013. `arXiv:1309.2756`, `doi:10.1103/PhysRevD.88.081302`.

[171] A.D. Supanitsky. Gamma rays and neutrinos from a cosmic ray source in the Galactic Center region. 2013. `arXiv:1312.7304`.

[172] V.A. Acciari et al. Observations of the shell-type SNR Cassiopeia A at TeV energies with VERITAS. *Astrophys.J.*, 714:163–169, 2010. `arXiv:1002.2974`, `doi:10.1088/0004-637X/714/1/163`.

[173] A. A. Abdo et al. Fermi-Lat Discovery of GeV Gamma-Ray Emission from the Young Supernova Remnant Cassiopeia A. *Astrophys. J. Lett.*, 710:L92–L97, February 2010. `arXiv:1001.1419`, `doi:10.1088/2041-8205/710/1/L92`.

[174] J. Albert et al. Observation of VHE gamma-rays from Cassiopeia A with the MAGIC telescope. *Astron.Astrophys.*, 474:937–940, 2007. `arXiv:0706.4065`, `doi:10.1051/0004-6361:20078168`.

[175] V.A. Acciari et al. Observation of Extended VHE Emission from the Supernova Remnant IC 443 with VERITAS. *Astrophys.J.*, 698:L133–L137, 2009. `arXiv:0905.3291`, `doi:10.1088/0004-637X/698/2/L133`.

[176] A.A. Abdo, M. Ackermann, M. Ajello, L. Baldini, J. Ballet, et al. Observation of Supernova Remnant IC443 with the Fermi Large Area Telescope. *Astrophys.J.*, 712:459–468, 2010. `arXiv:1002.2198`, `doi:10.1088/0004-637X/712/1/459`.

[177] Diego F. Torres, Ana Y. Rodriguez Marrero, and Elsa de Cea del Pozo. MAGIC J0616+225 as delayed TeV emission of cosmic-rays diffusing from SNR IC 443. *Mon.Not.Roy.Astron.Soc.*, 387:L59–L63, 2008. `arXiv:0804.2526`, `doi:10.1111/j.1745-3933.2008.00485.x`.

[178] M. Ackermann et al. The Imprint of The Extragalactic Background Light in the Gamma-Ray Spectra of Blazars. *Science*, 338:1190–1192, 2012. `arXiv:1211.1671`, `doi:10.1126/science.1227160`.

[179] Henric Krawczynski, S.B. Hughes, D. Horan, F. Aharonian, M.F. Aller, et al. Multiwavelength observations of strong flares from the TeV - blazar 1ES 1959+650. *Astrophys.J.*, 601:151–164, 2004. `arXiv:astro-ph/0310158`, `doi:10.1086/380393`.

[180] Sarira Sahu, Andres Felipe Osorio Oliveros, and Juan Carlos Sanabria. Hadronic-origin orphan TeV flare from 1ES 1959+650. *Phys.Rev.*, D87(10):103015, 2013. `arXiv:1305.4985`, `doi:10.1103/PhysRevD.87.103015`.

[181] F. Aharonian, A. Akhperjanian, and M. Beilicke. Detection of TeV gamma-rays from the bl lac 1es1959+650 in its low states and during a major outburst in 2002. *Astron.Astrophys.*, 406:L9–L14, 2003. `arXiv:astro-ph/0305275`, `doi:10.1051/0004-6361:20030838`.

[182] Michael K. Daniel et al. Spectrum of very high energy gamma-rays from the blazar 1ES1959+650 during flaring activity in 2002. *Astrophys.J.*, 621:181, 2005. `arXiv:astro-ph/0503085`, `doi:10.1086/427406`.

[183] J. Albert et al. Observation of VHE gamma-ray emission from the active galactic nucleus 1ES1959+650 using the Magic Telecope. *Astrophys.J.*, 639:761–765, 2006. `arXiv:astro-ph/0508543`, `doi:10.1086/499421`.

[184] R. Abbasi et al. Time-Dependent Searches for Point Sources of Neutrinos with the 40-String and 22-String Configurations of IceCube. *Astrophys.J.*, 744:1, 2012. `arXiv:1104.0075`, `doi:10.1088/0004-637X/744/1/1`.

[185] F. Krennrich, S.D. Biller, I.H. Bond, P.J. Boyle, S.M. Bradbury, et al. Measurement of the multi-TeV gamma-ray flare spectra of Markarian 421 and Markarian 501. *Astrophys.J.*, 1998. `arXiv:astro-ph/9808333`.

[186] F.A. Aharonian et al. Observations of mkn 421 during 1997 and 1998 in the energy range above 500 gev with the hegra stereoscopic Cherenkov telescope system. 1999. `arXiv:astro-ph/9905032`.

[187] F. Aharonian et al. Variations of the TeV energy spectrum at different flux levels of Mkn 421 observed with the HEGRA system of Cherenkov telescopes. *Astron.Astrophys.*, 393:89–100, 2002. `arXiv:astro-ph/0205499`, `doi:10.1051/0004-6361:20021005`.

[188] Kulkeep K. Yadav, P. Chandra, A.K. Tickoo, R.C. Rannot, S. Godambe, et al. Observations of TeV gamma-rays from Mrk 421 during Dec. 2005 to Apr. 2006 with the TACTIC telescope. *Astropart.Phys.*, 27:447–454, 2007. `arXiv:astro-ph/0701890`, `doi:10.1016/j.astropartphys.2007.01.005`.

[189] P. Chandra, R.C. Rannot, K.K. Yadav, A.K. Tickoo, K.K. Singh, et al. TeV Gamma-ray Observations of Markarian 421 using TACTIC during 2009-10. *J.Phys.*, G39:045201, 2012. `arXiv:1202.2984`, `doi:10.1088/0954-3899/39/4/045201`.

[190] F. Aharonian et al. Discovery of very high energy gamma-ray emission from Centaurus A with H.E.S.S. *Astrophys.J.*, 695:L40–L44, 2009. `arXiv:0903.1582`, `doi:10.1088/0004-637X/695/1/L40`.

[191] A.A. Abdo et al. Fermi Large Area Telescope View of the Core of the Radio Galaxy Centaurus A. *Astrophys.J.*, 719:1433–1444, 2010. `arXiv:1006.5463`, `doi:10.1088/0004-637X/719/2/1433`.

[192] J. van Santen. Recent results from neutrino telescopes. Presented at International Symposium on Very High Energy Cosmic Ray Interactions, CERN, Switzerland, 2014. URL: `https://indico.cern.ch/event/287474/`.

[193] C. Weaver. Icecube results for diffuse muon neutrinos. American Physical Society (APS) April Meeting, Savannah, Georgia, 2014. URL: `http://meetings.aps.org/link/BAPS.2014.APR.R8.1`.

[194] Markus Ahlers and Francis Halzen. Pinpointing Extragalactic Neutrino Sources in Light of Recent IceCube Observations. 2014. `arXiv:1406.2160`.

[195] Julia K. Becker, Wolfgang Rhode, Peter L. Biermann, and Kirsten Muenich. Astrophysical implications of high energy neutrino limits. 1. Overall diffuse limits. *Astropart.Phys.*, 28:98–118, 2008. `arXiv:astro-ph/0607427`, `doi:10.1016/j.astropartphys.2007.04.007`.

[196] Paolo Lipari. Perspectives of High Energy Neutrino Astronomy. *Nucl.Instrum.Meth.*, A567:405–417, 2006. `arXiv:astro-ph/0605535`, `doi:10.1016/j.nima.2006.05.249`.

[197] Martin Leuermann. Search for Diffuse Neutrino Point Sources Using a Multipole Analysis in IceCube. Master's thesis, RWTH Aachen University, 2013. URL: `http://www.physik.rwth-aachen.de/fileadmin/user_upload/www_physik/Institute/Inst_3B/Forschung/IceCube/publications/thesis_ML.pdf`.

[198] Pedro Abreu et al. Bounds on the density of sources of ultra-high energy cosmic rays from the Pierre Auger Observatory. *JCAP*, 1305:009, 2013. `arXiv:1305.1576`, `doi:10.1088/1475-7516/2013/05/009`.

[199] C. Blaksley, E. Parizot, G. Decerprit, and D. Allard. Ultra-high-energy cosmic ray source statistics in the GZK energy range. *A&A*, 552:A125, 2013. URL: `http://dx.doi.org/10.1051/0004-6361/201220178`, `doi:10.1051/0004-6361/201220178`.

[200] M. Ajello, M.S. Shaw, R.W. Romani, C.D. Dermer, L. Costamante, et al. The Luminosity Function of Fermi-detected Flat-Spectrum Radio Quasars. *Astrophys.J.*, 751:108, 2012. `arXiv:1110.3787`, `doi:10.1088/0004-637X/751/2/108`.

[201] M.G. Aartsen et al. Letter of Intent: The Precision IceCube Next Generation Upgrade (PINGU). 2014. `arXiv:1401.2046`.